Early Stages of High-Mass Star Formation: A Multiwavelength Investigation

A thesis submitted

in partial fulfillment for the award of the degree of

Doctor of Philosophy

by

NAMITHA ISSAC

Department of Earth and Space Sciences

Indian Institute of Space Science and Technology

Thiruvananthapuram, India

April 2021

Certificate

This is to certify that the thesis titled ***Early Stages of High-Mass Star Formation: A Multiwavelength Investigation*** submitted by **Namitha Issac**, to the Indian Institute of Space Science and Technology, Thiruvananthapuram, in partial fulfillment for the award of the degree of **Doctor of Philosophy** is a bona fide record of the original work carried out by her under my supervision. The contents of this thesis, in full or in parts, have not been submitted to any other Institute or University for the award of any degree or diploma.

Dr Anandmayee Tej
Professor
Dept. of Earth and Space Sciences

Dr Samir Mandal
Associate Professor & Head
Dept. of Earth and Space Sciences

Place: Thiruvananthapuram
Date: April 2021

Declaration

I declare that this thesis titled ***Early Stages of High-Mass Star Formation: A Multiwavelength Investigation*** submitted in partial fulfillment for the award of the degree of **Doctor of Philosophy** is a record of the original work carried out by me under the supervision of **Prof Anandmayee Tej**, and has not formed the basis for the award of any degree, diploma, associateship, fellowship, or other titles in this or any other Institution or University of higher learning. In keeping with the ethical practice in reporting scientific information, due acknowledgments have been made wherever the findings of others have been cited.

Place: Thiruvananthapuram
Date: April 2021

NAMITHA ISSAC
(SC16D001)

This thesis is dedicated to all the molecular clouds in the Universe waiting for any reason to form stars, all the protons waiting in queue to fuse to let a star shine bright, and all the other cosmic events for making the night sky a beautiful sight and an inspiration to keep going . . .

Acknowledgements

Words cannot describe the immense gratitude I have for my supervisor, Prof Anandmayee Tej. She has been more than a mentor to me, a true guide in every sense of the word. More than showering me with her vast knowledge, she instilled in me the vigour to learn and ask questions. She has kept me motivated throughout my PhD days, especially during some of the hard times. Thank you, for always pushing me just enough that I keep moving, but never tumble over. Your passion, zeal, and work ethics are some of the unmatched qualities I yearn to enforce in my life.

I am extremely thankful to my collaborators who have helped me shape my research with their valuable inputs and suggestions. I especially would like to thank Dr Tie Liu (SAO, China) for all his help and support during my research. Discussions with him have always been fruitful. I would also like to express my sincere thanks to Dr Watson Varricatt (UKIRT, USA) for his continued help and time with UKIRT data reduction and analysis. Speaking of data reduction, I cannot thank Dr Ishwara Chandra C H. (NCRA, Pune) enough. Being an expert in the field of radio astronomy, he has always been gracious enough to impart his vast knowledge in the field and have helped immeasurably with the radio data analysis. I would also like to express my sincere gratitude to Dr Sarita Vig (IIST), Dr Mathias Schultheis (Observatoire de la Côte, France), Dr Govind Nandakumar (ANU, Australia), and Dr Yuefang Wu (Peking University, China) for all the valuable discussions during the preparation of the manuscript drafts.

For the conversations I used to have with the faculty members of the Astronomy and Astrophysics group of IIST, Dr Anand Narayanan, Dr Jagadheep D, Dr Resmi Lekshmi, and Dr Samir Mandal, that have always yielded fruitful insights and kept me motivated, I am truly grateful. I am indebted to the members of my Doctoral Committee– Prof Chandrasekar A (Chairman, IIST), Dr Maheshwar Gopinath (IIA, Bangalore), Dr U S Kamath (IIA, Bangalore), Dr Samir Mandal (IIST), and Dr Naveen Surendran (IIST), for the constant assessment of my work. Their constructive criticisms have tremendously helped in enhancing the quality of my research. I thank Dr K S Dasgupta, former Director and Dr V K Dadhwal, present Director of IIST for providing the facilities and academic support to successfully carry out my research work at IIST. I also thank Dr Raju K George (Dean of Research and Development) and Dr Kuruvilla Joseph (Dean of Student Activities) for the

academic assistance. I am also thankful to the Research Council of IIST for their constant backing at all stages of the PhD program.

I wish to thank the staff of GMRT for the help with radio observations, that I have used extensively in my research work. I am truly obliged to our lab tutor, Mr Sai Krishnan. He has been of enormous help in the lab and has always managed to spiritually uplift me. A huge thanks to all the staff members of the Department for their endless help. I also would like to thank the administration, library, and canteen staff members of IIST, for all the support that made my stay in IIST comfortable.

It would be a great injustice if I do not acknowledge some really great souls who have made my roller-coaster life in IIST as exciting as it was. First of all, a huge thanks to all the fellow PhD, Master, and project students, whom I shared lab space with. Interactions with you have always been enjoyable. Special thanks to Kshitija, Kartika, Somnath, Suma, Jim, Joel, Ruskin, Prachi, Swapnil, Ravi, Sarwar, Sonu, Geethu, Sreelakshmi, Jyotirmoy, and Anindya. I cannot thank enough my ever so helpful senior, Dr Swagat Ranjan Das, for being an informal guide and always encouraging me. I owe a great deal to Dr Veena V S for being my go-to person everything astronomy. A big shout out to some very special people − Soumya, Fayza, Praveen and Manu, for listening to me vent when things got stressful; Veena, Aneesha, Ashish, and Sreelekshmi (the other one), for being my food, travel, and fun buddies; Shalina and Resmi, my ex- and current badminton partners, respectively, and my travel companions on the little road trips we took. Warm hugs to two people who are very close to my heart, Anupama and Dinil. You have always been by my side, even during the difficult times, and been my crutches I could lean on whenever I stumbled.

No words can justify the love and support my best friends, Veena, Devi and Simiya, have given me. Though I do not get to see you often, you have always managed to keep my sanity in check.

Last, but never the least, the biggest praise of all, goes to my family. They gave me wings to fly and asked me to fly to the stars, and guess what!, I have a thesis on stars. Their unwavering encouragement and reassurance have given me the confidence to tread the path of astronomy. My mother, Elizabeth, for your unconditional love and my father, Issac, for your lessons of perseverance, I thank you with every cell in my body, for you have led by example and not by words. Finally, I am eternally grateful to my dearest big brother, Richie, who has always been my pillar of support all my life.

NAMITHA ISSAC

Abstract

Massive stars ($M \gtrsim 8\,M_{\odot}$), through their radiative, mechanical and chemical feedback, play a vital role in the evolution of the galaxies and hence the Universe. Given their enormous luminosity of the order of $\sim 10^5\,L_{\odot}$, they dictate the energy budget of galaxies through powerful winds, strong radiations and supernova events. Despite being a key player, most aspects of the processes involved in the formation of massive stars remain unclear in both the observational as well as the theoretical front. Being deeply embedded, short-lived, and rare, poses observational challenges in studying this mass regime. Though several statistical studies have been conducted to explore the generic properties of high-mass star-forming regions, observational studies focussing on individual star-forming regions are few, especially towards the the initial stages of formation.

This motivates the investigation on the early phases of high-mass star formation presented in this thesis. Towards achieving this goal, we probe two extended green objects, EGOs G12.42+0.50 and G19.88-0.53, using the data obtained from different telescopes covering a wide wavelength range. These include dedicated observations as well as archival datasets. These sources are selected based on their large angular extent and flux densities at 4.5 μm and also being embedded within infrared dark clouds. The nature of the associated ionized gas emission is examined using low-frequency radio continuum observations carried out using the Giant Meterwave Radio Telescope, India. The ionized component of both EGOs display elongated morphology, with distinct radio components. The spectral index values, lying in the range $0.3 - 0.7$, derived from the radio flux densities, indicate that both the regions are dominated by thermal bremsstrahlung emission. These values of spectral index are consistent with the radio emission arising from an ionized thermal jet. Further, several observational manifestations, like weak radio emission, linear morphology, and association with large-scale molecular outflows with the jet candidate at its centroid, are consistent with the thermal radio jet scenario interpretation from radio observations. Shock-excited lines of H_2 and [FeII], as seen in the near-infrared spectra towards these sources, obtained using the United Kingdom Infrared Telescope, lend further support to the ionized jet scenario. However, given the compact and almost spherical morphology of one of the radio components associated with G12.42+0.50, we investigate the nature of the radio emission under the UC H II region framework under the assumption that the emission at 1390 MHz is optically thin and arises from a spherical, homogeneous and isothermal medium. The Lyman continuum flux hence derived, translates to an ionizing star of spectral type of B1-B0.5. Given compelling evidence supporting, both, the UC H II region and ionized jet scenarios,

we are prompted to consider the coexistence of the UC H II region with the ionized jet, both powered by the same massive young stellar object.

Cold dust emission mapped at far-infrared wavelengths, reveals massive dust clumps of masses $> 1000\,M_{\odot}$ enveloping the EGOs. Zooming-in on the inner regions of these clumps at millimeter wavelengths with high-resolution continuum data from SMA and ALMA unravel the presence of dense and compact dust cores deeply embedded within the cold dust clumps. Based on the mass and size estimates, all the dense cores detected towards G12.42+0.50 and G19.88-0.53 have the potential to form high-mass stars. Signature of a hub-filament system is seen in the *Spitzer*-IRAC 8.0 μm and far-infrared images of G12.42+0.50 and is supported by the constructed H_2 column density and dust temperature maps. Detailed investigation of the molecular gas kinematics using the archival dataset from JCMT agrees with bulk motion in the filaments and suggests a likely picture of gas inflow along the filaments to the massive dust clump enveloping G12.42+0.50. The gas kinematics study using the archival datasets from the MALT90 survey and JCMT also unveils the presence of both infall activity and large-scale outflow, suggesting an early stage of massive star formation in G12.42+0.50. Probing the gas kinematics using the archival ALMA data reveals G19.88-0.53 as an active protocluster with high-mass star-forming components spanning a wide evolutionary spectrum from hot cores in accretion phase to cores driving multiple outflows to possible UC H II regions.

Investigating the star-forming Planck Galactic Cold Clump, G133.50+9.01 using the molecular line observations from the Purple Mountain Observatory reveals a picture of two colliding clouds, G133a and G133b, triggering the formation of a complex network of filaments, dense cores and YSOs. Observational evidence suggests the likelihood of the collision of the two clouds, forming a shock-compressed layer in the intersection region, characterised by broad bridging features, a characteristic signature of cloud-cloud collision. The shocked layer exhibits an arc like morphology with enhanced excitation temperature and H_2 column density. Conforming with magneto-hydrodynamic simulations, the formation of a complex network of filaments with 14 embedded dense cores is deduced from the SCUBA-2 850 μm map, lying along the shocked layer, where the background magnetic field is amplified in the direction perpendicular to the filaments. An over-density of Class I and II YSOs along the intersection arc advocates for collision induced cluster formation in G133.50+9.01.

The in-depth, multiwavelength studies carried out as a part of this thesis work elaborates the potential of such studies to decipher various components and processes involved during the early phases of high-mass stars. Such detailed observational studies are key to establishing the much needed database required to validate the proposed theories.

Contents

List of Figures

List of Tables

Abbreviations

2MASS	2 Micron All Sky Survey
AIPS	Astronomical Image Processing System
ALMA	Atacama Large Millimeter Array
ATLASGAL	APEX Telescope Large Area Survey of the Galaxy
CDMS	Cologne Database for Molecular Spectroscopy
CMC	Cold Molecular Core
EGO	Extended Green Object
EM	Emission Measure
FIR	Far Infrared
FWHM	Full Width Half Maximum
GLIMPSE	Galactic Legacy Infrared Mid-Plane Survey Extraordinaire
GMC	Giant Molecular Cloud
GMRT	Giant Meterwave Radio Telescope
hfs	Hyperfine Structure
HC H II	Hypercompact H II Region
Hi-Gal	Herschel Infrared Galactic Plane Survey
HIPE	Herschel Interactive Processing Environment
HMC	Hot Molecular Core
HPBW	Half Power Bandwidth
IF	Ionization Front
IMF	Intial Mass Function
ISM	Interstellar Medium
IR	Infrared
IRAC	Infrared Array Camera
IRAS	Infra-Red Astronomical Satellite
IRDC	Infrared Dark Cloud
IRSA	Infrared Science Archive
JCMT	James Clerk Maxwell Telescope

LABOCA	Large APEX Bolometer Camera
LSR	Local Standard of Rest
LTE	Local Thermodynamic Equilibrium
MALT90 survey	Millimeter Astronomy Legacy Team 90 GHz survey
MIPS	Multiband Imaging Photometer for Spitzer
MIR	Mid Infrared
MSX	Midcourse Space Experiment
MYSO	Massive Young Stellar Object
NIR	Near Infrared
PACS	Photodetector Array Camera and Spectrometer
PDF	Probability Density Function
PSF	Point Spread Function
RMS survey	Red MSX Source Survey
SCUBA	Submillimetre Common-User Bolometer Array
SED	Spectral Energy Distribution
SMA	Submillimeter Array
SPIRE	Spectral and Photometric Imaging Receiver
TRAO	Taeduk Radio Astronomy Observatory
UC H II	Ultracompact H II Region
UIST	UKIRT Imager-Spectrometer
UKIDSS	UKIRT Infrared Deep Sky Survey
UKIRT	United Kingdom Infrared Telescope
UV	Ultra Violet
UWISH2	UKIRT Widefield Infrared Survey for H_2
WFCAM	Wide-Field Camera
WISE	Wide-field Infrared Survey Explorer
YSO	Young Stellar Object
ZAMS	Zero Age Main Sequence

Chapter 1

Introduction

The night sky has always intrigued the imagination of humankind since time immemorial. It has driven the best of minds to explore its vastness and the mysteries that lay within. The most fascinating of the night sky are the twinkling tiny specks, the stars. Stars constitute the fundamental building blocks of the Universe and are the primary tracers that unravel the history, structure and evolution of the Universe and its constituents. Hence, understanding their formation and properties are of paramount importance in astrophysics. Furthermore, the process of star formation influences the galaxy at all scales. While the numbers are dominated by the low-mass population, massive stars ($M \gtrsim 8\,M_{\odot}$), with their enormous luminosity of the order of $10^5\,L_{\odot}$ (Mottram et al., 2011), dictate the energy budget and hence the evolution of the galaxy. This mass regime has profound influence on the surrounding, ambient interstellar medium (ISM) through energetic stellar winds, large-scale molecular outflows, powerful radiation and supernova events at different phases of their lifetime. They emit copious amount of ultraviolet (UV) photons that can ionize the surrounding medium, resulting in expanding shock waves that can both initiate and inhibit star formation. As they approach the end of their spectacular life, massive stars bid adieu with a supernova explosion, which is by far the most enigmatic and energetic of stellar events. This cataclysmic event hurls the heavier elements synthesized in the stellar interior during the nuclear burning stages into the ISM, thus enriching it and also triggering further star formation. In spite of their consequential importance, most aspects (both theoretically and observationally) of the processes involved in the formation of massive stars are far less understood in contrast to the low-mass domain. Deciphering the initial stages of high-mass stars is particularly challenging and forms the basis of the observational investigations presented in this thesis.

1.1 Star formation in a nutshell

Stars form from the gravitational collapse of interstellar clouds. This seemingly simple and widely accepted statement encompasses a whole field of astrophysics that is still evolving. The intricacies involved in the formation process, particularly for the massive stars, are rather complicated. An overwhelming number of studies in the observational, theoretical, and computational front, have been carried out over the last few decades (e.g. Bonnell, Bate & Zinnecker, 1998; Kennicutt & Evans, 2012; Lada & Shu, 1990; McKee & Ostriker, 2007; Shu, Adams & Lizano, 1987; Zinnecker & Yorke, 2007). A broad overview of star formation is discussed in this section.

Stars form within cold, dense complexes of the ISM. These stellar nurseries are the *giant molecular clouds* (GMCs). GMCs are massive condensations, primarily composed of molecular hydrogen (H_2; $\sim 70\%$), helium and traces of heavier elements. Given that the H_2 molecule is homonuclear and symmetrical, it is not detected at the typical temperatures of GMCs ($10 - 15\,\mathrm{K}$). Instead, low transitions (e.g. $J = 1 - 0$ and $J = 2 - 1$) of the CO molecule, which are easily excited at these temperatures, are used as proxy for H_2 to trace the molecular gas distribution and study their characteristics. As seen from large-scale CO observations, GMCs are some of the largest structures in the Galaxy (e.g. the Orion nebula with a size of $\sim$120 pc; Stahler & Palla 2004). Typically, the masses are of the order of $10^4 - 10^6\,M_\odot$ and sizes range around $50 - 200\,\mathrm{pc}$ (Beuther et al., 2007; Williams, Blitz & McKee, 2000). The interstellar clouds can be broadly classified into three types: (1) dark clouds, made of gas at very low temperature ($\mathrm{T} \sim 10 - 20\,\mathrm{K}$) with high extinction, (2) diffuse clouds consisting of cold ($\mathrm{T} \sim 100\,\mathrm{K}$) atomic gas with low extinction, barring absorption at certain wavelengths, and (3) translucent clouds that are made of atomic and molecular gas with intermediate extinction (Ferrière, 2001).

Observations reveal that GMCs are inhomogeneous or "clumpy" with local regions of enhanced density (e.g. Bronfman et al., 1989; Myers & Benson, 1983). Based on the observed inhomogeneity and the associated substructures seen, Williams, Blitz & McKee (2000) propose a hierarchical classification into clouds, clumps, and cores. Clouds fragment to form 'clumps' that are agglomeration of material that further fragment into smaller units with higher temperatures and densities, called the 'cores'. These cores are the smallest structures in the cascading fragmentation of the GMCs. Depending on the stage of evolution of the cores, they are further classified as cold molecular cores (CMCs) or hot molecular cores (HMCs), the latter group involves internal heating due to newly forming stars. A pictorial representation of this hierarchical structure inside molecular clouds is depicted in

Fig. 1.1. The physical properties of these substructures are compiled from various papers (e.g. Beuther et al., 2007; Tan et al., 2014; Williams, Blitz & McKee, 2000) and presented in Table 1.1. In addition to the clumps and cores, interesting filamentary nature of GMCs is unveiled in large-scale mapping surveys of the Galactic plane in the far-infrared (FIR) regime (e.g. *Herschel* infrared Galactic plane survey (Hi-GAL), Molinari et al. 2010; Gould Belt Survey, André et al. 2010) carried out using the *Herschel Space Observatory* (Pilbratt et al., 2010). The complicated networks of filaments are believed to originate due to the supersonic turbulence in the ISM that pushes and compresses low-density gas into layers (André et al., 2014, and references there in). The compression due to supersonic turbulence along with gravity, causes the denser regions of the filaments to undergo gravitational collapse to form stars. Apart from these regions of enhanced density, several high-density clumps are also detected at locations where the filaments interact. Such structures, referred to as 'hub-filament systems', are common sites of high-mass star formation (e.g. Myers, 2009; Peretto et al., 2012; Yuan et al., 2018). Typically, these filaments have length scales of the order of $\sim$1 pc and central width of $\sim$0.1 pc (André et al., 2014). In some infrared dark clouds (IRDCs), the filament lengths reach upto several tens of pc (e.g. Beuther et al., 2011; Jackson et al., 2010).

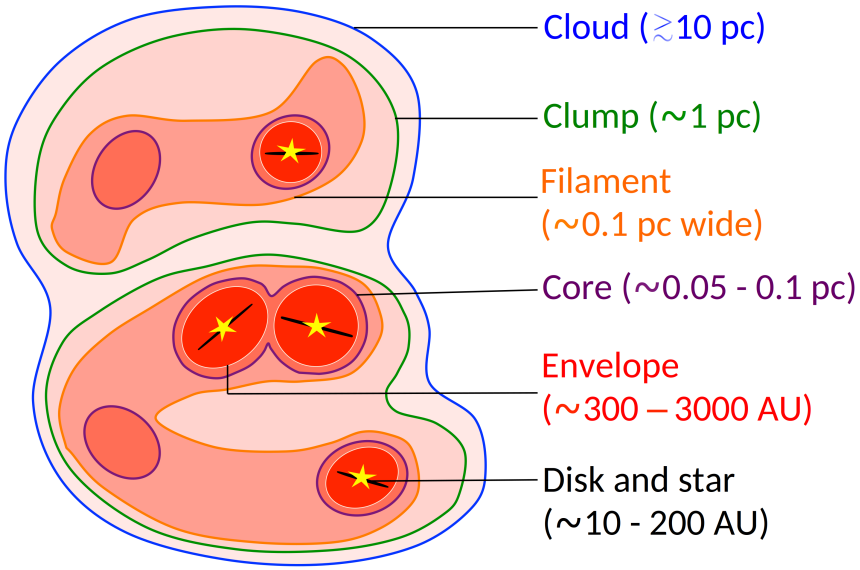

Figure 1.1: A pictorial representation of a molecular cloud showing hierarchical structures. This figure is taken from Pokhrel et al. (2018).

On galactic scales, the galactic tidal forces play a vital role and collapse happens if the gas becomes dense enough for its self-gravity to dominate. In comparison, the mechanisms differ at the GMC scale. Here, magnetic fields and turbulence become important along

Table 1.1: Physical properties of structures within the molecular clouds complied from various papers (Beuther et al., 2007; Tan et al., 2014; Williams, Blitz & McKee, 2000).

Component	Size (pc)	Mass ($M_\odot$)	Temperature (K)	Density (cm^{-3})
GMC	$50 - 200$	$10^4 - 10^6$	$10 - 15$	$10 - 300$
Cloud	$3 - 20$	$10^3 - 10^4$	$15 - 30$	$10^3 - 10^4$
Clump	$0.5 - 3$	$10^3 - 10^4$	$15 - 40$	$10^4 - 10^6$
CMC	$0.1 - 0.5$	$10^2 - 10^3$	$30 - 100$	$10^5 - 10^7$
HMC	≤ 0.1	10^2	$100 - 200$	$10^6 - 10^8$

with thermal pressure in counteracting gravity. The collapse process thus involves the dissipation of magnetic and turbulent support. This is achieved through the mechanism of *ambipolar diffusion* (also referred to as *ion-neutral drift*). The ionized particles in the GMCs are bound to the magnetic field, but the dominant neutral particles are not. Since the ionization fraction of the GMCs is sufficiently low ($\sim 10^{-6}$ or lower), the neutrals gradually drift across the magnetic field lines and allow contraction to proceed. The clouds eventually lose the magnetic and turbulent support, causing them to collapse on free-fall timescale. At this stage, the cloud maintains equilibrium only through thermal pressure balancing forces of self-gravity. Star formation ensues with density fluctuations in an initially uniform medium. For an isothermal medium with initial average density, ρ, and temperature, T, the minimum mass for gravitationally unstable density fluctuation, the *Jeans* mass, is given as (Spitzer, 1978)

$$M_J = \frac{5.57\, c^3}{G^{3/2}\, \rho^{1/2}} \tag{1.1}$$

where, $c = (kT/m)^{1/2}$ (k is the Boltzmann constant and m is the average particle mass) is the isothermal sound speed and G is the gravitational constant. Notwithstanding the inconsistency in the above formalism arising by not taking the collapse of the background medium into account (referred to as *Jeans swindle*; Binney & Tremaine 1987), *Jeans* mass provides a good estimate of the minimum mass at which the system undergoes gravitational collapse.

Density fluctuations are triggered by energetic events like shock propagation from a nearby supernova explosion, intense UV radiation and stellar wind/jets from massive stars, or collision of GMCs. Once the gravity dominates the internal pressure, the collapse of a spherical

cloud of uniform density ρ, occurs at the free-fall timescale (Shu, Adams & Lizano, 1987)

$$t_{\rm ff} = \left(\frac{3\pi}{32G\rho}\right)^{-0.5} = 3.4 \times 10^7 \, {\rm n}^{-0.5} \, {\rm yr} \tag{1.2}$$

where G is the gravitational constant and n is the number density. For a typical molecular cloud density of $n = 10^3 - 10^4 \, {\rm cm}^{-3}$ (refer Table 1.1), the free-fall timescale, $t_{\rm ff} \approx 10^6 - 10^5$ yr.

In the initial stages of contraction, the cloud is optically thin and hence the collapse happens isothermally. The gravitational energy lost during free-fall is radiated away without heating the cloud. Since the temperature remains constant and the density is increasing, the *Jeans* mass decreases. Any density fluctuations in the cloud leads to formation of clumps and cores within the collapsing cloud as the *Jeans* mass condition is locally satisfied. Such a cascading fragmentation results in the clumpy nature of the molecular clouds and the hierarchical structure observed. The cascading fragmentation ceases as the density increases and the cloud fragment becomes optically thick making the loss of potential energy as heat less efficient. This increases the temperature, and eventually, a critical density is reached, above which collapse becomes adiabatic, thus, inhibiting further fragmentation as the *Jeans* mass now increases with increase in temperature. This results in the formation of the smallest fragment which is classified as the core in the hierarchical structure. These cores act as 'seeds' for single star or binary system formation. Subsequently, the 'inside-out' collapse of this smallest fragment results in a 'core-halo' structure with a slowly contracting central core surrounded by an infalling envelope. The collapse continues until, eventually, the temperature at the core can exert a thermal pressure large enough to counter balance the gravitational contraction, leading to the formation of a hydrostatic core $-$ the forming protostar. The following sections give a brief outline of the theories of low-mass and high-mass star formation at different scales of the dense cores.

1.1.1 Formation of low-mass stars

The larger abundance of low-mass stars compared to high-mass stars (Kroupa, 2001); (Salpeter, 1955) and the proximity of low-mass star-forming regions to the Sun have aided the study of formation of low-mass stars in great detail. Understanding the processes involved in the formation of low-mass stars is the first step in proceeding towards deciphering the complexities associated with high-mass star formation. Excellent reviews on the theory of low-mass star formation are presented by Shu, Adams & Lizano (1987), Lada & Shu (1990) and Kennicutt & Evans (2012). A brief overview, adapted from these papers, is

discussed in this section.

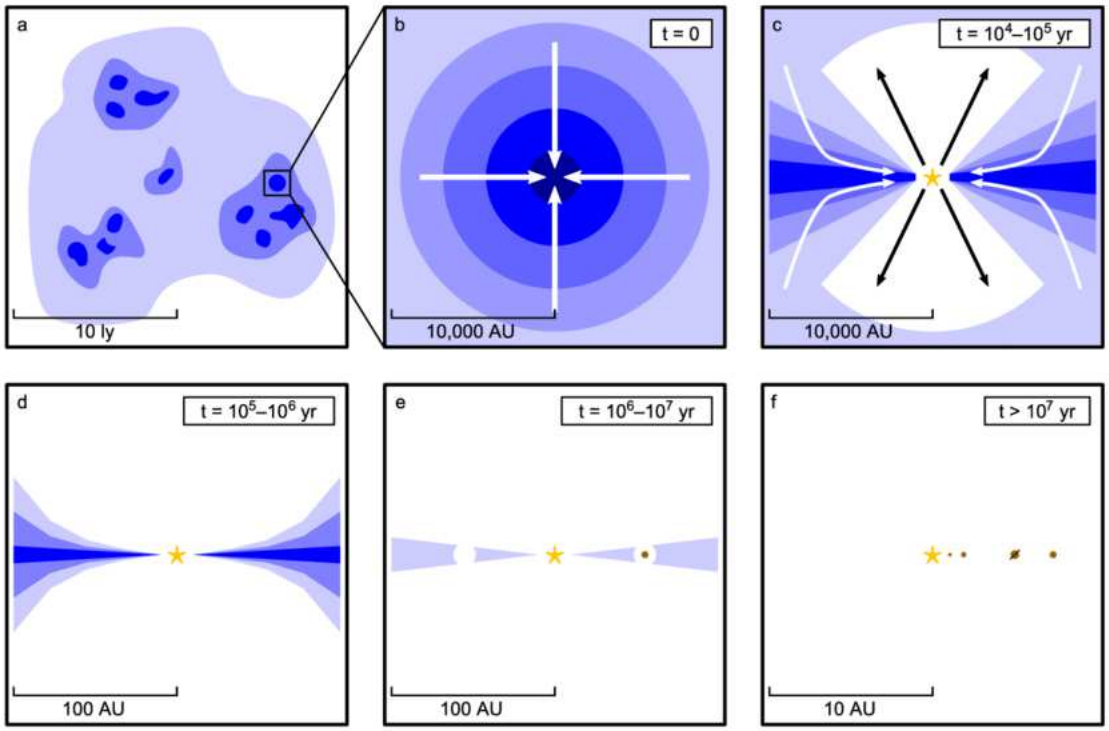

Figure 1.2: A schematic sketch of the different stages in low-mass star formation. This figure is taken from the PhD thesis of Steven H. Cuylle (2015) which was adapted from the PhD thesis of Ruud Visser (2009).

Fig. 1.2 shows a schematic sketch of the various stages in the formation of low-mass stars. Low-mass star formation begins in slowly rotating cores of enhanced density within the enveloping molecular cloud. The dense core collapses under gravity, leading to the formation of a central protostar surrounded by an infalling envelope. As the protostar contracts, the angular momentum conservation causes the envelope to spin down to a circumstellar disk, through which the protostar continues to accrete. The excess angular momentum is carried away by stellar winds through the channels of weakest resistance, i.e., the poles along the rotation axis, leading to collimated jets. These jets dig cavities in the surrounding envelope, through which energy and momentum are injected into the envelope and expose the surrounding ambient medium to winds and UV radiation from the forming star. Overtime, the surrounding circumstellar material dissipates as the jets widen, leaving behind a remnant disk where a planetary system might eventually form. The accretion stops in about $\sim 10^7$ years, with the depletion of the accreting material. By this time, the temperature and pressure at the centre of the protostar is high enough to trigger nuclear fusion

reactions. Core hydrogen burning announces the beginning of the star's journey in the main-sequence.

1.1.2 High-mass star formation

Though the processes involved in low-mass star formation lay the foundation for exploring the mechanisms involved in the formation of massive stars, theoretically, the models are not directly transposable. The idea of a bimodal star formation theory, wherein the processes involved in the low- and high-mass regimes were conceived to be different, dates back to the studies by Herbig (1962), Mezger & Smith (1977) and Elmegreen & Lada (1977). The two principal differences between low- and high-mass star formation are the timescales over which they form and the size scales involved in their formation. As a consequence of these differences, one is required to address the following fundamental issues pertaining to high-mass star formation:

- *Radiation pressure problem*:
  The time in which a protostar of mass M accretes matter from the surrounding envelope, called the accretion timescale is defined as

$$t_{\rm acc} = \frac{M}{\dot{M}} \tag{1.3}$$

  where $\dot{M}$ is the mass accretion rate. For low-mass stars, the typical mass accretion rate is $\dot{M} \sim 10^{-5}\,M_{\odot}\,{\rm yr}^{-1}$. At this rate, the accretion timescale for $1\,M_{\odot}$, $9\,M_{\odot}$, and $15\,M_{\odot}$ is calculated to be 1×10^5, 9×10^5, and 1.5×10^6 yr, respectively. As accretion continues, the gravitational potential energy is radiated away. The time over which the protostar radiates its entire reserve of thermal energy while maintaining a constant luminosity and before hydrogen burning ensues at the stellar core is called the thermal timescale or the Kelvin-Helmholtz (KH) timescale, given by

$$t_{\rm KH} = \frac{GM^2}{RL} \tag{1.4}$$

  where, M, R, and L are the mass, radius, and luminosity, respectively, of the protostar. Iben (1965) estimated the KH timescales for $1\,M_{\odot}$, $9\,M_{\odot}$, and $15\,M_{\odot}$ to be 5×10^7 yr, 1.5×10^5 yr, and 6×10^4 yr, respectively. Fig. 1.3 shows the variation of the accretion timescale at accretion rates of 10^{-4} (red) and $10^{-3}\,M_{\odot}\,{\rm yr}^{-1}$ (green) and the KH timescale for a range of masses. Comparing the two timescales, it is

evident that the KH timescale is longer than the accretion timescale ($t_{\rm KH} \gg t_{\rm acc}$) in case of low-mass stars which implies that accretion is over before the hydrogen burning begins. Whereas, in case of high-mass stars, the KH timescale is shorter than the accretion timescale ($t_{\rm KH} \ll t_{\rm acc}$). This indicates that for spherical accretion and any reasonable accretion rate, the stellar core begins to fuse hydrogen and enters the main-sequence, while the star is still accreting and not has reached its final mass. This holds even if enhanced accretion rate ($10^{-3}\,M_{\odot}\,{\rm yr}^{-1}$) is considered. The crossover between $t_{\rm KH}$ and $t_{\rm acc}$ occurs at $M \approx 8\,M_{\odot}$ for typical accretion rates of $10^{-5}\,M_{\odot}\,{\rm yr}^{-1}$ (Cesaroni et al., 2007), upwards of which defines the high-mass domain. The onset of nuclear fusion exerts a large radiation pressure on the infalling gas and dust. This can exceed the gravitational pressure, thereby halting further accretion and hence setting an upper limit on the final mass of the star. This is known as the 'radiation pressure problem'. Based on numerical calculations for a spherical, symmetrical accretion flow, the maximum mass a high mass star can attain is $\sim 40\,M_{\odot}$ (Kahn, 1974; Kuiper et al., 2010; Wolfire & Cassinelli, 1987).

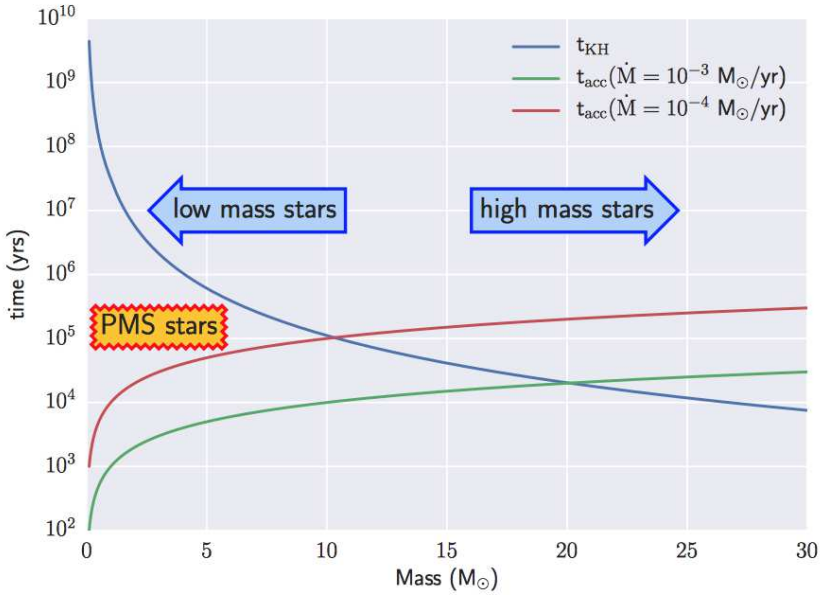

Figure 1.3: A plot of the Kelvin-Helmholtz time scale and accretion time scale for varying accretion rates of high mass stars and low mass stars. This figure is taken from Schilke (2015).

- *Fragmentation problem*:

  The other crucial issue involves the large scales of the star-forming clumps. High-mass stars are believed to form in massive clumps. Theoretically (e.g. Bonnell &

Bate, 2006; Krumholz, Klein & McKee, 2007; Seifried et al., 2011), it is seen that density fluctuations within these clumps leads to fragmentation, thus making them too small for the formation of massive stars. With improvements in resolution, signatures of fragmentation are observationally seen as well (Zhang et al., 2009).

Regardless of these theoretical limitations, observational studies have found evidences for the existence of stars with masses $\gtrsim 100\ M_{\odot}$ (e.g. Crowther et al., 2010; Heap et al., 1991). Several theories have been proposed over the years to address the above limitations. The most prominent theories under debate are discussed in the following section.

Proposed theoretical models

Over the years, tremendous efforts have been going on to model a universal theory elucidating the formation mechanism of stars across the mass range. Extensive research is being carried out to investigate whether high-mass stars formation could be understood as a 'scaled-up' version of the processes involved in the low-mass domain via the core accretion hypothesis. Alternate theories like competitive accretion and stellar merger are also quite popular and widely studied. These models implore very different initial conditions on the gas to collapse. Cloud-cloud collision is another mechanism that is gaining popularity in triggering the formation of massive star in clusters. However, the debate is still not sealed on which is the most viable mechanism for the formation of massive stars. The proposed models are briefly discussed in this section.

- **Monolithic collapse and core accretion**

  The core accretion model is essentially a scaled-up version of the standard model of low-mass star formation. This model assumes a top-down fragmentation process, wherein the molecular cloud fragments into smaller entities, the clumps and cores, under the influence of self-gravity, turbulence and magnetic field. The fragmentation ends in a gravitationally stable massive core which resists further collapse (Krumholz & Bonnell, 2009; McKee & Tan, 2003). This theory works under the assumption that the pre-stellar core mass function is directly correlated to the stellar initial mass function (IMF).

  Effects of supersonic turbulence and high pressure are incorporated in this model, giving rise to the 'Turbulent core' model (McKee & Tan, 2003). The supersonic turbulence maintains the quasi-static equilibrium of the massive core against gravitational collapse. The high pressure and density calls for high accretion rates of material from the clump encompassing the massive core. This model starts with

massive near-virial-equilibrium starless cores that will eventually collapse to form individual stars. While abandoning spherical accretion, the star grows in mass via enhanced accretion through a circumstellar disk with accretion rates as high as $\sim 10^{-4} - 10^{-3}\, M_{\odot}\, \mathrm{yr}^{-1}$ (Cesaroni et al., 2007). The radiation from the stellar core escapes through the cavities created by the jets and outflows. Invoking disk accretion coupled with jets adequately circumvents the radiation pressure problem.

Existence of high-mass starless cores is the key to support the above monolithic collapse model. Tan et al. (2013) and more recently, Kong et al. (2017) have carried out the Atacama Large Millimeter/submillimeter Array (ALMA) $\mathrm{N_2D^+}\,(3-2)$ observations to search for massive starless cores in IRDCs. The results of dynamical analysis of six of the detected 141 cores are seen to be consistent with the proposed core accretion model. The highlight of the results presented in Kong et al. (2017) is the detection of a very massive core ($\sim 170\, M_{\odot}$). Further studies towards confirming the starless nature of this is proposed by the authors.

- **Competitive accretion**

  An alternate approach to model high-mass star formation is considered with the Competitive Accretion hypothesis (Bonnell et al., 1997, 2001). Unlike monolithic collapse, this model argues that the matter is accreted from different parts of the clump while the star formation process has already begun. The parental cloud fragments into several cores, all of which are potential star-forming cores depending on their position in the cluster and the size of the accretion domain. A natural consequence of this model is the formation of massive stars in clusters. A large reservoir of gas and dust is available from which the protostars 'compete' for nourishment. Initially, none of the cores have enough mass to form massive stars. Each core accretes at different rates depending on its location in the cluster. Massive stars have a tendency to form at the centre of the protocluster, where the gravitational potential is the largest. As the protostars compete for the resources, the more massive protostars at the centre, that have stronger gravitational fields, funnel matter to themselves. Because of the limited gas reservoir, the accretion domains of the protostars begin to overlap. Thus, protostars at a positional disadvantage are left to accrete matter from the overlapping accretion domain (Zinnecker & Yorke, 2007).

  An observational study consistent with this model is present by Liu et al. (2013). These authors discuss the scenario for the protocluster, G10.6-0.4, wherein the central core has the maximum mass, while the off-centre cores have much smaller

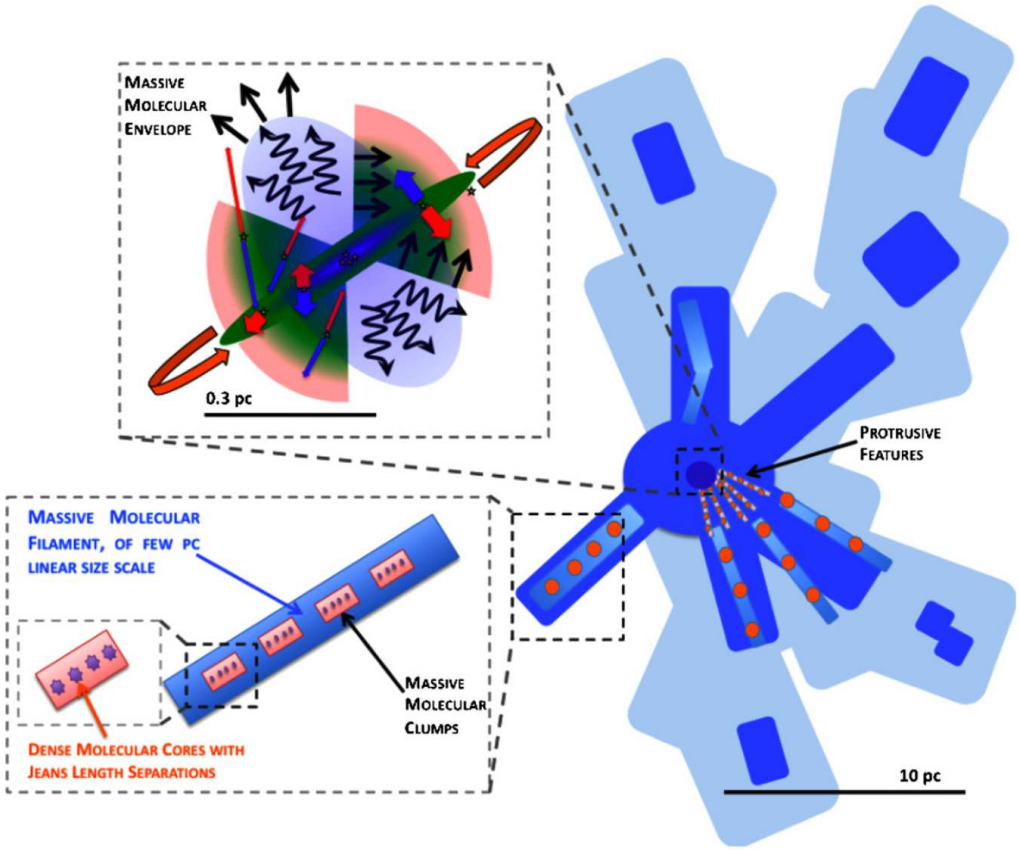

Figure 1.4: A schematic model of the observed molecular structure of the protocluster, G10.6-0.4. The model presents the hierarchical structure formation in a filamentary, OB-cluster-forming molecular cloud. Light blue corresponds to the parent molecular cloud and bright blue represents the denser regions of the cloud. The even denser filaments are depicted in blue gradient. Embedded within the filaments are massive clumps shown in red circles. A zoom-in on these clumps reveals dense cores. The protocluster is located at the central region of the massive molecular envelope, the blow-up of which is shown towards the top-left. More description on the massive molecular envelope can be found in Liu, Zhang & Ho (2011). This figure is taken from Liu et al. (2012).

masses. Fig. 1.4 gives a large-scale schematic representation of the molecular structure of the protocluster from Liu et al. (2012). The protostars in the G10.6-0.4 are accumulating mass from the gas reservoir, with the filaments facilitating the mass accretion on to the central cluster forming region. The overall collapse of the clump and the accretion through the filaments favour the 'Competitive Accretion Model' for G10.6-0.4.

- **Stellar mergers**

  Stellar mergers or coalescence, as the name suggests, is the process where massive stars are formed through the physical merging of multiple low-mass progenitors (Bonnell, Bate & Zinnecker, 1998). According to this model, the cores and protostars follow the evolution sequence of low-mass stars in a dense and clustered environment ($\sim 10^8\,\mathrm{pc}^{-3}$). This model was introduced to overcome the radiation pressure problem. However, such high densities required for mergers is seldom observed.

- **Cloud-cloud collision**

  In recent years, there is growing observational evidence that cloud-cloud collision can trigger star and cluster formation (e.g. Gong et al., 2017; Liu et al., 2018a,c; Sano et al., 2018; Torii et al., 2015) and is proposed as a viable mechanism for massive star formation. Hydrodynamic simulations of cloud-cloud collision by Habe & Ohta (1992), Anathpindika (2010), Takahira, Tasker & Habe (2014), and Takahira et al. (2018) consider the head-on collision between a small spherical cloud with a large spherical cloud, which is referred to as the 'Habe-Ohta' model. A schematic diagram of the sequence of events during cloud-cloud collision based on this model is given in Fig. 1.5(a). In Phase 1, the spherical, small and large clouds approach each other and collide. A compressed layer is formed at the interface creating a U-shaped cavity in the large cloud in Phase 2, where the diameter of the cavity is almost equal to that of the small cloud. In Phase 3, the small cloud has fully merged into the compressed layer where dense cores and star(s) will eventually form. Surface density plots from the simulation results obtained by Takahira, Tasker & Habe (2014) for cloud collision at $10\,\mathrm{km\,s}^{-1}$ are shown in Fig. 1.5(b). Phase 1 is prior to the onset of collision, at time 0 Myr. In the course of the collision, the small cloud decelerates due to collisional interaction, thereby decreasing the collision velocity. Phase 2 is after a time lapse of 1.6 Myr, when the small cloud penetrates into the large cloud. The cavity created by the collision is much clearer in Phase 2 [inner], which shows only the site of collision. These simulations reveal that collisionally compressed interfaces form dense, self-gravitating cores if the gas column density at the compressed layer becomes large enough.

  The 'Habe-Ohta' model, however does not consider the effects of magnetic field. Based on their magneto-hydrodynamic (MHD) simulations, Inoue & Fukui (2013) propose a scenario where supersonic collisions boost the magnetic field strength and gas density in the shock-compressed layer. This results in an enhanced mass accre-

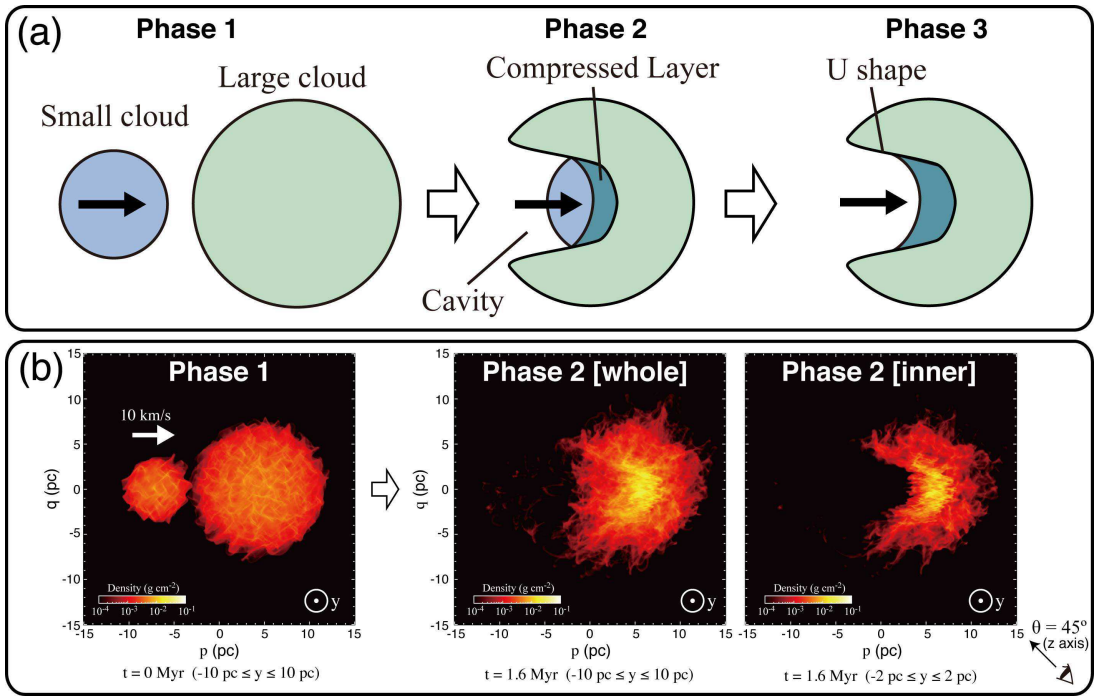

Figure 1.5: (a) The schematic illustration of the sequence of events during cloud-cloud collision based on the Habe-Ohta model between two spherical clouds of different sizes. (b) Top view of the surface density plots from the simulation results obtained by Takahira, Tasker & Habe (2014) for cloud collision at $10\,\mathrm{km\,s^{-1}}$. This figure is taken from Fukui et al. (2020).

tion rate and also a large effective *Jeans* mass, the two prime ingredients for massive star formation. The shocked layer collapses into dense filaments, where the magnetic field is amplified in the direction perpendicular to the filament. The clouds are compressed multi-dimensionally except in the direction perpendicular to the background magnetic field, which results in filamentary structures. A number of pre-stellar cores, accreting mass from the natal cloud are formed in these filaments.

Recent studies by Gong et al. (2017, 2019) show evidence of collision triggered cluster formation of low- and intermediate-mass stars as well. In spite of the complexities involved in deciphering cloud kinematics from stellar feedback, observationally, many cloud-cloud collision candidates have been discovered (Hayashi et al., 2020, and references therein). If cloud collision is frequent in disk galaxies like the Milky Way (Tasker & Tan, 2009), then detailed investigation of cloud-cloud collision candidates can shed crucial light on triggered star formation under different physical conditions. Fukui et al. (2020) provide an excellent review on the current status of

observations and theoretical understanding of cloud-cloud collisions and also discusses future directions in this area.

1.2 Evolutionary sequence in star formation

As discussed in previous sections, the evolutionary sequence followed by low-mass stars is quite well established. But same cannot be said for high-mass stars. The pre-main sequence evolutionary track of both low- and high-mass stars are summarized in this section.

1.2.1 Low-mass stars

Observationally, the pre-main sequence evolution of low-mass stars is classified in four distinct stages: Class 0, I, II, and III on the basis of the spectral energy distribution (SED). The classification scheme is based on the spectral index (α) in the infrared wavelengths (Adams, Lada & Shu, 1987), given by

$$\alpha = \frac{d\log(\lambda\, S_\lambda)}{d\log(\lambda)} \tag{1.5}$$

where S_λ is the flux density at wavelength λ. SEDs of the different evolutionary stages of low-mass star formation are presented in Fig. 1.6.

Class 0 objects are the youngest young stellar objects (YSOs) (age $\leq 10^4$ yrs) and are deeply embedded with high accretion rates. They are invisible at optical wavelengths and extremely faint at near-infrared (NIR) wavelengths. The SEDs of these sources peak in FIR and submillimeter wavelengths. Class I objects ($\alpha > 0$) are more evolved (age $\sim 10^5$ yrs) relative to Class 0 objects. They are still embedded within circumstellar disks and envelopes and hence still optically invisible. The SEDs of these sources peak in mid-infrared (MIR) and FIR wavelengths. After $\sim 10^6$ yrs, most the envelope is swept away by stellar winds and outflows, thereby exposing the circumstellar disk. The YSOs in this stage are identified as Class II YSOs, also known as T Tauri stars ($-2 < \alpha < 0$). This stage is characterized by strong emission lines and the YSOs are optically visible. The Class II sources show large infrared excess because of the optically thick accretion disks. As the material in the accretion disk is consumed, the mass accretion declines, revealing the central protostar without any infrared excess. Some circumstellar material may exist as a thin disk. The SEDs of the YSOs in this stage, called Class III YSOs ($\alpha < -2$) display a single reddened blackbody with negligible infrared excess. The Class III sources with an age of $\sim 10^7$ yrs are close to the zero-age-main-sequence (ZAMS), where the temperature

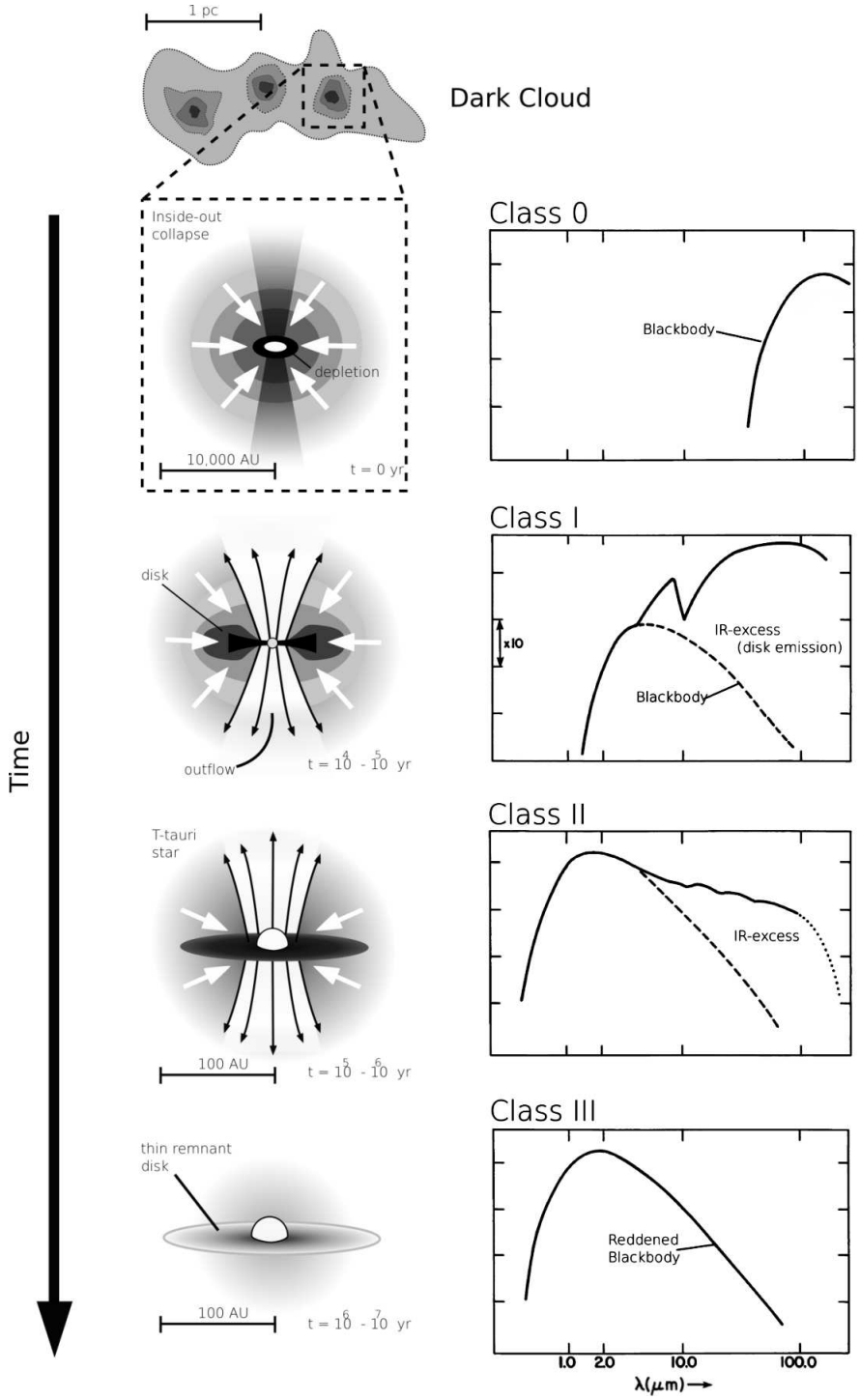

Figure 1.6: Schematic representation of the protostellar classification of low-mass stars. The typical SED of each class is shown in thr right column. This figure is taken from the PhD thesis of Purcell (2006).

and pressure are high enough to trigger hydrogen fusion reaction in the core.

1.2.2 High-mass stars

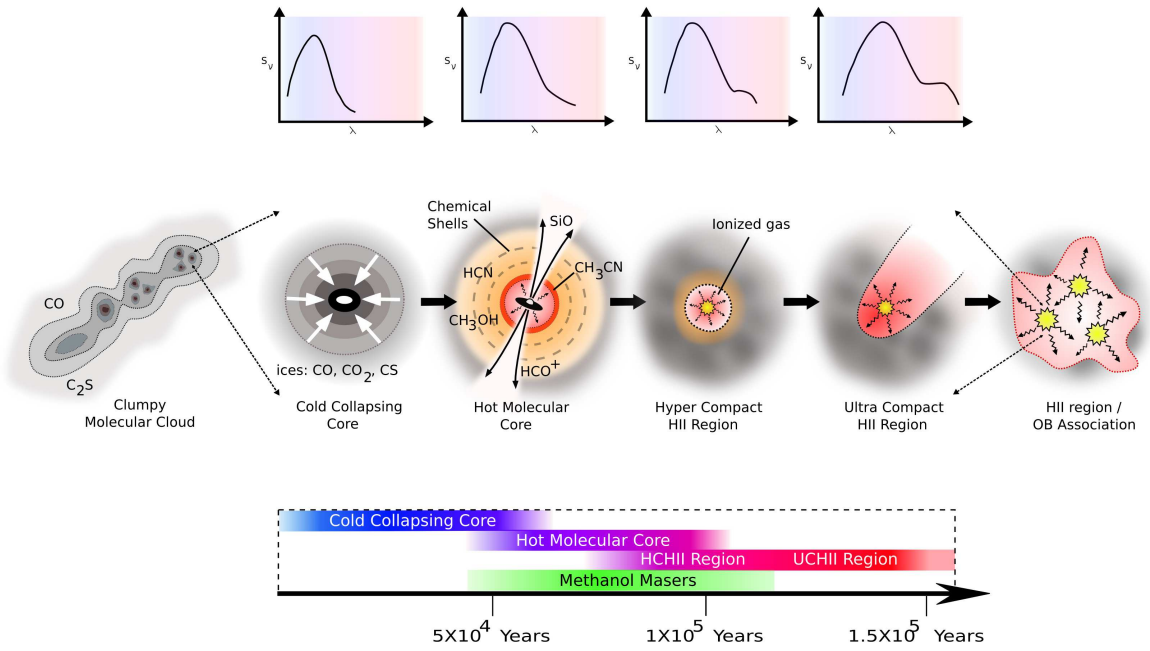

Figure 1.7: A schematic portrayal of the evolutionary stages in the formation of high-mass stars. The middel-panel depicts each stage and their corresponding SEDs are given in the top-panel. The bottom-panel describes the timeline of evolution. This figure is taken from the website of Dr Cormac Purcell (http://web.science.mq.edu.au/~cpurcell/public/images).

In comparison to the evolution of the low-mass stars, the evolutionary track of high-mass stars is not as clearly established. Before being visible at optical wavelengths, the massive stars spend $\sim 15\%$ of their lifetime in an embedded phase (Churchwell, 2002; Zinnecker & Yorke, 2007). Observations from MIR through radio wavelengths give a general idea of the evolutionary progression of massive stars while in the embedded phase. The evolution of massive protostars is presumed to follow a path where the star formation begins within IRDCs in clumpy substructures. Subsequently, they evolve into HMCs, followed by hyper-compact (HC)/ultracompact (UC) H II regions. Fig. 1.7 illustrates a schematic picture of the evolutionary sequence starting from the left. Each of the observable stages are briefly described in this section.

Infrared dark clouds and massive clumps

IRDCs are believed to be the birth sites of massive stars and star clusters (Rathborne, Jackson & Simon, 2006; Rathborne, Simon & Jackson, 2007). They appear as distinct dark extinction features against the bright diffuse Galactic background at infrared wavelengths. These massive clouds have morphologies varying from elongated to compact structures. On larger scales, they often display filamentary morphology that can extend to a hundred parsec (Contreras et al., 2016; Jackson et al., 2010; Ragan et al., 2014), and at smaller scales, they fragment into dense clumps and starless cores (Battersby et al., 2010; Zhang et al., 2017). IRDCs are massive with masses ranging between $10^2 - 10^3\,M_\odot$ and typically have densities of $n > 10^5\,\mathrm{cm}^{-3}$ and temperatures, $T < 20\,\mathrm{K}$ (Rathborne, Jackson & Simon, 2006; Simon et al., 2006).

Towards submillimeter and millimeter wavelengths, the dust continuum observations reveal significant substructures of clumps and cores within IRDCs. The clumpy nature of IRDCs indicate that they are in the process of fragmentation (Contreras et al., 2016), and hence represent the initial stages of star formation. Some of the clumps within IRDCs show signatures of ongoing high-mass star formation, such as molecular outflows, bright $\mathrm{CH_3OH}$ and $\mathrm{H_2O}$ masers, bright MIR emission, UC H II regions and massive YSOs (MYSOs) (e.g. Sanhueza et al., 2010), while some are devoid of any star formation activity. The latter serve as good candidates to probe the earliest phases of star formation, prior to collapse. Active star formation is also observed at sites where multiple filaments converge, mimicking a hub-filament system (e.g. Kumar et al., 2020; Myers, 2009; Peretto et al., 2012, 2014). The presence of $70\,\mu\mathrm{m}$ emission has been used to distinguish between protostellar and starless cores within these clouds. From their study of a sample of IRDCs, Ragan et al. (2012) suggest that cores lacking $70\,\mu\mathrm{m}$ emission are likely to be less evolved than those with $70\,\mu\mathrm{m}$ emission.

High-mass protostellar objects and hot molecular cores

High-mass protostellar objects (HMPOs) are a class of sources tracing the early stages of high-mass star formation. They have the same star formation potential as that of infrared-quiet clumps, but are more evolved, where infrared-quiet clumps are precursors to UC H II regions and cold enough not to be detected at NIR and MIR wavelengths (Motte, Bontemps & Louvet, 2018, and references therein). HMPOs have luminosity $> 3 \times 10^3\,L_\odot$ and host massive protostellar embryos. In the HMPO phase, high-mass protostars would have accreted more than half of their final mass. This class of objects exhibits evidence of strong

accretion, like bipolar outflows and active infall, and have mass accretion rates ranging from $10^{-4} - 10^{-2}\,M_{\odot}\,\mathrm{yr}^{-1}$ (e.g. Wyrowski et al., 2016).

HMCs are compact (size ≤ 0.1 pc), dense ($> 10^{7}\,\mathrm{cm}^{-3}$), and warm ($\geq 100$ K) condensations of molecular gas that are characterized by a rich chemistry of complex organic molecules (Herbst & van Dishoeck, 2009). HMCs that have little to no emission at centimeter wavelengths represent a stage where massive protostars draw their luminosity by actively accreting matter and UC H II regions have not formed yet (Beuther et al., 2007; Kurtz et al., 2000). Further, they are too young and embedded to be detected at optical and IR wavelengths. The HMC phase is a stage where accretion is active and are characterized by temperatures that are higher than the enveloping molecular cloud. This causes the ice from the dust grains to evaporate and contribute to the rich chemistry of the HMCs that show large abundance of complex organic molecules like CH_3OH, CH_3CN, CH_3OCH_3, $HCOOCH_3$. Molecular line studies towards HMCs provide a large database of thermal and non-thermal molecular lines emission. Methanol (CH_3OH) maser emission is a characteristic feature of the HMC phase. At temperatures above 90 K organic species like CH_3OH and H_2CO evaporate from the grain mantles. The gas phase reaction of these molecules produce more complex molecules like HC_3N and CH_3CN. These complex molecules are seldom seen in the cold interstellar medium making them excellent signposts of HMCs.

H II regions

Massive OB stars emit enormous amounts of UV photons. These UV photons ionize the hydrogen in the surrounding ISM to form H II regions. Basically, these are photoionized nebulae formed around massive stars. The H II regions emit at radio wavelengths via thermal *free-free* emission mechanism. In the initial stages, the MYSO(s) powering the H II region is obscured by the accreting envelope and the UV and optical radiation from the star is absorbed by the ambient dust and re-emitted in the infrared. Based on their evolutionary phase, H II regions are classified as HC, UC, compact, and extended or classical H II regions. HC H II regions are extremely compact with size < 0.01 pc and dense ($n_e \sim 10^{5}\,\mathrm{cm}^{-3}$). They expand to form UC H II regions that are still small having typical sizes of ~ 0.1 pc. They are still very dense with electron density, $n_e \sim 10^{4}\,\mathrm{cm}^{-3}$. These eventually expand to larger and low density, compact H II regions with sizes ranging from $0.1 - 0.3$ pc. Extended or classical H II regions can have sizes upto several parsecs and represent a more evolved state. Elaborate reviews on the nature of H II regions can be found in Wood & Churchwell (1989), Churchwell (2002), Hoare et al. (2007) and Anderson et al. (2019).

High-resolution interferometric observations have unveiled varying morphologies of the UC H II regions. Based on the morphology of radio emission, they are further classified as spherical, core-halo, shell, and cometary (Wood & Churchwell, 1989). Another morphology, termed bipolar, is also included in the classification scheme (Deharveng et al., 2015). The diverse morphologies of the H II regions can be attributed to several factors like age, ionized and molecular gas dynamics, density of the ISM, and also the relative motion of the ionizing star with respect to the surrounding medium (Churchwell, 2002).

1.2.3 Observational constraints

Although the proposed theoretical models have been able to explain various aspects of high-mass star formation, a global, unified picture connecting all the models is still not established. The deficiency of observational support owing to the intrinsic properties of high-mass stars and their birth sites have hindered the efforts to constrain the models. Observational investigation of high-mass star formation, especially the early evolutionary phases is challenging since they are short-lived as compared to low-mass stars and remain in an embedded phase for most of the pre-stellar and protostellar phases before entering the main-sequence. This leads to high extinction, making the investigation of the early phases of their evolution difficult. Adding to this, the number of high-mass stars in the Milky Way is constrained by the stellar IMF (Kroupa, 2001; Salpeter, 1955) making them rare. As a consequence of rarity, the statistical distribution of high-mass stars places them at large distance from the sun ($\gtrsim$1 kpc). Moreover, high-mass stars are often seen to form in clustered environments leading to confusion. The large distances and confusion would call for high angular resolution observations for the detection of high-mass stars and to investigate the mechanisms involved in their formation. For instance, dense core structures within massive clumps of the G9.62+0.19 complex (Liu et al., 2017) and G286.21+0.17 (Cheng et al., 2018) are revealed using high angular resolution observations made with ALMA.
Despite the challenges, state-of-the-art numerical simulations and tremendous advancement in observational facilities have enabled us to probe high-mass star-forming regions and obtain a better insight of the complex processes associated.

1.3 Extended Green Objects (EGOs)

The Galactic Legacy Infrared Mid-Plane Survey Extraordinaire (GLIMPSE, Benjamin et al. 2003) surveyed the Galactic plane using the Infrared Array Camera (IRAC) on-board *Spitzer Space Telescope* at angular resolutions of $< 2''$. The survey detected the presence of

a significant population of objects displaying enhanced and extended emission in the IRAC 4.5 μm band. Following the conventional colour coding of GLIMPSE colour-composite images, these objects were christened as 'green fuzzies' or 'extended green objects' (EGOs) by Chambers et al. (2009) and Cyganowski et al. (2008), respectively. Cyganowski et al. (2008) compiled a catalogue of more than 300 EGOs identified in the GLIMPSE I survey area ($10^\circ < l < 65^\circ$ and $295^\circ < l < 350^\circ$, $b = \pm 1^\circ$). Based on the morphology and angular scale of the 4.5 μm emission, EGOs are catalogued as "likely" and "possible" outflow candidates. Additional four EGOs are catalogued as "outflow-only" candidates for which the extended outflow emission is separated from the central source. Fig. 1.8 shows the colour-composite images of three such EGOs catalogued by Cyganowski et al. (2008), where (a) G35.20-0.74 is a "likely" outflow candidate, (b) G40.28-0.22 is a "possible" outflow candidate and (c) G19.01-0.03 is an "outflow-only" candidate. The signature extended and enhanced emission at 4.5 μm is clearly seen. Subsequently, Chen et al. (2013a) updated the catalogue with the identification of 98 more EGOs from the GLIMPSE II survey. Majority of the EGOs catalogued by Cyganowski et al. (2008) are bright and compact, but more extended than point sources.

(a) G35.20-0.74 (b) G40.28-0.22 (c) G19.01-0.03

Figure 1.8: *Spitzer*-IRAC colour-composite images of a sample of EGOs using IRAC 3.6 μm (blue), 4.5 μm (green) and 8.0 μm (red) bands. These EGOs are catalogued by Cyganowski et al. (2008) from the GLIMPSE survey.

Post-detection, several studies have focussed on ascertaining the nature of these objects (Chambers et al., 2009; Chen et al., 2013b; Cyganowski et al., 2009, 2011a,b; Lee et al., 2012; Marston et al., 2004; Rathborne et al., 2005; Takami et al., 2012). Extensive research has been conducted in the recent years to identify the spectral carriers responsible for the enhanced 4.5 μm emission (e.g. Davis et al., 2007; De Buizer & Vacca, 2010; Noriega-Crespo et al., 2004; Reach et al., 2006; Smith & Rosen, 2005; Takami et al., 2012). Some

of the above studies have associated EGOs with shock-excited H_2 line and/or CO bandhead emission in protostellar jets.

De Buizer & Vacca (2010) were the first to report the direct spectroscopic identification of the origin of the extended green emission. Their observations indicate that, for the "likely" outflow source, G19.88-0.53, the extended 4.5 μm emission is seen within the outflow and is possibly due to the H_2 emission line at 4.695 μm covered by the IRAC 4.5 μm band. The models of protostellar jets by Smith & Rosen (2005) also predict strong H_2 lines from outflows with the strongest H_2 emission in the IRAC 4.5 μm band. Supporting evidence for the 4.5 μm emission arising from protostellar outflows comes from the detection of H_2 lines in the NIR spectrum towards the star-forming region, DR21, associated with a bipolar outflow and harbouring an EGO (Davis et al., 2007). Here the emission at 2.12 μm and 4.5 μm have very similar morphologies. Similarly, the IRS 5-37 μm spectra towards the outflow system, HH 46/47, also associated with an EGO, reveals prominent H_2 lines arising from the outflow cavity (Noriega-Crespo et al., 2004).

1.3.1 Association with infrared dark clouds and methanol masers

As discussed earlier, IRDCs are known to be sites of the earliest stages of massive star formation. IRDCs are clearly visible in silhouette against the bright diffuse background in the GLIMPSE images, especially at 8.0 μm. Of all the EGOs catalogued, around $\sim 67\%$ (Cyganowski et al., 2008) are seen to be embedded within IRDCs indicating that these objects mostly trace the earliest phases of high-mass star formation. More evidence to support this claim comes from the association of EGOs with methanol masers.

Majority of the EGOs sampled by Cyganowski et al. (2008) are associated with both, Class I and Class II CH_3OH masers and have 24 μm counterparts. However, the spatial distribution of the Class I and Class II CH_3OH masers are different. Class I and Class II CH_3OH masers are excited at different conditions. The 6.7 GHz Class II CH_3OH masers are radiatively pumped by the infrared radiation from the warm dust of the star-forming regions. It excites the CH_3OH molecules to a torsionally excited state (Cragg, Sobolev & Godfrey, 2005, and references therein). Various studies have shown that the 6.7 GHz Class II CH_3OH masers are distinct signposts of massive star formation and are not detected towards low-mass star-forming regions (Ellingsen, 2006; Szymczak, Pillai & Menten, 2005). More than 73% of the "likely" outflow candidate EGOs and more than 27% of "possible" outflow candidate EGOs are associated with Class II CH_3OH masers (Cyganowski et al., 2008). In their study, Chen, Ellingsen & Shen (2009) also discovered that two-thirds of EGOs are associated with Class I CH_3OH masers. The collisionally ex-

cited Class I CH_3OH masers have a strong correlation with molecular outflows traced by SiO and H_2 in high-mass star-forming regions (Johnston et al., 1992; Kurtz, Hofner & Álvarez, 2004; Plambeck & Menten, 1990). However, several other studies (Kalenskii et al., 2010; Kalenskii, Kurtz & Bergman, 2013, and references therein) have detected them towards low-mass star-forming regions as well. While Class II CH_3OH masers are spatially concentrated and usually coincident with the 24 μm emission, the Class I CH_3OH masers are more spatially distributed and appear to trace the edges of the 4.5 μm emission. The co-spatial distribution of the 6.7 GHz masers with 24 μm emission conforms with the prediction that the warm dust near the MYSOs provide suitable condition for radiative pumping of this maser species. Furthermore, Cyganowski et al. (2009) show that HCO^+ $(3-2)$ detected towards all the EGOs in their sample display broad line wings, a signature of outflow, consistent with the expectation that 44 GHz Class I CH_3OH masers are tracers of molecular outflows. These results lend strong statistical support to EGOs being MYSOs in an early evolutionary phase of active accretion and driving outflows.

1.3.2 Infrared association and mid-infrared colours

On comparison with IRAS sources, Cyganowski et al. (2008) found that while some of the EGOs can be identified with IRAS point sources, the mean angular separation between an EGO and the nearest IRAS point source is $\sim 85''$. Though most of the EGOs do not seem to be associated with IRAS point sources, it does not necessarily mean the absence of emission at IRAS wavelengths. Given the poor resolution of IRAS, the lack of emission can be attributed to confusion or positional uncertainty.

EGOs are believed to be driven by outflows from massive protostars, with the spectral carriers possibly being molecular line of H_2 or CO bandhead or ionic line of [FeII] at 4.6 μm. However, to substantiate this hypothesis, spectroscopic studies at MIR wavelengths covering the IRAC 4.5 μm band is very limited. From the spectroscopic study towards EGOs, covering the IRAC 4.5 μm band, De Buizer & Vacca (2010) detected three individual EGO knots around one of the two EGOs (G19.88-0.53) investigated. Fig. 1.9 shows the three colour-composite image of G19.88-0.53 from De Buizer & Vacca (2010) and the *L*- and *M*-band spectra extracted from the EGO knots and the central MYSO. The *M*-band spectrum (sampling the IRAC 4.5 μm band) obtained using the Gemini Telescope's near-infrared spectrometer, NIRI, reveal strong H_2 emission line at 4.695 μm, supporting the above hypothesis.

In the NIR domain, a few studies have focused towards narrow-band imaging and spectroscopy of EGOs (e.g. Caratti o Garatti et al., 2015; Lee et al., 2013, 2012; Onaka et al.,

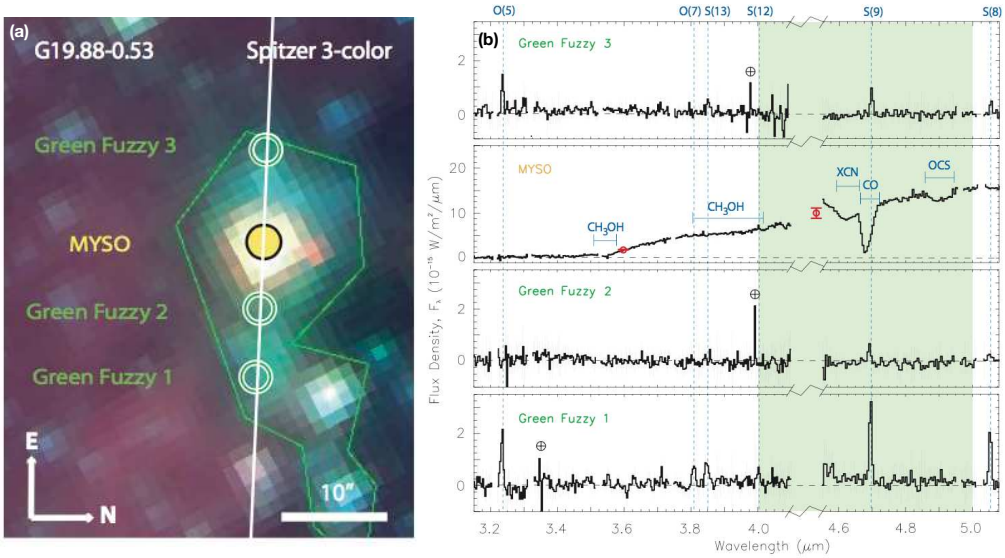

Figure 1.9: (a) Three colour-composite *Spitzer*-IRAC image of G19.88-0.53.The NIRI slit position is shown by the white line. The MYSO and the three EGO knots ('Green Fuzzy') are marked by circles. (b) *L*- and *M*-band spectra extracted from the locations marked by circles in (a). These figures are taken from De Buizer & Vacca (2010).

2016). The H_2 $(1-0)$ S(1) line at 2.12 μm is an excellent tracer of shock-excited emission arising from molecular outflow in the NIR regime. Lee et al. (2013, 2012) examined the narrow-band H_2 $(1-0)$ S(1) images from the United Kingdom Infrared Telescope (UKIRT) Wide Infrared Survey for H2 (UWISH2) and the NIR continuum data from the UKIRT Infrared Deep Sky Survey Galactic Plane Survey (UKIDSS-GPS) of 94 EGOs in the northern Galactic plane. Their study revealed that most of the EGOs ($\sim 62\%$) classified as "likely" outflow candidates are associated with H_2 line emission from protostellar outflows. An example of one such EGO, G34.20-0.74 from Lee et al. (2012), is described in Fig. 1.10, showing clear extended green emission in the *Spitzer*-IRAC colour-composite image. The emission at 24 μm mapped with the Multiband Imaging Photometer for Spitzer (MIPS) is saturated. The UKIDSS *K*-band image also shows extended emission along the direction of the 4.5 μm emission. The continuum-subtracted H_2 line image shows an hourglass shaped bipolar H_2 outflow with a wide opening angle ($\sim 40^{\circ}$) in the north-east and south-west direction.

With the aim of deriving the physical properties of massive jets from high-mass YSOs, Caratti o Garatti et al. (2015) carried out NIR imaging (H_2 and K_S bands) and low-resolution spectroscopic ($0.92 - 2.50\,\mu$m) survey of 18 EGOs. The observed H_2 emission in these objects display diverse morphologies, starting from simple bipolar outflows to

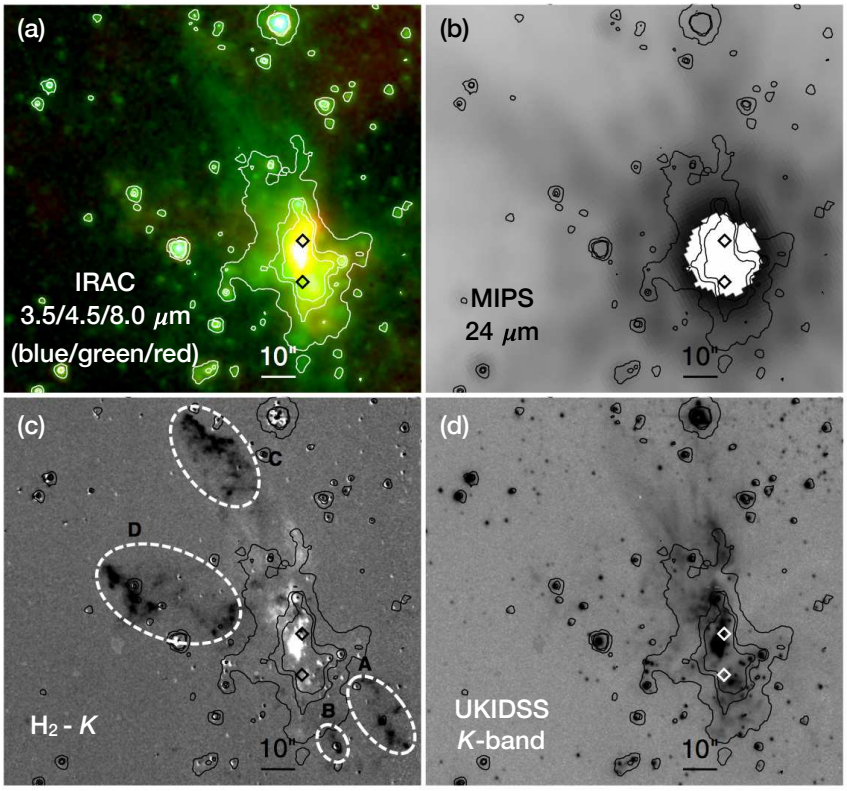

Figure 1.10: Images of the EGO G25.30-0.74. (a) *Spitzer*-IRAC colour-composite image. (b) *Spitzer*-MIPS 24 μm image. The white part in the 24 μm map is saturated. (c) Continuum-subtracted H_2 image. (d) UKIDSS *K*-band image. The contours represent the 4.5 μm emission, the levels of which are arbitrarily chosen for the best comparison of flux density at 4.5 μm to that at other wavebands. The diamonds mark the positions of two UC H II regions. The dashed ellipses highlight the H_2 outflow (Molecular hydrogen objects; MHO 2431 A-D). This figure is taken from Lee et al. (2012).

monopolar flows, precessing jets, and asymmetric lobes. Further, all the jets in the sample show a high degree of collimation, indicating a possible disk origin for these jets. These authors suggest that the H_2 knots detected towards the source G34.20-0.74 indicate precessing jets, rather than a wide angle bipolar outflow. The spectra extracted towards the knots also reveal strong H_2 emission lines as well as [FeII] lines. Of all the sources considered by Caratti o Garatti et al. (2015), [FeII] emission is detected towards $\sim 50\%$ of them, which is also considered as a good tracer of jets/outflows. In terms of the physical parameters derived, the massive jets associated with the 18 EGOs seems to be a scaled-up version of their low-mass counterparts.

For EGOs with counterparts in other IRAC bands and at 24 μm, the flux densities at wavelengths > 4.5 μm is dominated by emission from the central MYSO. The IRAC colour-

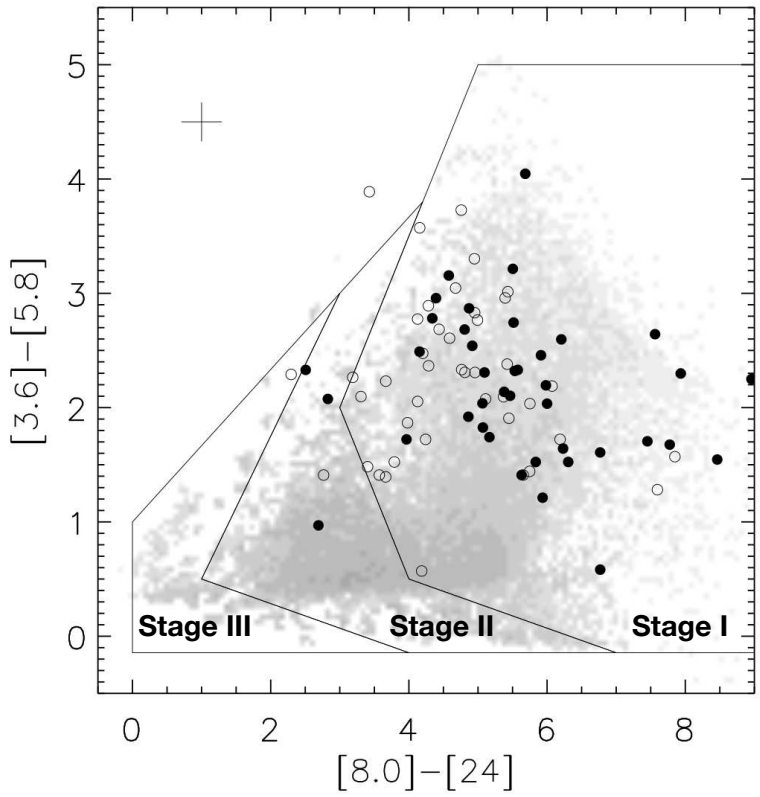

Figure 1.11: Colour-colour plot of EGOs taken from Cyganowski et al. (2008). Filled and open circles correspond to the “likely" and “possible” outflow candidates, respectively, with emission in all the IRAC bands and at 24 μm. The cross at the top left is the error bar. The grid of YSO models is shown in the grey scale, from Robitaille et al. (2006). The black lines delineate the different evolutionary stages. At the right are the youngest sources with infalling envelopes (Stage I); the middle region correspond to sources with optically thick disks (Stage II); and at the left are sources with optically thin disks (Stage III).

colour diagram of EGOs, classified as “likely” and “possible” outflow candidates with emission at all IRAC bands and at 24 μm, is shown in Fig. 1.11. Each line in the plot delineates the different evolutionary stages, Stage I, II, and III. These stages are based on the nomenclature followed by Robitaille et al. (2006), where, Stage I objects have significant infalling envelopes, Stage II and Stage III objects are characterized by optically thick and thin disks, respectively. Majority of the EGOs in the above categories populate the region of the colour-colour space corresponding to the youngest YSOs surrounded by an infalling envelope (Stage I), indicating that EGOs trace the early stages of high-mass star formation.

1.3.3 Kinematic signatures

As seen in Fig. 1.11, most of the catalogued EGOs are surrounded by accreting envelopes. Thus, EGOs should trace a population of sources going through an active accretion stage of massive protostellar evolution with ongoing outflow activity. Several molecular line studies towards EGOs have tried to explore the gas kinematics of EGOs and the associated molecular cloud. A brief literature review of these studies is presented in this section.

Protostellar infall

Several studies have focussed on examining infall activity towards EGOs (e.g. Chen et al., 2010; He, Takahashi & Chen, 2012; Yu & Wang, 2015). As is well known, optically thick molecular lines are excellent tracers of infall activity. The infall motion can be identified from the asymmetric profile of an optically thick line (e.g. $\mathrm{HCO^+}$, HCN). A spherical cloud undergoing collapse will have the collapsing region on the far side moving towards the observer, and on the near side moving away. This gives rise to red and blueshifted or double peaked line profiles with an absorption dip for an optically thick molecular line emission from the cloud. In comparison, for an optically thin transition, the line profile is symmetric and shows a peak at the self absorption dip which is also the systemic velocity of the cloud. The double peaked line of the optically thick transition is characterized by a blue-skewed profile, known as 'blue asymmetric profile'.

In Fig. 1.12(a) is shown a schematic representation of the above scenario, adapted from Evans (1999), wherein an infalling cloud is surrounded by a static envelope. Towards the centre of the cloud, the velocity of the infalling material increases. In a spherically collapsing cloud, a centrally peaked temperature and density distribution results in increase in the excitation temperature towards the centre. The material with higher excitation temperature is closest to the observer in the case of blueshifted emission, and for the redshifted emission, the material with lower excitation temperature is closest. In an inside-out collapse model, the central collapsing region has a velocity distribution $v \propto r^{0.5}$ and is surrounded by a static envelope. Such a distribution causes the velocity field to have two points with same Doppler shift along any line-of-sight, as is illustrated in Fig. 1.12(b). In this figure, the Doppler shift at points R1 and R2 will be the same ($V_{\rm R1} = V_{\rm R2}$) and at points B1 and B2 will be the same ($V_{\rm B1} = V_{\rm B2}$). Hence, the redshifted emission from the point R2 with a higher excitation temperature will be obscured by the emission at R1, which has a lower excitation temperature. Contrary to this, blueshifted emission from B2 is not affected along the line of sight. The weaker redshifted peak results in the characteristic blue-skewed

profile in collapsing clouds. The self-absorption dip arises because of the static envelope surrounding the infalling region.

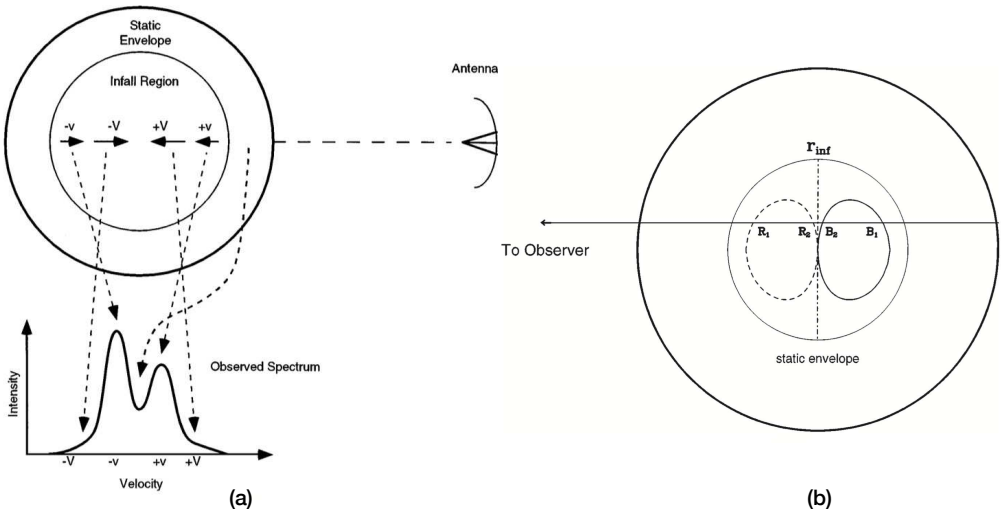

Figure 1.12: (a) A schematic picture of spherical cloud undergoing collapse surrounded by a static envelope. The magnitude of the velocity increases towards the centre. The corresponding blue-asymmetric profile with a self-absorption dip for an optically thick line is also plotted. (b) In this diagram, portraying a spherical cloud undergoing collapse, the ovals trace the loci of constant line-of-sight velocity. These figures are taken from Evans 1999.

The blue-asymmetry is quantified by the asymmetry parameter, δV (Mardones et al., 1997),

$$\delta V = \frac{(V_{\rm thick} - V_{\rm thin})}{\Delta V_{\rm thin}} \tag{1.6}$$

where, $V_{\rm thick}$ is the peak velocity of the optically thick line, $V_{\rm thin}$ is the peak velocity of the optically thin line and $\Delta V_{\rm thin}$ is the FWHM of the optically thin line. According to Mardones et al. (1997), the criteria for a bona fide blue-skewed profile is $\delta V < -0.25$.
Such signature infall profiles are observed towards low-mass star-forming regions (Di Francesco et al., 2001; Mardones et al., 1997) and high-mass star-forming regions (Wu & Evans, 2003; Wyrowski et al., 2016; Zapata et al., 2008). Apart from the blue-asymmetric profiles, 'inverse P-Cygni profiles' or 'redshifted absorption profiles' are also generally considered as evidence of gas infall (Liu, Wu & Zhang, 2013; Wu et al., 2009). In such profiles, the redshifted absorption feature originates from the dense gas along the line of sight and located towards the near side of the observer and moving away. The emission component is due to the gas on the far side of the central source with its motion towards

the observer.

Chen et al. (2010) carried out a systematic survey of molecular lines including $\mathrm{HCO^+}\,(1-0)$, $^{12}\mathrm{CO}\,(1-0)$, $^{13}\mathrm{CO}\,(1-0)$, and $\mathrm{C^{18}O}\,(1-0)$ towards a sample of 88 EGOs in the northern hemisphere using the Purple Mountain Observatory 13.7-m radio telescope. The study aimed to search for evidence of infall and to derive the physical properties of these sources. From the analysis of the optically thick $\mathrm{HCO^+}$ line and the optically thin $\mathrm{C^{18}O}$ line, Chen et al. (2010) found that a significant number of EGOs in the sample show active infall. Typical infall velocity, $\sim 2\,\mathrm{km\,s^{-1}}$ and mass infall rates, ranging from 4×10^{-2} to $1 \times 10^{-4}\,M_\odot\,\mathrm{yr^{-1}}$, estimated are consistent with those of other massive star-forming regions and also similar to the predicted theoretical values. Based on this, Chen et al. (2010) conclude that EGOs possibly trace a population MYSOs in an actively accreting initial phase of protostellar evolution.

Jets and outflows

Massive molecular outflows are a common feature seen in high-mass star-forming regions (e.g. Beuther et al., 2002c; Liu et al., 2016b; Qiu et al., 2009). Outflows are seen mostly during the early phases of star formation when the protostar is actively accreting matter from the circumstellar material. Since EGOs trace a population of sources in an early evolutionary stage and are believed to be driven by outflows, a handful of studies have tried to examine the jet/outflow properties of these sources (e.g. Caratti o Garatti et al., 2015; Cyganowski et al., 2011b). As discussed in Section 1.3.2, Caratti o Garatti et al. (2015) derived the physical properties of H_2 jets from the NIR observations towards a sample of 18 EGOs. From the high angular resolution millimeter observations towards two EGOs, G11.92-0.61 and G19.01-0.03, Cyganowski et al. (2011b) present substantial evidence showing that these MYSOs drive massive bipolar outflows.

Tracers of jets and outflows

In the early stages, the outflows are embedded within the molecular cloud envelope. The molecular transitions of H_2,$(1-0)$ S(1) line at 2.12 μm in the NIR regime and the rotational transition lines of the CO molecule in the millimeter regime are well-accepted tracers of outflow activity in star-forming regions (Beuther et al., 2002c; Varricatt et al., 2010; Zhang et al., 2001).

The CO molecule is easily excited and hence is an efficient tracer of the cold molecular swept-up ambient material. Different transitions trace the kinematic structure of different parts of the molecular cloud. Transitions from higher rotational levels of the CO molecule

(e.g., $J = 3 - 2$) have higher critical density and hence their emission arises from denser parts of the star-forming region like the dense dust cores. Whereas, lower level transitions (e.g., $J = 2 - 1$, $J = 1 - 0$) effectively trace the kinematics of the low-density regions of the natal cloud (Rygl et al., 2013). In addition to this, the different isotopologues of CO are tracers of different conditions of the molecular cloud. The ^{12}CO is optically thick and can map the spatial and kinematic extent of the outflow. On the other hand, ^{13}CO and C^{18}O are considered to be optically thin and are high-density tracers (Lo et al., 2015).

H_2 line emission at NIR and MIR wavelengths are powerful tracers of shock-excited gas from protostellar jets. The jets are heated to typically a few 1000 K, giving rise to thermal emission from shock fronts. In addition, silicon monoxide (SiO) is also believed to be a tracer of collimated molecular jets and shocks in the ISM because it is formed due to the sputtering of Si atoms from the grains due to fast shocks (Hatchell, Fuller & Millar, 2001; López-Sepulcre et al., 2011; Miettinen et al., 2006). Protostellar jets are revealed by SiO emission towards several high-mass star-forming regions (e.g. Cesaroni et al., 1999; Codella et al., 2013; Leurini et al., 2013).

Massive molecular outflows often co-exist with ionized jets (Anglada, 1996; Purser et al., 2016). Jets are believed to entrain gas and dust from the cocooning molecular cloud. Ionized jet, moving away from the protostar through the polar axis, carrying away excess angular momentum, is a source of momentum to drive H_2 outflows as well as large-scale molecular outflows. The detection of jets provide an indirect evidence for the presence of circumstellar accretion disk around the protostar (Cesaroni et al., 2006).

Properties of jets and outflows

Emission from ionized jets dominates the centimeter wavelength, where the emission originates due to the thermal *free-free* emission mechanism. Typically, ionized jets have spectral index values of the range of $0.4 - 0.9$ (e.g. Panagia & Felli, 1975; Purser et al., 2016; Reynolds, 1986; Sanna et al., 2016), where the spectral index, α is defined as

$$S_\nu \propto \nu^\alpha \tag{1.7}$$

Here S_ν is the flux density at frequency ν. From the centimeter observation of a number of outflow sources, Anglada (1996) has complied a list of characteristic features exhibited by ionized jets which are as follows.

1. Elongated morphology of the centimeter emission at subarcsecond scales with a high degree of collimation.

2. Weak radio emission, with flux densities of the order of $\sim 0.5 - 10$ mJy.

3. Alignment with large-scale molecular outflows, with the driving source(s) at the centroid of the outflow.

4. Rising or flat spectral index as one would expect for a thermal *free-free* emission.

5. Association with both high and low-luminosity objects.

6. The dynamical timescales of the jet should only be a few years, indicating that the emission traces an extremely early stage of evolution.

In recent years, several observational studies have also shown spectral index values, $\alpha < -0.1$, along the jet axis, away from the cores around the knots of ionized emission. Such values of spectral index are consistent with the presence of non-thermal emission (e.g. Masqué et al., 2019; Obonyo et al., 2019; Vig et al., 2018). This behaviour of radio spectrum is attributed to synchrotron emission, arising due to the relativistic motion of charged particles accelerated by the strong shocks from protostellar jets. This interpretation is supported by several theoretical studies as well (Anglada, Rodríguez & Carrasco-González, 2018, and references therein). The radio spectrum from protostellar jets may have contribution from both thermal as well as non-thermal components. The two can, however, be separated by examining the SEDs over a large range of radio frequencies. The non-thermal emission is expected to dominate at low frequencies.

Observed outflows from protostars are seen to have varying degrees of collimation. The youngest YSOs drive highly collimated jets/outflows, a result of their accretion from the circumstellar disk surrounding them. The collimation factor of the outflows appears to decrease with age and lumninosity of the source (e.g. Arce et al., 2007; Beuther & Shepherd, 2005). The dynamical timescale of the outflows is a crucial parameter from which one can estimate the evolutionary stage of the driving source. This quantity is given by the expression (Qiu et al., 2009)

$$T_{\rm dyn} = \frac{L_{\rm flow}}{v_{\rm max}} \tag{1.8}$$

where $L_{\rm flow}$ is the half length of the end-to-end extension of the outflow and $v_{\rm max}$ is the maximum flow velocity from the systemic velocity of the molecular cloud harbouring the protostar. Relatively shorter timescales of the order of $\sim 10^4$ yr indicate that the outflow is driven by dense compact cores or HMCs. However if the timescales are $\gtrsim 10^5$ yr, the driving source is more evolved and has begun to power an UC H II region (Qiu et al., 2009,

and references therein).

Given that EGOs exhibit different characteristics at different wavelengths, the best way to comprehensively scrutinize the nature of these objects would be to follow a multiwavelength approach.

1.4 Motivation and outline of this thesis

An extensive literature review into formation of stars revealed the importance of studying the earliest phases of high-mass star formation. This thesis work focusses on the early stages of the formation of high-mass stars through a multifrequency path. As is clearly evident from the discussion presented earlier, EGOs offer a potential sample to probe the early phases of massive star formation. EGOs are a fairly new class of protostellar objects discovered, having interesting morphologies and statistical properties.Various surveys and statistical studies aimed at understanding the general properties of these sources, brought to light the association of these sources with collimated H_2 jets/outflows and massive molecular outflows. Recent studies have speculated that EGOs, in all likelihood, would in fact harbour protoclusters rather than single protostars (Towner et al., 2019). So as to get a better insight into individual EGOs and their specific nature, we formulated the research problem of carrying out observational investigation of a selected sample of EGOs (G12.42+0.50 and G19.88-0.53) through various bands of the electromagnetic spectrum starting from radio wavelengths to NIR wavelengths. Though there exists ample literature supporting the presence of ionized jets from young protostellar objects through high-frequency radio observations, the studies dedicated to probing them at low radio frequencies is very limited. This thesis work aims to specifically look for evidence of ionized jets arising from EGOs through the low-frequency radio bands. This low-frequency domain also offers an added advantage of identifying non-thermal emission from jets.

EGO G12.42+0.50 is catalogued as a "possible" outflow candidate with an extended morphology and large integrated flux density of 1.4 Jy (Cyganowski et al., 2008) in the IRAC $4.5\mu\mathrm{m}$ band. G19.88-0.53, on the other hand, is catalogued as a "likely" outflow candidate, with discernible $4.5\,\mu\mathrm{m}$ emission knots (Fig. 1.9a) and integrated flux density of 0.6 Jy. The large angular extent and flux densities of these EGOs, along with them being embedded within IRDCs, make these sources excellent representatives of EGOs tracing the earliest stages of high-mass star formation.

We use the low-frequency radio continuum observations made using the Giant Meterwave

Radio Telescope (GMRT), India to probe the ionized emission associated with the sources of interest. Supporting NIR imaging and spectroscopic observations with the UKIRT, Hawaii, help understanding the nature of the jets/outflows powered by the target source. With additional, high-quality archival data available for the targets, the gas kinematics and dust emission are also studied. A rigorous in-depth study of these sources unveiled many interesting results. Further, while attempting to understand the scenario of cluster formation in G133.50+9.01, molecular line data of the complex revealed a very exciting picture and led us to explore cloud-cloud collision signatures and present the interpretation. In presenting the work done, the thesis is structured in the following way

- **Chapter 1:** This (the current chapter) chapter gives an overall introduction to star formation with particular emphasis on the formation of high-mass stars - the theoretical models and the evolutionary sequence. This chapter also introduces EGOs and gives a brief discussion on the nature of these objects and the current status of research towards these objects.

- **Chapter 2:** This chapter presents the details of various observations conducted along with an elaborate discussion on the associated data reduction techniques. Details of various archival datasets that have been used to investigate the nature of the different components associated with the target sources is also presented in this chapter.

- **Chapter 3:** This chapter deals with the study of the EGO, G12.42+0.50, to probe the early phases of high-mass star formation. The associated ionized, dust, and molecular components of this source are studied in detail employing various observational and archival data at NIR, MIR, FIR, (sub)millimeter and radio wavelengths. The radio continuum emission advocates for a scenario of coexistence of an UC H II region and an ionized thermal jet possibly powered by the same MYSO. Study of the molecular gas kinematics reveals the presence of both infall activity and large-scale outflow, and also bulk gas inflow along a complex network of filaments, mimicking a hub-filament system.

- **Chapter 4:** A multiwavelength analysis of star formation associated with the EGO, G19.88-0.53 is discussed in this chapter. With multiple detected radio and millimeter components, G19.88-0.53 unveils as harbouring a protocluster rather than a single MYSO. An ionized thermal jet is detected which is found to be associated with a massive, dense and hot ALMA 2.7 mm core driving a bipolar CO outflow. Detailed investigation of the gas kinematics unveils G19.88-0.53 as an active protocluster with

high-mass star-forming components spanning a wide evolutionary spectrum from hot cores in accretion phase to cores driving multiple outflows to possible UC H II regions.

- **Chapter 5:** In this chapter, we present a likely cloud-cloud collision candidate, G133.50+9.01, triggering the formation of filaments, cores, and a stellar cluster. Morphologically, the cloud complex appears to be made of two colliding molecular clouds, the intersection region of which is characterized by broad bridging features, characteristic of collision. The shock-compressed layer formed at the interaction front resembles an arc-like structure with enhanced excitation temperature and H_2 column density. A complex network of filaments is detected at 850 μm with embedded dense cores, all spatially well correlated with the shock-compressed layer. A stellar cluster revealed through an overdensity of identified Classes I and II YSOs along the intersection arc corroborates with a likely collision induced origin.

- **Chapter 6:** The final chapter summarizes the results and interpretations from the thesis. A brief discussion on the ongoing work related to the radio data analysis of EGO G34.26+0.15 is also presented. In addition, the future scope and plans for proceeding beyond the thesis work is also outlined in this chapter.

Chapter 2

Observation, Data Reduction and Archival Data

The study carried out in this thesis follows a multiwavelength approach. The selected star-forming regions are probed at infrared, submillimeter, millimeter, and radio wavelengths. Fig. 2.1 shows the potential of each wavelength regime towards an in-depth investigation of the various components of the complexes under study. Data from various telescopes operating at different wavelength regimes are employed to build a comprehensive picture and to understand the underlying physical processes associated. Data from Legacy as well as the upgraded GMRT are used to examine the nature of the ionized gas emission from the EGOs. Emission from shock indicators is probed at NIR and MIR wavelengths by carrying out imaging and spectroscopic observations using UKIRT. MIR and FIR data from *Spitzer Space Telescope*, *Herschel Space Observatory* and the APEX Telescope Large Area Survey of the Galaxy (ATLASGAL) are used to probe the nature of the associated warm and cold dust components. The properties of compact dense cores are explored using high-resolution millimeter observations from Submillimeter Array (SMA) and the archives of ALMA. Observed and archival molecular line data from various telescopes are utilised to investigate the kinematics of the molecular cloud and dense cores associated with the regions under scrutiny. This chapter outlines the details of the observations carried out and the data reduction procedures adopted. In addition, the various archival datasets used are also discussed.

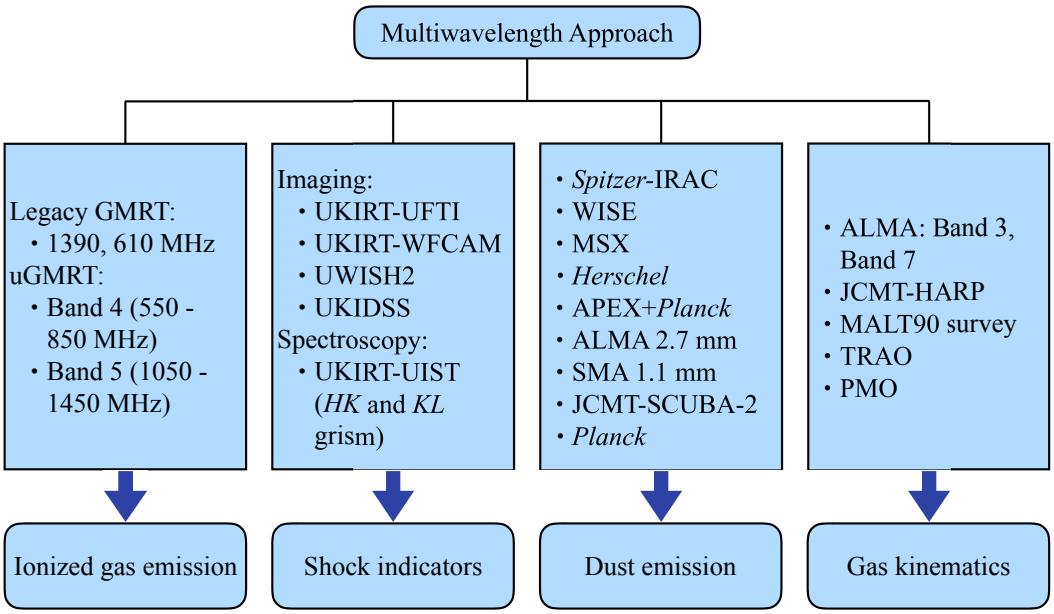

Figure 2.1: Block diagram of various observational and archival data used for the multi-wavelength study of the high-mass star-forming complexes investigated in this thesis.

2.1 Low frequency radio interferometric observations using GMRT

While radio astronomers have the great advantage of being able to carry out observations using ground based facilities, large wavelengths limit the angular resolution attainable ($\theta \sim \lambda/D$). In order to obtain high-resolution radio maps, radio astronomers use single dish telescopes with large diameters operating at shorter wavelengths (centimeter and millimeter). However, to attain subarcsecond resolutions at meter wavelengths, one employs a technique called 'aperture synthesis' based on interferometry. A radio interferometer measures the interference pattern from an antenna pair. The output from each antenna pair is multiplied and time averaged to get a complex spatial coherence function in the *uv* plane called the 'visibility'. Visibilty is a function of three variables, (u, v, w) that define the coordinate system of antenna spacing. For a coplanar array, the visibility relates to the source

brightness as the Fourier transform of the source brightness, given by

$$V(u, v, 0) = \iint I(l, m) e^{-2\pi i(ul+vm)}\, dl\, dm \tag{2.1}$$

where, $V(u, v, 0)$ is the visibility between two points in the *uv* plane with baseline coordinates $(u, v, 0)$. $I(l, m)$ is the intensity of the source which is a function of (l, m), that are direction cosines of the source in the (u, v) coordinate system. This expression is valid under the consideration that the observation is coplanar, i.e. $w = 0$, and the source brightness distribution is limited to a small region of the sky.

As the large synthesised aperture is only sampled at the antenna locations, the visibilities in the *uv* plane will not be continuous. But with the rotation of the Earth, over the period of the observation run, one samples more and more of the *uv* plane. With a long observation run using large arrays like GMRT with 30 antennas, the sampling of the *uv* plane is sufficiently dense to allow extremely high quality reconstruction of intricate details of complex radio sources. This technique of using the Earth's rotation to improve the *uv* coverage is called the 'Earth rotation aperture synthesis'.

2.1.1 Radio continuum observations

Radio continuum observations towards G12.42+0.50 and G19.88-0.53 were carried out at low radio frequencies using the GMRT (with the upgraded configuration, uGMRT for the second source) located at Pune, India. GMRT offers a hybrid configuration of 30 antennas arranged in a Y-shaped layout. Each antenna is a parabolic dish with a diameter of 45 m. The three arms contain 18 evenly placed antennas and provide the largest baseline of ~ 25 km. The central $1\,\mathrm{km} \times 1\,\mathrm{km}$ region houses 12 antennas that are randomly oriented with shortest possible baseline of ~ 100 m. Fig. 2.2 shows the location, the Y-shaped layout of the GMRT antennas, and a close-up view of a few antennas. This hybrid configuration enables radio mapping of small-scale structures at high-resolution, along with large-scale, diffuse emission at low-resolution. A comprehensive overview of GMRT systems can be found in Swarup (1991), and discussions on the upgradation are presented in Gupta et al. (2017).

The radio continuum observations aim to probe the nature of the ionized gas emission associated with the sources under study. The observations were made with these sources at the phase centre. Since the amplitude of the visibility function is proportional to the flux density of the source, it can be converted to the flux density of the target source. For this, we measured the visibility of a source of known and non-variable flux density to get the

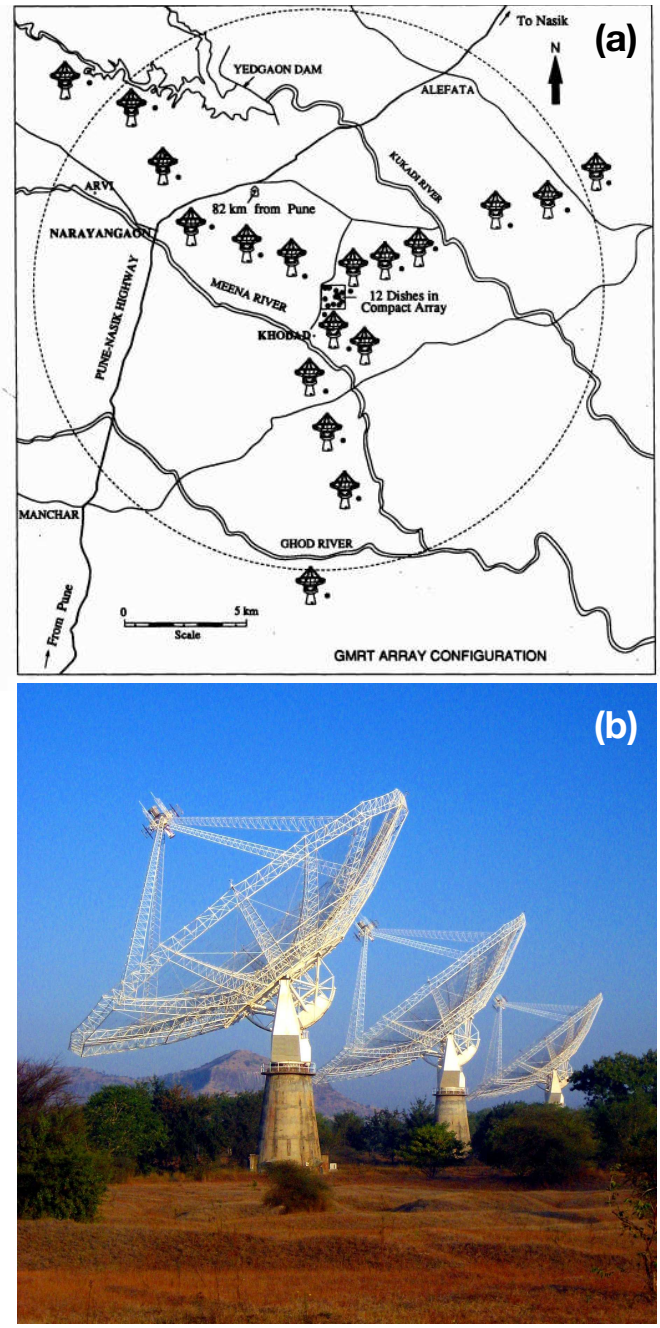

Figure 2.2: (a) Y-shaped array configuration of the GMRT antennas. The length of the three arms are $\sim$14 km each and the central region is $\sim 1\,\mathrm{km} \times 1\,\mathrm{km}$. (b) A close-up view of three antennas of GMRT. (Images are taken from http://gmrt.ncra.tifr.res.in)

flux density of the target source. These sources with known flux densities are called flux density or primary calibrators. Due to the changes in the upper ionosphere, the complex antenna gain also varies with time. In order to account for this, periodic observations of

an unresolved source of known structure were made between target observations. This source is referred to as the phase calibrator, the flux density of which is calibrated using the flux density of the flux calibrator. To probe our regions of interest, at all angular scales, full synthesis observations were carried out. The observing sequence followed is depicted in Fig. 2.3 where each observing run requires at least two observations of the primary flux calibrator(s), usually at the beginning and end of the observation cycle. Observations of the phase calibrator is interspersed between target observations. Typically the target is observed for $\sim$ 40 mins followed by the phase calibrator for $\sim$ 5 mins with the cycle continuing over the allotted timeframe. For our observations we have used VLA calibrators 3C286 and 3C48 as primary flux calibrators and 1822-096, 1911-201 and 1743-038 as phase calibrators. To sample the complex morphology of the sources and obtain high-fidelity imaging, the integration time was fixed so as to achieve low *rms* noise of few tens of μJy and adequate *uv* coverage. The details of the observations are listed in Table 2.1.

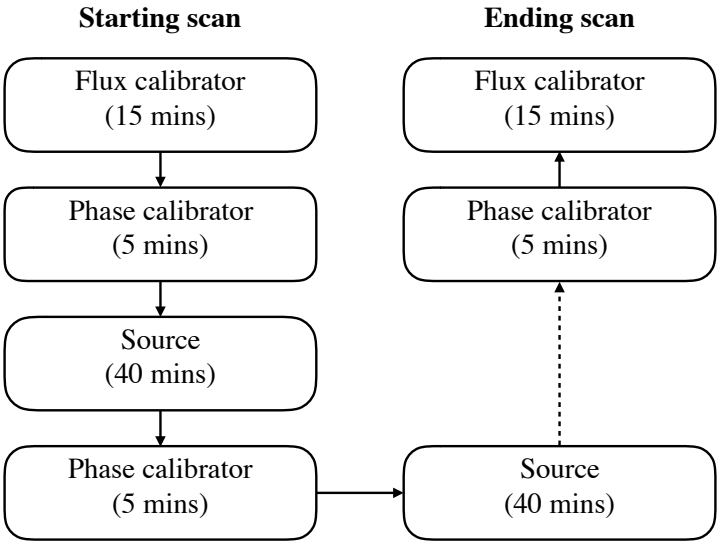

Figure 2.3: Flow chart of sequence followed for GMRT observations.

2.1.2 Data reduction procedure

GMRT radio continuum data reduction is carried out using the National Radio Astronomy Observatory (NRAO) Astronomical Image Processing Software (AIPS). It is a software package for calibration, data analysis, and imaging of radio astronomical data. A flow chart illustrating the tasks involved is shown in Fig. 2.4. A brief overview of the procedure

Table 2.1: Details of radio continuum observations using GMRT.

Details	G12.42+0.50		G19.88-0.53	
	610 MHz	1390 MHz	550−850 MHz (Band 4)	1050−1450 MHz (Band 5)
Date of Observation	21 July 2017	22 August 2017	19 June 2018	18 June 2018
Proposal code	32_063(S2) (PI: N. Issac)	32_063(S1) (PI: N. Issac)	34_047(S1) (PI: N. Issac)	34_047(S2) (PI: N. Issac)
Bandwidth (MHz)	32	32	300	400
Flux calibrators	3C286	3C286, 3C48	3C286	3C286
Phase calibrators	1822-096	1911-201	1822-096	1743-038
Integration time (hrs)	~ 5	~ 5	~ 5	~ 5
Synthesized beam	$7.6'' \times 4.8''$	$3.0'' \times 2.4''$	$11.5'' \times 7.6''$	$4.3'' \times 2.7''$
rms (μJy beam^{-1})	94	29.7	100−150	44−47

and tasks involved is given below.

1. **Loading data into AIPS and indexing:**
   The raw data obtained from GMRT come in a binary format with '.lta' extension. To make these compatible with the AIPS environment these are converted to the FITS format using the tasks `LISTSCAN` and `GVFITS`. Once the raw data are converted to FITS format these are imported into the AIPS environment using the task `FITLD`. This task reads the *uv* data from the FITS file and creates a file with extension '.FITLD' in AIPS. A set of extension tables containing the information regarding history, antenna names, source list, frequency, bandwidths, etc. are included within this file. The task `INDXR` indexes the *uv* data files and creates the NX table. This task also creates the calibration table, CL1 with null entries that will serve as a template to the new CL tables generated subsequently.

2. **Preliminary flagging and calibration:**
   The initial portion of each scan may be corrupted. This happens because the telescope may be slewing when data acquisition is switched on. The task, `QUACK` is used to remove these initial (~ 0.3 mins) data points from each scan. The flagged data are written to a flag (FG) table in the *uv* data file. The data can be displayed using the task `TVFLG` to identify non-working antennas. The bad antennas, if any, are then flagged using the task `UVFLG`. It is crucial that bad antennas be removed before the calibration process, since the presence of these antennas during calibration could result in inaccurate antenna gains. Since each frequency band is divided into

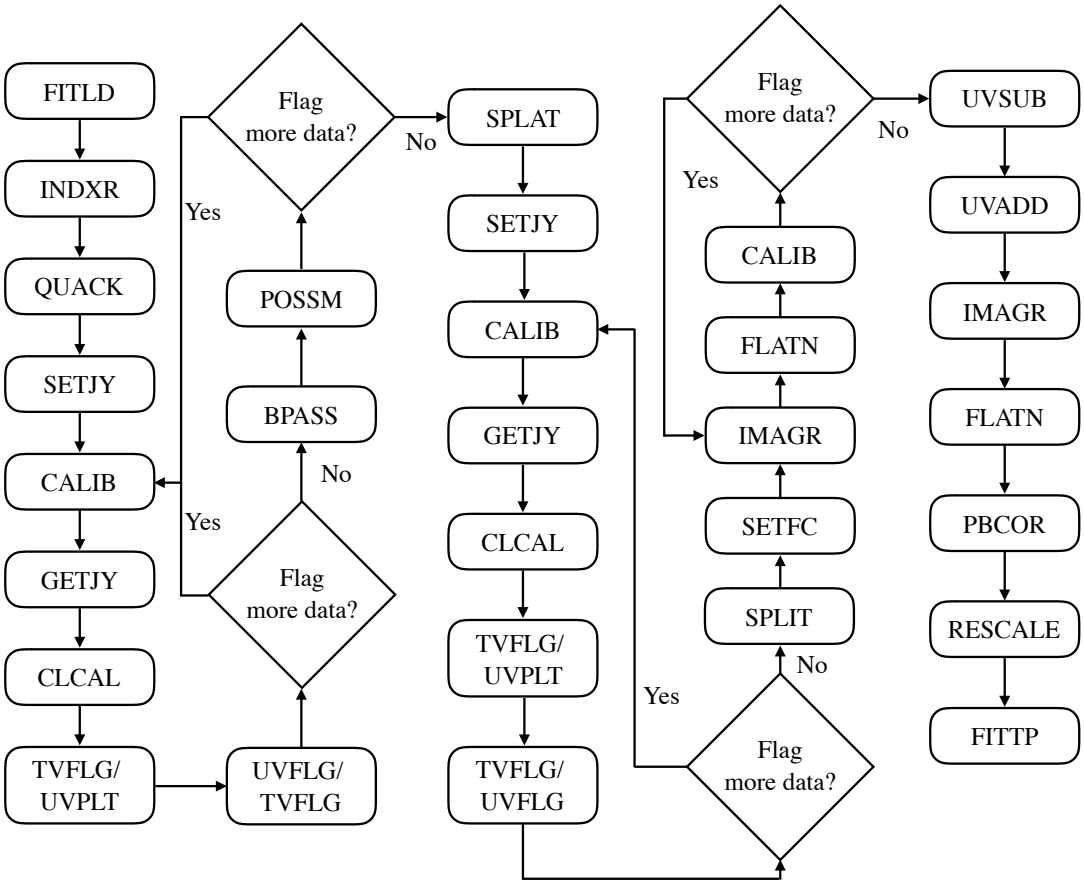

Figure 2.4: Flow chart illustrating the sequence of tasks from AIPS used for the calibration and imaging of GMRT radio continuum data.

multiple channels (256 channels for Legacy GMRT and 2048 channels for uGMRT), a reference channel (usually near the middle of the band) is selected for initial flagging and calibration purposes. Also, an antenna (typically one within the arms of the Y-shaped array), with low noise is chosen as a reference antenna. These are done by inspecting the *uv* data using `TVFLG`.

Once the bad antennas are removed, the data are then calibrated. As a first step in the calibration cycle, we use the task `SETJY` to assign the flux density of the flux calibrators. The flux density values of the VLA flux calibrators, that we have used in our observations exist within this task. This is followed by the calibration task, `CALIB`, which computes the antenna based gains for the primary calibrators to be applied to the *uv* dataset. A solution (SN) table containing the complex gain solutions is created and attached to the *uv* file. Following calibration, we use the task `GETJY` to determine the flux density of the phase calibrator. Finally, the solutions

from the SN table is applied using the task CLCAL. This creates a new CL2 table which contains the flux calibration of all the sources. This task completes one cycle of calibration. The calibrated data are then examined using the display tasks TVFLG and UVPLT with the DOCALIB=1, so as to display the calibrated data. Any bad data points corrupted by radio frequency interference (RFI), bad baselines or time ranges are identified and flagged. The calibration process is repeated after removing the SN and CL2 tables. The flagging-calibration loop is continued till all (as far as possible) bad data points are removed.

3. **Bandpass calibration:**
   The initial steps of calibration discussed are done over one channel. However, the antenna gains vary over the passband, mainly due to the antenna based band-shape and residual fixed delay errors. The bandpass calibration is performed over all the channels to correct for the frequency dependence of the antenna gains using the task BPASS. This task writes the bandpass response functions to the BP table. For our observations, the flux calibrator also serves as the bandpass calibrator. The bandpass functions from the BP table are visualized using the task POSSM. Using this plot, bad channels are identified and flagged using UVFLG. Following the removal of bad channels, the calibration loop is repeated beginning from CALIB after deleting the SN, CL2 and BP tables.

4. **Channel averaging and calibration:**
   Once the initial calibration steps are completed, the channels are averaged employing the task SPLAT. This is done to improve the signal-to-noise ratio and it also reduces the data volume. However, averaging leads to bandwidth smearing effects. Bandwidth smearing is the chromatic aberration in the image when the visibilities from a finite bandwidth are gridded as if monochromatic. Hence, channel averaging is restricted to keep the bandwidth smearing negligible. The maximum number of channels that can be safely averaged at GMRT frequencies are given below:

   - 1280 MHz: $40 - 48$ channels ($5 - 6$ MHz)
   - 610 MHz: $24 - 32$ channels ($3 - 4$ MHz)

   The output 'SPLAT' file has fewer number of channels than the original *uv* dataset. The flagging-calibration loop is re-run on all the averaged channels starting from SETJY, to remove bad data from all the channels and to improve the calibration solutions. The calibrated SPLAT file has multiple sources. For the purpose of imaging,

we separate out the target source from the SPLAT file using the task SPLIT, after applying the calibration solutions. The calibrated *uv* data file of the target source is written to the SPLIT file.

5. **Imaging and self-calibration of the target source:**
While performing wide-field imaging, the w-term effect (non-coplanarity) comes into picture when a 2D sky brightness map is constructed from 3D image volume. When imaging a large angular region, the sky can no longer be treated as a 2D plane, especially at low frequencies. The use of the standard CLEAN task will create distortions around sources and this effect becomes increasingly serious with the distance from the phase centre. To account for this distortion, one must make use of a wide-field imaging algorithm that involves constructing facets. In AIPS, task SETFC produces facets, creating an output 'BOXFILE' which contains the information about the facets. For a source of size θ, the number of facets required, N, is the ratio of the solid angle of the mapped region (θ_f^2) to the solid angle of the synthesised beam (θ^2), given as

$$N = \frac{2\theta_f^2 \, B_{max}}{\lambda} \tag{2.2}$$

where B_{max} is the longest projected baseline and λ is the wavelength. The final calibrated *uv* data of the target source from the SPLIT file are used to generate the brightness distribution of the target field using the the task IMAGR. The output BOXFILE from SETFC is used as an input to this task. IMAGR does the Fourier transform of the visibilities and generates the 'dirty beam'. The convolution of the dirty beam with the source brightness gives the 'dirty map'. The CLEAN algorithm (Högbom, 1974) in the IMAGR task performs the deconvolution. This algorithm represents the radio sky as a number of point sources and uses an iterative method to determine the location and strength of these sources. Boxes are drawn around the point sources which are called the CLEAN components that are CLEANed during each minor iteration cycle. The Fourier transform of the CLEAN components are computed and subtracted from the visibility data at the end of each major iteration cycle and a residual dirty image is computed. The source model constructed after the CLEANing consists of the CLEAN components, which is convolved with the CLEAN beam and then added to the residual image. The output from the IMAGR task consists of multiple images depending on the number of facets. These images are then combined to construct a single image using the task FLATN.

The quality of the image is significantly affected by the temporal fluctuations of the the Earth's atmosphere, which can affect the response of the antennas. The phase errors due to these fluctuations can be minimized by carrying out phase-only self-calibration of the visibility, based on the model image from the output of `IMAGR`. The task `CALIB` is used for performing the task of self-calibration. Several iterations of self-calibration are done until the phase variations are minimum.

The quality of the images are further improved by removing low-level noise from the *uv* data file. The model image consisting of the CLEAN components are subtracted from the *uv* data file using the task `UVSUB`. This creates an output '.UVSUB' file. Bad data, if any, from the residual *uv* data file are flagged and the CLEAN components are added back using the same task. The output of this is written to a '.UVADD' file. The `IMAGR` task is run on the UVADD file. The image is again inspected and `UVSUB` is repeated, if required.

6. **Primary beam correction and rescaling:**
   The final image is required to be corrected for the reduced sensitivity at the edges of the primary beam. To achieve this, the image is divided by the response of the primary beam using the task `PBCOR`.

   The system temperature of GMRT, at a particular frequency, is given by,

$$T_{\rm sys} = T_{\rm sky} + T_{\rm erc} \tag{2.3}$$

   where $T_{\rm erc}$ is the effective receiver temperature and $T_{\rm sky}$ is the sky brightness temperature due to the Galactic diffuse emission. At higher frequencies, the sky temperature is negligible compared to the effective receiver temperature. However, towards lower frequencies (e.g., 610 MHz), the contribution from Galactic diffuse emission becomes significant, and this is particularly relevant for observations made close to the Galactic plane (Marcote et al., 2015). Since our sources (G12.42+0.50 and G19.88-0.53) are close to the Galactic plane and the flux calibrators are located away from this plane, rescaling of the final images becomes necessary. The scaling factor is estimated under the assumption that the Galactic diffuse emission follows a power-law spectrum. The sky temperature at frequency, ν is determined using the

equation

$$T_{\rm sky} = T_{\rm sky}^{408}\left(\frac{\nu}{408\,{\rm MHz}}\right)^{\gamma}, \tag{2.4}$$

where γ is the spectral index of the Galactic diffuse emission which is taken to be -2.55 (Roger et al., 1999) and $T_{\rm sky}^{408}$ is the sky temperature at 408 MHz obtained from the all-sky 408 MHz survey of Haslam et al. (1982). The correction to the system temperature to account for the Galactic diffuse emission, $(T_{\rm sky}+T_{\rm sys})/T_{\rm sys}$ is used to scale the fluxes at each frequency. The task `RESCALE` is used to rescale the images with the estimated scaling factor.

2.2 NIR Observations using UKIRT

NIR imaging and spectroscopic observations were carried out using UKIRT, a 3.8-m infrared reflecting telescope located in Mauna Kea, Hawaii. UKIRT consists of four instruments namely, Wide-Field Camera (WFCAM), UKIRT 1-5 μm Imager Spectrometer (UIST), UKIRT 1-2.5 μm Fast-Track Imager (UFTI), and Michelle 10-20 μm imager and long-slit spectrograph. Observations towards G12.42+0.50 and G19.88-0.53 were carried out using WFCAM and UIST.

2.2.1 Imaging

We imaged G12.42+0.50 in the broad-band *H* filter and the narrow-band filter centred on the [FeII] line at 1.644 μm using the UKIRT-WFCAM, (Casali et al., 2007). WFCAM consists of four 2048 $\times$ 2048 HgCdTe Rockwell Hawaii-II arrays, each with a field of view of $13.65' \times 13.65'$ and a pixel scale of $0.4''$ pixel^{-1}. Details of the imaging observations are included in Table 2.2. The initial data reduction process is carried out by the Cambridge Astronomical Survey Unit (CASU).

Table 2.2: Details of UKIRT-WFCAM imaging observations towards G12.42+0.50.

Date (yyyymmdd)	Filter	Exposure time (s)	Integration time (s)
20170705	*H*	5	180
20170705	[FeII]	40	1440

Continuum subtraction of the narrow-band [FeII] image is performed following the steps described in Varricatt, Davis & Adamson (2005). This procedure employs multiple Starlink packages. The sky background is fitted and removed from the images using the KAPPA tasks `SURFIT` and `SUB`. It is crucial to align images before subtracting one from the other. The [FeII] and *H*-band images are aligned using the task `WCSALIGN`. Since the seeing conditions were different for the [FeII] and *H*-band observations, the image with lower point spread function (PSF) is smoothed to the full width at half maximum (FWHM) of the image with larger PSF. This minimizes residuals seen in the continuum-subtracted images owing to varying PSFs. For scaling the broad-band image, sky-subtracted flux counts of discrete point sources in both the narrow-band and broad-band images are measured. The average value of the ratio of the fluxes (*H*/[FeII]) is computed and used to scale the *H*-band image. Subsequently, the scaled *H*-band image is subtracted from the [FeII] image to construct the continuum-subtracted image [FeII] line image.

2.2.2 Spectroscopy

Spectroscopic observations towards G12.42+0.50 and G19.88-0.53 were obtained with UKIRT-UIST, (Ramsay Howat et al., 2004). UIST consists of a 1024×1024 InSb array. In spectroscopy mode, the camera with a plate scale of $0.12''\,\mathrm{pixel}^{-1}$ was used. Observations were carried out using the 4 ($\sim 0.48''$)-pixel-wide and $120''$ long slit. The spectra of G12.42+0.50 and G19.88-0.53 were obtained using the *HK* grism set-up that covers the spectral range of $1.395 - 2.506\,\mu\mathrm{m}$ with spectral resolution of 500. The spectroscopic observation of G12.42+0.50 was also done using the *KL* grism set-up that has a wavelength coverage of $2.229 - 2.987\,\mu\mathrm{m}$ with spectral resolution of 700. Flat-field and Argon arc lamp observations were performed ahead of the target observations on each night. The slit was oriented such that it samples the extended, $4.5\,\mu\mathrm{m}$ emission associated with the EGOs under study. In Fig. 2.5, the orientation of the slit for observation is displayed on the *Spitzer*-IRAC colour composite image of G12.42+0.50. Selected telluric standard stars were observed with the same instrument settings as for the target. This spectra is required for telluric and instrumental corrections. Since the target sources have an extended morphology, nodding along the slit would result in overlapping of the extended emission features. In order to avoid this, the science target observation was performed by nodding between the target and a blank sky position. However, for the standard star, the source was nodded along the slit in an ABBA pattern between two positions A and B along the slit (Perez M. & Blundell, 2009; Ramírez et al., 2009). Details of the observation are given in Table 2.3.

Table 2.3: Details of UKIRT-UIST spectroscopic observations towards G12.42+0.50 and G19.88-0.53.

Source	Date (yyyymmdd)	Grism	Exposure time (s)	Integration time (s)	Standard star (spectral type)	Slit position α(J2000)	Slit position δ(J2000)	Slit orientation (east of north)
G12.42+0.50	20150402	HK	120	720	SAO 160915 (A0V)	18 10 51.1	-17 55 50.0	55°
G12.42+0.50	20150405	KL	50	300	SAO 160915 (A0V)	18 10 51.1	-17 55 50.0	55°
G19.88-0.53	20150402	HK	120	720	SAO 142372 (A5 IV/V)	18 29 14.7	-11 50 16.7	88°

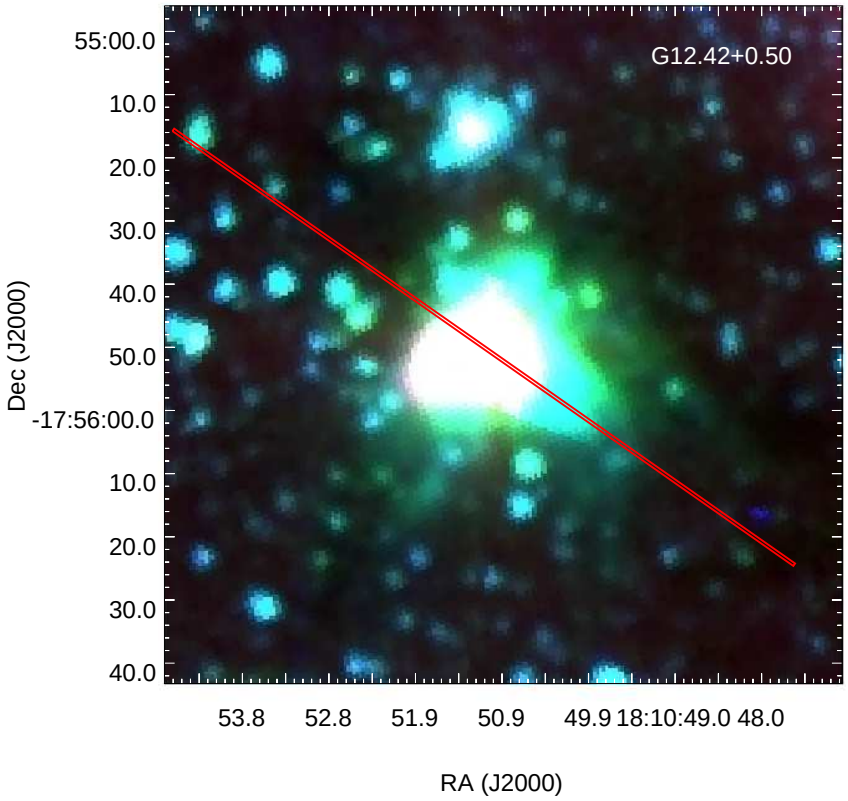

Figure 2.5: *Spitzer*-IRAC colour composite image of EGO, G12.42+0.50. The orientation of the slit is represented by a red rectangle, the dimensions matching the slit.

The initial data reduction is carried out by the `ORAC-DR` pipeline at UKIRT. The pipeline takes care of bad-pixel masking and flat-fielding of each frame of the standard star and target observation. Flat-fielding is done with the flat frame observation made ahead of the target observation on the same night. The sky frames are subtracted from the standard star frames to eliminate airglow lines. Following this, the frames are grouped and averaged into

a single standard star spectral frame. The ORAC−DR pipeline also groups the frames of the target observation into a single target spectral frame. Subsequent procedures involved in the reduction of the standard star and the target source are carried out using suitable tasks from the Starlink packages, FIGARO and KAPPA (Currie et al., 2008). A flow chart describing the steps involved and the Starlink tasks used to reduce the standard star and the target spectra is given in Fig. 2.6 and the steps involved are briefly described here.

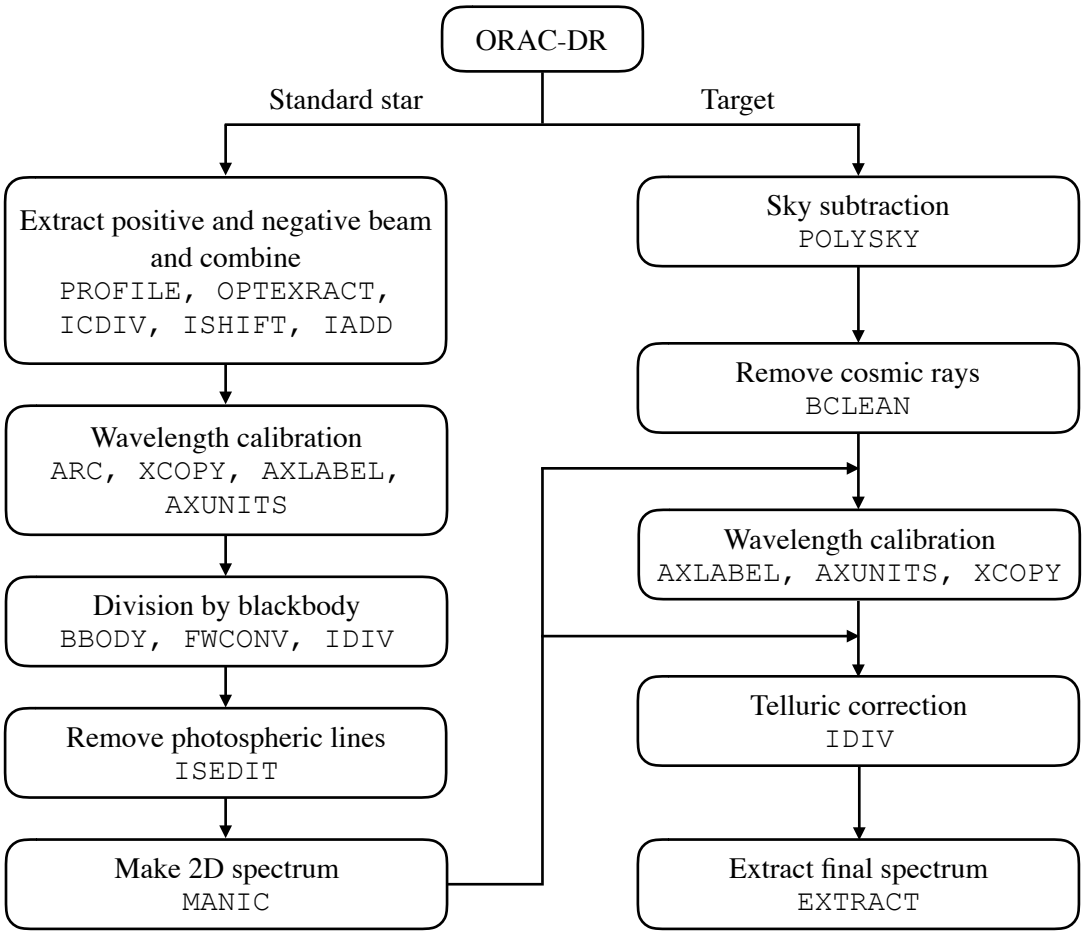

Figure 2.6: Flow chart illustrating the sequence of steps involved and the tasks used in the reduction and extraction of the spectra from UKIRT spectroscopic data.

1. **Standard star spectra:**
   For each observing run, during the standard star observation, the source was nodded along the slit in an ABBA pattern between two positions A and B. Thus, the sky-subtracted, grouped frame has a positive and a negative beam. The positive and

negative spectra are extracted from the standard star spectral image. The negative spectrum is inverted and shifted with respect to the positive spectrum. The two are then added and divided by a factor of 2 so that the flux is not overestimated. Subsequent to this, the wavelength calibration of the standard star spectrum is performed using the Argon arc lamp observation and the known wavelength line list of the Argon *HK* and *KL* spectra. Following wavelength calibration, the standard star spectrum is divided by a blackbody spectrum of temperature similar to the photospheric temperature of the standard star using the task `BBODY`, so as to normalize it before performing telluric correction of the target spectrum. Prior to telluric correction of target source spectrum, the photospheric lines are removed from the standard star spectrum by a careful interpolation of the continuum across these lines using the task `ISEDIT`. The photospheric lines from the standard star are identified from the UKIRT technical reference section[1]. The stellar spectrum is then projected onto a 2D plane using the task `MANIC` thus creating a spectral image of the standard star spectrum.

2. **Target source spectra:**
   As our target sources have extended emission, sky subtraction is done by subtracting the off-slit sky from the on-target spectral image, following which the subtraction of the residual sky is achieved with the FIGARO task, `POLYSKY`. Subsequent to sky subtraction, the rows of bad data, if any, and the cosmic rays from the CCD image are removed using the task `BCLEAN`. This task runs a non-interactive algorithm on a CCD image to detect and remove bad rows and cosmic rays. Wavelength calibration of the target spectral image is performed employing the wavelength calibrated standard star spectral image as the reference spectrum. Finally, telluric correction of the target spectrum is achieved by dividing the bad-pixel masked, flat-fielded, sky-subtracted and wavelength calibrated target spectral image by the reduced standard star spectral image. As the sky conditions were not photometric during our observations, we have not performed the flux calibration of any of the target sources.

The final reduced spectral image of the target source is examined and compared with the UKIDSS K-band images of the EGOs G12.42+0.50 and G19.88-0.53 to identify the regions showing extended and/or knotty *K*-band emission. Spectra are then extracted along different apertures sampling the extended *K*-band emission.

[1] https://www.ukirt.hawaii.edu/astronomy/calib/spec_cal/brackett.html

2.3 SMA observation

G12.42+0.50 was observed using the Submillimeter Array (SMA) on 2008 July 1 and 8. SMA operates in the millimeter and submillimeter regime covering the wavelength range $0.3 - 1.7$ mm. Commissioned in 2003, SMA is the first imaging interferometric telescope operating at submillimeter wavelengths. It consists of 8 movable antennas, where each antenna is composed of a smooth parabolic reflector, 6 m in diameter. The observation of G12.42+0.50 was carried out in its extended configuration. The phase reference center is $\alpha_{\rm J2000} = 18^{\rm h}10^{\rm m}51.8^{\rm s}, \delta_{\rm J2000} = -17^{\circ}55'56''$. In both observations, QSO 1924-292 was observed for gain correction and Callisto was used for flux-density calibration. The absolute flux level is accurate to about 15%. Bandpass is corrected by observing QSO 3C454.3. The 345 GHz receivers were tuned to 267 GHz for the lower sideband and 277 GHz for the upper sideband. The frequency spacing across the spectral band is 0.812 MHz or $\sim 0.9\,{\rm km\,s^{-1}}$. The 1.1 mm continuum data were acquired by averaging all the line-free channels over both the upper and lower spectral bands in the two datasets. The visibility data are calibrated with the IDL superset MIR package and imaged with the MIRIAD package. The MIRIAD task `SELFCAL` is employed to perform self-calibration on the continuum data. The synthesized beam size and *rms* noise of the continuum emission, from combining both compact and extended configuration data, are $\sim 1.5'' \times 1.0''$ and $\sim 3\,{\rm mJy\,beam^{-1}}$, respectively.

2.4 SCUBA-2 850 μm data

The dust continuum observation towards the cloud complex G133.50+9.01, at 850 μm was carried out in November 2014 using Submillimeter Common-User Bolometer Array 2 (SCUBA-2, Holland et al. 2013) on the James Clerk Maxwell Telescope (JCMT). JCMT is a 15-m telescope single-dish telescope operated by the East Asian Observatory. It operates in the submillimeter wavelength regime. The SCUBA-2 instrument is an array that operates at 450 μm and 850 μm simultaneously with a total of 5120 bolometers per wavelength. It has a field of view of $\sim 45\,{\rm arcmin^2}$ and can provide an effective beam size of $9.8''$ at 450 μm and $14.5''$ at 850 μm bands (Dempsey et al., 2013). For the 850 μm observation towards G133.50+9.01, the "CV Daisy" mapping mode was used with a mapping area of about $12'' \times 12''$. The data are reduced using `SMURF` in the Starlink package. The *rms* level is around $18.1\,{\rm mJy\,beam^{-1}}$.

2.5 TRAO observation

The molecular line data for the $J = 1 - 0$ transition of ^{13}CO towards G12.42+0.50 were obtained from the Taeduk Radio Astronomy Observatory (TRAO). TRAO is a 14 m radio telescope with a single-horn receiver system operating in the frequency range of 86 to 115 GHz and is located on the campus of the Korea Astronomy and Space Science Institute (KASI) in Daejeon, South Korea. The primary reflector has a surface accuracy of $< 130\,\mu$m *rms*, and the telescope also has a pointing accuracy better than $10''$. The main FWHM beam sizes for the ^{12}CO $(1-0)$ and ^{13}CO $(1-0)$ lines are $45''$ and $47''$, respectively. The system temperature ranges from 150 K, for 86-110 GHz to 450 K, for 115 GHz and ^{12}CO (Liu et al., 2018b).

2.6 PMO observation

The ^{12}CO $(1-0)$ and ^{13}CO $(1-0)$ lines towards the molecular cloud complex G133.50+9.01 was observed with the Purple Mountain Observatory 13.7-m telescope (PMO-13.7 m) in August 2013, as a part of PMO survey of Planck Galactic Cold Clumps (Liu, Wu & Zhang, 2012; Wu et al., 2012; Zhang et al., 2018). The nine beam array receiver system in single-sideband mode was used as the front end (Shan et al., 2012). The half-power beam width (HPBW) is $56''$ and the main-beam efficiency is ~ 0.45. ^{12}CO $(1-0)$ and ^{13}CO $(1-0)$ lines were obtained simultaneously. FFTS spectrometers were used as back ends, which have a total bandwidth of 1 GHz and 16384 channels, corresponding to a velocity resolution of $0.16\,\mathrm{km\,s^{-1}}$ for the ^{12}CO $(1-0)$ and $0.17\,\mathrm{km\,s^{-1}}$ for the ^{13}CO $(1-0)$. The on-the-fly (OTF) observing mode was utilized. The scan speed was $20''\,\mathrm{s^{-1}}$ and the mapping area is $22' \times 22'$. These data are smoothed with a beam size of $\sim 63''$. The typical *rms* noise level per channel is 0.3 K in T_A^* for the ^{12}CO $(1-0)$ and 0.2 K for the ^{13}CO $(1-0)$.

2.7 Archival datasets

In addition to the dedicated observations carried out towards the regions of study, in this thesis we have made extensive use of available archival datasets to probe the nature of emission from different components associated with the star-forming regions. In the discussion that follows, brief descriptions of the surveys and the datasets are given.

2.7.1 NIR data from UWISH2 and UKIDSS survey

The UKIRT Widefield Infrared Survey for H_2 (UWISH2) is a $180\,\mathrm{deg}^2$ survey of the Galactic Plane to probe the $1-0\,\mathrm{S}(1)$ ro-vibrational line of H_2 (λ = 2.122 μm) (Froebrich et al., 2011). The UWISH2 survey began in July 2009 and was completed in August 2011. This survey used the WFCAM at UKIRT to survey the inner Galactic plane ($10^\circ \lesssim l \lesssim 65^\circ$; $-1.3^\circ \lesssim b \lesssim +1.3^\circ$). Observations were made using a narrow-band filter ($\Delta\lambda = 0.021\,\mu\mathrm{m}$) centred at 2.122 μm with integration time of 720 s per pixel. The median seeing of the images is $\sim 0.7''$. The H_2 images have a 5σ detection limit of point sources of $K \sim 18$ mag and a surface brightness limit of $10^{-19}\,\mathrm{W\,m^{-2}\,arcsec^{-2}}$ when averaged over the typical seeing. CASU processed UWISH2 image of the region associated with G12.42+0.50 is retrieved from the archives.

We also use the *K*-band (2.2 μm) image obtained as part of the UKIRT Infrared Deep Sky Survey Galactic Plane Survey (UKIDSS-GPS, Lucas et al. 2008) from the WFCAM Science Archive. GPS is one of the five surveys within UKIDSS and surveys $> 1800\,\mathrm{deg}^2$ of the northern and equatorial Galactic plane at Galactic latitudes $-5^\circ < b < +5^\circ$ in the *J*, *H* and *K* filters. The *K*-band UKIDSS image and the narrow-band H_2 image from the UWISH2 survey are used to construct the continuum-subtracted H_2 line image of G12.42+0.50. Continuum subtraction is carried out following the same procedures outlined in Section 2.2.1.

2.7.2 MIR data from the *Spitzer* Space Telescope

The MIR wavelengths enable us to probe the warm dust environment associated with the EGOs. For this we make use of the MIR images available from the archives of the *Spitzer Space Telescope*. This telescope, that operated in the infrared regime, was launched in 2003. *Spitzer* carried three instruments on-board, namely, the Infrared Array Camera (IRAC, Fazio et al. 2004), the Multiband Imaging Photometer for *Spitzer* (MIPS, Rieke et al. 2004), and the Infrared Spectrograph (IRS, Houck et al. 2004). The IRAC instrument has simultaneous broadband imaging capability at 3.6, 4.5, 5.8, and 8.0 μm with angular resolutions $\sim 2''$. The large-scale Galactic plane survey, GLIMPSE, was carried out using IRAC. In order to probe the emission at MIR wavelengths towards G12.42+0.50 and G19.88-0.53, we use the level-2 Post-Basic Calibrated data (PBCD) images from this survey. The GLIMPSE images are retrieved from NASA/IPAC Infrared Science Archive (IRSA)[2].

[2]https://sha.ipac.caltech.edu/applications/Spitzer/SHA/

2.7.3 MIR data from the Midcourse Space Experiment

The Midcourse Space Experiment (MSX, Price et al. 2001) Galactic Plane Survey mapped the Galactic plane ($|b| < 5^{\circ}$), areas missed by the Infra-Red Astronomical Satellite (IRAS), and regions of high source density. With a spatial resolution of $\sim 18.3''$, it mapped the Galactic plane at four MIR spectral bands, 8.28, 12.13, 14.65, and 21.3 μm. In order to investigate the physical properties of the dust core associated with G12.42+0.50, we use the 12.13 and 14.65 μm MSX band images. The images are obtained from NASA/IPAC IRSA.

2.7.4 MIR data from WISE

To identify the stellar population associated with G133.50+9.01, we use the MIR archival data from the Wide-field Infrared Survey Explorer (WISE, Wright et al. 2010). WISE mapped the sky at the MIR wavelengths, 3.4, 4.6, 12, and 22 μm, with angular resolutions of 6.1, 6.4, 6.5, and 12.0$''$, respectively. We retrieve sources from the ALLWISE[3] catalog using NASA/IPAC IRSA. ALLWISE combines the data from the WISE cryogenic and NEOWISE (Mainzer et al., 2011) post-cryogenic survey phases. Combining the two data products, ALLWISE provides enhanced photometric sensitivity and accuracy, and better astrometric precision.

2.7.5 FIR data from *Herschel* Hi-GAL survey

FIR data used to study the nature of the cold dust emission is retrieved from the archives of the *Herschel Space Observatory*. This 3.5-m telescope, which was launched in 2009, covers the spectral regime of $55 - 671\,\mu$m (Pilbratt et al., 2010). On-board *Herschel* are the Photodetector Array Camera and Spectrometer (PACS, Poglitsch et al. 2010), Spectral and Photometric Imaging Receiver (SPIRE, Griffin et al. 2010), and the Heterodyne Instrument for the Far Infrared (HIFI, de Graauw et al. 2010). To study the nature of the cold dust emission associated with G12.42+0.50 and G19.88-0.53, we retrieve images from the archives of the Hi-GAL survey (Molinari et al., 2010). This survey is an Open Time Key Program of the *Herschel Space Observatory* that photometrically mapped the inner Milky Way ($|l| < 60^{\circ}$; $|b| < 1^{\circ}$) in five wavebands, 70, 160, 250, 350, and 500 μm. Hi-GAL observations were carried out in 'parallel mode' with PACS covering 70 and 160 μm and SPIRE covering 250, 350, and 500 μm. We use the level 2 processed images from PACS

[3]http://wise2.ipac.caltech.edu/docs/release/allwise/

and SPIRE, having resolutions of 5, 13, 18.1, 24.9 and 36.4″ at 70, 160, 250, 300, and 500 μm, respectively.

2.7.6 Submillimeter data from APEX+Planck

The dust emission mapped at submillimeter wavelengths traces the initial stages of high-mass star formation as they probe the denser parts of the ISM where stars form. ATLASGAL (Schuller et al., 2009) is a project aimed at the systematic survey of the inner Galactic plane with the Large APEX Bolometer Camera (LABOCA) array. LABOCA is an array of 295 bolometers with its bandpass centred at 870 μm. This instrument is mounted on the Atacama Pathfinder Experiment (APEX), a 12-m telescope located in Chajnantor. The ATLASGAL survey mapped $\sim 400\,\mathrm{deg}^2$ of the inner Galaxy with a resolution of $19.2''$ and pixel size of $6''$. Apart from this, the *Planck*/High Frequency Instrument (HFI, Lamarre et al. 2010) surveyed the sky at 353 GHz as part of the *Planck* mission. The *Planck* satellite was launched in 2009 with the aim of measuring the spatial anisotropies of the cosmic microwave background (Planck Collaboration et al., 2011). It observed the sky at nine frequency bands covering the range $30-857$ GHz with angular resolutions varying from $32.3'$ to $4.6'$. The HFI instrument provides high-sensitivity dust maps at 353 GHz (850 μm), with an angular resolution of $4.6'$. Csengeri et al. (2016) combined the images from the ATLASGAL survey and the images from *Planck*/HFI. The combined APEX+Planck maps, with bandpass centred at 850 μm, covers emission at larger angular scales, thus revealing the structure of the cold Galactic dust in more detail. The combined image has an angular resolution of $21''$ and a pixel size of $3.4''$. We extract the combined APEX+Planck images of the regions associated with G12.42+0.50 and G19.88-0.53 to examine the properties of the cold dust clump enveloping the EGOs.

2.7.7 (Sub)millimeter data from ALMA

ALMA archival data at 2.7 mm (Band 3) and 870 μm (Band 7) are used to study the G19.88-0.53 complex. ALMA is the world's largest ground-based facility operating in the (sub)millimeter regime. ALMA comprises of a large array of fifty 12-m antennas, and a compact array of four 7-m antennas and twelve 7-m antennas. The observations towards G19.88-0.53 were carried out during 2017-2018 (PI: S. Leurini #2017.1.00377.S). The high- and medium-resolution ALMA observations were obtained with the 12-m array in the FDM Spectral Mode and the low-resolution observations used the 7-m array in the ACA Spectral Mode. The high-resolution 2.7 mm continuum map, with a beam size of

$0.46'' \times 0.28''$, is used to identify the compact dust cores associated with G19.88-0.53. Along with the continuum observations, data cubes in both the bands are also retrieved to probe the kinematics of the dense cores associated with G19.88-0.53. Three datasets with resolutions, $16.9'' \times 8.0''$, $2.6'' \times 2.2''$, and $0.46'' \times 0.28''$ and velocity resolution of $0.67\,\mathrm{km\,s^{-1}}$ in Band 3 ($84 - 116\,\mathrm{GHz}$) and two datasets with resolutions $5.2'' \times 2.6''$ and $0.67'' \times 0.47''$ and velocity resolution of $0.86\,\mathrm{km\,s^{-1}}$ in Band 7 ($275 - 373\,\mathrm{GHz}$) are used. In Band 3, *rms* of 4.2, 3.6 and 17 mJy are achieved for high-, medium- and low-resolution observations, respectively. In Band 7, *rms* of 3.5 and 17 mJy are achieved for high- and low-resolution observations, respectively. Analysis of molecular line data is carried out using CLASS90 (Continuum Line Analysis Single-dish Software), a GILDAS[4] software (Grenoble Image and Line Data Analysis Software).

2.7.8 Molecular line data from MALT90 survey

To understand the gas kinematics in the G12.42+0.50 complex, molecular line data towards this region are obtained from the Millimeter Astronomy Legacy Team 90 GHz survey (MALT90, Foster et al. 2011; Jackson et al. 2013). This survey was aimed at characterising the physical and chemical evolution of high-mass star-forming regions and probed over 2000 dense clumps across the Galaxy identified from the ATLASGAL 870 μm survey. The MALT90 survey, carried out using the Australia Telescope National Facility (ATNF) Mopra 22-m telescope, has simultaneously mapped the transitions of 16 molecules near 90 GHz with a spectral resolution of $0.11\,\mathrm{km\,s^{-1}}$. The Mopra Telescope is a 22-m single-dish radio telescope operated by The Commonwealth Scientific and Industrial Research Organisation's Astronomy and Space Science division. The list of all the 16 transitions covered in this survey is given in Table 2.4, adopted from Jackson et al. (2013).

2.7.9 Molecular line data from HARP-JCMT

Apart from the molecular line data from the MALT90 survey, we also make use of the CO line observation towards G12.42+0.50 from JCMT. The molecular line data for the $J = 3 - 2$ transition of ^{12}CO, ^{13}CO and C^{18}O are downloaded from the archives of the Heterodyne Array Receiver Program (HARP, Buckle et al. 2009) mounted on JCMT. HARP is a Single Sideband (SSB) array receiver that can be tuned between 325 and 375 GHz and has an instantaneous bandwidth of $\sim$2 GHz and an Intermediate Frequency of 5 GHz. It comprises of 16 detectors laid out on a 4×4 grid, with an on-sky projected beam separation

[4]http://www.iram.fr/IRAMFR/GILDAS

Table 2.4: Spectral lines in the MALT90 survey. This table is adopted from Jackson et al. (2013).

Transition	Frequency (MHz)	Tracer
$N_2H^+\,(1-0)$	93173.772	Density, chemically robust
$^{13}CS\,(2-1)$	92494.303	Optical depth, column density, $V_{\rm LSR}$
H41 α	92034.475	Ionised gas
$CH_3CN\,5(0)-4(0)$	91987.086	Hot core
$HC_3N\,(10-9)$	90978.989	Hot core
$^{13}C^{34}S\,(2-1)$	90926.036	Optical depth, column density, $V_{\rm LSR}$
$HNC\,(1-0)$	90663.572	Density; cold chemistry
$HC^{13}CCN\,(10-9)$	90593.059	Hot core
$HCO^+\,(1-0)$	89188.526	Density; kinematics
$HCN\,(1-0)$	88631.847	Density
$HNCO\,4(1,3)-3(1,2)$	88239.027	Hot core
$HNCO\,4(0,4)-3(03)$	87925.238	Hot core
$C_2H\,(1-0)\,3/2-1/2$	87316.925	Photodissociation region
$HN^{13}C\,(1-0)$	87090.859	Optical depth, column density, $V_{\rm LSR}$
$SiO\,(1-0)$	86847.010	Shock/outflow
$H^{13}CO^+\,(1-0)$	86754.330	Optical depth, column density, $V_{\rm LSR}$

of $30''$. At 345 GHz the beam size is $14''$ (Buckle et al., 2009).

2.7.10 Dust polarization data from Planck

To determine the orientation of the magnetic field in the region associated with G133.50+9.01, we use the *Planck* 353 GHz (850 μm) dust continuum polarization data (Planck Collaboration et al., 2016a). The polarization data including the Stokes *I*, *Q* and *U* maps used are from the *Planck* Public Data Release 2 Full Mission Map with PCCS2 Catalog[5] (Planck Collaboration et al., 2016b). These maps have a beam size of $\sim 5'$ and a pixel size of $\sim 1'$.

Employing all the observational and archival datasets detailed in this chapter, we have carried out extensive multiband analysis of a selected sample of sources. The analyses, discussed in subsequent chapters, gives a wider perception of the different components of the star-forming regions under investigation and also their associated environments.

[5]https://irsa.ipac.caltech.edu/applications/planck/

Chapter 3

Initial phases of high-mass star formation: A multiwavelength study towards the extended green object G12.42+0.50

As discussed in Chapter 1, EGOs are believed to be tracers of the earliest stages of high-mass star formation. Investigations of these objects reveal crucial information regarding the complex mechanisms, like infall and jets/outflowsm, that are associated with high-mass star formation. Although statistical studies at NIR wavelengths and of molecular lines at sub-mm wavelengths towards EGOs are abundant, comprehensive multiwavelength scrutiny of individual EGOs, though important, is sparse. In addition, dedicated radio observations are also limited.

The formation processes of stars are known to be associated with high-velocity collimating winds involving MHD processes occurring in the protostellar accretion disk. Particularly, in MYSOs, photoionization is a dominant feedback process that ionizes the disk wind. Within a few tens to hundreds AU from the central protostar, the wind is paritally ionized giving rise to *free-free* radio emission. As we move to the larger scale wind-ISM interaction, the entrainment of molecular gas by the jet manifests as outflows. Given the strong accretion phase in MYSOs, the energetics of the associated jets and outflows will be pronounced, scaling with the mass of the driving source. Jets are also signposts of disk-fed accretion process. Thus a detailed study of the nature of the radio emission and molecular gas kinematics of EGOs of a selected sample of EGOs would be a significant contribution to the field of massive star formation. In Chapters 3 and 4, we investigate two EGOs, G12.42+0.50 and G19.88-0.53, respectively, using dedicated observations with GMRT and UKIRT supported with the valuable archival data.

In this chapter, we focus on the EGO, G12.42+0.50 catalogued as a "possible" outflow can-

didate and associated with the luminous infrared source, IRAS 18079-1756 (Cyganowski et al., 2008). The kinematic distance ambiguity towards G12.42+0.50 has been resolved by He, Takahashi & Chen (2012). Following them and Chen et al. (2010), we adopt a distance of 2.4 kpc in our study. Vutisalchavakul & Evans (2013) estimate the far-infrared (FIR) luminosity, from the IRAS fluxes, to be $\sim 10^4 \mathrm{L}_\odot$. From literature, G12.42+0.50 is designated as an UC H II (Jaffe et al., 1984; Wu et al., 2007). G12.42+0.50 has been observed as part of several surveys such as the Millimeter Astronomy Legacy Team 90 GHz (MALT90) survey (Foster et al., 2011; Jackson et al., 2013) and the 6 cm Red MSX Source survey by Urquhart et al. (2009). The latter was aimed at identifying candidate MYSOs. Apart from this, a millimeter study of southern IRAS sources by Osterloh, Henning & Launhardt (1997) reports IRAS 18079-1756 as an outflow candidate from the red- and blueshifted molecular outflow features observed in the $\mathrm{CO}\,(2-1)$ transition and a redshifted line dip in the $\mathrm{CS}\,(2-1)$ transition. $\mathrm{H_2O}$ maser emission is detected towards G12.42+0.50 (Cyganowski et al., 2013; Jaffe, Guesten & Downes, 1981). Chen et al. (2011), in their study, have identified a 95 GHz Class I methanol maser towards G12.42+0.50. In addition, a few molecular line surveys also include G12.42+0.50 (Cyganowski et al., 2013; Shirley et al., 2003).

In Fig. 3.1, we present the NIR and the MIR colour-composite images of the field of G12.42+0.50 developed from the UKIDSS (Section 2.7.1) and *Spitzer*-IRAC (Section 2.7.2) data, respectively. The images not only reveal the characteristic, extended and enhanced 4.5 μm emission defining the EGOs, but also show extended *K*-band nebulosity associated with G12.42+0.50. The morphology of the *K*-band emission is more confined to a narrower north-east and south-west stretch with a distinct dark lane in-between. A network of filamentary structures are seen towards the south-west and west, being more prominent in the NIR colour composite image. These filaments seem to converge towards G12.42+0.50 suggesting a 'hub-filament' scenario. Such systems have been detected in other star-forming complexes and discussed in various studies (Peretto et al., 2013; Yuan et al., 2018). Two IRDCs, SDC 12.427+0.502 and SDC 12.408+0.512 from the catalogue of *Spitzer* dark clouds by Peretto & Fuller (2009), are seen to lie on either side of G12.42+0.50 and marked on the images in Fig. 3.1.

3.1 Emission from ionized gas

The radio continuum maps at 1390 and 610 MHz, probing the ionized gas emission associated with G12.42+0.50, are shown in Fig. 3.2. The 1390 MHz map reveals the presence

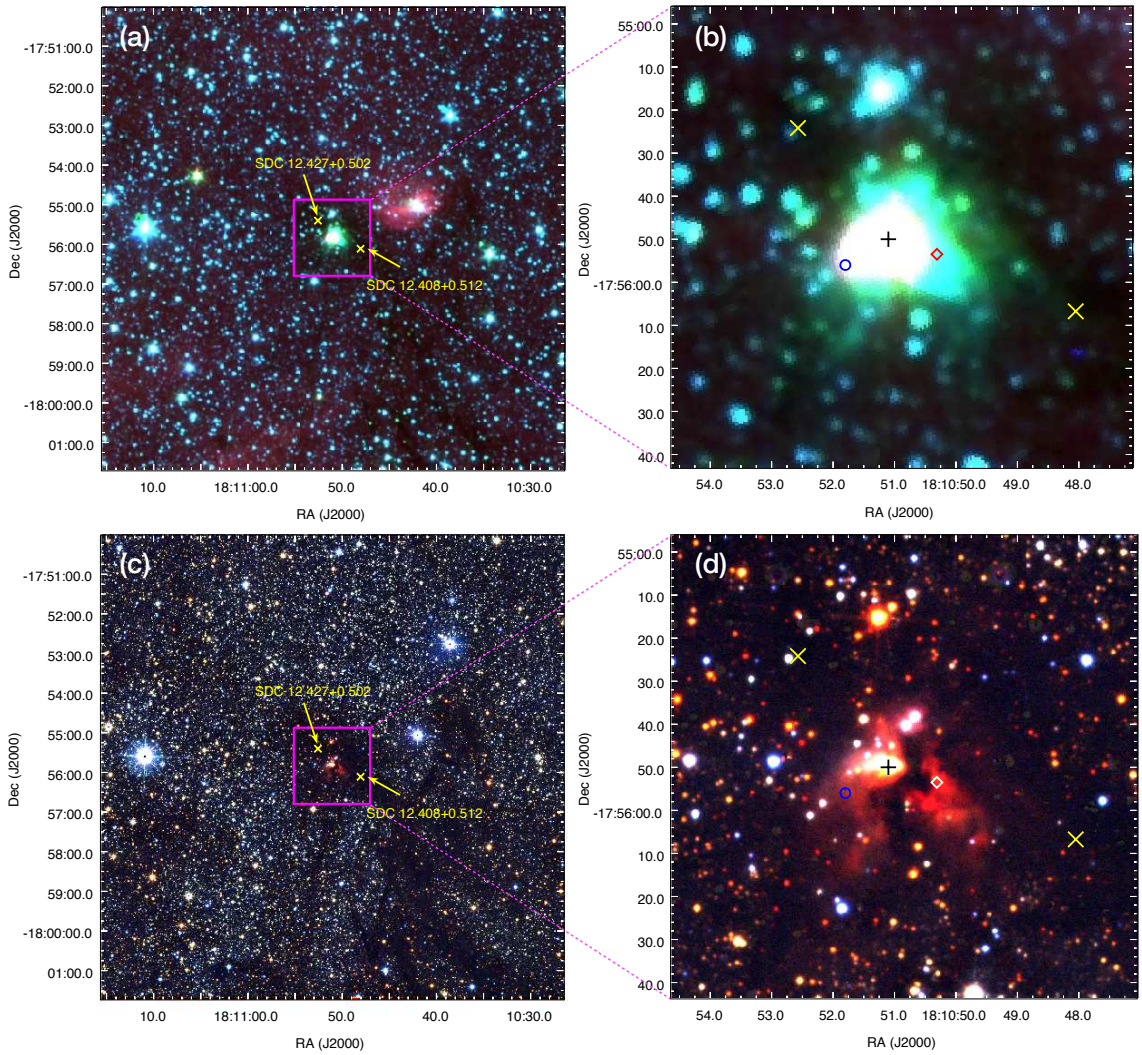

Figure 3.1: (a) Colour composite image of the region around G12.42+0.50 using IRAC 3.6 μm (blue), 4.5 μm (green) and 8.0 μm (red) bands. (b) A zoom-in showing the EGO G12.42+0.50. IRDCs are shown with the '$\times$' symbol and the position of IRAS 18079-1756 associated with G12.42+0.50 is indicated with a diamond mark. The cross marks the position of the 2MASS point source, J18105109-1755496. The location of the H_2O maser is shown as a blue circle. (c) and (d) are colour composites created from the UKIDSS *J* (1.25 μm), *H* (1.63 μm) and *K* (2.20 μm) band data, covering the same area as in (a) and (b), respectively.

of a linear structure in the north-east and south-west direction comprising of an extended emission with two distinct and compact components, labelled R1 and R2 in the figure. The component R1 is well resolved, whereas R2 seems to be barely resolved. In this figure, we also plot the contours of the high-resolution 6 cm (5 GHz) map obtained using VLA by Urquhart et al. (2009) as part of the RMS survey towards candidate massive YSOs. Both

components are also visible in the 6 cm map. In comparison, the lower-resolution 610 MHz shows a single, almost spherical emission region with the peak position coinciding with R1. However, a discernible elongation is evident towards R2. In addition, the 1390 MHz map shows a narrow extension in the north-west and south-east direction. Given that the maps (especially 1390 MHz) have low level stripes in the said direction, it becomes difficult to comment on the genuineness of this feature. Table 3.1 compiles the coordinates, peak and integrated flux densities of R1 and R2. The deconvolved sizes and integrated flux densities are estimated by fitting 2D Gaussians using the task `IMFIT` from Common Astronomy Software Application (CASA)[1] (McMullin et al., 2007)). At 610 MHz, the components are not resolved so the values obtained are assigned to R1 and hence should be treated as upper limits. For the component R1, the 5 GHz values are quoted from Urquhart et al. (2009). As for the component R2, that is barely resolved in both 1390 MHz and 5 GHz maps, we have set an upper limit to its size at both frequencies. This is taken to be the FWHM of the respective restoring beams (Urquhart et al., 2009). Further, at 5 GHz, we take the peak flux density to be the same as the integrated flux density.

Table 3.1: Peak coordinates, peak and integrated flux densities, and deconvolved sizes of the components R1 and R2 associated with G12.42+0.50.

	Peak Coordinates		Deconvolved size ($'' \times ''$)			Peak flux (mJy beam^{-1})			Integrated flux (mJy)		
Component	RA (J2000)	Dec (J2000)	610 MHz	1390 MHz	5* MHz	610 MHz	1390 MHz	5 * MHz	610 MHz	1390 MHz	5* MHz
R1	18 10 51.10	-17 55 49.30	2.6×0.6	1.9×1.7	1.4×1.2	4.4	5.3	3.5	4.7	7.9	6.2
R2	18 10 50.76	-17 55 52.80	-	1.5×1.2 †	1.1×0.6 †	-	0.6	1.1	-	0.7	1.1

† Upper limits which is half the FWHM of the restoring beam.
* Values for R1 are from Urquhart et al. (2009) and for R2 they are estimated from the available map.

In order to get an in-depth knowledge of the nature of the observed radio emission, we generate the spectral index map using our 1390 and 610 MHz maps. The spectral index, α, is defined as $S_\nu \propto \nu^\alpha$, where, S_ν is the flux density at frequency ν. GMRT is not a scaled array, hence, each frequency is sensitive to different spatial scales. To circumvent this, we generate new maps in the *uv* range ($0.7 - 47\mathrm{K}\lambda$) common to both frequencies. Keeping in mind the requirement of same pixel size and resolution, pixel and beam-matching is taken into account while generating the new maps. The spectral index map is then constructed using the task `COMB` in AIPS. Further, to ensure reliable estimates of the spectral index, we retain only those pixels with flux density greater than 5σ (σ being the *rms* noise of the map) in both maps. The generated spectral index map and the corresponding error map, which has the same resolution as that of the 610 MHz map ($\sim 7.6'' \times 4.8''$), are presented

[1] https://casa.nrao.edu

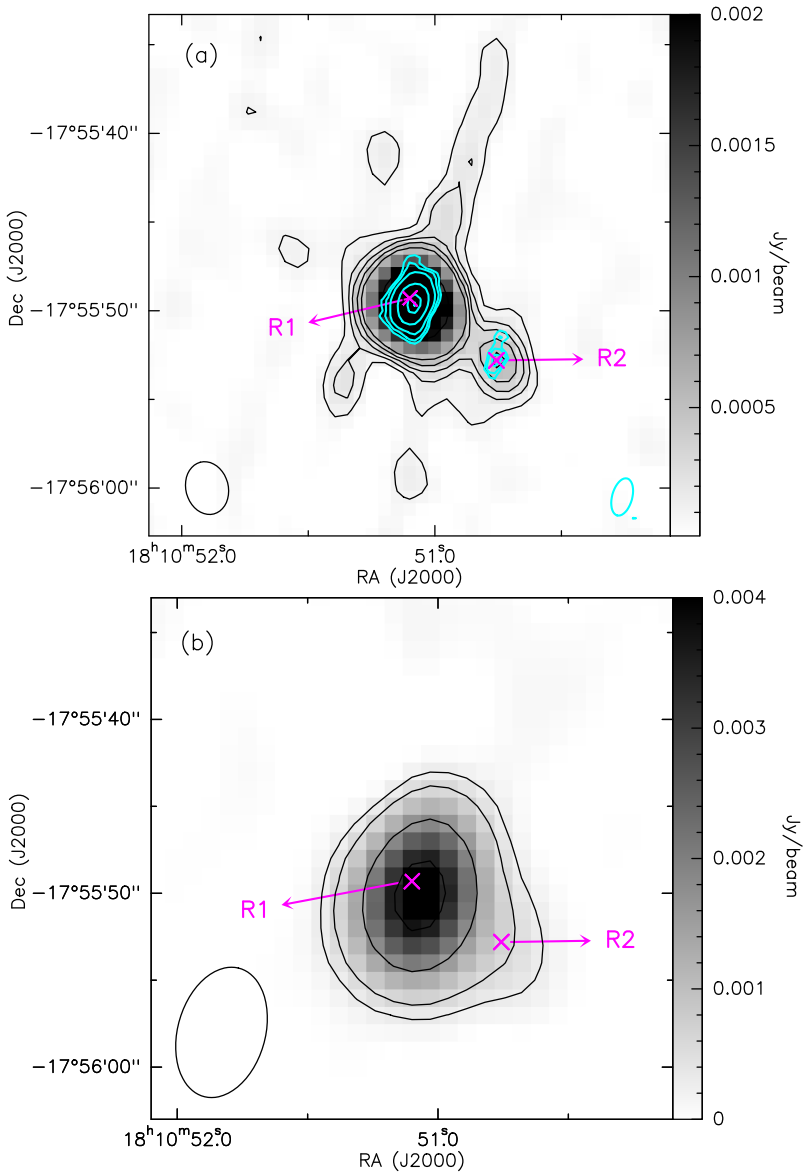

Figure 3.2: (a) The grey scale shows the high resolution radio continuum image of G12.42+0.50 at 1390 MHz with the contour levels 3, 6, 9, 18, 63, 150, and 172 times σ ($\sigma \sim 29.7\,\mu\mathrm{Jy\,beam^{-1}}$). The beam size is $\sim 3.0'' \times 2.4''$. Positions of R1 and R2 are also labelled. The contours of the 6 cm radio map are overlaid in cyan with the contour levels 3, 4, 6, 12, 21 and 24 σ ($\sigma \sim 0.15\,\mu\mathrm{Jy\,beam^{-1}}$) and the beam size is $\sim 2.2'' \times 1.1''$. (b) The radio continuum map of G12.42+0.50 at 610 MHz with contour levels 3, 6, 18, 38, and 60 times σ ($\sigma \sim 94\,\mu\mathrm{Jy\,beam^{-1}}$). The beam size is $\sim 7.6'' \times 4.8''$. The positions of the two radio peaks detected in the 1390 MHz map is indicated by 'x'. The restoring beams in the 1390 and 610 MHz bands are represented as open ellipses towards the bottom-left of each image and of the 6 cm map is represented as an open cyan ellipse towards the bottom-right in (a).

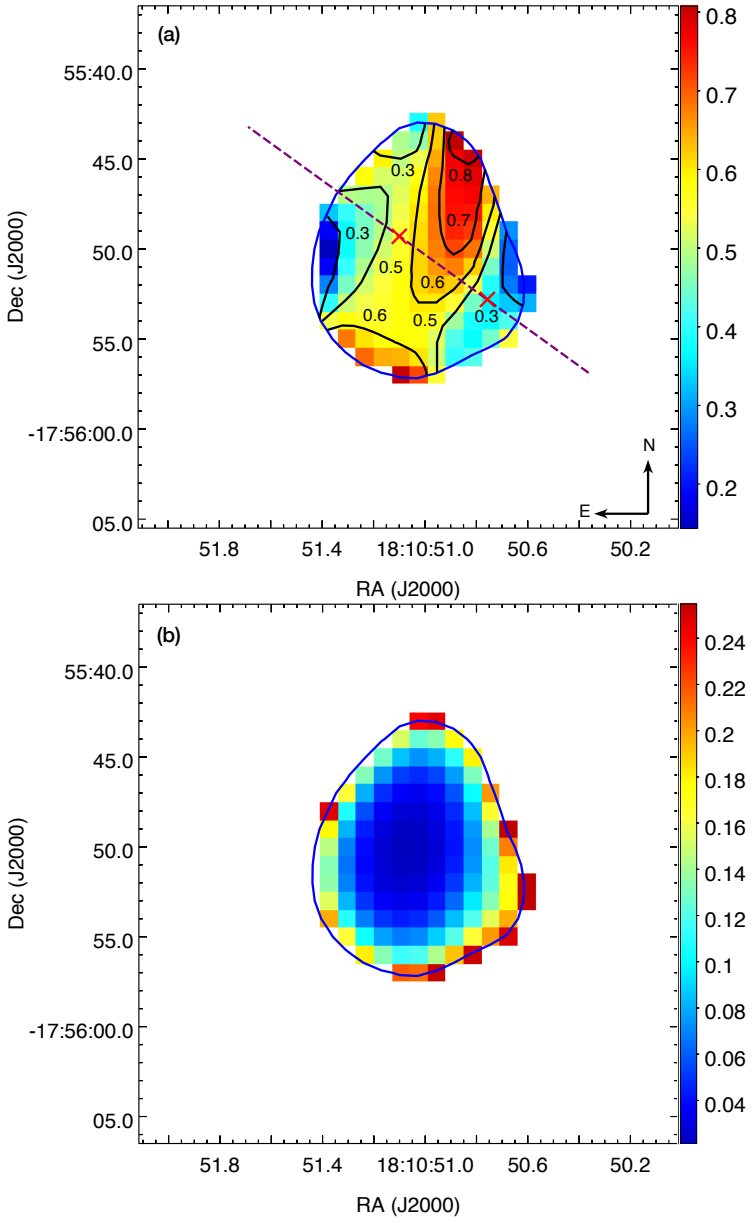

Figure 3.3: (a) Spectral index map of G12.42+0.50 between 1390 and 610 MHz. Black curves represent the spectral index levels. The blue contour shows the 5σ ($\sigma \sim 0.4 \times 10^{-4}$ Jy beam^{-1}) level of the 610 MHz map used to construct the spectral index map. The red 'x's mark the positions of the radio components, R1 and R2. The dashed purple line indicates the possible direction of the ionized jet. The spectral index varies from 0.3 to 0.7 along the possible jet axis. The error map is shown in (b). The errors involved are $\lesssim 0.15$, barring a few pixels at the edges.

in Fig. 3.3. As seen from the figure, the spectral index values vary between 0.3 and 0.9 with the estimated errors involved being less than ~ 0.15, barring a few pixels at the edges. These values indicate that the region is dominated by thermal bremsstrahlung emission of

varying optical depth (Curiel et al., 1993; Kobulnicky & Johnson, 1999; Rodriguez et al., 1993; Rosero et al., 2016). Moreover, spectral index values in the range of $0.4-0.9$ are also typically seen in regions associated with thermal jets (e.g. Panagia & Felli, 1975; Purser et al., 2016; Reynolds, 1986; Sanna et al., 2016). We will revisit these results obtained in a later section where we explore various scenarios to adequately explain the nature of the radio emission.

3.2 Emission from shock indicators

As discussed in the introduction, there is growing evidence in literature associating EGOs with MYSOs, notwithstanding the ongoing debate regarding their exact nature. Several mechanisms, like shocked emission in outflows, fluorescent emission or scattered continuum from MYSOs (De Buizer & Vacca, 2010; Noriega-Crespo et al., 2004; Takami et al., 2012), are invoked to identify the spectral carriers of the enhanced 4.5 μm emission. The picture of shocked emission from outflows suggests the spectral carriers to be molecular and atomic shock indicators like H_2 and [FeII] as well as the broad CO bandhead. All of these have distinct features within the 4.5 μm IRAC band. However, Simpson et al. (2012), while investigating the population of MYSOs in the G333.2-0.4 region, opine that the excess 4.5 μm could not be attributed to the H_2 lines as these would be too faint to be detected at this wavelength. Instead, they support a scattered continuum or the CO bandhead origin. From the *L*- and *M*-band spectra of two EGOs, De Buizer & Vacca (2010) show the H_2 line hypothesis to be consistent with one of them (G19.88-0.53), while in the other target (G49.27-0.34), the spectra shows only continuum emission. So far, spectroscopic studies of EGOs in the 4.5 μm and the NIR are few (Caratti o Garatti et al., 2015; De Buizer & Vacca, 2010; Onaka et al., 2016), thus keeping the debate on their nature ongoing. In the NIR domain, a few studies have focussed towards narrow-band imaging (Lee et al., 2013, 2012). Based on the UWISH2 survey images, Lee et al. (2013, 2012) present a complete H_2 line emission census of EGOs in the Northern Galactic Plane.

3.2.1 Narrow-band imaging

H_2 line emission towards G12.42+0.50 has been investigated in Lee et al. (2012). They ascribe the extended emission seen in the continuum-subtracted image to be the result of residuals of continuum subtraction rather than real H_2 line emission. In order to carefully scrutinize the NIR picture of G12.42+0.50, we revisit the H_2 line emission from images retrieved from the UWISH2 survey. In addition, we also probe the [FeII] line image which

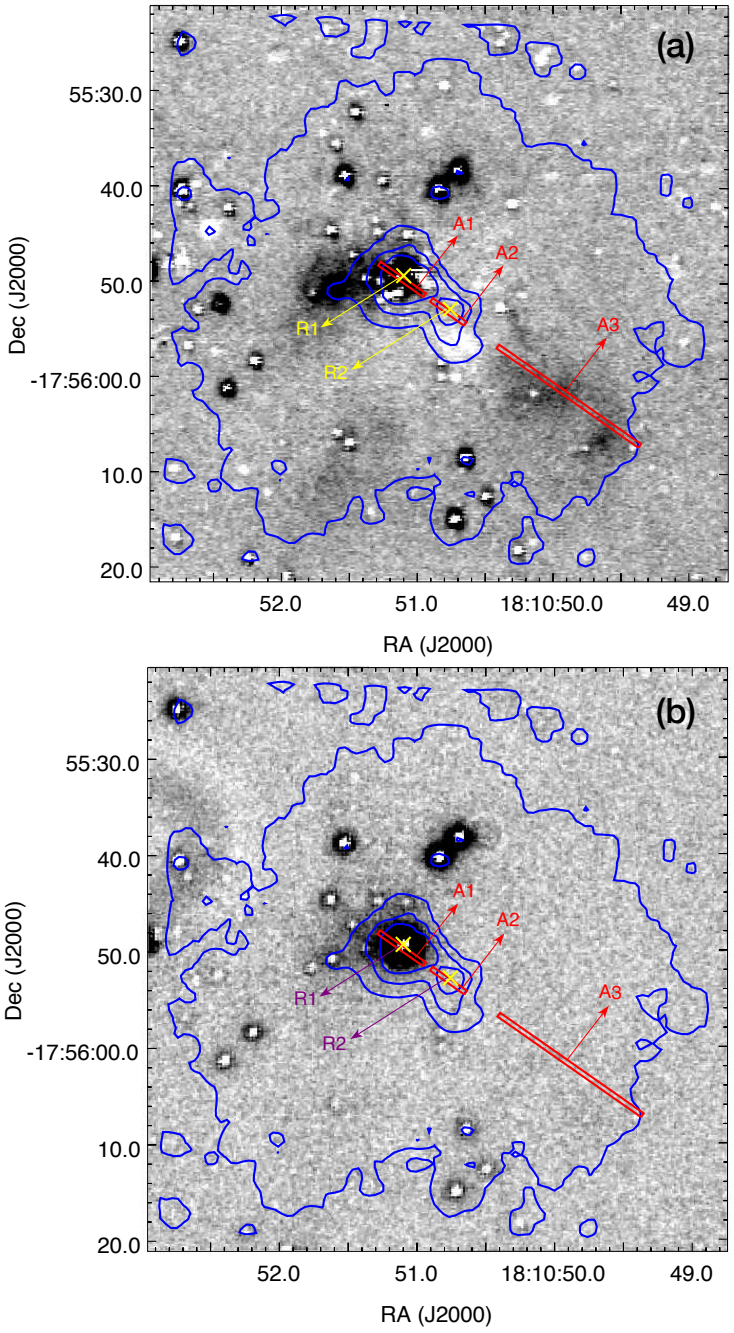

Figure 3.4: (a) Continuum subtracted H_2 image made using the UWISH2 survey data. (b) Continuum subtracted [FeII] image made using UKIRT-WFCAM observations towards G12.42+0.50. The positions of the identified radio components R1 and R2 are indicated. The blue contours represent the 4.5 μm emission with the levels 3, 60, 120, and 220σ ($\sigma \sim 1.5\,\mathrm{MJy\,sr^{-1}}$). The red rectangles show the orientation of the slit and denote the apertures used for spectra extraction (see text in Section 3.2.2).

is a robust indicator of shocks as compared to the H_2 lines (Shinn et al., 2014).
Following the procedure outlined in Section 2.2.1 we construct the continuum subtracted H_2 and [FeII] line images which are presented in Fig. 3.4. In the continuum-subtracted H_2 image, the morphology is similar to that obtained by Lee et al. (2012). An extended emission is seen towards the peak of the 4.5 μm emission coinciding with the location of the the radio component R1. Ideally a narrow-band continuum filter should enable a better continuum subtraction but in the absence of the same, we have ensured PSF matching and proper scaling of the broad *K*-band image. Contrary to the suggestion by Lee et al. (2012), we believe that the extended H_2 line emission detected in the continuum-subtracted image is genuine. This finds strength in the spectra obtained and discussed in the next section. In addition, diffuse line emission is seen towards the north-east and east of R1 as well towards the south-west. The continuum-subtracted [FeII] image shows a weak, extended emission coinciding with the brighter part of the H_2 line emission.

3.2.2 NIR spectroscopy

As is clear from earlier discussions, studies towards identifying the spectral carriers of the 4.5 μm emission are crucial in understanding the nature of EGOs and confirming their association with MYSOs. Given the lack of sensitive spectrometers in the 4.5 μm region, spectroscopy in the NIR becomes indispensable. We probe G12.42+0.50 with NIR spectroscopy to understand further the results obtained from narrow-band imaging. From the continuum-subtracted line images shown in Fig. 3.4 and the UKIDSS *K*-band image shown in Fig. 3.1, presence of faint nebulosity around the peak position (that coincides with the 4.5 μm peak) and towards the south-west is clearly visible. The slit orientation shown in Fig. 3.4 ensures that the regions harbouring the radio components and the extended H_2 line emission towards the north-east of the peak and the detached elongated nebulosity towards the south-west are probed.
The *HK* spectra extracted over the three identified apertures (marked in Fig. 3.4) are shown in Fig. 3.5. The top-panel of Fig. 3.5 shows the spectrum over aperture A1 with the line details listed in Table 3.2. This aperture covers the radio component R1 and portions of the extended H_2 emission seen towards the north-east of the 4.5 μm peak. The spectrum shows clear detection of three emission lines of molecular H_2 with the most prominent feature being the $1-0\mathrm{S}(1)$ line at 2.122 μm. No H_2 line is detected in the blue part ($1.5-1.8\,\mu$m) of the spectrum but there is a weak [FeII] line detected at 1.644 μm These lines of H_2 and [FeII] are commonly observed in outflows/jets. In addition, He I at 2.059 μm is also seen in the extracted spectrum. Apart from the emission lines, the continuum slope is seen rising

towards the red thus, indicating a highly reddened source. Fig. 3.5 also plots the extracted spectra over the apertures A2 and A3 in the middle and lower panels, respectively. Aperture A2 covers the second radio component R2 and aperture A3 samples the detached, extended emission seen towards the south-west. No emission lines above the noise level are detected in these and the spectra displayed are flat.

In Fig. 3.6, we present the extracted spectra in the *KL* band. The displayed spectra has been truncated at 2.45 μm due to poor signal-to-noise ratio owing to less than optimal sky transparency. In aperture A1, three additional emission lines of molecular H_2 are prominent. The other two apertures do not show the presence of any spectral feature. The detected lines are listed in Table 3.2.

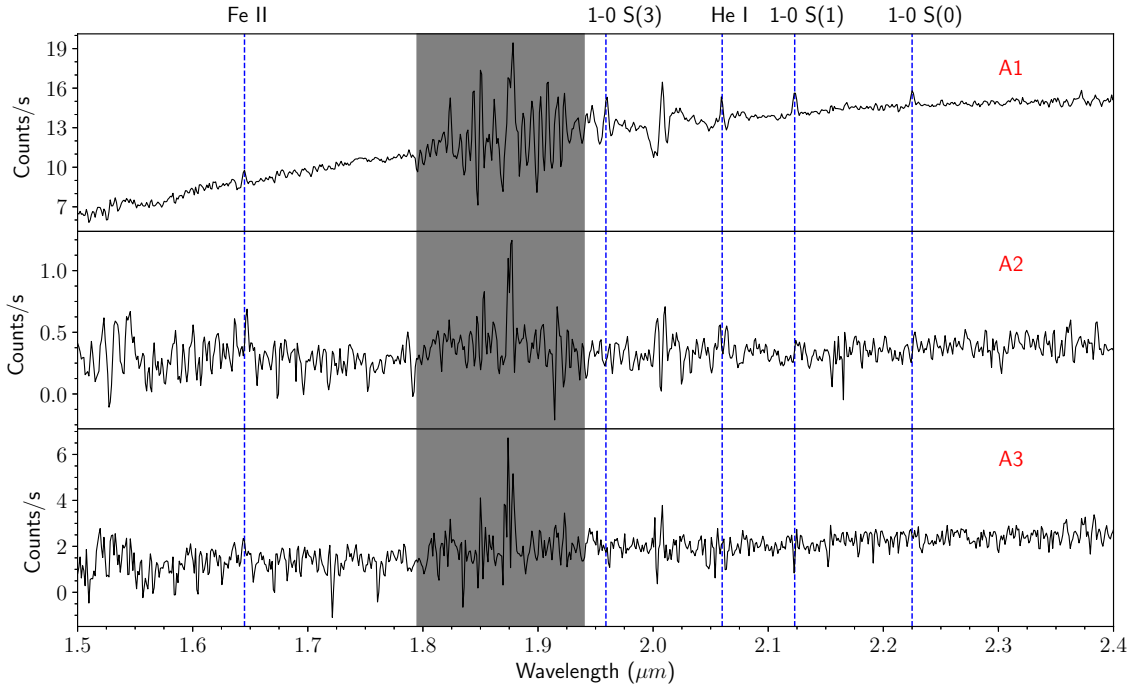

Figure 3.5: The *HK* spectrum of G12.42+0.50 extracted over the apertures A1, A2 and A3. The aperture A1 covers the radio component R1 and the extended H_2 emission seen towards the north-east, A2 covers the second radio component R2 and A3 samples the detached, extended emission seen towards the south-west. The shaded area marks the region of poor sky transparency. The identified spectral lines along aperture A1 are marked over the spectrum with the details given in Table 3.2. No emission lines above the noise level are detected in the spectra extracted over A2 and A3.

The observed H_2 line emissions seen in the spectra of G12.42+0.50 can be attributed to either thermal or non-thermal excitation. The thermal emission mostly originates from shocked neutral gas in outflows/jets that are heated up to a few 1000 K, whereas, the non-

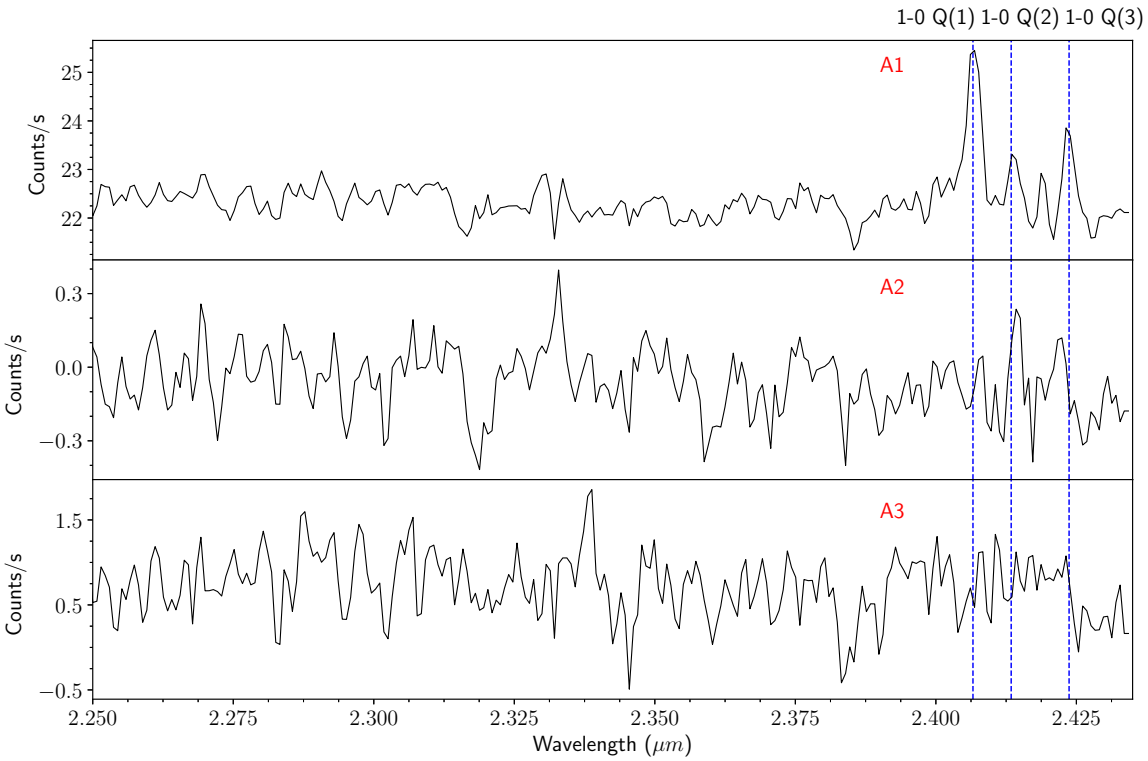

Figure 3.6: The *KL* spectrum of G12.42+0.50 extracted over the apertures A1, A2 and A3. The regions covered by all the three apertures are the same as given in Fig. 3.5. The identified spectral lines along aperture A1 are marked over the spectrum with the details given in Table 3.2. No emission lines above the noise level are detected in the spectra extracted over A2 and A3.

Table 3.2: Lines detected in the spectra extracted from aperture A1 towards G12.42+0.50.

Line	Wavelength (μm)
[FeII]	1.644
H_2 1-0 S(3)	1.958
He I	2.059
H_2 1-0 S(1)	2.122
H_2 1-0 S(0)	2.224
H_2 1-0 Q(1)	2.407
H_2 1-0 Q(2)	2.413
H_2 1-0 Q(3)	2.424

thermal emission is understood to be due to UV fluorescence by non-ionizing UV photons. These two competing mechanisms populate different energy levels thus yielding different line ratios (Caratti o Garatti et al., 2015; Davis et al., 2003; Veena et al., 2016). UV fluo-

rescence excites higher vibrational levels. The H_2 lines detected in G12.42+0.50 originate from the upper vibrational level, $\nu = 1$ suggesting a low level of excitation. The absence of high vibrational state transitions supports the shock-excited origin of the detected lines. Lack of fluorescent H_2 line emission in G12.42+0.50 may also be due to veiling of UV photons from the central star due to high extinction. Nevertheless, given the association with an outflow source, shock-excited origin is most likely the case.

3.3 Emission from the dust component

The dust emission at MIR and FIR wavelengths sampled in the IRAC, Hi-Gal, APEX+Planck and SMA wavelengths ($3.6\,\mu\mathrm{m} - 1.1\,\mathrm{mm}$) in the region associated with G12.42+0.50 is shown in Fig. 3.7. In the IRAC bands, various emission mechanisms come into play and contribute towards the warm dust component (Watson et al., 2008). Thermal emission from the circumstellar dust heated by the stellar radiation and emission from the UV excited polycyclic aromatic hydrocarbons in the photodissociation regions are known to be the dominant contributors. In the shorter IRAC wavelengths (3.6, $4.5\,\mu\mathrm{m}$), where mostly the stellar sources are sampled, emission from the stellar photosphere would also be appreciable. Apart from this, shock-excited H_2 line emission and diffuse emission in the Brα and Pfβ lines would also exist. Further, in case of H II regions, one expects significant contribution from the Lyα heated dust (Hoare, Roche & Glencross, 1991). The morphology in the IRAC bands is similar and the emission becomes more prominent at $8.0\,\mu\mathrm{m}$. Dark filamentary features (bright in the negative images shown) are seen in silhouette towards the south-west in the $8.0\,\mu\mathrm{m}$ map. The skeletons of the six clearly identified filamentary features are overlaid on the $8.0\,\mu\mathrm{m}$ map. In addition, an extended emission feature is seen towards the north-west of G12.42+0.50, being prominent in the 5.8, 8.0, and $70\,\mu\mathrm{m}$ images. Two infrared dust bubbles (MWP1G012417+005383 and MWP1G012419+005399) are found to be associated with this feature and are marked in Fig. 3.7(d). No further literature is available on these bubbles so we drop them in further discussion.

As we move towards the longer wavelengths, cold dust emission associated with G12.42+0.50 becomes enhanced and more extended. From the APEX+Planck combined $870\,\mu\mathrm{m}$ map, we identify two clumps using the 2D *Clumpfind* algorithm (Williams, de Geus & Blitz, 1994) with 2σ ($\sigma = 0.3\,\mathrm{Jy\,beam^{-1}}$) threshold and optimum contour levels. The apertures of the identified clumps are overlaid on the $870\,\mu\mathrm{m}$ map in Fig. 3.7(j). While one of the clumps, hereafter C1, is associated with G12.42+0.50, another clump lies towards the south-east of G12.42+0.50 at an angular distance of $\sim 6'$. From the $\mathrm{H^{13}CO^{+}}$ molecu-

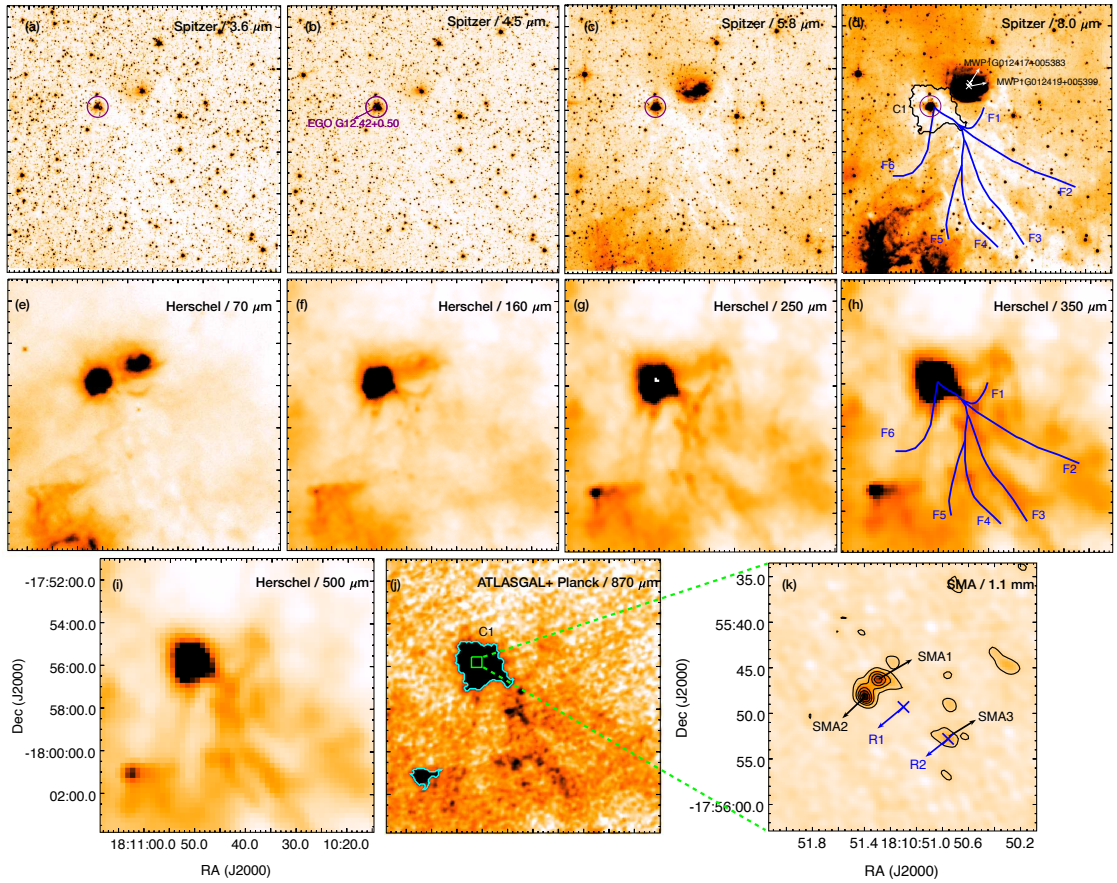

Figure 3.7: Dust emission in the region associated with G12.42+0.50 at the mid- and far-infrared wavelengths ($3.6\,\mu\mathrm{m} - 1.1\,\mathrm{mm}$). All the images from (a)-(j) have the same field of view. Skeletons of six clearly identified filaments are overlaid on the 8.0 and $350\,\mu\mathrm{m}$ maps. The position of the EGO, G12.42+0.50 is shown within a purple circle on the 3.6, 4.5, 5.8 and $8.0\,\mu\mathrm{m}$ IRAC maps. The location of the two infrared dust bubbles (MWP1G012417+005383 and MWP1G012419+005399) are indicated by white 'x's on the $8.0\,\mu\mathrm{m}$ map, (d). (d) and (j) show the retrieved aperture of clump C1. Another clump detected towards south-east of G12.42+0.50 is shown in the $870\,\mu\mathrm{m}$ map, (j). (k) shows the SMA 1.1 mm map with the contour levels 3, 12, 21, 30 and 39 times σ ($\sigma \sim 3\,\mathrm{mJy\,beam^{-1}}$). The blue 'x's on the 1.1 mm map mark the positions of the radio components R1 and R2.

lar line data (Section 3.4), we estimate the LSR velocity of this clump to be $31.5\,\mathrm{km\,s^{-1}}$. Comparing this with the estimated LSR velocity of G12.42+0.50 ($18.3\,\mathrm{km\,s^{-1}}$), it is unlikely that the clump has any association with G12.42+0.50. The identified filaments now appear in emission and are shown on the $350\,\mu\mathrm{m}$ map. Interestingly, these filaments seem to converge towards clump C1. As mentioned in the introduction, the morphology has an uncanny resemblance to a hub-filament structure, detailed discussion of which is presented

in Section 3.6.3. Furthermore, in the high-resolution 1.1 mm SMA map, the inner region of the cold dust clump, C1 associated with G12.42+0.50 is seen to harbour two, dense and bright compact cores labelled on the map as SMA1 and SMA2. Additionally, a few bright emission knots are detected in the SMA map including the one highlighted as SMA3 which coincides with the radio component R2.

3.3.1 Properties of SMA cores

From the SMA 1.1 mm map shown in Fig. 3.7(k), SMA1 and SMA2 show up as dense, compact cores possibly in a binary system. SMA3, on the other hand, looks more like a clumpy region of density enhancement. Following the method described by Kauffmann et al. (2008) the masses of the SMA components are computed using the equation

$$M = 0.12\,M_{\odot}\left(\mathrm{e}^{1.439(\lambda/\mathrm{mm})^{-1}(T/10\,\mathrm{K})^{-1}}-1\right)\left(\frac{\kappa_{\nu}}{0.01\,\mathrm{cm^2\,g^{-1}}}\right)^{-1}\left(\frac{F_{\nu}}{\mathrm{Jy}}\right)\left(\frac{d}{100\,\mathrm{pc}}\right)^{2}\left(\frac{\lambda}{\mathrm{mm}}\right)^{3} \quad (3.1)$$

where the opacity is

$$\kappa_{\nu} = 0.1(\nu/1000\,\mathrm{GHz})^{\beta}\,\mathrm{cm^2 g^{-1}} \quad (3.2)$$

β is the dust emissivity spectral index which is fixed at 2.0 (André et al., 2010; Beckwith et al., 1990; Hildebrand, 1983). F_{ν} is the integrated flux density of each component, d is the distance to the source and λ is the wavelength taken as 1.1 mm. The temperature, T is taken to be 26.8 K for SMA1 and SMA2 and 22.7 K for SMA3, from their positions in the dust temperature map (Section 3.3.3). The peak positions and flux densities, integrated flux densities, the deconvolved sizes and the masses of the 1.1 mm SMA cores are presented in Table 3.3. The deconvolved sizes and integrated flux densities of the cores are evaluated by fitting 2D Gaussians to each component using the 2D fitting tool of CASA viewer. From the mass and size estimates, SMA1 and SMA2 qualify as potential high-mass star-forming cores satisfying the criterion, $m(r) > 870\,M_{\odot}(r/\mathrm{pc})^{1.33}$ (Kauffmann et al., 2010b).

3.3.2 SED modelling of C1

In an attempt to understand the properties of the dust clump, C1 associated with G12.42+0.50, we model the infrared flux densities with a two-component modified blackbody using the

Table 3.3: Physical parameters of the 1.1 mm continuum emission near G12.42+0.50.

Component	Peak position		Deconvolved size	Integrated flux	Peak flux	Mass
	RA (J2000)	Dec (J2000)	($''\times''$)	(mJy)	(mJy beam^{-1})	($M_\odot$)
SMA1	18 10 51.3	-17 55 46.3	1.4×0.5	190	109	14.8
SMA2	18 10 51.4	-17 55 48.1	1.3×0.4	221	136	17.2
SMA3	18 10 50.8	-17 55 52.8	1.5×0.7	57	34	5.5

following functional form (Lis & Menten, 1998)

$$S_\nu = [\Omega_1\ a\ B_\nu(T_1) + \Omega_2\ (1-a)\ B_\nu(T_2)](1-e^{-\tau_\nu}) \tag{3.3}$$

where

$$\tau_\nu = \mu_{\rm H_2} m_{\rm H} \kappa_\nu N({\rm H_2}) \tag{3.4}$$

where S_ν is the integrated flux density of C1, Ω_1 and Ω_2 are the solid angles subtended by the apertures used for estimating the flux densities at the FIR and MIR wavelengths, respectively. a is the ratio of optical depth in the warmer component to the total optical depth, $B_\nu(T_1)$ and $B_\nu(T_2)$ are the blackbody functions at dust temperatures T_1 and T_2, respectively, $\mu_{\rm H_2}$ is the mean molecular weight (taken as 2.8; Kauffmann et al., 2008), $m_{\rm H}$ is the mass of hydrogen atom and $N({\rm H_2})$ is the hydrogen column density The dust opacity, κ_ν is given by Eqn. 3.2. For opacity, we assume the function $\kappa_\nu = 0.1(\nu/1000\,{\rm GHz})^\beta\,{\rm cm^2\,g^{-1}}$, where β is the dust emissivity spectral index for which, a value of 2.0 is adopted as in the previous section.

Table 3.4: Integrated flux densities of the dust core associated with G12.42+0.50.

Wavelength (μm)	3.6	4.5	5.8	8.0	12.13	14.65	70	160	250	350	500	870
Flux density (Jy)	0.6	0.9	3.3	8.4	57.7	129.8	1942.6	2575.5	1140.7	535.3	182.5	35.9

In addition to the *Spitzer*-IRAC, *Herschel* and ATLASGAL wavebands, we have also included flux densities from the MSX survey[2] at 12.13 and 14.65 μm to constrain the model in the MIR wavelength. The integrated flux densities of the dust clump at the MIR wavelengths are measured within the area defined by the 4σ contour level of the 8.0 μm image (274 arcsec^2) and longward of 70 μm, the integration is done over the area defined by the *Clumpfind* aperture for C1 (13720 arcsec^2). Background emission is estimated using the

[2]https://irsa.ipac.caltech.edu/applications/MSX/MSX/

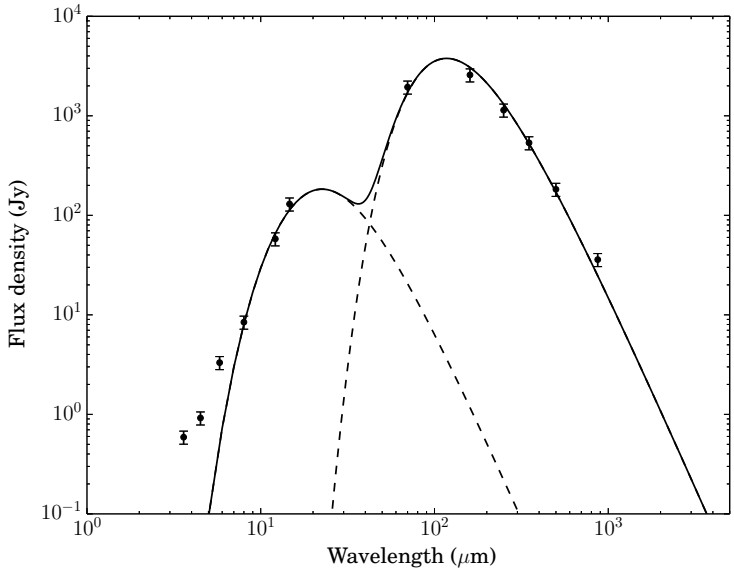

Figure 3.8: Spectral energy distribution of the dust core associated with G12.42+0.50 in the wavelength range of 3.6 to 870 μm. Assumed 15% errors are indicated. The solid curve represents the best fit two-component model with a warm component at 183 K and a cold envelope at 25 K.

same apertures on nearby sky region (visually scrutinized to be smooth) and subtracted. Estimated flux densities are listed in Table 3.4. Launhardt et al. (2013); Schuller et al. (2009) use a conservative 15% uncertainty in the flux densities of the *Herschel* bands. We adopt the same value here for all the bands. Model fitting is carried out using the non-linear least square Levenberg-Marquardt algorithm with T_1, T_2, $N(\mathrm{H_2})$ and a taken as free parameters. The best fit temperature values are 25.0$\pm$1.0 K (cold) and 183.2$\pm$12.0 K (warm), respectively. The model fit also gives an estimate of the hydrogen column density, $N(\mathrm{H_2}) = 2.1 \times 10^{22}\,\mathrm{cm^{-2}}$. This result shows that the dust clump in G12.42+0.50 consists of an inner warm component surrounded by an extended outer, cold envelope traced mostly by the FIR wavelengths. It should be noted here that we have excluded the data points below 8.0 μm while fitting the model. This is because the emission at 4.5 and 5.8 μm may largely be dominated by shock excitation and the 3.6 μm emission may arise from even hotter components. The SED and the best fit modified blackbody are shown in Fig. 3.8. The bolometric luminosity estimated from the two-component SED model over $8.0 - 870\,\mu\mathrm{m}$ is $2.8 \times 10^4\,L_\odot$. It is a factor of 1.6 higher to that obtained by Vutisalchavakul & Evans (2013), who use the IRAS band flux densities. However, our values are in fair agreement to the estimate of $3.2 \times 10^4\,\mathrm{L_\odot}$ (Osterloh, Henning & Launhardt, 1997) where flux densities

between $2.1 - 1.3\,\mathrm{mm}$ are included.

3.3.3 Nature and distribution of cold dust emission

We probe the nature of the cold dust associated with G12.42+0.50, using the *Herschel* FIR bands which cover the wavelength range ($160 - 500\,\mu\mathrm{m}$) and the combined APEX+Planck data at 870 μm. The dust temperature and the line-of-sight average molecular hydrogen column density maps are generated by a pixel-by-pixel modified single-temperature blackbody model fitting. While fitting the model, we assume the emission at these wavelengths to be optically thin. Following the discussion in several papers (Anderson et al., 2010; Battersby et al., 2011; Das et al., 2018; Peretto et al., 2010), we exclude the 70 μm data point as the optically thin assumption would not hold. In addition, the emission here would have significant contribution from the warm dust component thus modelling with a single-temperature blackbody would over-estimate the derived temperatures. Given this, the model fitting is done with only five points which lie on the Rayleigh-Jeans tail.

The first step towards the generation of the temperature and column density maps is to have the maps from SPIRE, PACS and APEX+Planck in the same units. The units of the SPIRE map which is in $\mathrm{MJy\,sr^{-1}}$ is converted to $\mathrm{Jy\,pixel^{-1}}$ which is the unit for the 160 μm PACS map. Similarly, the APEX+Planck map that has the unit of $\mathrm{Jy\,beam^{-1}}$ is also converted to $\mathrm{Jy\,pixel^{-1}}$. The maps are at different resolutions and pixel sizes. The pixel-by-pixel routine makes it mandatory to convolve and regrid the maps to a common resolution and pixel size of $36''$and $14''$, respectively which are the parameters of the 500 μm map (as it has the lowest resolution). Convolution kernels are taken from Aniano et al. (2011) for the *Herschel* maps. Since no pre-made convolution kernel is available for the APEX+Planck map, we use a Gaussian kernel. These preliminary steps are carried out using the software package, HIPE[3]

The maps include sky/background emission which is a result of the cosmic microwave background and the diffuse Galactic emission. In order to correct for the flux offsets due to this background contribution, we select a relatively uniform and dark region (free of bright, diffuse or filamentary emission) at a distance of $\sim 0.25^{\circ}$ from G12.42+0.50. The same region is used for background subtraction in all the five bands. Using the method described in several papers (Battersby et al., 2011; Das et al., 2017, 2018; Launhardt et al., 2013; Ramachandran et al., 2017) the background values, I_{bg} are estimated to be -2.31,

[3]The software package for *Herschel* Interactive Processing Environment (HIPE) is the application that allows users to work with the Herschel data, including finding the data products, interactive analysis, plotting of data, and data manipulation.

2.15, 1.03, 0.37 and 0.08 Jy pixel^{-1} at 160, 250, 350, 500 and 870 μm, respectively. The negative flux value at 160 μm is due to the arbitrary scaling of the PACS images.
To probe an extended area encompassing G12.42+0.50 and the related filaments, we select a $12.8' \times 12.8'$ region centred at $\alpha_{\rm J2000} = 18^{\rm h}10^{\rm m}41.8^{\rm s}, \delta_{\rm J2000} = -17^{\circ}57'23''$. The model fitting algorithm was based on the following formulation (Battersby et al., 2011; Launhardt et al., 2013; Mallick et al., 2015; Ward-Thompson & Robson, 1990):

$$S_{\nu}(\nu) - I_{bg}(\nu) = B_{\nu}(\nu, T_d)\ \Omega\ (1 - e^{-\tau_{\nu}}) \tag{3.5}$$

where τ_{ν} is given by Eqn. 3.4, S_{ν} is the observed flux density, $B_{\nu}(\nu, T_d)$ is the Planck function, T_d is the dust temperature, Ω is the solid angle in steradians, from where the flux is measured (solid angle subtended by a $14'' \times 14''$ pixel) and the rest of the parameters are the same as used in the previous section. Following the same procedure discussed in Section 3.3.2, SED modelling for each pixel is carried out keeping the dust temperature, T_d and column density, $N(\rm H_2)$ as free parameters. The dust temperature and column density maps generated are displayed in Fig. 3.9 along with the reduced χ^2 map. The reduced χ^2 map indicates that the fitting uncertainties are small with a maximum value of 4 towards the bright central emission where the 250 μm image (Fig. 3.7g) has a few bad pixels. The column density map reveals a dense, bright region towards clump, C1 that envelopes G12.42+0.50. Also clear is increased density along the filamentary structures identified in Section 3.3. The apertures of the clump C1 identified from the 870 μm is overlaid on the maps. Using 3×3 pixel grids, local column density peaks are identified above 3σ threshold ($\sigma = 2.3 \times 10^{21}\,\rm cm^{-2}$). 11 additional clumps were thus identified located within the 3σ contour. Subsequent to this, a careful visual inspection is done and ellipses are marked to encompass most of the clump emission.
Two high-temperature regions are seen in the dust temperature map that coincide with G12.42+0.50 and the two bubbles discussed earlier. The warmest temperature in the map is found to be 28.6 K and is located a pixel to the north-east of SMA1, SMA2 and peak position of R1. The mean dust temperature and column density of C1 is found to be 19.9 K and $3.3 \times 10^{22}\,\rm cm^{-2}$, respectively. It has to be noted here that the mean temperature we obtain here is less than the temperature of the cold component we estimate from the two-component model by $\sim 5\,\rm K$. This is because, unlike the two-component modelling, here we do not include the emission at 70 μm. Similarly the column density we obtain here is greater than the column density estimated using the two-component fit by a factor of ~ 1.6. A striking feature noticed is the distinct low dust temperatures along the filaments.

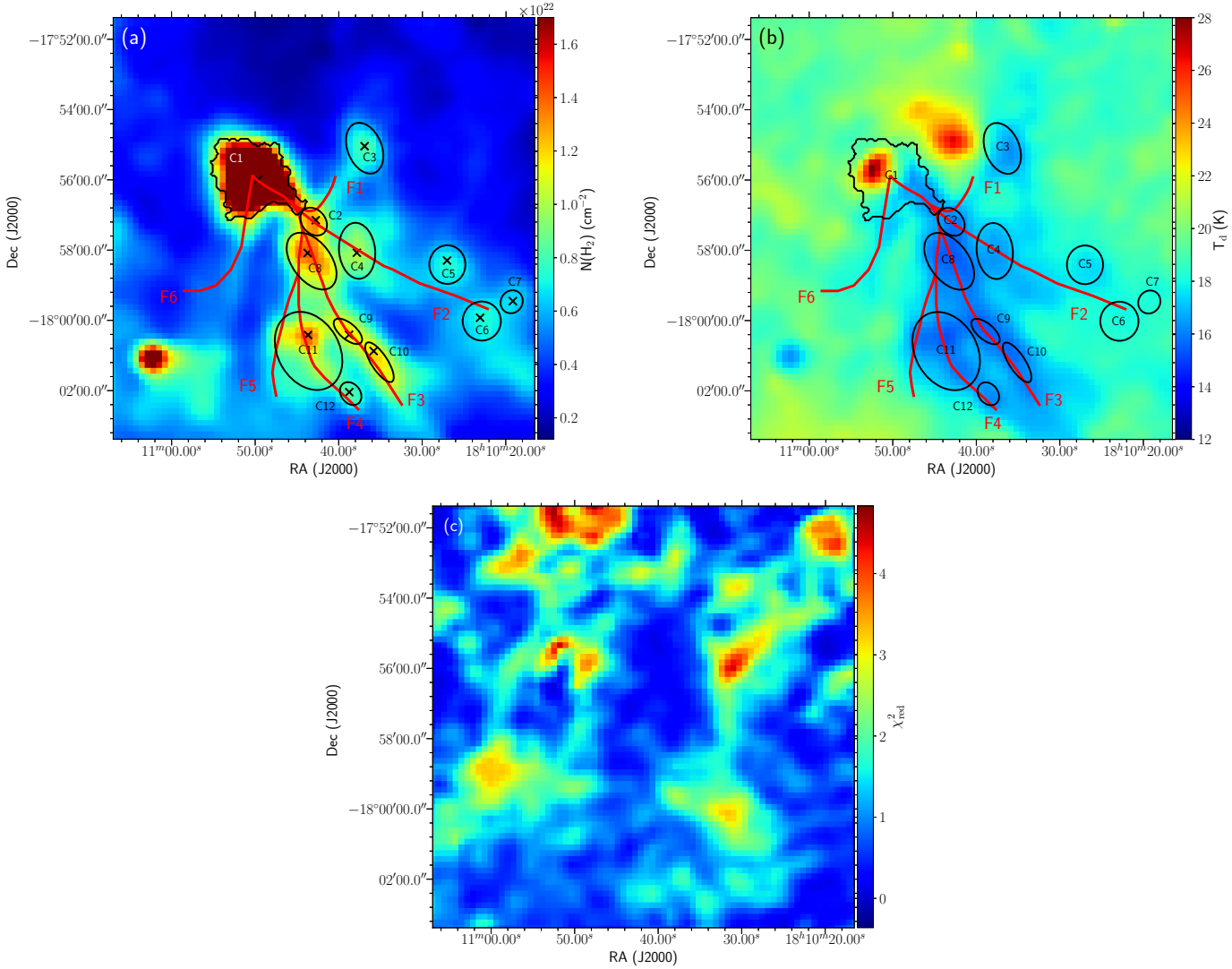

Figure 3.9: (a) Column density, (b) Temperature and (c) Reduced χ^2 maps towards G12.42+0.50 generated using the *Herschel* FIR data and the APEX+Planck data. The *Clumpfind* retrieved clump,C1 and the visually identified clumps from the column density map are marked on the maps. The 'x's mark the positions of the peak column densities of each clump in the column density map. Skeletons of the filaments identified from the 8.0 μm map is overlaid on the column density and temperature maps.

3.3.4 Properties of cold dust clumps

Several physical parameters of the identified clumps are derived. The enclosed area within the *Clumpfind* retrieved aperture of C1 is used to determine the effective radius, $\mathrm{r} = (\mathrm{A}/\pi)^{0.5}$ (Kauffmann et al., 2010a), where A is the area. For the visually identified clumps ($\mathrm{C2} - \mathrm{C12}$), the effective radius is taken to be the geometric mean of the semi-major and semi-minor axes of the ellipses bounding the clumps. From the derived column density values, we estimate the mass of the dust clumps using the following expression

$$M_{\mathrm{C}} = \mu_{\mathrm{H_2}} m_{\mathrm{H}} A_{\mathrm{pixel}} \Sigma N(\mathrm{H_2}) \tag{3.6}$$

where A_{pixel} is the area of a pixel in cm^2, $\mu_{\mathrm{H_2}}$ is the mean molecular weight (2.8), m_{H} is the mass of hydrogen atom. The volume number density of the clump is estimated using the expression,

$$n_{(\mathrm{H_2})} = \frac{3\,M_{\mathrm{C}}}{4\pi R^3 \mu m_{\mathrm{H}}} \tag{3.7}$$

The peak position, radius, mean temperature and column density, integrated column density, mass, and volume number density of the identified clumps are listed in Table 3.5. The clump enclosing G12.42+0.50, C1 is the largest and most massive clump having a radius 0.8 pc, column density $3.3 \times 10^{22}\,\mathrm{cm}^{-2}$ and mass $1375\,M_{\odot}$. He et al. (2015) derives the radius, column density and mass of the clump associated with G12.42+0.50 to be 0.57 pc, $1.3 \times 10^{23}\,\mathrm{cm}^{-2}$ and $724\,M_{\odot}$, respectively. Apart from a larger size estimated by us, the other factors contributing to this difference in the estimated values of mass and column density are the different opacity and dust temperature values adopted by He et al. (2015).

Table 3.5: Derived physical parameters of identified clumps associated with G12.42+0.50. The peak position, radius, mean temperature and column density, total column density, mass, and volume number density of the identified clumps are listed.

Clump	Peak position		Radius	Mean T_d	Mean $N(\mathrm{H_2})$	$\Sigma N(\mathrm{H_2})$	Mass	$n(\mathrm{H_2})$
	RA (J2000)	Dec (J2000)	(pc)	(K)	(10^{22} cm^{-2})	(10^{23} cm^{-2})	($M_{\odot}$)	(10^{3} cm^{-3})
C1	18 10 49.64	-17 55 59.40	0.8	19.9±1.9	3.3±0.9	23.2	1375	10.4
C2	18 10 42.75	-17 57 08.92	0.3	16.1±0.4	1.2±0.1	1.0	59	10.7
C3	18 10 36.91	-17 55 02.54	0.4	17.1±0.8	0.7±0.1	1.5	92	4.2
C4	18 10 37.83	-17 58 04.57	0.4	16.7±0.7	0.9±0.1	2.1	127	4.9
C5	18 10 27.03	-17 58 17.79	0.4	17.7±0.9	0.7±0.1	1.1	66	4.4
C6	18 10 23.08	-17 59 55.48	0.4	18.1±0.9	0.7±0.1	1.2	70	4.3
C7	18 10 19.16	-17 59 27.19	0.2	18.2±0.8	0.7±0.1	0.4	24	7.2
C8	18 10 43.71	-17 58 04.98	0.5	15.8±0.6	1.2±0.2	3.6	214	6.0
C9	18 10 38.76	-18 00 24.61	0.2	15.6±0.7	1.2±0.2	0.7	41	11.1
C10	18 10 35.81	-18 00 52.40	0.3	16.0±0.8	1.1±0.2	0.9	55	9.5
C11	18 10 43.67	-18 00 24.95	0.7	16.3±0.8	1.0±0.2	6.0	359	3.5
C12	18 10 38.73	-18 02 02.59	0.2	16.3±1.1	0.8±0.2	0.5	29	9.7

Given that the clump, C1, is in global collapse (refer Section 3.6.1), we estimate the mass of the most massive star, $M_{\rm max}$ that can form in clump, using a stellar IMF of Kroupa (2001), following the formulation (Svoboda et al., 2016),

$$M_{\rm max} = 20\left[\frac{\sigma_{\rm sf} M_{\rm C}}{0.3 \times 1064\, M_{\odot}}\right]^{1/1.3} M_{\odot} \tag{3.8}$$

Here, $\sigma_{\rm sf}$ is the star-forming efficiency in the clump which is assumed to be 30% in this work (Lada & Lada, 2003) and $M_{\rm C}$ is the mass of the clump. The most massive star that can form in this clump is estimated to be $\sim 24\, M_{\odot}$. This indicates that the clump, C1, associated with G12.42+0.50 is indeed capable of bearing massive stars.

3.4 Molecular line emission from G12.42+0.50

Table 3.6: Details of the detected molecular line transitions towards the clump, C1 enveloping G12.42+0.50. The details are extracted from Table 2 of Miettinen (2014) and Table 2 of Foster et al. (2011).

Transition	Comments
$H^{13}CO^{+}\,(1-0)$	six hyperfine (hf) components; high-density and ionization tracer
$C_2H\,(1-0)\,3/2-1/2$	three hf components; photodissociation region tracer
HCN $(1-0)$	three hf components; high-density and infall tracer
$HCO^{+}\,(1-0)$	high-density, infall, kinematics and ionization tracer
HNC $(1-0)$	three hf components; high-density and cold gas tracer
$HC_3N\,(10-9)$	six hf components; High-density and hot-core tracer
$N_2H^{+}\,(1-0)$	15 hf components, seven have a different frequency; high density and CO-depleted gas tracer

The molecular line emission provides information on the kinematics and chemical structure of a molecular cloud in addition to throwing light on its evolutionary stage. Data from the MALT90 survey, JCMT archives and observation from TRAO are used to probe these aspects in the star-forming region associated with G12.42+0.50.

Of the 16 molecules covered by the MALT90 survey, 7 molecular species, namely HCO^{+}, $H^{13}CO^{+}$, HCN, HNC, C_2H, N_2H^{+} and HC_3N are detected towards the clump C1 enveloping G12.42+0.50. The details of the detected transitions taken from Miettinen (2014) and Foster et al. (2011) are listed in Table 3.6. Miettinen (2014) also gives an excellent review on the physical conditions and environment required for the formation of these

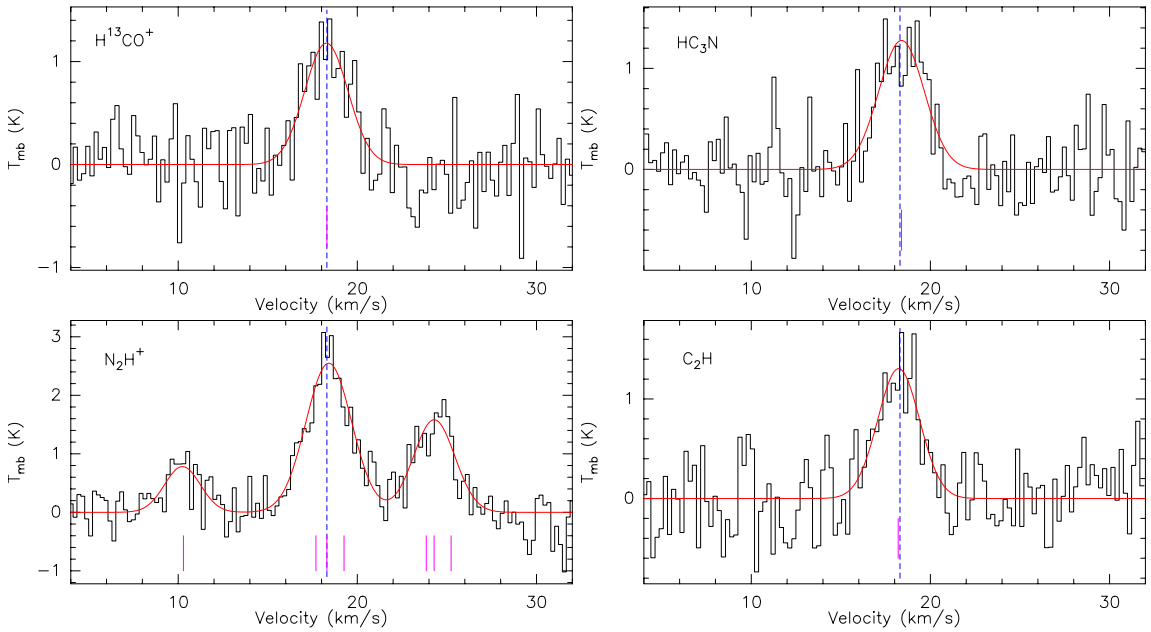

Figure 3.10: Spectra of the optically thin molecular lines ($H^{13}CO^+$, HC_3N, C_2H and N_2H^+) associated with G12.42+0.50 obtained from the MALT90 survey. The spectra are extracted towards the peak of the 870 μm ATLASGAL emission. The dashed blue line indicates the LSR velocity, 18.3 km s^{-1}, estimated from the the optically thin $H^{13}CO^+$ line. The magenta lines indicate the location of the hyperfine components for each transition.

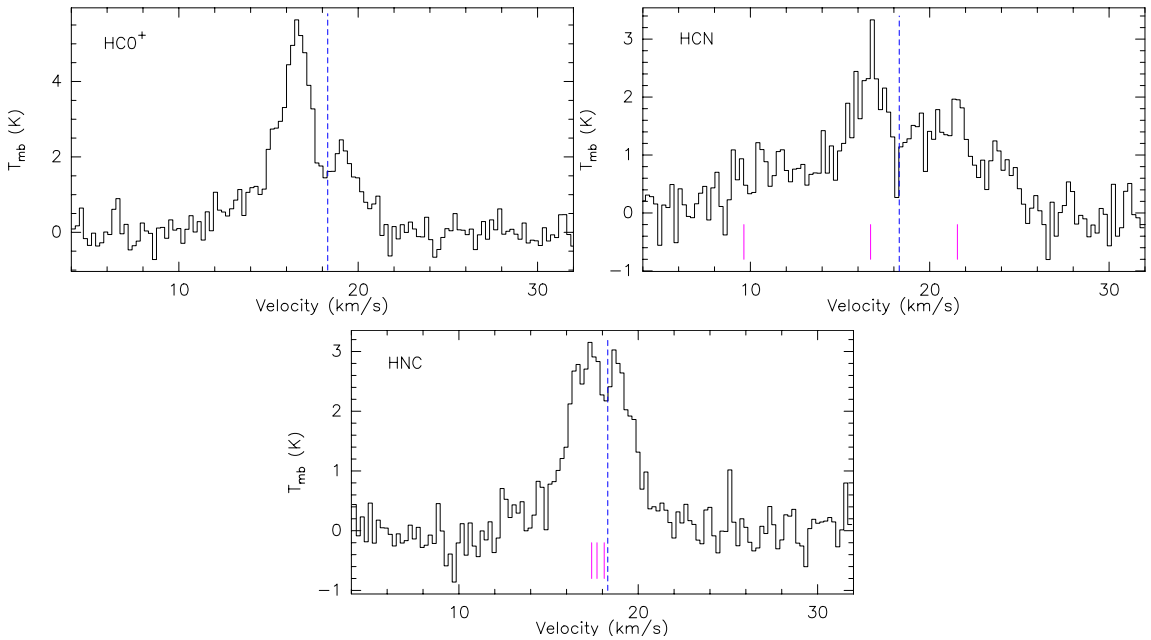

Figure 3.11: Same as Fig. 3.10 but for the optically thick transitions of HCO^+, HCN, and HNC.

Table 3.7: Parameters of the optically thin molecular lines detected towards G12.42+0.50. The line width (ΔV), main beam temperature ($T_{\rm mb}$) and velocity integrated intensity ($\int T_{\rm mb}$) are obtained from the `hfs` fitting method of CLASS90 for all the molecules except for $H^{13}CO^+$, for which a single Gaussian profile is used to fit the spectrum. The column densities (N) of molecules are estimated using RADEX, and their fractional abundances (x) are determined using the mean H_2 column density of the clump, C1.

Transition	ΔV ($\rm km\,s^{-1}$)	$T_{\rm mb}$ (K)	$\int T_{\rm mb}$ ($\rm K\,km\,s^{-1}$)	N ($10^{14}\,\rm cm^{-2}$)	x (10^{-9})
$H^{13}CO^+$	2.9	1.2	3.6	0.1	0.3
N_2H^+	3.2	2.5	8.5	4.1	12.4
HC_3N	3.0	1.3	4.1	1.4	4.2
C_2H	2.7	1.3	3.8	5.5	16.7

species. The spectrum of each molecule is extracted towards the 870 μm, ATLASGAL emission peak. The spectra of the optically thin molecular species, $H^{13}CO^+$, C_2H, N_2H^+ and HC_3N, are shown in Fig. 3.10 and the spectra of the optically thick molecular species, HCO^+, HCN and HNC, are plotted in Fig. 3.11. We use the hyperfine structure (`hfs`) method of CLASS90 to fit the observed spectra for the optically thin transitions of C_2H, N_2H^+ and HC_3N. Since the molecule $H^{13}CO^+$ has no hyperfine components, a single Gaussian profile is used to fit the spectrum. The Gaussian fit yields a LSR velocity of $18.3\,\rm km\,s^{-1}$, which is consistent with the value estimated using the N_2H^+ line of the same survey ($18.3\,\rm km\,s^{-1}$; Yu & Wang 2015). The fit to the spectra are indicated by solid red line, and the LSR velocity and the location of the hyperfine components are indicated by the dashed blue and solid magenta lines, respectively in Fig. 3.10. The retrieved line parameters that include the peak velocity ($V_{\rm LSR}$), line width (ΔV), main beam temperature ($T_{\rm mb}$) and the velocity integrated intensity ($\int T_{\rm mb}$) are tabulated in Table 3.7. Beam correction is applied to the antenna temperature to obtain the main beam temperature using the equation, $T_{\rm mb} = T_A/\eta_{\rm mb}$ (Rathborne et al., 2014), where $\eta_{\rm mb}$ is assumed to be 0.49 (Ladd et al., 2005) for the MALT90 data.

To estimate the column density of these transitions, we use RADEX, a one dimensional non-local thermodynamic equilibrium radiative transfer code (van der Tak et al., 2007). The input parameters to RADEX include the peak main beam temperature, background temperature assumed to be 2.73 K (Purcell et al., 2006; Yu & Wang, 2015), kinetic temperature, which is assumed to be same as the dust temperature (Liu et al., 2016a; Sanhueza et al., 2012; Yu & Xu, 2016), line width, and H_2 number density. The dust temperature

and H_2 number density towards the clump, C1 of G12.42+0.50 are taken from Table 3.5 presented in Section 3.3.4. The column densities of the optically thin transitions are also tabulated in Table 3.7. From the mean hydrogen column density of the clump, we also calculate the fractional abundances of the detected molecules. These estimates are in good agreement with typical values obtained for IR dark clumps and IRDCs (Miettinen, 2014; Vasyunina et al., 2011).

From Fig. 3.11, it is evident that the $J = 1 - 0$ transitions of the molecules, HCO^+, HCN and its metastable geometrical isomer, HNC, display distinct double-peaked line profiles with self-absorption dips coincident with the LSR velocity. The blue-skewed profile seen in HCO^+ is very prominent with the blueshifted emission peak being much stronger than the redshifted one. In case of the HCN transition, the central hyperfine component shows a blue-skewed double profile where the redshifted component is rather muted in the noise. Such blue asymmetry is usually indicative of infalling gas (Wu & Evans, 2003; Wyrowski et al., 2016). In Section 3.6.1, we discuss in detail the HCO^+ line profile. In comparison, in the HNC transition, the blueshifted and redshifted peaks have similar intensities. Similar line profiles are detected towards the star-forming region AFGL 5142 (Liu et al., 2016b). These authors have attributed it to low-velocity expanding materials entrained by high-velocity jets. An alternate reason could be of a collapsing envelope. In case of G12.42+0.50, however, no conclusive explanation can be proposed given the resolution of the data. Higher resolution observations are hence required to resolve the kinematics and explain the double peaked profile of HNC.

Table 3.8: The retrieved parameters, peak velocities, velocity widths and peak fluxes of the molecular transitions $^{12}CO\,(3-2)$, $^{13}CO\,(3-2)$, $C^{18}O\,(3-2)$ and $^{13}CO\,(1-0)$ towards G12.42+0.50. R and B in parentheses denote the red and blueshifted components.

Transition	V ($km\,s^{-1}$)		ΔV ($km\,s^{-1}$)		T_{mb} (K)	
$^{12}CO\,(3-2)$	21.0 (R)	15.8 (B)	2.8 (R)	3.7 (B)	10.7 (R)	29.1(B)
$^{13}CO\,(3-2)$	19.9 (R)	16.6 (B)	2.0 (R)	3.9 (B)	7.7 (R)	21.9 (B)
$C^{18}O\,(3-2)$	19.3 (R)	17.4 (B)	1.2 (R)	2.4 (B)	6.6 (R)	11.2 (B)
$^{13}CO\,(1-0)$	17.8		3.0		13.3	

The rotational transition line data of the isotopologues of the CO molecule, $^{12}CO\,(3-2)$, $^{13}CO\,(3-2)$ and $C^{18}O\,(3-2)$ taken from archives of JCMT and $^{13}CO\,(1-0)$ observed with TRAO are used to understand the large-scale outflows associated with G12.42+0.50.

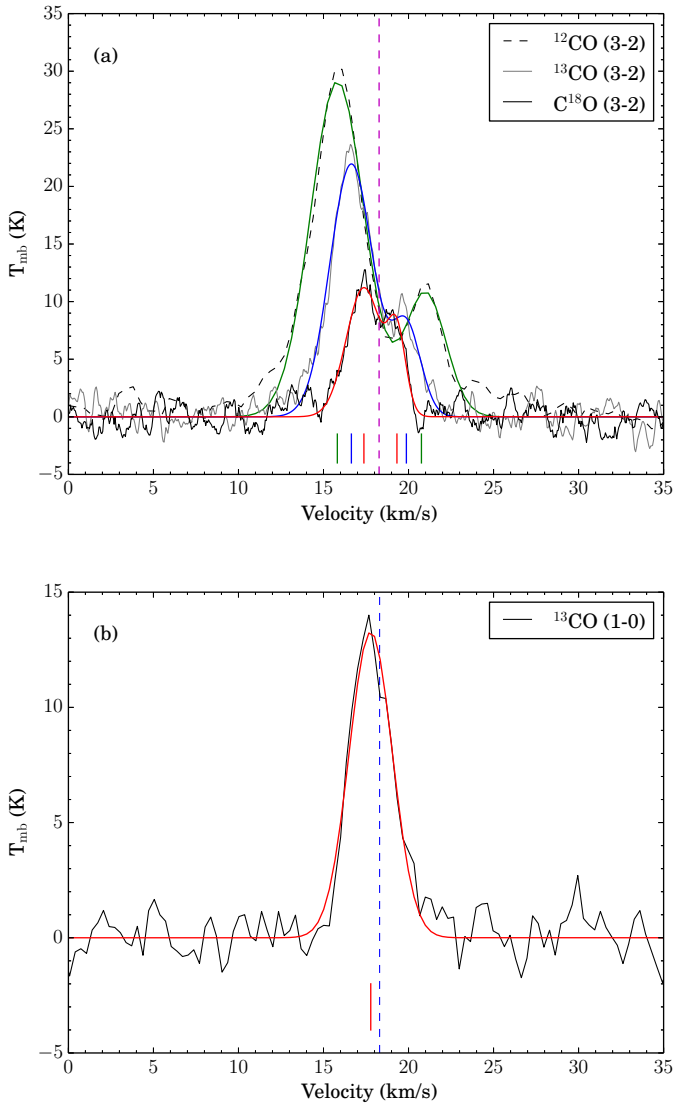

Figure 3.12: (a) Rotational transition lines of isotopologues of the CO $(3-2)$ observed towards G12.42+0.50 fitted with double Gaussians. The spectra of ^{12}CO, ^{13}CO and C^{18}O are boxcar-smoothed by three, eight and eleven channels which correspond to velocity smoothing of 1.2, 3.4 and $4.6\,\mathrm{km\,s^{-1}}$, respectively. The fit to the ^{12}CO spectrum is depicted in green, ^{13}CO in blue and C^{18}O in red. The dashed magenta line corresponds to the LSR velocity, $18.3\,\mathrm{km\,s^{-1}}$. The positions of the red- and blueshifted components are indicated in green, blue and red lines for ^{12}CO, ^{13}CO and C^{18}O lines respectively. (b) Spectrum of the $J = 1 - 0$ transition of ^{13}CO obtained from TRAO. The Gaussian fit to the spectrum is sketched in red. The dashed blue line corresponds to the LSR velocity. The spectrum shows a blue shifted single peak, indicated by a red line. The red and blue lobes are not resolved, probably due to larger beam size of TRAO compared to JCMT.

The rotational transitions of the CO molecule is an excellent tracer of outflow activity in star-forming regions (Beuther et al., 2002c; Zhang et al., 2001). Different transitions trace different conditions of the ISM and probe different parts of the cloud. While the CO $J = 3 - 2$ transition has a distinct upper energy level temperature and critical density of 33.2 K and $5 \times 10^4\,\mathrm{cm}^{-3}$, respectively (Kaufman et al., 1999), the lower J CO transitions effectively trace the kinematics of low density material of the cloud (Rygl et al., 2013). Typically, the ^{12}CO line is optically thick and the ^{13}CO and C^{18}O lines are optically thin and are high density tracers. While ^{12}CO can effectively map the spatial and kinematic extent of the outflows and ^{13}CO can map them to some extent, the C^{18}O can trace the cloud cores under the optically thin assumption (Lo et al., 2015). The spectra of these molecular species are extracted towards the peak of the 870 μm, ATLASGAL emission and shown in Fig. 3.12(a) and (b). The spectra of the isotopologues of CO $(3 - 2)$ transition show red and blueshifted profiles. However, the ^{13}CO $(1 - 0)$ transition shows a single component, blueshifted profile. This is due to the large beam size of TRAO where the blue and the red components are unresolved. A double Gaussian is used to fit the spectra of ^{12}CO $(3 - 2)$, ^{13}CO $(3 - 2)$ and C^{18}O $(3 - 2)$, and a single Gaussian profile is fitted to the ^{13}CO $(1 - 0)$ line. The fitted profiles are also shown in the Figures. The retrieved parameters are peak velocities, velocity widths, and peak fluxes which are listed in Table 3.8. Beam correction is applied to the antenna temperature, taking η_{mb} to be 0.64 for the JCMT (Buckle et al., 2009) and 0.54 for TRAO (Liu et al., 2018b). Detailed discussion on the outflow feature will be presented in Section 3.6.2.

3.5 Nature of radio emission

Based on the GMRT maps and the radio spectral index estimation, two scenarios unfold in understanding the nature of the radio emission. The thermal radio emission could be explained as due to individual UC H II regions or given the association with an EGO, one can explore the case of an ionized jet. We discuss the possibilities of these two scenarios in the following sections.

3.5.1 UC H II region

We first investigate under the UC H II region framework. Morphologically, R1 appears to be a compact, spherical radio source. The association of R1 with a hot molecular core ($\sim$183 K; Section 3.3.2) supports the interpretation of the emission as being due to photoionization, since hot cores are often associated with UC H II regions (Beltrán et al., 2016;

Churchwell, 2002; Kurtz et al., 2000). Assuming the continuum emission at 1390 MHz to be optically thin and arising from a homogeneous, isothermal medium, we derive the Lyman continuum photon flux ($N_{\rm Ly}$), the emission measure (EM) and the electron number density ($n_{\rm e}$). These physical parameters are estimated using the following formulation (Schmiedeke et al., 2016)

$$\left[\frac{N_{\rm Ly}}{\rm s^{-1}}\right] = 4.771 \times 10^{42} \left[\frac{S_\nu}{\rm Jy}\right] \left[\frac{T_{\rm e}}{\rm K}\right]^{-0.45} \left[\frac{\nu}{\rm GHz}\right]^{0.1} \left[\frac{d}{\rm pc}\right]^{2} \tag{3.9}$$

$$\left[\frac{\rm EM}{\rm pc\ cm^{-6}}\right] = 3.217 \times 10^{7} \left[\frac{S_\nu}{\rm Jy}\right] \left[\frac{\nu}{\rm GHz}\right]^{0.1} \left[\frac{T_{\rm e}}{\rm K}\right]^{0.35} \left[\frac{\theta_{\rm src}}{\rm arcsec}\right]^{-2} \tag{3.10}$$

$$\left[\frac{n_{\rm e}}{\rm cm^{-3}}\right] = 2.576 \times 10^{6} \left[\frac{S_\nu}{\rm Jy}\right]^{0.5} \left[\frac{\nu}{\rm GHz}\right]^{0.05} \left[\frac{T_{\rm e}}{\rm K}\right]^{0.175} \left[\frac{\theta_{\rm src}}{\rm arcsec}\right]^{-1.5} \left[\frac{d}{\rm pc}\right]^{-0.5} \tag{3.11}$$

where S_ν is the integrated flux density of the ionized region, $T_{\rm e}$ is the electron temperature, ν is the frequency, $\theta_{\rm src}$ is the deconvolved size of the ionized region, and d is the distance to the source. We estimate $T_{\rm e}$ from the derived electron temperature gradient in the Galactic disk by Quireza et al. (2006). We use their empirical relation, $T_{\rm e} = (5780 \pm 350) + (287 \pm 46) R_{\rm G}$, where $R_{\rm G}$ is the Galactocentric distance. $R_{\rm G}$ is estimated to be 5.7 kpc following Xue et al. (2008). This yields an electron temperature of 7416±437 K. The derived physical parameters of the UC H II region are listed in Table 3.9.

Table 3.9: Physical parameters of the radio continuum emission from the UC H II region associated with component R1 of G12.42+0.50.

Source	$\theta_{\rm src}$ ($''$)	Radius (pc)	$T_{\rm e}$ (K)	$N_{\rm Ly}$ (10^{45} s^{-1})	log ($N_{\rm Ly}$)	EM (pc cm^{-6})	$n_{\rm e}$ (cm^{-3})	$t_{\rm dyn}$ (10^{-3} yr)
R1	1.8	0.01	7416±437	4.1	45.6	1.8×10^6	9.4×10^3	0.4

If a single ZAMS star is responsible for the ionization of this UC H II region, then from Panagia (1973), the estimated Lyman continuum photon flux corresponds to a spectral type of $\rm B1 - B0.5$. Following Davies et al. (2011), the Lyman continuum flux from the UC H II region is suggestive of a massive star of mass $\sim 9 - 12\,M_\odot$. As discussed earlier, the estimate is made under the assumption of optically thin emission. Hence, this result only provides a lower limit, since the emission at 1390 MHz could be partially optically thick as is evident from our radio spectral index estimations. In addition to this, several studies show that there could be appreciable absorption of Lyman continuum photons by dust (Arthur et al., 2004; Inoue, Hirashita & Kamaya, 2001; Paron, Petriella & Ortega, 2011). It is

further noticed that if the total infrared luminosity of G12.42+0.50 (2.8×10^4, Section 3.3.2) were to be produced by a ZAMS star, it would correspond to a star with spectral type between $\mathrm{B0-O9.5}$ (Panagia, 1973). Taking a B0 star, the Lyman continuum photon flux is expected to be $2.3\times10^{47}\,\mathrm{s^{-1}}$. At optically thin radio frequencies such a star could generate an H II region with a flux density of ~ 400 mJy, which is higher than observed flux density value of 7.9 mJy observed. This could be suggestive of the central source going though a strong accretion phase, with it still being in a pre-UC H II or very early UC H II region phase (Guzmán, Garay & Brooks, 2010). An intense accretion activity could stall the expansion of the H II region which results in weaker radio emission. The above picture is congruous with the infall scenario associated with R1 and the evidence of global collapse of the molecular cloud associated with G12.42+0.50. Detailed discussion on molecular gas kinematics are presented in Section 3.6.1.

From the Lyman continuum photon flux and the electron density estimates, we compute the radius of the Strömgren sphere, that is defined as the radius at which the rate of ionization equals the rate of recombination, assuming that the H II region is expanding in a homogeneous and spherically, symmetric medium. The radius of the Strömgren sphere, R_s is given by the expression,

$$R_s = \left(\frac{3N_{\mathrm{Ly}}}{4\pi n_0^2 \alpha_B}\right)^{1/3} \tag{3.12}$$

where α_B is the radiative recombination coefficient taken to be $2.6\times10^{-13}\,\mathrm{cm^3\,s^{-1}}$ (Kwan, 1997) and n_0 is the mean number density of atomic hydrogen which is estimated to be $2.1\times10^4\,\mathrm{cm^{-3}}$ from the clump detected in the column density map (Section 3.3.3). Thus, the radius of the Strömgren sphere, R_s for the resolved component, R1 is calculated to be 0.007 pc. Using this, the dynamical age the H II region is determined from the expression

$$t_{\mathrm{dyn}} = \left[\frac{4\,R_s}{7\,c_i}\right]\left[\left(\frac{R_{\mathrm{H\,II}}}{R_s}\right)^{7/4} - 1\right] \tag{3.13}$$

where $R_{\mathrm{H\,II}}$, is the radius of the H II region, c_i is the isothermal sound speed in the ionized medium, which is typically assumed to be $10\,\mathrm{km\,s^{-1}}$. $R_{\mathrm{H\,II}}$ is estimated to be 0.01 pc by taking the geometric mean of the deconvolved size given in Table 3.1. The dynamical age of the UC H II region associated with component R1 is determined to be 0.4×10^3 yr. Since this estimation is made under a not so realistic assumption that the medium in which the H II region expands is homogeneous, the results obtained may be considered representative at best. The derived physical parameters of the UC H II region are tabulated in Table 3.9.

The estimated values of electron density and emission measure are in the range found for UC H II regions around stars of spectral type $\mathrm{B1} - \mathrm{B0.5}$ (Kurtz, Churchwell & Wood, 1994). Furthermore, the size estimates for UC H II regions are proposed to be $\lesssim 0.1\,\mathrm{pc}$ (Kurtz, 2002; Wood & Churchwell, 1989), in agreement with that derived for the component R1. The dynamical timescales obtained indicate a very early phase of the UC H II region (Churchwell, 2002; Wood & Churchwell, 1989). Wood & Churchwell (1989) estimate that it would take $\sim 10^4$ yr for an UC H II region to expand against the gravitational pressure of the confining dense molecular cloud.

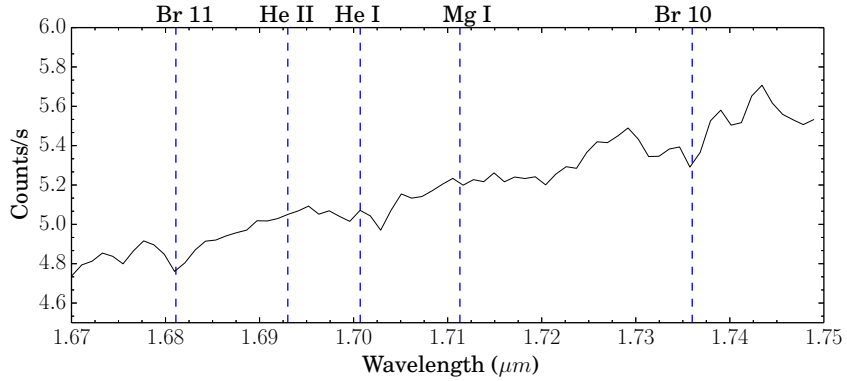

Figure 3.13: The UKIRT-UIST spectrum extracted over a 6 pixel wide aperture centered on the radio component, R1 is shown here. The spectral range is chosen to be the same as the VLT-ISAAC spectrum towards the infrared source, IRAS 18079-1756, associated with G12.42+0.50, studied by Kendall, de Wit & Yun (2003). The absorption lines identified by these authors are indicated in the plot.

On a careful scrutiny of the point sources in the region, it is seen that a red 2MASS[4] source (J18105109-1755496; J = 13.727, H = 11.011, K = 9.351) is located at the peak position of R1 (within $\sim 0.3''$). Investigating its location in *JHK* colour-colour diagrams (e.g Fig. 6(d) of Das et al. (2017)) suggests a highly embedded Class II YSO which in all likelihood could be the ionizing source. Detailed spectroscopic observations of this source is presented in Kendall, de Wit & Yun (2003). In the observed wavelength range of $1.67 - 1.75\,\mu\mathrm{m}$, the VLT/ISAAC *H*-band spectra, presented by these authors, show the presence of broad absorption features of He I ($\sim 1.7\,\mu\mathrm{m}$) and hydrogen. We did a careful examination of our UKIRT spectroscopic observations. We extracted the spectrum over a 6 pixel wide aperture (estimated from other stellar sources along the slit) centred on R1, a zoom in of which is shown in Fig. 3.13. The spectral range is chosen such that it matches

[4]This publication makes use of data products from the Two Micron All Sky Survey, which is a joint project of the University of Massachusetts and the Infrared Processing and Analysis Center/California Institute of Technology, funded by the NASA and the NSF

the VLT spectrum of Kendall, de Wit & Yun (2003) (refer Fig. 5 of their paper). Inspite of the poor signal-to-noise, the spectrum does show hint of the Br 11 line and possibly the Br 10 line as well as detected by Kendall, de Wit & Yun (2003). Based on these absorption lines and the absence of the 1.693 μm He II absorption line, Kendall, de Wit & Yun (2003) suggest this source to be a main-sequence star of spectral type B3 (± 3 subclasses). This is consistent with the spectral type derived from our measured radio flux densities. However, the absence of emission lines in their observed spectra prompted the authors to speculate a late evolutionary stage. This contradicts the results obtained from our *HK* and *KL* spectra which show the presence of several emission lines that are listed in Table 3.2, indicating an early evolutionary phase. The results from the molecular line analysis discussed in Section 3.6 is also in agreement with this picture. The compact component R2 can either be an independent UC H II region or an externally ionized density clump. If we consider it as an UC H II region then the observed Lyman continuum flux translates to an ionizing source of spectral type $\mathrm{B3} - \mathrm{B2}$ (Panagia, 1973) and a mass of $6 - 9\,M_{\odot}$ (Davies et al., 2011).

3.5.2 A possible thermal jet?

Even with the compelling possibility of R1 being an UC H II region, we explore an alternate scenario along the lines of a possible thermal jet. This is motivated by the very nature of G12.42+0.50 which is identified as an EGO and hence likely to be associated with jets/outflows. Further, several observational manifestations are consistent with the characteristics of thermal radio jets listed in Anglada (1996) and Rodriguez (1997).
G12.42+0.50 is a weak radio source (integrated flux density < 10 mJy) displaying a linear morphology, including components R1 and R2, in the north-east and south-west direction. It is also seen to be associated with a large scale molecular outflow (Fig. 3.15(a), Section 3.6.2) with the candidate jet located at its centroid position and the observed elongation aligned with the outflow axis. From the radio spectral index map shown in Fig. 3.3, we see that along the direction of the radio components R1 and R2, the spectral index varies between $\sim 0.3 - 0.7$. These values of spectral index are consistent with the radio continuum emission originating due to the thermal free-free emission from an ionized collimated stellar wind (Anglada et al., 1998; Panagia & Felli, 1975; Reynolds, 1986). Similar range of spectral index values are also cited in literature for systems harbouring thermal radio jets (Anglada et al., 1994; Guzmán, Garay & Brooks, 2010; Sanna et al., 2016). Additional support for the thermal jet hypothesis comes from the angular size spectrum. Guzmán et al. (2016) and Hofner et al. (2017) have discussed the trend of the angular size spectrum

where the jet features show a decrease in size with frequency as expected from the variation of electron density with frequency (Panagia & Felli, 1975; Reynolds, 1986). In case of G12.42+0.50, the 1390 MHz and 5 GHz sizes show this trend with the upper limit from 610 MHz being consistent. It should be noted here that in the 5 GHz map, all structures upto $\sim 20''$ would be well-imaged (Urquhart et al., 2009). However, the size dependence is not conclusive given the resolution of the two maps. Presence of shock-excited emission lines in the NIR (Section 3.2) further corroborates with this ionized jet scenario. Additionally, a H_2O maser is seen to be associated with G12.42+0.50 (Cyganowski et al., 2013), located at an angular distance of $\sim 12''$ from the radio peak. The position of this is indicated in Fig. 3.1(b) and (c) and Fig. 3.15(b). H_2O masers have often been found in the vicinity of thermal radio jets, and in some cases both the thermal jet and H_2O masers are powered by the same star (Gomez, Rodriguez & Marti, 1995).

The two competing schemes deliberated above are in good agreement with our observation making it difficult to be biased towards any. However, recent studies speculate about the co-existence of UC/HC H II regions and ionized jets. From the investigation of the nature of the observed centimeter radio emission in G35.20-0.74N, Beltrán et al. (2016) discuss the possibility of it being a UC H II region as well as a radio jet being powered by the same YSO suggesting an interesting transitional phase where the UC H II region has started to form while infall and outflow processes of the main accretion phase is still ongoing. Similar scenario is also invoked for the MYSO, G345.4938+01.4677 by Guzmán et al. (2016). Both these examples conform well with our results. Guzmán, Garay & Brooks (2010) discuss about a string of radio sources which are likely to be the ionized emission due to shocks from fast jets wherein the separation of the inner lobe from the central object is ~ 0.03 pc. Garay et al. (2003) also examines a radio triple source in which case the central source harbours a high-mass star in an early evolutionary phase and ejects collimated stellar wind which ionizes the surrounding medium giving rise to the observed radio emission. In this case, the separation between the central source and the radio lobe is ~ 0.14 pc. For G12.42+0.50, component R2, at a distance of ~ 0.07 pc from R1, can also be conjectured to be a clumpy, enhanced density region (SMA3) ionized by the emanating jet. The star-forming region of G12.42+0.50 has also been speculated to be harbouring a cluster (Jaffe et al., 1984; Kendall, de Wit & Yun, 2003). With the detection of R1, R2, SMA1 and SMA2, it reveals itself as a potentially active star-forming complex.

3.6 Kinematic signatures of gas motion

3.6.1 Infall activity

The double-peaked, blue-asymmetric HCO^+ line profile with a self-absorption dip shown in Fig. 3.11 is a characteristic signature of infall activity (De Vries & Myers, 2005; Peretto, André & Belloche, 2006; Peretto et al., 2013; Yuan et al., 2018). In order to probe the gas motion in the entire clump associated with G12.42+0.50, we generate a grid map of the HCO^+ line profile which is presented in Fig. 3.14(a). HCO^+ line profiles are displayed in blue. For comparison, we also plot the optically thin transition, $H^{13}CO^+$, in red. The grey scale map shows the 4.5 μm map emission with the ATLASGAL contours (in green) overlaid. The spectra shown here are averaged over regions gridded to an area given by the square of the beam size ($36''$) of the Mopra radio telescope. The HCO^+ spectrum displays blue-skewed line profiles in all the grids within ATLASGAL contour revealing a strong indication of the clump in global collapse. For the molecular cloud to be collapsing, the gravitational energy of the cloud has to overcome the kinetic energy that supports it from collapsing. The gravitational stability of the cloud can be inspected using the virial parameter, $\alpha_{\rm vir} = 5\sigma^2 R/(GM_{\rm C})$ which needs to be lower than unity (Bertoldi & McKee, 1992) for a collapsing cloud. σ is the velocity dispersion which is taken from the FWHM of the optically thin $H^{13}CO^+$ line and is estimated to be $1.2\,{\rm km\,s^{-1}}$. Taking R and $M_{\rm C}$ as the radius and mass of the clump, C1, the virial parameter, $\alpha_{\rm vir}$ is calculated to be ~ 0.9. In comparison, Yuan et al. (2018) obtain a value of 0.58 for the EGO G022.04+0.22 and Pillai et al. (2011) in their study of massive cores obtain values in the range $0.1 - 0.8$. Given the presence of infall and outflow activity, that could significantly increase the velocity dispersion, the derived estimate towards G12.42+0.50 is likely to be an overestimate.

Table 3.10: The infall velocity, $V_{\rm inf}$ and mass infall rate, $\dot{M}_{\rm inf}$ of the clump, C1 associated with G12.42+0.50, estimated using the blue-skewed optically thick HCO^+ line

$V_{\rm LSR}$ (km s^{-1})	$V_{\rm inf}$ (km s^{-1})	δV	$\dot{M}_{\rm inf}$ ($10^{-3}\,M_\odot\,{\rm yr}^{-1}$)
18.3	1.8	-0.6	9.9

To support the picture of protostellar infall, we estimate the infall velocity and mass infall rate. First, to quantify the blue-skewness of the HCO^+ profile, we calculate the asymmetry

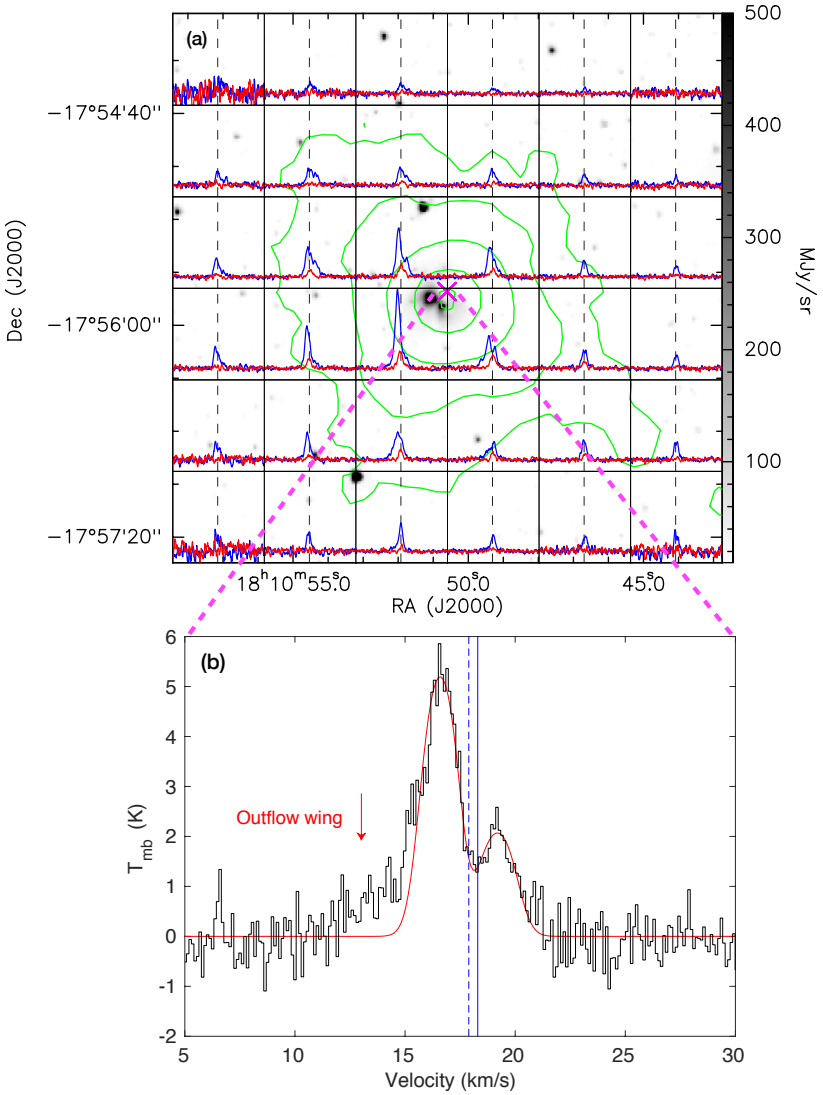

Figure 3.14: (a) The grey scale shows the 4.5 μm map. The green contours represent the ATLASGAL 870 μm emission. The contour levels are 3, 9, 27, 72 and 108 times σ ($\sigma \sim 0.06\ Jy\,beam^{-1}$). The HCO^+ spectrum shown in blue and the $H^{13}CO^+$ spectrum shown in red are overlaid. The spectra are boxcar-smoothed by five channels that corresponds to a velocity smoothing of $0.6\,km\,s^{-1}$. The dashed vertical lines indicate the LSR velocity estimated by averaging the peak positions of the $H^{13}CO^+$ line in all the regions where the line is detected. The peak position of the 870 μm emission is marked by a magenta 'x'. (b) The HCO^+ spectrum extracted towards the ATLASGAL 870 μm peak . The best fit obtained using the 'two-layer' model is shown in red. The solid blue line represents the LSR velocity, $18.3\,km\,s^{-1}$ derived from the optically thin $H^{13}CO^+$ line and the dashed blue line represents the LSR velocity obtained from the model fit. The red arrow points to a blue-wing which could indicate a possible molecular outflow.

parameter, δV, using the following expression (Yu & Wang, 2013),

$$\delta V = \frac{(V_{\rm thick} - V_{\rm thin})}{\Delta V_{\rm thin}} \tag{3.14}$$

Here, δV is defined as the ratio of the difference between the peak velocities of the optically thick line, $V_{\rm thick}$ and the optically thin line, $V_{\rm thin}$, and the FWHM of the optically thin line denoted by $\Delta V_{\rm thin}$. Using values of $V_{\rm thin} = 18.3\,{\rm km\,s^{-1}}$ and $\Delta V_{\rm thin} = 2.9\,{\rm km\,s^{-1}}$ from the Gaussian fit to the $H^{13}CO^+$ line and $V_{\rm thick} = 16.5\,{\rm km\,s^{-1}}$, the peak of the blue component of the HCO^+ line, δV is estimated to be -0.6. According to Mardones et al. (1997), the criteria for a bona fide blue-skewed profile is $\delta V < -0.25$. Furthermore, we estimate the mass infall rate ($\dot{M}_{\rm inf}$) of the envelope using the equation, $\dot{M}_{\rm inf} = 4\pi R^2 V_{\rm inf} \rho$ (López-Sepulcre, Cesaroni & Walmsley, 2010), where $V_{\rm inf}$ = $V_{\rm thin} - V_{\rm thick}$ = $V_{\rm H^{13}CO^+} - V_{\rm HCO^+}$ is the infall velocity and ρ is the average volume density of the clump given by $\rho = M_{\rm C}/\frac{4}{3}\pi R^3$. The clump mass, $M_{\rm C}$ and radius, R are taken from Section 3.3.4. The infall velocity, $V_{\rm inf}$ and the mass infall rate are estimated to be $1.8\,{\rm km\,s^{-1}}$ and $9.9\times10^{-3}\,M_\odot\,{\rm yr^{-1}}$, respectively. The mass infall rate estimate is higher compared to the value of $6.4\times10^{-3}\,M_\odot\,{\rm yr^{-1}}$ derived by He et al. (2015). As discussed in Section 3.3.4, our clump mass and radius estimates are higher. Nevertheless, both the estimates fall in the range seen in other high-mass star-forming regions (Chen et al., 2010; Liu et al., 2013; López-Sepulcre, Cesaroni & Walmsley, 2010).

To further understand the properties of the infalling gas, we extend our analysis and fit the HCO^+ line with a 'two-layer' model following the discussion in Liu et al. (2013). Here, we briefly repeat the salient features of the model with a description of the equations and the terms. In this model, a continuum source is located in between the two layers, with each layer having an optical depth, τ_0 and velocity dispersion, σ, and an expanding speed, $V_{\rm rel}$ with respect to the continuum source. This is the infall velocity introduced earlier. $V_{\rm rel}$ is negative if the gas is moving away and positive when there is inward motion. The brightness temperature at velocity, V is given by

$$\Delta T_{\rm B} = (J_{\rm f} - J_{\rm cr})[1 - exp(-\tau_{\rm f})] + (1-\Phi)(J_{\rm r} - J_{\rm b}) \times [1 - exp(-\tau_{\rm r} - \tau_{\rm f})] \tag{3.15}$$

where

$$J_{\rm cr} = \Phi J_{\rm c} + (1-\Phi) J_{\rm r} \tag{3.16}$$

and

$$\tau_{\rm f} = \tau_0 \exp\left[\frac{-(V - V_{\rm rel} - V_{\rm cont})^2}{2\sigma^2}\right] \tag{3.17}$$

$$\tau_{\rm r} = \tau_0 \exp\left[\frac{-(V + V_{\rm rel} - V_{\rm cont})^2}{2\sigma^2}\right] \tag{3.18}$$

Here $J_{\rm c}$, $J_{\rm f}$, $J_{\rm r}$, $J_{\rm b}$ are the Planck temperatures of the continuum source, the "front" layer, the "rear" layer and the cosmic background radiation, respectively. J is the blackbody function at temperature, T and frequency, ν and is expressed as

$$J = \frac{h\nu}{k} \frac{1}{\exp(T_0/T) - 1} \tag{3.19}$$

where $T_0 = h\nu/k$, h is Planck's constant, and k is Boltzmann's constant. Φ and $V_{\rm cont}$ are the filling factor and systemic velocity (or the LSR velocity) of the continuum source, respectively. The $\rm HCO^+$ profile and the fitted spectrum (in red) are displayed in Fig. 3.14(b). The LSR velocities determined from the model fit (dashed blue) and the optically thin transition of $\rm H^{13}CO^+$ (solid blue) are also shown in the figure. The blue component of the $\rm HCO^+$ line shows a clear presence of broadened wing likely to be due to outflow. To avoid contamination from this outflow component, we restrict the velocity range between $16.1 - 21.0\,{\rm km\,s^{-1}}$ while fitting the model. The model derived parameters are listed in Table 3.11. The model fitted values are fairly consistent (slightly smaller) with our previous estimates.

Table 3.11: Best fit parameters retrieved from the model for the self-absorbed $\rm HCO^+$ line observed towards G12.42+0.50.

τ_0	Φ	$J_{\rm c}$ (K)	$J_{\rm f}$ (K)	$J_{\rm r}$ (K)	$V_{\rm cont}$ ($\rm km\,s^{-1}$)	σ ($\rm km\,s^{-1}$)	$V_{\rm rel}$ ($\rm km\,s^{-1}$)
1.3	0.3	13.9	7.4	10.6	17.9	0.7	1.3

3.6.2 Outflow feature

Massive molecular outflows are ubiquitous in star-forming regions (Beuther et al., 2002c) and often co-exist with ionized jets (e.g. Anglada, 1996; Purser et al., 2016). The jets are believed to entrain the gas and dust from the ambient molecular cloud, thus driving molecular outflows. According to several studies, broad wings of the optically thick lines like

HCO^+ are well accepted signatures of outflow activity (e.g. Klaassen & Wilson, 2007; Schneider et al., 2010; Smith et al., 2013). As mentioned in the previous section, broadening of the blue wing of the infall tracer line of HCO^+ is seen in G12.42+0.50. Given the association with an EGO and the alignment with a large scale CO outflow features, the origin of the broad blue wing can be attributed to be due to the outflow. Alternate scenarios like unresolved velocity gradients (Tackenberg et al., 2014) or gravo-turbulent fragmentation (Klessen et al., 2005) have been invoked for broadened wings but are less likely to be the case here. In this section, we focus on the rotational transition lines of CO that are well known tracers of molecular outflow, and investigate the outflow kinematics of the molecular cloud associated with G12.42+0.50 using the archival data of the isotopologues of $\mathrm{CO}\,(3-2)$ transition from JCMT and $^{13}\mathrm{CO}\,(1-0)$ observation from TRAO.

The red and blueshifted velocity profiles of the CO transitions shown in Fig. 3.12(a) can be attributed to emission arising from distinct components of the CO gas that are moving in opposite directions away from the central core. We note that the peaks have different shifts with respect to the LSR velocity with the $^{12}\mathrm{CO}\,(3-2)$ line showing the maximum shift and $\mathrm{C}^{18}\mathrm{O}\,(3-2)$ line has the minimum shift. The peaks of the red component of $^{12}\mathrm{CO}\,(3-2)$, $^{13}\mathrm{CO}\,(3-2)$ and $\mathrm{C}^{18}\mathrm{O}\,(3-2)$ transitions are shifted by 2.5, 1.6 and $1.0\,\mathrm{km\,s^{-1}}$ from the LSR velocity. For the blue component the shifts are 2.5, 1.7 and $0.9\,\mathrm{km\,s^{-1}}$, respectively. $^{12}\mathrm{CO}$ molecule, having the lowest critical density among the three, effectively traces the outer envelope of the molecular cloud, hence showing the maximum shift and the $\mathrm{C}^{18}\mathrm{O}$ molecule, the densest among the three species is a tracer of the dense core of the molecular cloud and thus shows the minimum shift.

In order to map the outflow in the vicinity of G12.42+0.50, we construct the zeroth moment map of the two components using the task, `IMMOMENTS` in CASA. The zeroth moment map is the integrated intensity map that gives the intensity distribution of a molecular species within the specified velocity range. The $^{12}\mathrm{CO}\,(3-2)$ emission is integrated from the peak of the blueshifted profile to the blue wings that corresponds to the lower velocity channels ranging from $9.3-15.8\,\mathrm{km\,s^{-1}}$ for the blue component and from the peak of the redshifted profile to the red wing that corresponds to the higher velocity channels ranging from $20.8-25.3\,\mathrm{km\,s^{-1}}$ for the red component. The contours are shown overlaid on the *Spitzer* IRAC colour composite image in Fig. 3.15(a). The figure reveals the presence of two distinct, spatially separated red and blue lobes. High-velocity gas is also seen towards the tail of the blue component. The location of the 1.1 mm dense cores, SMA1, SMA2 and SMA3 are also marked in this figure. The central part covering the brightest portion of the IRAC emission (location of the EGO), is shown in Fig. 3.15(b) with the spatial

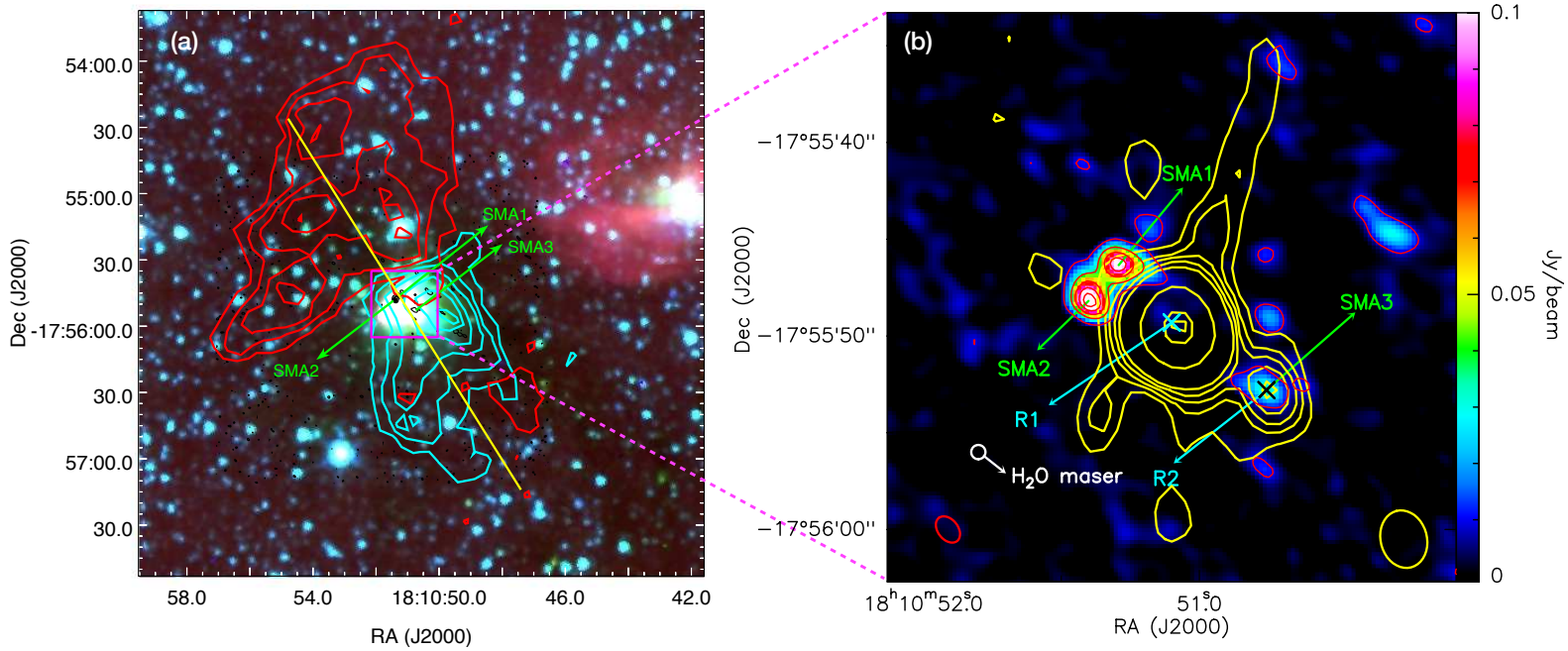

Figure 3.15: (a) The *Spitzer* IRAC colour composite image of G12.42+0.50, overlaid with the SMA 1.1 mm emission contours in black, with the contour levels same as in Fig. 3.7(k). The ^{12}CO $(3-2)$ emission integrated from the peak of the blueshifted profile to the blue wings ($9.3 - 15.8\,\mathrm{km\,s^{-1}}$) is represented using blue contours and from the peak of the red profile to the red wings ($20.8 - 27.3\,\mathrm{km\,s^{-1}}$) is represented using red contours. The contours start from the 5σ level for both the red and blue lobes and increases in steps of 3σ and 4σ, respectively ($\sigma = 2.7\,\mathrm{K\,km\,s^{-1}}$ for red lobe and $\sigma = 2.3\,\mathrm{K\,km\,s^{-1}}$ for blue lobe). The yellow line defines the cut along which the position-velocity (PV) diagram is made. The cut is selected in such a way that it passes through the red and blue lobes and also through the extended green emission. The red and blue lobes of the molecular outflow lie along a similar axis as the ionized jet. (b) The colour scale represents the 1.1 mm continuum emission from SMA observed towards G12.42+0.50 with the contour levels same as in Fig. 3.7(k). Radio emission at 1390 MHz is represented by yellow contours with the contour levels same as that in Fig. 3.2(a). The restoring beams of the 1390 MHz map and 1.1 mm map are indicated at the bottom- right and left of the image, respectively. The 'x's indicate the positions of R1 and R2. The white circle marks the position of the H_2O maser in the vicinity of G12.42+0.50.

distribution of the ionized gas overlaid on the 1.1 mm dust emission. To corroborate with the zeroth moment map showing the outflow lobes, in Fig. 3.16, we show the position-velocity (PV) diagram constructed along the outflow direction (position angle of $\sim 32°$; east of north) highlighted in Fig. 3.15(a). The direction along which the PV diagram is made is chosen such that both the red and blue lobes are sampled and it also covers the region of extended 4.5 μm emission of G12.42+0.50. The zero offset in the PV diagram corresponds to the position of the central coordinate of the EGO, G12.42+0.50 ($\alpha_{\rm J2000} = 18^{\rm h}10^{\rm m}51.1^{\rm s}, \delta_{\rm J2000} = -17°55'50''$). As expected, the PV diagram also clearly reveals distinct red and blue components of the ^{12}CO $(3-2)$ emission from the LSR velocity of the cloud represented by a red dashed line. Towards the lower region of the PV diagram we can trace a weaker redshifted ^{12}CO $(3-2)$ component consistent with the high-velocity tail seen in the zeroth moment map.

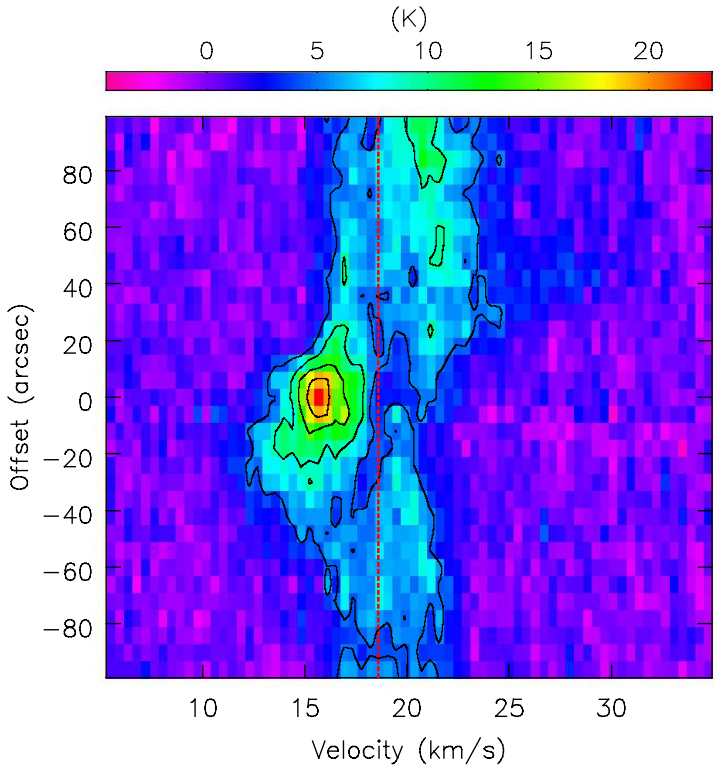

Figure 3.16: The PV diagram of the ^{12}CO $(3-2)$ transition along the cut shown in yellow in Fig. 3.15(a) at a position angle of 32°. The contour levels are 4, 9, 14 and 18 times σ ($\sigma \sim 1.0$ K). The zero offset in the PV diagram corresponds to the position of the central coordinate of G12.42+0.50 ($\alpha_{\rm J2000} = 18^{\rm h}10^{\rm m}51.1^{\rm s}, \delta_{\rm J2000} = -17°55'50''$). The LSR velocity, 18.3 km s^{-1}, is represented by the dashed red line.

To further probe the velocity structure of the cloud associated with G12.42+0.50, we generate channel maps of the ^{12}CO $(3-2)$ emission following the method outlined in Sanna

et al. (2014). To define suitable velocity ranges and identify the blue and redshifted outflow emission, we set the inner limits of the velocity at $\sim V_{\rm LSR} \pm {\rm FWHM}/2$, where FWHM is the $H^{13}CO^+$ linewidth. Taking the offset to be $\pm 1.5\,{\rm km\,s^{-1}}$ from the LSR velocity, the inner velocity limit for the red and the blueshifted lobes are estimated to be $19.8\,{\rm km\,s^{-1}}$ and $16.8\,{\rm km\,s^{-1}}$, respectively. The channel maps constructed are shown in Fig. 3.17. Each grid displays a pair of maps with a velocity width of $1\,{\rm km\,s^{-1}}$. Prominent outflow features begin to appear at velocities $\sim$ 13.8 and $21.8\,{\rm km\,s^{-1}}$ from the blue and red components, respectively. Beyond these velocities there is no contribution from the central core. Closer to the LSR velocity, the emission is rather complex making it difficult for the outflow features to be discernible. This is understandable since near the LSR velocity, the emission from the outflow components is likely to be contaminated by the infall motion and contribution from the diffuse gas. The channel maps are comparable to those presented by Qiu et al. (2009) for the region G240.31+0.07 with similar complex velocity structure near the LSR. The channel maps also show the presence of a redshifted component between velocities $20.8 - 22.8\,{\rm km\,s^{-1}}$ overlaping with the blue lobe towards the south-west. As will be discussed later in Section 3.6.3, such a velocity distribution can be indicative of accretion through filaments.

Morphologically, the spatially separated red and blue lobes associated with G12.42+0.50 resembles a wide-angle bipolar outflow seen in the star-forming region G240.31+0.07 studied by Qiu et al. (2009). These authors suggest the wide-angle bipolar outflow as the ambient gas being swept up by an underlying wide-angle wind and is driven by one of the three mm peaks located close to the geometric centre of the bipolar outflow. Only a handful of studies have found the presence of wide-angle bipolar molecular outflows associated with high-mass star formation (e.g. Qiu et al., 2009; Shepherd et al., 1998). Shepherd et al. (1998) investigate the likely driving source of the poorly collimated molecular outflow associated with G192.16. Coexistence of wide-angle CO outflow with shock-excited H_2 emission, prompted them to conclude that the G192.16 outflow is powered by the combination of a disk-wind and a jet. Given the likely association of G12.42+0.50 with an ionized jet supported by the presence of shock-excited NIR H_2 lines, we propose a similar picture of coexistence of disk-wind and a jet, where the wide-angle bipolar CO outflow is likely to be driven by the underlying wide-angle wind.

Of crucial importance is the identification of the driving source for this outflow. Marseille et al. (2008) elucidates about the star-forming region IRAS 18151-1208, where two detected bipolar outflows are shown to be powered by two mm sources, MM1 and MM2. They have also detected a third mm core, MM3 that does not show any outflow activity.

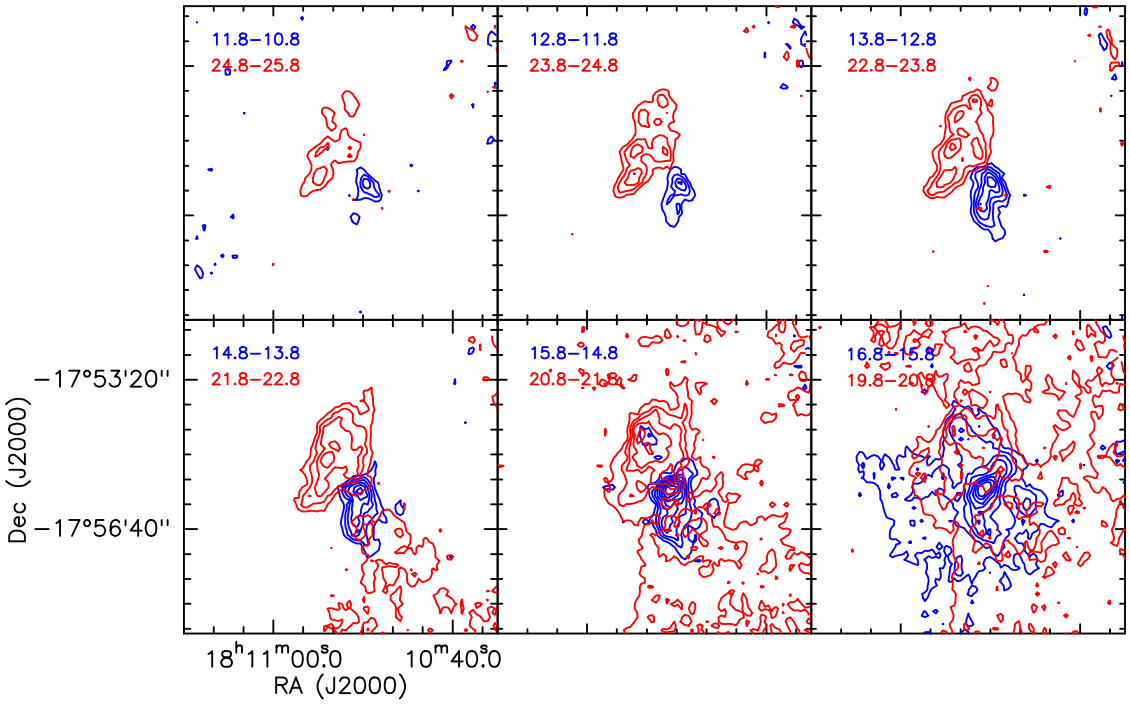

Figure 3.17: Channel maps of ^{12}CO $(3-2)$ line associated with molecular cloud harbouring G12.42+0.50. Each box contains a pair of maps corresponding to the red- and blueshifted emission at the same offset from the LSR velocity. The channel widths are indicated at the top left of each map. The red contours correspond to the red wing and the blue contours correspond to the blue wing. The contours start from the 3σ level of each map and increases in steps of 3σ.

Beuther et al. (2002c), in their statistical study of massive molecular outflows, state that a large fraction of their sample show bipolar outflow and these are seen to be associated with massive mm sources and in most cases, are centred on the mm peaks. As seen in Fig. 3.15, two mm cores (SMA1 and SMA2) are located towards the centroid of the bipolar outflow associated with G12.42+0.50. These are shown to be potential high-mass star-forming cores, Further, the absence of radio emission and IR sources imply a very early evolutionary phase. We further investigate whether SMA1 and/or SMA2 are the powering sources of the CO bipolar outflow in G12.42+0.50.

Following Qiu et al. (2009), the dynamical timescale of the outflow seen associated with G12.42+0.50 is computed using the expression, $T_{\rm dyn} = L_{\rm flow}/v_{\rm max}$, where $L_{\rm flow} \sim 1.2\,{\rm pc}$ is the half length of the end-to-end extension of the flow and $v_{\rm max} \sim 9.0\,{\rm km\,s^{-1}}$ is the maximum flow velocity from the LSR velocity of the cloud. This yields a dynamical timescale of the outflow that is 1.3×10^5 yr. Comparing with the results obtained by Qiu et al. (2009), Shepherd et al. (1998) and Shepherd, Testi & Stark (2003), our estimated value

is in agreement with massive molecular outflow from an UC H II region. This result supports our unfolding picture of radio component R1, where coexistence of an UC H II region and an ionized thermal jet is seen and the large-scale CO outflow can also be attributed to the UC H II region. However, it should also be kept in mind that unlike Qiu et al. (2009), there is no SMA core coinciding with R1. Moreover, their results are based on interferometric observations, whereas, the JCMT CO outflow data used here are from single-dish measurements. In these single-dish observations, the inner outflow jets are mostly unresolved and the measurements are less sensitive to high-velocity outflow emission resulting in an overestimation of the dynamical ages. Hence, one cannot rule out the possibility of SMA1 and/or SMA2 being the outflow driving sources similar to the case of AFGL 5142 (Liu et al., 2016b). If indeed the binary cores, SMA1 and SMA2 are the outflow driving cores, then the nature of the radio emission in R1 (and R2) can be thought of as ionized jet emission driven by the mm cores which also drives the large scale CO outflows detected. Possibility of multiple outflows from the mm cores and the UC H II region also exists (Beuther et al., 2002a; Beuther, Schilke & Stanke, 2003). This advocates for high-resolution observations for a better understanding.

3.6.3 Hub-filament system

From the above discussion we hypothesize a picture of global collapse of the molecular cloud harbouring the EGO, G12.42+0.50. Interestingly, Fig. 3.7(d) and (h), unfold the presence of large scale filamentary structures along the south-west direction of G12.42+0.50, all merging at the location of the clump, C1 enveloping G12.42+0.50. As mentioned earlier, the concurrence of a collapsing cloud with converging filaments suggest a hub-filament system. In literature, hub-filament systems are common in sites of high-mass star formation (e.g. Liu et al., 2016b; Peretto et al., 2013; Yuan et al., 2018). In such systems, converging flows are detected where matter funnels in through the filaments into the hub, where accretion is most pronounced. Morphologically, the molecular cloud system associated with G12.42+0.50 resembles the hub-filament system associated with the star-forming region, G22 (Yuan et al., 2018) and the IRDC, SDC335 ($\mathrm{SDC335.579-0.292}$) (Peretto et al., 2013). To delve deeper into this picture, we investigate the velocity structure of the filaments. To proceed, we construct the channel maps of the $^{12}\mathrm{CO}$ emission which are illustrated in Fig. 3.18. The velocity ranges are selected by examining the JCMT $^{12}\mathrm{CO}$ data cube and choosing the range where the $^{12}\mathrm{CO}$ emission is detected. The velocity width of each channel is chosen to be $0.5\,\mathrm{km\,s^{-1}}$ similar to that used by Leurini et al. (2019) to investigate the $\mathrm{C^{18}O}\,(2-1)$ emission associated with IRDC, G351.776-0.527. The

spatial coincidence of the ^{12}CO emission with the filaments is remarkable. The gas associated with the filaments is consistently redshifted with respect to the LSR velocity of the clump, C1. The velocity of the cloud along the filaments peak in the velocity range of $\sim 18 - 23\,\mathrm{km\,s^{-1}}$. The variation in velocity suggests bulk gas motion along the filaments. From the channel maps we can see that the velocity of the molecular gas along the filament decreases as it approaches the central core, with the maximum velocity at the south-west end of the filament. It has to be noted here that the $^{12}\mathrm{CO}\ (3-2)$ transition is also a tracer of molecular outflow and as shown in Section 3.6.2, G12.42+0.50 is also an outflow source. Hence, the decrease in velocity near the clump, C1 may be attributed to the interaction with the molecular outflow.

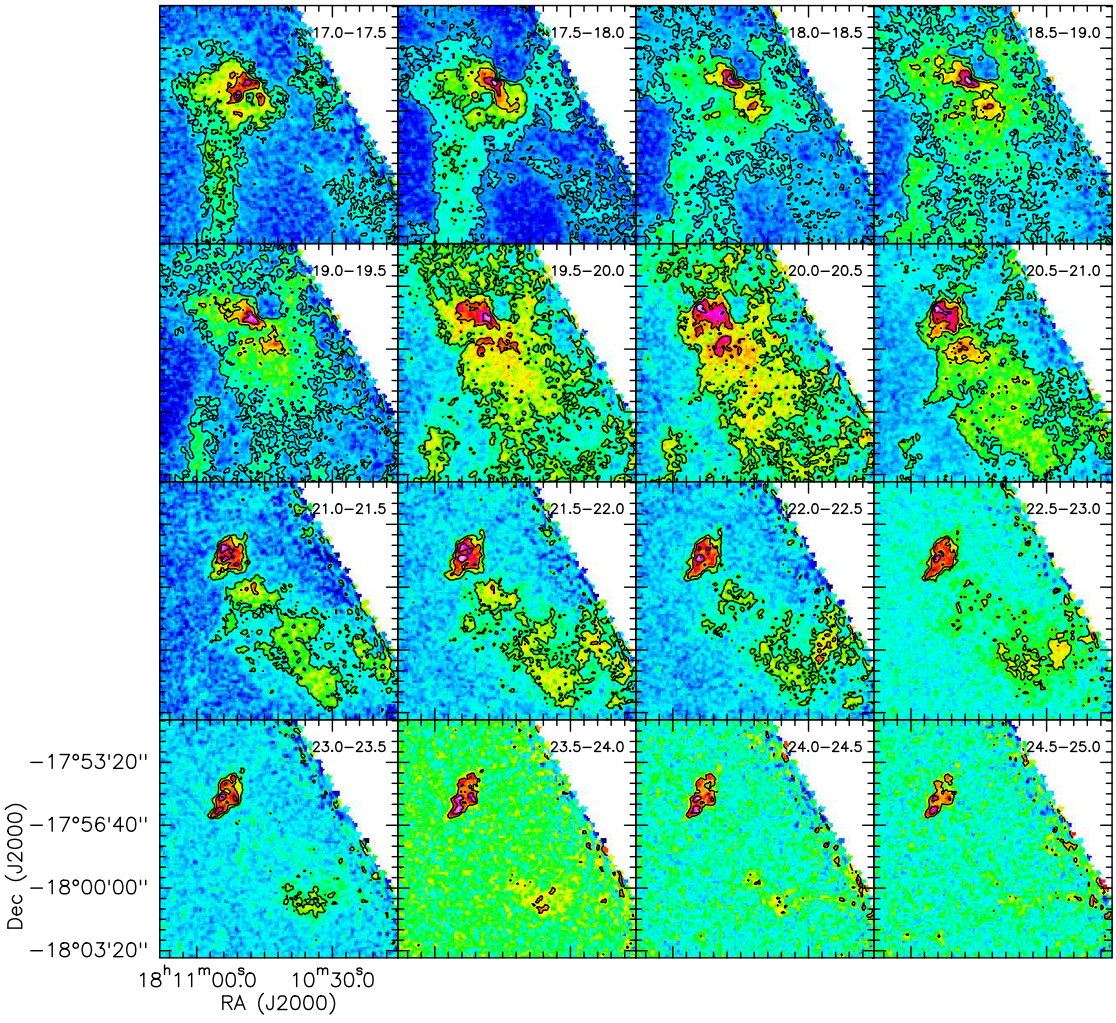

Figure 3.18: Channel maps of ^{12}CO emission is shown here with each channel having a velocity width of $0.5\,\mathrm{km\,s^{-1}}$. For each map, the black contours represent the ^{12}CO emission starting from the 3σ level and increasing with a step of 3σ.

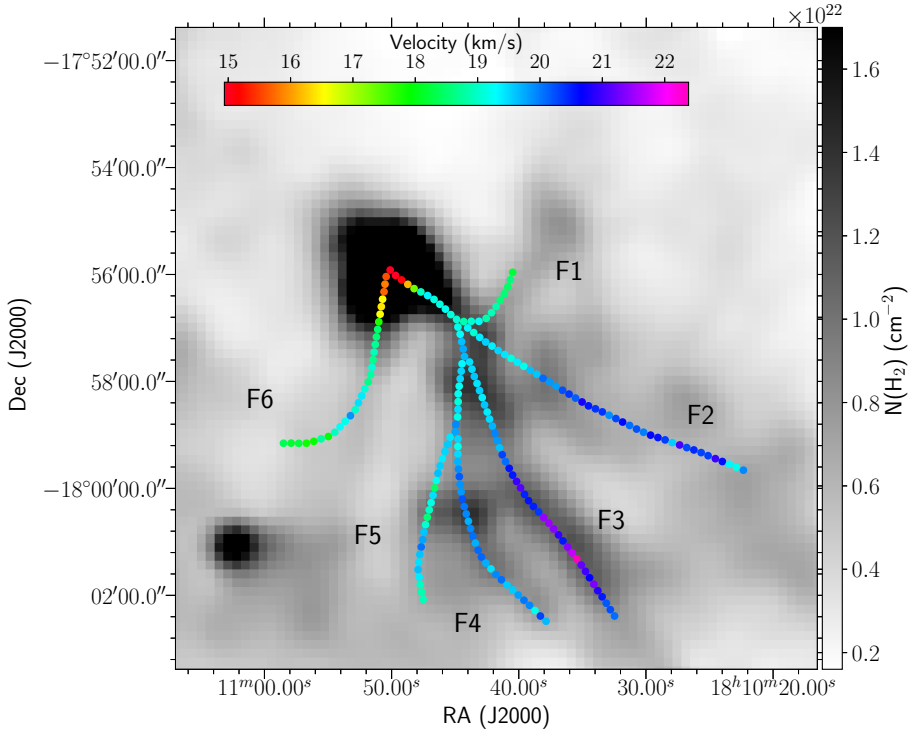

Figure 3.19: The velocity peaks of ^{12}CO $(3-2)$ extracted along the filaments is overlaid on the column density map of the region associated with G12.42+0.50 shown in grey scale. The positions of all the filaments are also labelled.

To further elaborate on the velocity structure, we extract the spectra of ^{12}CO $(3-2)$ along the filaments with a step size of half the angular resolution ($\sim 15''/2$) of the JCMT-HARP observation. The peak velocities estimated by fitting 1D Gaussian profiles to the spectra are shown in Fig. 3.19 as colour-coded circles overlaid on the H_2 column density map. Along the filaments, F1 and F6 it can be seen that the velocity is within the range $17-19\,\mathrm{km\,s^{-1}}$, closer to the LSR velocity, and increasing towards the clump, C1. However, along the filaments F2, F3, and F4 the velocity is on the higher side of the LSR velocity, ranging from $19-21\,\mathrm{km\,s^{-1}}$ and decreasing towards the central clump, C1. But in the case of filament, F5, we do not clearly notice any velocity gradient, and the values are seen to vary in the range $19-20\,\mathrm{km\,s^{-1}}$. Similar velocity gradients along filaments are detected in star-forming regions such as SDC335 (Peretto et al., 2013), G22 (Yuan et al., 2018) and AFGL 5142 (Liu et al., 2016b). Following these authors, we also attribute the velocity gradients to be due to gas inflow through filaments. A number of other mechanisms have also been proposed, which include filamentary collapse, filament collision, rotation, expansion and wind-acceleration to explain the observed velocity distributions (Peretto et al., 2014).

If the velocity distribution were to be explained by expansion scenario, we should have observed red-skewed velocity profiles of optically thick lines (HCO^+, HCN and HNC) towards the clump, C1 (Liu et al., 2018b). On the contrary, we observe blue-skewed velocity profiles, hence rendering the expansion picture to be unlikely. Further, we do not observe any cloud collision signature of enhanced line-widths at the junction (Yuan et al., 2018). The molecular outflow likely to be driven by the thermal jet in the clump, C1, cannot possibly explain the red-skewed velocity along the filaments, $F2 - F5$, since these fall along the blue lobe of the detected outflow. Also, in general, outflows are located between filaments (Liu et al., 2016b). Hence, on comparison with earlier studies and the lack of evidence to prove otherwise, we infer that the observed velocity gradient is a result of gas inflow along the filaments, although there could be contribution from the outflowing gas. Nonetheless, $^{12}CO\ (3-2)$ being an optically thick molecular line transition, cannot effectively probe the velocity distribution within the filaments. Thus, high resolution observations of optically thin lines would give a better picture. As discussed in Section 3.3.4, 11 eleven clumps, $C2 - C12$, lie along the identified filaments. It is also seen that along the filaments the dust temperature is lower than C1. The mass estimates show that these are less massive than the central core (clump, C1). Yuan et al. (2018), in the study of the hub-filament system associated with G22, finds two clumps more massive than the other clumps along the filament. These clumps, that dominate the emission at wavelengths longer than 24 μm are the most active star-forming regions in G22. This concurs well with G12.42+0.50, where the most massive clump, C1, is an active star-forming clump.

3.7 Summary

We carried out a comprehensive multiwavelength study towards the EGO, G12.42+0.50 and its associated environment. Our main results are summarized as follows

1. The radio continuum emission mapped at 1390 MHz reveals a linear structure extended in the north-east and south-west direction with the presence of two compact radio components, R1 and R2 that are unresolved at 610 MHz. The peak emission at 610 MHz is coincident with the component R1.

2. We explore different scenarios to explain the nature of the ionized emission. Under the UC H II framework, assuming the emission at 1390 MHz to be optically thin, the observed Lyman continuum flux translates to an ionizing source of spectral type of $B1 - B0.5$. An alternative picture of ionized thermal jet is examined, given vari-

ous observed characteristics including the spectral index values of $0.3 - 0.9$ in the region. We are prompted to consider the co-existence of the UC H II region with an ionized jet being powered by the same YSO. IRAS 18079-1756 (2MASS J18105109-1755496), a deeply embedded Class II YSO is likely to be the driving source.

3. Presence of shock-excited H_2 and [FeII] line emission is confirmed from NIR narrow-band imaging and spectroscopy in concurrence with the jets/outflows picture.

4. A massive central clump, C1 is identified from the 870 μm map which envelopes the detected radio and the enhanced and extended 4.5 μm emission. The clump has a mass $1375\,M_{\odot}$ and total luminosity $2.8 \times 10^4\,L_{\odot}$. Two-component modeling shows the presence of an inner warm component surrounded by an extended outer, cold envelope traced mostly by the FIR wavelengths.

5. Seven molecular species from the MALT90 survey are detected towards the EGO, G12.42+0.50. The optically thick lines, HCO^+ and HCN show signatures of protostellar infall. From the blue-skewed profile of the HCO^+ line, infall velocity and mass infall rate are estimated to be $1.8\,\mathrm{km\,s^{-1}}$ and $9.9 \times 10^{-3}\,M_{\odot}\,\mathrm{yr}^{-1}$.

6. From the line observations of the $J = 3-2$ transition of the molecular species ^{12}CO, ^{13}CO and $C^{18}O$, we detect the presence of a wide-angle bipolar outflow. From the dynamical age, $1.3 \times 10^5\,\mathrm{yr}$, of the bipolar outflow it seems likely that the UC H II region drives the same though the possibility of the SMA cores (SMA1 and SMA2) being the powering source(s) cannot be ruled out.

7. Signature of a hub-filament system is seen in the 8.0 μm and FIR images and is supported by the constructed column density and dust temperature maps. A detailed study of the gas kinematics agrees with bulk motion in the filaments and suggest a likely picture of gas inflow along the filaments to C1.

8. A conjectured hypothesis of the EGO, G12.42+0.50, satisfying the multiwavelength observations, could be an active star-forming complex where very early evolutionary cores (SMA1 and SMA2) are seen. Apart from this, an accreting (likely through filaments) MYSO in an initial phase of an UC H II region and driving a large-scale molecular outflow entrained by a likely ionized thermal jet is detected.

Chapter 4

Multiwavelength investigation of extended green object G19.88-0.53: Revealing a protocluster

In this chapter, we conduct a rigorous multiwavelength investigation of the region associated with the EGO, G19.88-0.53, which is catalogued as a “likely" outflow candidate associated with the infrared source, IRAS 18264-1152 (Cyganowski et al., 2008). The kinematic distance ambiguity to G19.88-0.53 has been resolved and it is placed at the near distance of 3.31 kpc (Ge et al., 2014; Roman-Duval et al., 2009). The bolometric luminosity of the Red MSX Source (RMS), G019.8817-00.5347, associated with IRAS 18264-1152 is estimated to be $7.8 \times 10^3\, L_{\odot}$ (Lumsden et al., 2013). This number has been recently refined to $4.7 \times 10^3\, L_{\odot}$ in the RMS survey website[1]. Class I and II methanol masers and $\mathrm{H_2O}$ maser are detected towards the region (Beuther et al., 2002d; Chen et al., 2011; Sridharan et al., 2002).

Fig. 4.1 displays the infrared (IR) morphology of G19.88-0.53. The colour composite images use the *Spitzer*-IRAC (Fazio et al., 2004) and the UKIDSS-Galactic Plane Survey (Lucas et al., 2008) bands. Both plots show extended emission in the east-west direction with the enhanced IRAC 4.5 $\mu\mathrm{m}$ emission elongated westwards beyond the UKIDSS K band nebulosity. The *Simbad* database also reveals the presence of an IRDC possibly associated with G19.88-0.53 and is marked in the figure.

[1] http://rms.leeds.ac.uk/cgi-bin/public/RMS_DATABASE.cgi

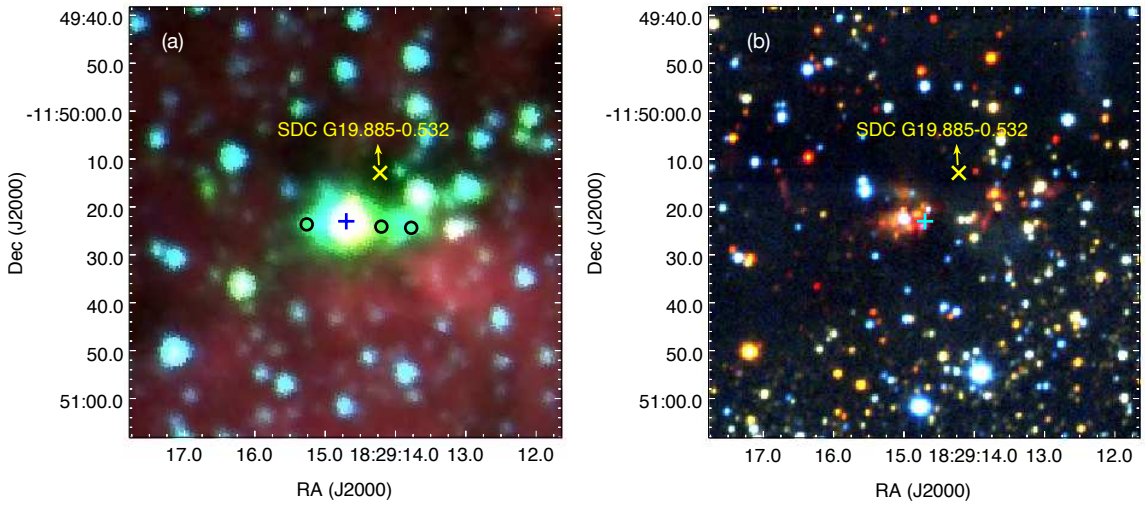

Figure 4.1: (a)IRAC colour composite image of the region around G19.88-0.53 where the 3.6, 4.5, and 8.0 μm bands are displayed in red, green, and blue, respectively. Location of the identified IRDC is shown with the '$\times$' symbol. The '$+$' marks the position of the MYSO located at 4.5 μm emission peak and the black circles are the positions of the EGO knots discussed by De Buizer & Vacca (2010). (b)UKIDSS colour composite image of the same region. Here, *J* (1.25 μm), *H* (1.63 μm) and *K* (2.20 μm) band data are shown in red, green, and blue, respectively.

4.1 Low-frequency radio emission

Using the uGMRT, we probe the low-frequency domain of the ionized emission associated with G19.88-0.53. In Band 4, none of the sub-band images have detection above the 3σ level, while faint, elongated emission is seen in the Band 5 maps. Two sub-band images at 651.4 and 1391.6 MHz are shown in Fig. 4.2(a) and (b), respectively. The 1391.6 MHz map clearly reveals the presence of an elongated, two-component emission feature in the east-west direction. The two distinct and compact radio components are labelled R1 and R2. The deep uGMRT maps in Band 5 with a *rms* level of $\sim$ 45 μJy beam^{-1} enables the detection of the weak ionized emission. For comparison, in Fig. 4.2(c), the 20 cm (1.4 GHz) VLA map (*rms* of 0.3 mJy beam^{-1}) retrieved from the MAGPIS[2] archive is displayed, where no emission is detected. The contours of the 4.5 μm emission plotted show that the radio emission is confined to the central part of the EGO.

The radio emission associated with G19.88-0.53 has been studied by Zapata et al. (2006), Rosero et al. (2016), and Rosero et al. (2019) using VLA. Based on observations at 3.6 cm (8.5 GHz), 1.3 cm (22.5 GHz) and 7 mm (43.3 GHz), Zapata et al. (2006) classify this

[2]https://third.ucllnl.org/gps/

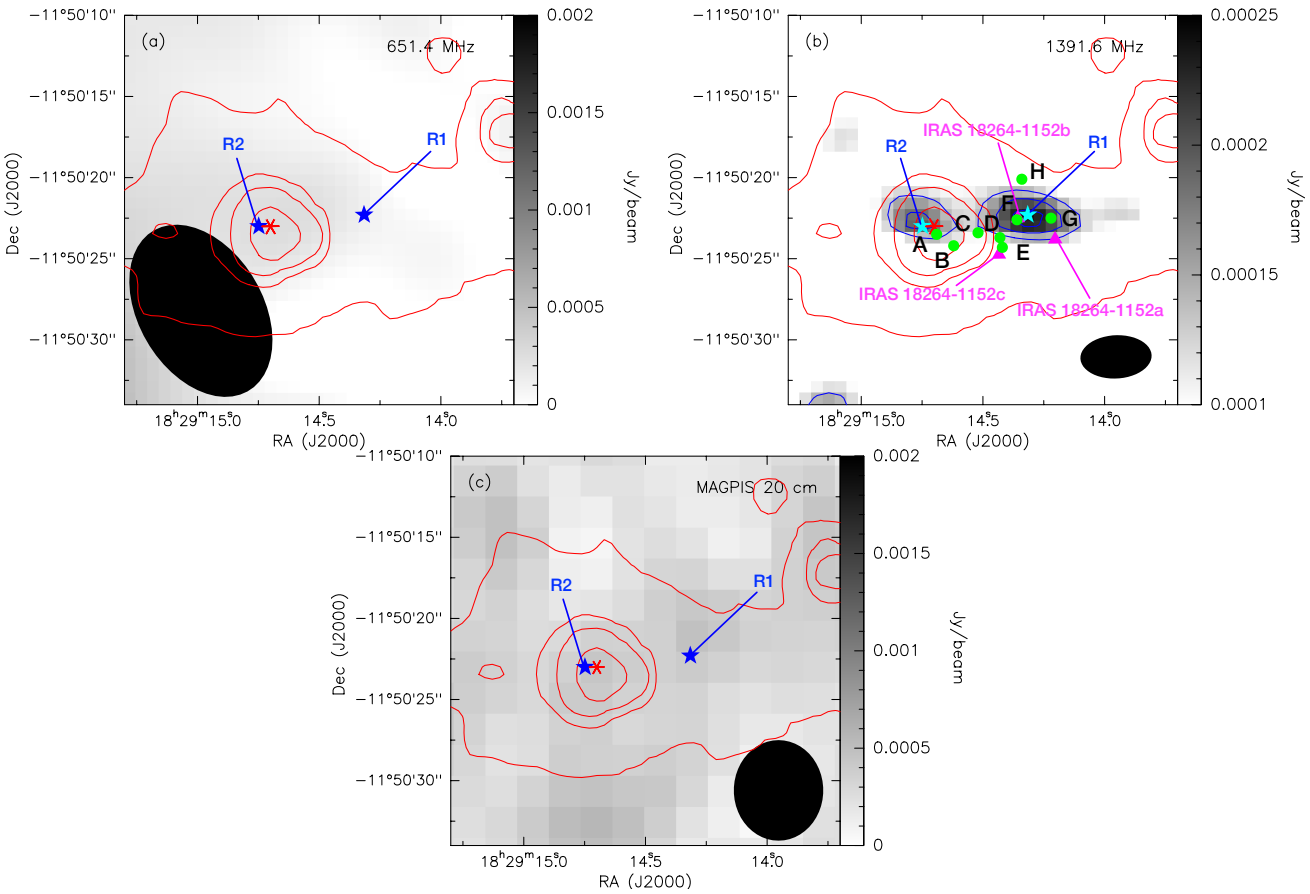

Figure 4.2: (a) The grey scale in this image corresponds to the 651.4 MHz map in the band $550 - 850$ MHz (Band 5). It has a beam size of $11.5'' \times 7.6''$. (b) The grey scale here shows the radio continuum map of G19.88-0.53 at the frequency 1391.6 MHz in the band $1050 - 1450$ MHz (Band 5) with the contour levels 3, 4, 5, and 6σ ($\sigma = 45\,\mu\mathrm{Jy\,beam^{-1}}$. This map has a beam size of $4.3'' \times 2.7''$. Radio sources $\mathrm{A} - \mathrm{H}$, identified by Rosero et al. (2016), are marked by filled circles and the three radio components IRAS 18264-1152a, IRAS 18264-1152b and IRAS 18264-1152c, identified by Zapata et al. (2006), are indicated by filled triangles. (c) The grey scale represents the MAGPIS map at 20 cm that has a beam size of $6.2'' \times 5.4''$. Contours of the 4.5 μm emission are overlaid in red on all the maps, with the contour levels 3, 9, 30 and 120σ ($\sigma = 5.0\,\mathrm{MJy\,sr^{-1}}$). The positions of the two radio components, R1 and R2 are marked by '$\star$'s, and the position of the MYSO (De Buizer & Vacca, 2010) associated with G19.88-0.53 is indicated with '$*$' in all the maps. The beams of all the images are represented in black ellipses.

Table 4.1: Physical parameters of radio components R1 and R2 associated with G19.88-0.53.

Component	Peak position		Peak flux density
	RA (J2000)	Dec (J2000)	($\mathrm{mJy\,beam^{-1}}$)
R1	18 29 14.3	-11 50 22.3	0.25±0.01
R2	18 29 14.7	-11 50 23.0	0.20±0.01

source as a 'triple stellar system' and identify three radio components (IRAS 18264-1152a, b, and c), the positions of which are shown in Fig. 4.2. In the recent paper, Rosero et al. (2016) present high-sensitivity, subarcsecond resolution observations at 6 cm (4.9 and 7.4 GHz) and 1.3 cm (20.9 and 25.5 GHz), where twelve compact radio sources are detected towards G19.88-0.53. Eight among them, sources $\mathrm{A-H}$, lie within the 3σ level of the 4.5 μm emission and are marked Fig. 4.2. The component R1 is co-spatial (within $\sim 1''$) with the radio sources, F and IRAS 18264-1152b. Component R2 has similar positional match with the radio source, A. The position of the MYSO located at the 4.5 μm emission peak (De Buizer & Vacca, 2010) also agrees well with the coordinates of R2. However, this component is not detected in the VLA maps presented by Zapata et al. (2006).
The position of the components and the peak flux densities are listed in Table 4.1. Component R1 is barely resolved and component R2 is unresolved in the uGMRT maps. It is thus difficult to get a reliable estimate of the integrated flux density for these unresolved sources with weak emission (Rosero et al., 2016; Urquhart et al., 2009). Hence, in the estimation of the spectral index we use the peak flux density. Following the discussion in Urquhart et al. (2009), the upper limits to the deconvolved sizes of R1 and R2 are taken to be half the FWHM of the restored beam size. This gives a value of $2.1'' \times 1.3''$ for the components.

4.2 Near-infrared line emission

As propounded by several authors (Caratti o Garatti et al., 2015, and references therein), shock-excited lines of H_2 and [FeII] and broad bandheads of CO are the spectral carriers responsible for the enhanced 4.5 μm emission of EGOs. Of the few spectroscopic studies of EGOs (e.g. Caratti o Garatti et al., 2015; De Buizer & Vacca, 2010; Issac et al., 2019; Onaka et al., 2016), De Buizer & Vacca (2010) focussed on MIR spectroscopy of two EGOs including G19.88-0.53 using the NIRI instrument on the Gemini North telescope. The spectra extracted towards the three associated knots of G19.88-0.53 show the presence

of the shock-excited $0-0$ S(9) line of H_2 at 4.695 μm. Moreover no continuum emission was detected towards these knots. In our study, we investigate the NIR regime to identify shock indicators and confirm the association of G19.88-0.53 with protostellar outflows.

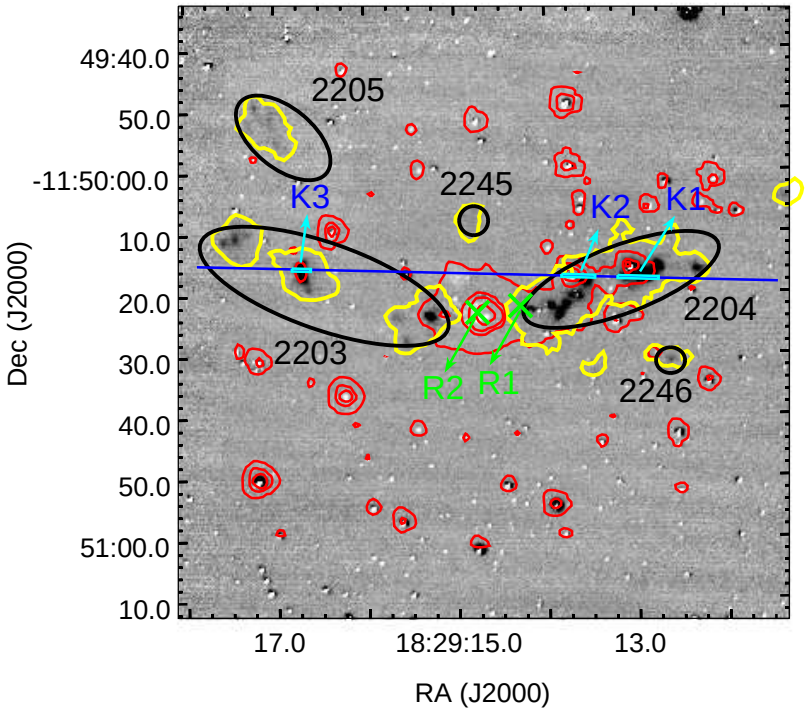

Figure 4.3: Continuum subtracted H_2 image of G19.88-0.53 from Varricatt et al. (2010). The positions of the identified radio components, R1 and R2 are marked by '$\times$'s. The contours of the 4.5 μm emission are given in red with the contour levels same as Fig. 4.2. The blue line indicates the orientation of the slit and the cyan rectangles are the apertures over which the spectra are extracted. The MHOs (2203-2205,2245,2246) identified by Varricatt et al. (2010), Lee et al. (2012), and Ioannidis & Froebrich (2012) are highlighted in the black ellipses. The yellow contours trace the location and extent of the H_2 knots identified by Froebrich et al. (2011).

The H_2 line image towards G19.88-0.53, presented in Varricatt et al. (2010) reveals the presence of a bipolar outflow in the east-west direction which is consistent with CO outflow detected by Beuther et al. (2002c). Same results were obtained by Lee et al. (2012) using the UWISH2 survey and they enlist G19.88-0.53 as an EGO with a large-scale (angular scale of $\sim 1.6'$) bipolar outflow. In Fig. 4.3 we display the continuum-subtracted H_2 line image from Varricatt et al. (2010) where the orientation of the slit position for UIST observations is marked. The identified apertures, K1, K2, and K3, over which the spectra

are extracted are also highlighted in the figure. Molecular hydrogen objects (MHOs) from the catalogue of molecular hydrogen emission-line objects[3] (Davis et al., 2010) are also indicated. MHO 2245 and MHO 2246 are new additions to the catalogue by Lee et al. (2012) and Ioannidis & Froebrich (2012), respectively. Identified locations and extent of H_2 knots from Froebrich et al. (2011) are also shown in the figure. Apertures K1 and K2 probe the knots in MHO 2204 and K3 samples the central knot in MHO 2203. The extracted spectra are shown in Fig. 4.4 where we see strong detections of several H_2 lines. The lines detected and their corresponding wavelengths are listed in Table 4.2.

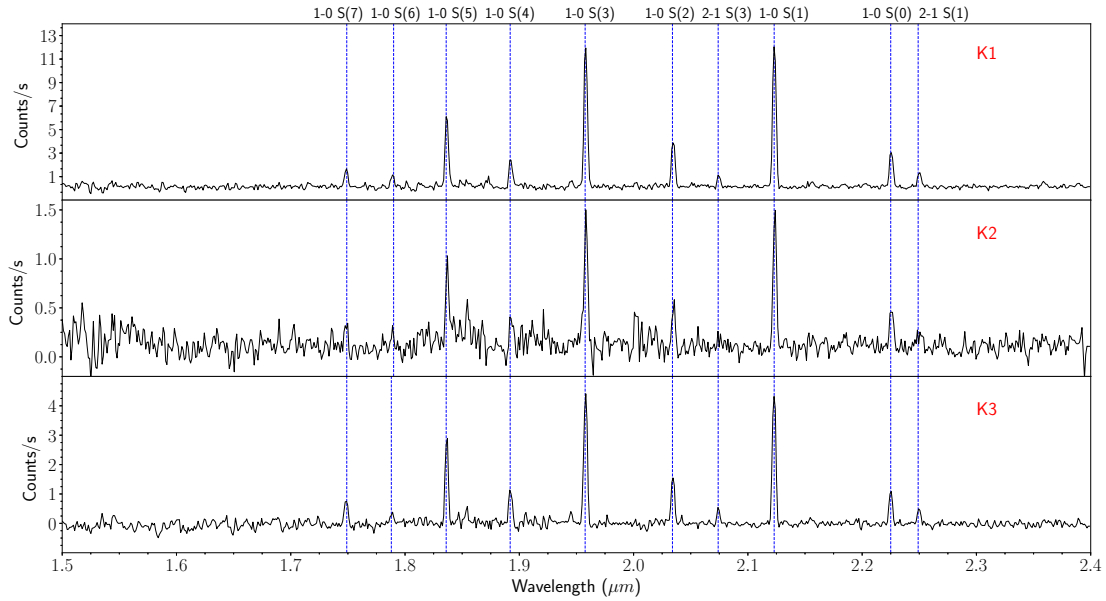

Figure 4.4: The *HK* spectrum of G19.88-0.53 extracted over the apertures K1, K2 and K3 covering three H_2 knots (refer Fig. 4.3). The spectral lines identified along all the three apertures are marked over the spectra and the details of these lines are given in Table 4.2.

The H_2 lines detected in the spectra could have either a thermal or a non-thermal origin. Jets and outflows that are heated to typically few 1000 K can give rise to thermal emission from shock fronts. Whereas, non-thermal emission is ascribed to fluorescence produced by non-ionizing UV photons. Shock excited emission arises from low levels of excitation, whereas UV fluorescence populates both high and low-v states (Caratti o Garatti et al., 2015; Davis et al., 2003). Our spectra do not show the presence of transitions with $v \geq 6$. In addition, the ratio of $1-0\,\mathrm{S}(1)/2-1\,\mathrm{S}(1)$ is estimated to be $\sim 8:1$. These suggest the origin of the detected H_2 lines to be due to thermal excitation. However, the absence of relevant fluorescent H_2 emission in G19.88-0.53 can also be attributed to high extinction

[3]http://cdsweb.u-strasbg.fr/cgi-bin/qcat?J/A+A/511/A24

Table 4.2: Lines detected in the spectra extracted along the apertures K1, K2 and K3 towards G19.88-0.53.

Line	Wavelength (μm)
H_2 $1-0$ S(7)	1.7480
H_2 $1-0$ S(6)	1.7880
H_2 $1-0$ S(5)	1.8358
H_2 $1-0$ S(4)	1.8920
H_2 $1-0$ S(3)	1.9576
H_2 $1-0$ S(2)	2.0338
H_2 $2-1$ S(3)	2.0735
H_2 $1-0$ S(1)	2.1218
H_2 $1-0$ S(0)	2.2235
H_2 $2-1$ S(1)	2.2477

that screens the UV photons emanating from the central star. Nonetheless, morphological resemblance of the extended H_2 emission knots to a bipolar jet and the association with an outflow source supports the shock excitation scenario. The shock-excited origin of the detected H_2 lines confirms that the transitions of this molecule within the IRAC 4.5 μm band are among the spectral carriers responsible for the enhanced 'green' emission that classifies G19.88-0.53 as an EGO.

4.3 Emission from dust

IRAC bands trace the thermal emission associated with the warm dust component and emission from the polycyclic aromatic hydrocarbons excited by the UV photons in the photodissociation regions. However, emission from the stellar photosphere dominates the shorter wavelength bands (3.6 and 4.5 um) (Watson et al., 2008). In addition to this, the 4.5 μm band includes emission from shock-excited H_2 lines and CO ($v= 1-0$) band at 4.6 μm with contribution from the Brα and Pfβ lines. The spatial distribution of dust emission towards G19.88-0.53 is shown in Fig. 4.5(a), which is a colour composite image generated using the IRAC 8.0, 4.5, and 3.6 μm bands. The APEX+Planck 870 μm contours are overlaid along with the contours of the 4.5 μm emission. A clump is clearly identified at 870 μm. Warm dust sampled at 8.0 μm is seen to be extended towards the south and west of the clump and, at 870 μm, a clearly discernible large-scale filamentary structure is visible with the clump located within it.

4.3.1 Dust clump

From the APEX+Planck 870 μm map, a clump is identified using the two-dimensional *Clumpfind* procedure (Williams, de Geus & Blitz, 1994) with a 3σ ($\sigma = 0.3\,\mathrm{Jy\,beam^{-1}}$) threshold and optimum contour levels. The aperture of this clump coincides with the 3σ level contour of the 870 μm emission. To investigate the nature of the cold dust associated with the identified clump, we assume the FIR emission to be optically thin and model the same with a modified single-temperature blackbody following the formalism discussed in detail in Section 3.3.3. The SED and the best fit modified blackbody are shown in Fig. 4.6. The model derived dust temperature and line-of-sight column density values are 18.6$\pm$1.2 K and $5.3 \pm 1.0 \times 10^{22}\,\mathrm{cm^{-2}}$, respectively. The mass of the clump is estimated to be $1911\,M_{\odot}$. This is in good agreement with the estimate of $\sim 2100\,M_{\odot}$ derived by Beuther et al. (2002b, 2005) from the 1.2 mm emission. Both these values derived from dust emission are lower by a factor of ~ 2 in comparison with the value of $3900\,M_{\odot}$ obtained from the $H^{13}CO^{+}$ line emission (Qiu et al., 2007). The discrepancy could be due to the fact that the $H^{13}CO^{+}$ line traces the lower density gas and could even be slightly optically thick as opposed to the optically thin assumption we have employed while estimating the clump mass. Moreover, the $H^{13}CO^{+}$ is likely to be affected by outflows and shocks associated with the clump. The derived clump parameters are listed in Table 4.3.

Table 4.3: Physical parameters derived for the clump identified to be associated with G19.88-0.53. The peak position of the 870 μm emission, radius, mean temperature and column density, mass, and volume number density of the clump are listed.

Peak position		Radius	Mean T_d	Mean $N(H_2)$	Mass	$n(H_2)$
RA (J2000)	Dec (J2000)	(pc)	(K)	($10^{22}\,\mathrm{cm^{-2}}$)	($M_{\odot}$)	($10^{3}\,\mathrm{cm^{-3}}$)
18 29 14.14	-11 50 28.57	0.7	18.6$\pm$1.2	5.3$\pm$1.0	1911	18.0

The line-of-sight average H_2 column density and dust temperature maps of G19.88-0.53 are generated by a pixel-by-pixel modified single-temperature blackbody model fitting under an optically thin assumption, similar to G12.42+0.50, following the method discussed in Section 3.3.3. *Herschel* FIR maps covering the wavelength range of $160 - 500\,\mu$m and the combined APEX+Planck map at 870 μm, convolved and regridded a common resolution and pixel size of 36 and 14$''$, respectively, are used for the pixel-by-pixel modified blackbody modelling. We estimate the background flux, I_{bg} at each band, which includes the emission from the cosmic microwave background and the diffuse Galactic emission,

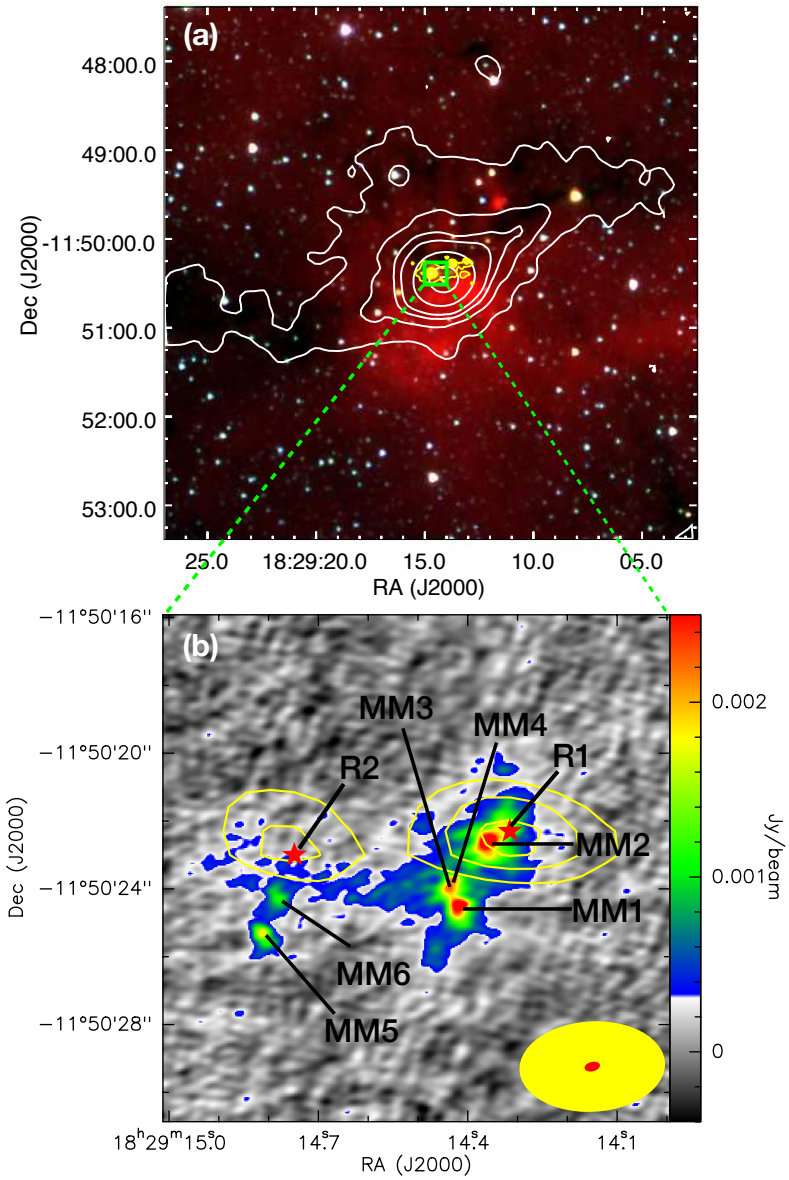

Figure 4.5: (a) Colour composite image of the region associated with G19.88-0.53, using IRAC 3.6 μm (blue), 4.5 μm (green) and 8.0 μm (red) bands. The white contours depict the APEX+Planck 870 μm emission with levels 2, 3, 4, 5, 9, 20, and 26σ ($\sigma = 0.3$ Jy beam^{-1}). The yellow contours represent the 4.5 μm emission with the contour levels same as in Fig. 4.2. (b) The high resolution 2.7 mm ALMA map towards G19.88-0.53 is depicted in the colour scale. The positions of the two radio components and the six mm peaks identified are marked on the map. The yellow contours represent emission at 7 mm from Zapata et al. (2006) with contour levels at 4, 8, 18, 22, and 26σ ($\sigma = 53.8\,\mu$Jy beam^{-1}). The filled black triangles are the positions of the radio peaks identified by these authors. The beams of the 2.7 and 7 mm maps are shown as filled red and yellow ellipses, respectively, towards the bottom right of the image.

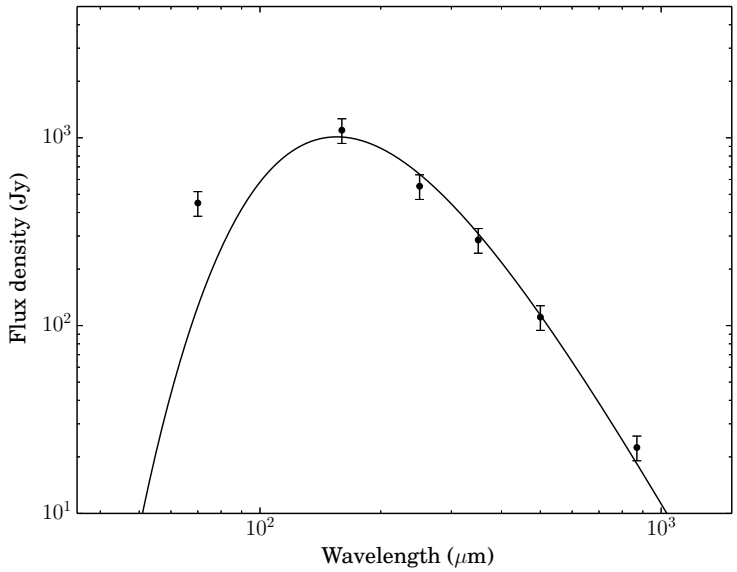

Figure 4.6: Spectral energy distribution of the APEX+Planck clump associated with G19.88-0.53 in the wavelength range 70 to 870 μm. The integrated flux density within the clump, represented by black circles is plotted in log-scale with a 15% error bar. The best-fit modified blackbody model is represented by the solid curve. The data point corresponding to 70 μm is excluded in the SED fitting.

from relatively uniform and dark region devoid of bright, diffuse or filamentary emission at a distance of $\sim 0.5^{\circ}$ from G19.88-0.53. The hence generated temperature and column density maps are displayed in Fig. 4.7 together with the reduced χ^2 map.The fitting uncertainties are small as is clear from the reduced χ^2 map, with the highest value of ~ 4. The *Clumpfind* retrieved aperture of the cold dust clump is overlaid on the dust temperature and H_2 column density maps in Fig. 4.7. From the H_2 column density map, we can see an enhanced density region over the clump aperture. A high temperature region is also seen in the dust temperature map within the clump having a peak temperature of 20.2 K.

4.3.2 Millimeter cores

The high-resolution ALMA 2.7 mm dust continuum map displayed in Fig. 4.5(b) shows the presence of six dense, compact dust cores labelled $\mathrm{MM1-MM6}$. Contours of the 7 mm VLA map from the study by Zapata et al. (2006) is overlaid on the image. The 7 mm emission is more extended, especially in the east-west direction. In an earlier study, Qiu et al. (2007) have mapped IRAS 18264-1152 at 1.3 and 3.4 mm with Plateau de Bure Interferometer. They identify two peaks at both the wavelengths. Their western peak seems to be in the vicinity of cores, $\mathrm{MM1-MM4}$ and the eastern component likely associated

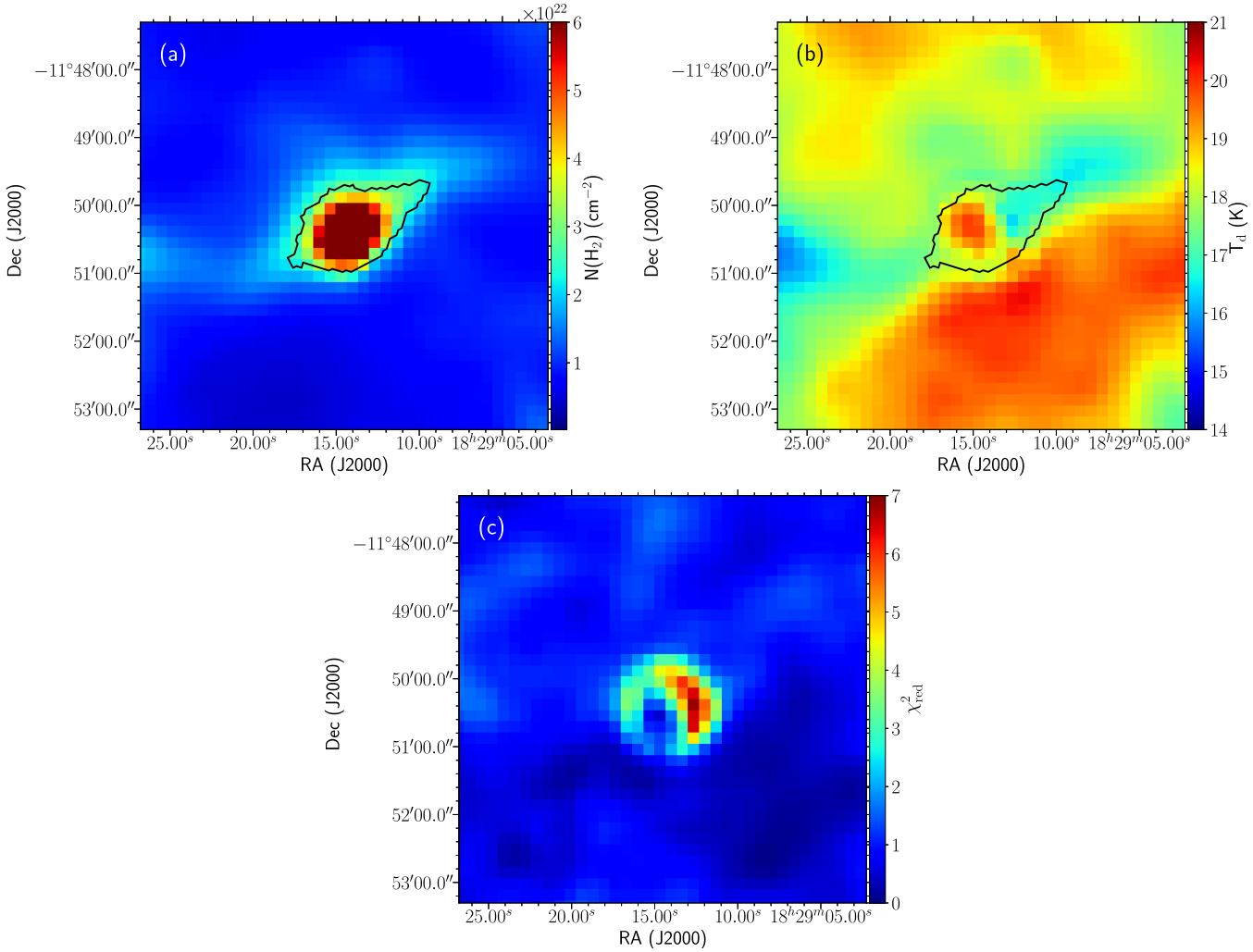

Figure 4.7: (a) Column density, (b) Temperature and (c) Reduced χ^2 maps towards G19.88-0.53 generated using the *Herschel* FIR data and the APEX+Planck data. The aperture of the *Clumpfind* identified clump is overlaid on the column density and temperature maps.

with cores, MM5 and MM6. Parameters of the identified mm cores are listed in Table 4.4. The deconvolved sizes of the cores are estimated by fitting 2D Gaussians to each component using the 2D fitting tool of CASA viewer. MM3 and MM4 are unresolved in the map, hence the quoted size, integrated and peak flux density refer to the combined region covering both the cores.

Table 4.4: Physical parameters of the 2.7 mm cores associated with G19.88-0.53.

Core	Peak position		Deconvolved size	Integrated flux density	Peak flux density	$V_{\rm LSR}$	ΔV
	RA (J2000)	Dec (J2000)	($''\times''$)	(mJy)	(mJy beam^{-1})	(km s^{-1})	(km s^{-1})
MM1	18 29 14.4	-11 50 24.5	0.65×0.44	10.7	3.4	44.2	6.0
MM2	18 29 14.4	-11 50 22.6	1.49×0.94	30.9	3.5	45.3	5.7
MM3	18 29 14.4	-11 50 24.0	0.98×0.50	11.9*	2.3*	43.3*	4.5*
MM4	18 29 14.4	-11 50 23.7	0.98×0.50	11.9*	2.3*	43.3*	4.5*
MM5	18 29 14.8	-11 50 25.3	0.74×0.26	5.4	1.9	43.3	2.3
MM6	18 29 14.8	-11 50 24.3	0.62×0.46	3.9	1.1	42.3	1.6

* MM3 and MM4 are unresolved in the map, hence the quoted deconvolved size, integrated, peak flux density, LSR velocity, and velocity width refer to the combined region covering both the cores.

4.4 Molecular line emission

Molecular line observations are tools for understanding the kinematics and chemical environment of a molecular cloud and and its stage in the evolutionary sequence. In this work, we use archival data from ALMA to study the emission from molecular lines in the region associated with G19.88-0.53.

4.4.1 CH_3OH line emission

A forest of $\rm CH_3OH$ lines are detected towards the mm cores in ALMA Band 7 $(275 - 373\,\rm GHz)$ within a frequency interval of 3 GHz $(337.1 - 340.1\,\rm GHz)$. This is expected as the $\rm CH_3OH$ molecule is believed to be present in massive star forming regions from the very early stages (Wirström et al., 2011). For identification of the lines, the data cube is corrected for the LSR velocity of $43.6\,\rm km\,s^{-1}$ (Beuther et al., 2002b; Qiu et al., 2007). Subsequently, the detected lines are identified by comparing with the rest frequencies reported in the molecular databases, NIST[4] (Lovas, 2004), CDMS[5] (Müller et al., 2005), and JPL[6] (Pickett et al., 1998). The CDMS and JPL databases are interactively loaded on the

[4]http://physics.nist.gov/cgi-bin/micro/table5/start.pl
[5]https://cdms.astro.uni-koeln.de/cdms/portal
[6]https://spec.jpl.nasa.gov

spectra employing the Weeds extension of CLASS90. The extracted spectra towards the mm cores are plotted in Fig. 4.8 displaying the identified set of $A-$ and $E-CH_3OH$ lines corresponding to the $J = 7-6$ transition. It should be noted here that for cores MM3 and MM4, the separation is less than the beam size, hence the combined spectrum is plotted in the figure. CH_3OH lines are seen to be much stronger towards MM1 and MM2 as compared to the other cores. The accurate identification of the detected lines enables us to determine the LSR velocities of the individual cores which are listed in Table 4.4.

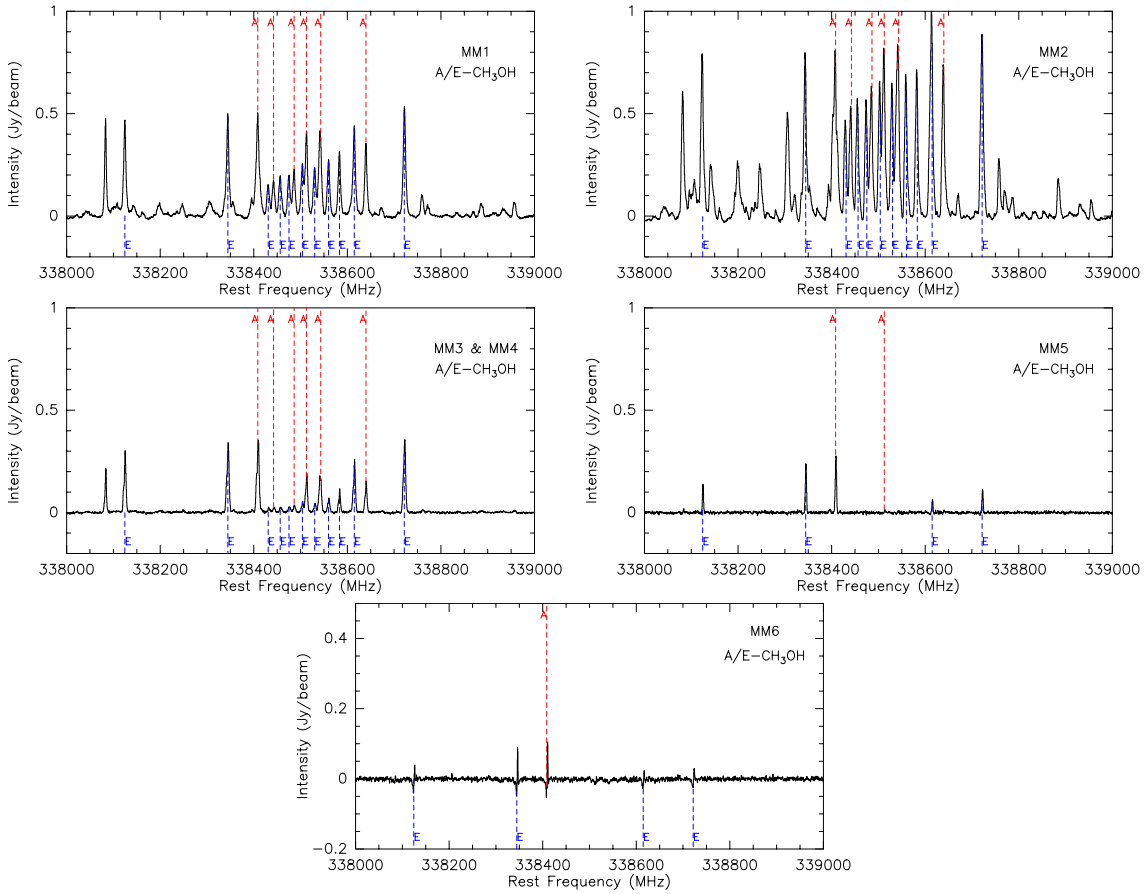

Figure 4.8: Spectra of the $A/E-CH_3OH$ lines detected towards the mm cores associated with G19.88-0.53 extracted from the high-resolution Band 7 spectral cube. The dashed red and blue lines indicate the peak positions of the $A-CH_3OH$ and $E-CH_3OH$ lines, respectively.

4.4.2 Emission in isotopologues of CO

In the ALMA Band 3 $(84-116\,\mathrm{GHz})$ and Band 7 $(275-373\,\mathrm{GHz})$, we detect three CO transitions, $^{13}CO\,(1-0)$, $C^{18}O\,(1-0)$ and $C^{17}O\,(3-2)$, with rest frequencies 110.2013543,

109.7821734, and 337.7061123 GHz, respectively. The rotational transition lines of the isotopologues of CO are well known tracers of both outflow and inflow motion (Beuther et al., 2002c; Kutner & Tucker, 1975; Wu et al., 2009; Zhang et al., 2001). Transitions from different energy levels probe the kinematic structure of different parts of the molecular clouds. Since transitions from higher rotational levels of CO molecules have a higher critical density, their emission arises from high density regions like the dense cores. On the other hand, emission lines corresponding to lower J transitions trace the kinematics of the low density regions of the molecular cloud (Rygl et al., 2013).

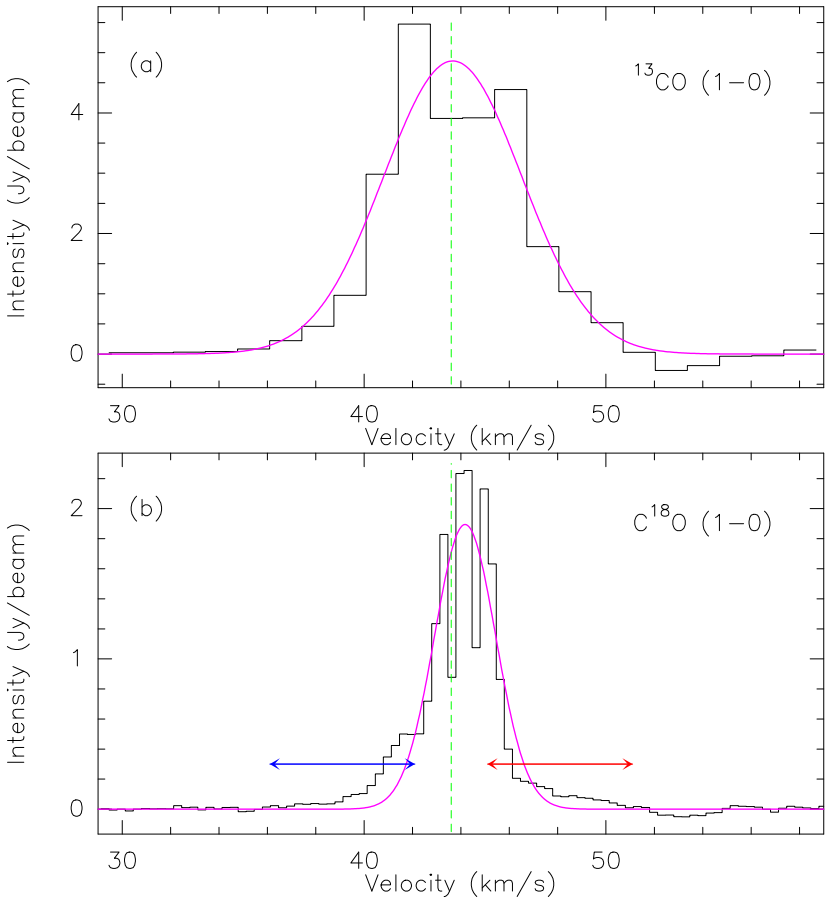

Figure 4.9: Low-resolution spectra of the (a) $^{13}\mathrm{CO}\,(1-0)$ and (b) $\mathrm{C}^{18}\mathrm{O}\,(1-0)$ lines towards G19.88-0.53. The area over which the spectra are extracted covers all the cores. The vertical green line denotes the LSR velocity, $43.6\,\mathrm{km\,s^{-1}}$. The red and blue arrows in (b) spans the range over which the integrated intensity map is constructed to trace the outflow wings (discussed in Section 4.7.2).

Low-resolution spectra probing the $^{13}\mathrm{CO}\,(1-0)$ and $\mathrm{C}^{18}\mathrm{O}\,(1-0)$ molecular line emission is plotted in Fig. 4.9. The beam covers all the cores. Single Gaussians are used to fit these spectra. The $^{13}\mathrm{CO}\,(1-0)$ line peaks at the LSR velocity of the dust clump. Multiple

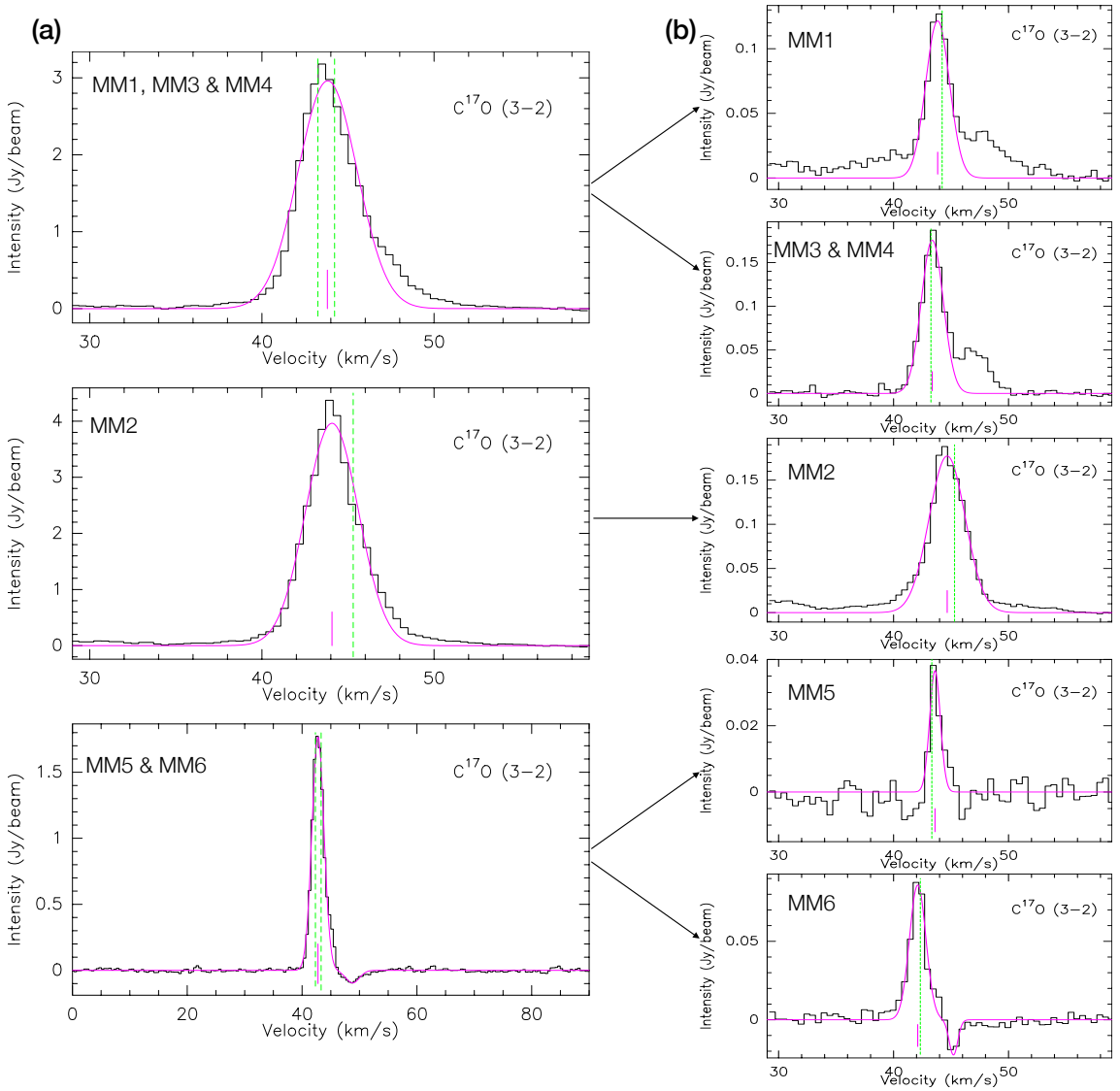

Figure 4.10: The $J = 3 - 2$ transition of $C^{17}O$ towards the mm cores associated with G19.88-0.53 from the (a) low-resolution ($5.2'' \times 2.6''$) data averaged over the beam and (b) high resolution ($0.67'' \times 0.47''$) data averaged over a region covering each core. The magenta curve represents the best fit to each spectrum. Double Gaussians are used to fit the spectra towards MM5 and MM6 (low-resolution) and MM6 (high-resolution). The dashed green line denotes the LSR velocity of each core. The magenta lines in the spectra mark the emission peaks.

peaks noticeable in $C^{18}O\,(1-0)$ spectrum are the combined effect of the cores and the peak velocities are consistent with the LSR velocities derived for the cores. In case of the $C^{17}O\,(3-2)$ line, spectra from the lower resolution Band 7 data cube are extracted over the beam area covering three regions (1) MM1, MM3, and MM4 (2) MM2, and (3)

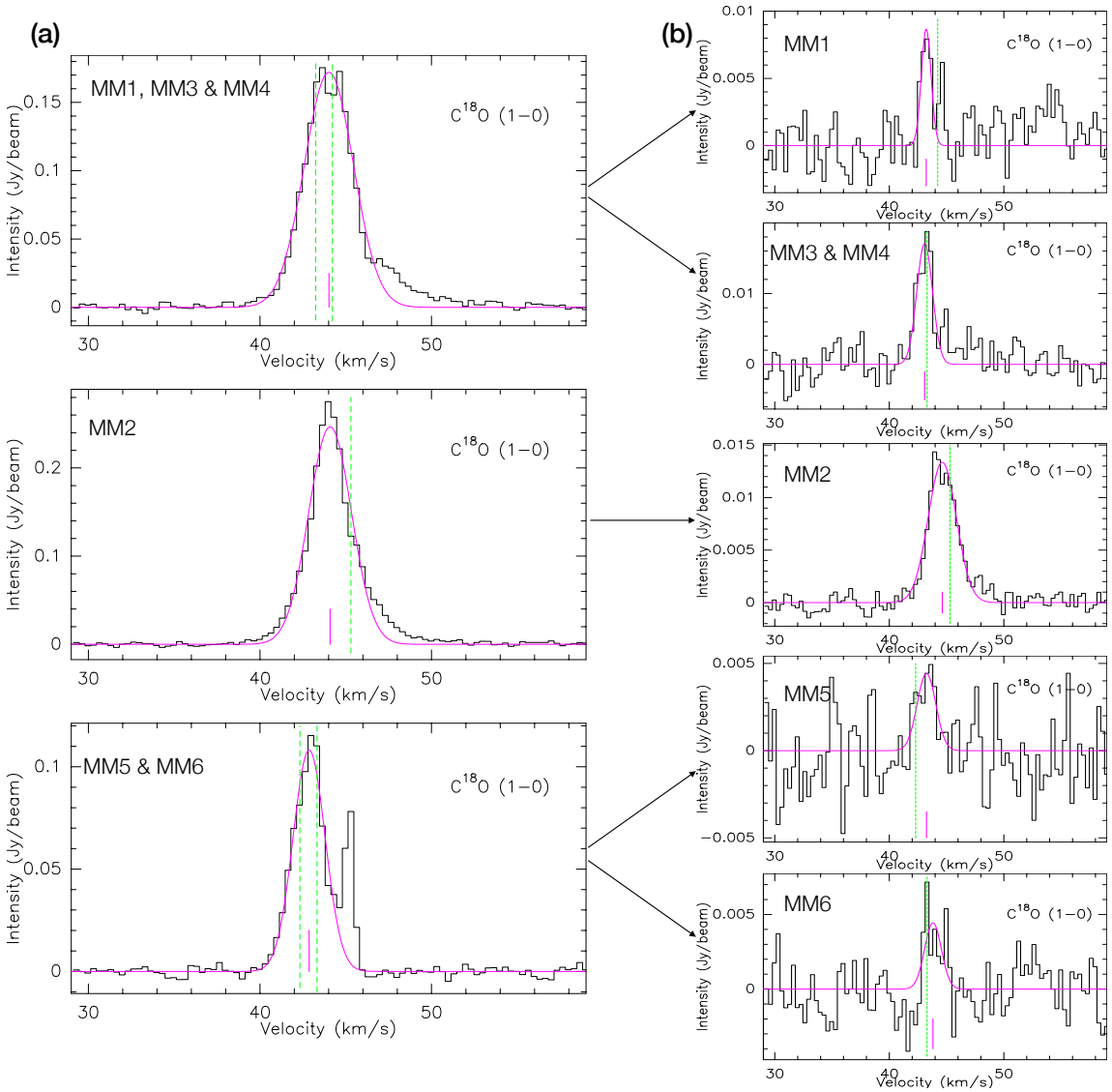

Figure 4.11: Same as Fig. 4.10 for the $C^{18}O\,(1-0)$ transition detected towards the mm cores associated with G19.88-0.53 from the (a) medium-resolution ($2.6'' \times 2.2''$) data extracted over the same region as in Fig. 4.10(a) and (b) high-resolution ($0.46'' \times 0.28''$) data averaged over a region covering each core.

MM5 and MM6 and shown in Fig. 4.10(a). Region (1), covering MM1, MM3, and MM4, shows a clear red wing. However, for region (2), probing MM2, the wing is not very prominent. In case of region (3), an inverse P-Cygni profile is seen. A double Gaussian is used to fit this profile. Fig. 4.10(b) shows the high-resolution spectra of this line. As discussed earlier, since the separation between MM3 and MM4 is less than the beam size, the spectrum is extracted over a region covering both cores. Given the signal-to-noise ratio of the high-resolution spectra for MM1, MM3, and MM4 it is difficult to interpret the

Table 4.5: Parameters of the isotopologues of the CO molecule detected towards G19.88-0.53 from spectral data cubes at different spatial resolutions. The LSR velocity ($V_{\rm LSR}$), line width (ΔV), intensity and velocity integrated intensity ($\int I_\nu dV$) of each transition are obtained from the single or double Gaussian profiles fits to the extracted spectra.

Core	$V_{\rm LSR}$ ($\rm km\,s^{-1}$)	ΔV ($\rm km\,s^{-1}$)	Intensity ($\rm Jy\,beam^{-1}$)	$\int I_\nu dV$ ($\rm Jy\,beam^{-1}\,km\,s^{-1}$)
^{13}CO $(1-0)$				
Low-resolution ($16.9'' \times 8.0''$)				
MM1-MM6	43.7	6.7	4.9	34.8
$C^{17}O$ $(3-2)$				
Low-resolution ($5.2'' \times 2.6''$)				
MM1, MM3 & MM4	43.8	4.0	3.0	12.7
MM2	44.1	3.6	4.0	15.3
MM5 & MM6	42.8 (B)	2.5 (B)	1.8 (B)	4.6 (B)
	48.8 (R)	2.8 (R)	-0.1 (R)	-0.3 (R)
High-resolution ($0.67'' \times 0.47''$)				
MM1	43.8	2.4	0.1	0.3
MM2	44.7	3.7	0.2	0.7
MM3 & MM4	43.4	2.3	0.2	0.4
MM5	43.6	1.1	0.04	0.04
MM6	42.1 (B)	1.7 (B)	0.09 (B)	0.2 (B)
	45.2 (R)	0.9 (R)	-0.02 (R)	-0.02 (R)
$C^{18}O$ $(1-0)$				
Low-resolution ($16.9'' \times 8.0''$)				
MM1-MM6	44.2	3.0	1.9	6.0
Medium-resolution ($2.6'' \times 2.2''$)				
MM1, MM3 & MM4	44.0	3.4	0.2	0.6
MM2	44.1	2.9	0.2	0.8
MM5 & MM6	42.9	2.2	0.1	0.3
High-resolution ($0.46'' \times 0.28''$)				
MM1	43.2	1.0	0.01	0.01
MM2	44.6	2.9	0.01	0.04
MM3 & MM4	43.1	1.6	0.02	0.03
MM5	43.8	1.7	0.004	0.01
MM6	43.2	1.9	0.004	0.01

second red-shifted peaks seen as genuine additional components. These features are mostly broad outflow wings. Core MM6 displays a distinct inverse P-Cygni profile and is fitted by a double Gaussian.

Medium resolution $C^{18}O\,(1-0)$ line spectra extracted over the same three regions used for the $C^{17}O\,(3-2)$ spectra are plotted in Fig. 4.11(a) with the high-resolution spectra presented in Fig. 4.11(b). Similar features are seen though the signal-to-noise of the high-resolution spectra, especially for MM5 and MM6, is poor compared to that of the $C^{17}O\,(3-2)$ line spectra. Also, the medium resolution combined spectrum for MM5 and MM6 shows an additional red-shifted narrow component which is difficult to understand. This component is, however, not detected in the high-resolution spectrum extracted over the same region, and hence could possibly be an artifact. Line parameters for the three transitions of CO determined by fitting Gaussian profiles using CLASS90 are listed in Table 4.5.

4.5 Ionized jet

Given that G19.88-0.53 is classified as an EGO, and hence likely associated with a jet/outflow, we are prompted to investigate the nature of the associated radio emission. As seen in Fig. 4.2(b), the ionized emission associated with G19.88-0.53 exhibits a linear morphology consisting of the components R1 and R2 in the east-west direction. The radio emission from both the components is weak ($\sim 0.2\,\mathrm{mJy}$) and they are located towards the centroid of a large scale ($\sim 1'$) molecular outflow (Fig. 4.16a, Section 4.7.2). These traits are in agreement with the typical observational features expected in ionized jets (Anglada, 1996; Obonyo et al., 2019; Purser et al., 2016; Rodriguez, 1997; Rosero et al., 2019).

The spectral index is a crucial parameter that helps in understanding the nature of the radiation mechanism. This is defined as $S_\nu \propto \nu^\alpha$, where, S_ν is the flux density at frequency ν. As discussed in Section 4.1, G19.88-0.53 is not detected in Band 4. Further, weak emission in Band 5 would render the in-band spectral index estimation highly unreliable as has also been discussed by Rosero et al. (2016). Emission at 1391.6 MHz encompasses the component IRAS 18264-1152b. This makes it possible to use this uGMRT sub-band and VLA maps from Zapata et al. (2006) to derive the spectral index of R1. An accurate determination of the spectral index requires same spatial scales to be probed at the frequencies used. The synthesized beam sizes of uGMRT 1391.6 MHz and VLA 8 GHz (3.6 cm) maps are nearly identical indicating similar *uv* coverage and hence similar spatial scales probed. This is not the case for the 1.3 cm data. For this, we convolve the map to the match the resolution of the other two frequencies. The radio SED is shown in Fig. 4.12. For 651.4 MHz, we obtain an upper limit for the flux density (*rms* of the map) which is shown in the plot. For the VLA maps, we use the peak flux density as well. The fit to the radio

SED of component R1 (IRAS 18264-1152b) yields a spectral index value of 0.58 ± 0.19. that corroborates well with radio continuum emission originating due to the thermal free-free emission from an ionized collimated stellar wind (Rosero et al., 2019, and references therein). For component R2, similar analysis of spectral index estimation is not possible given that this component is not detected in the VLA maps of Zapata et al. (2006).

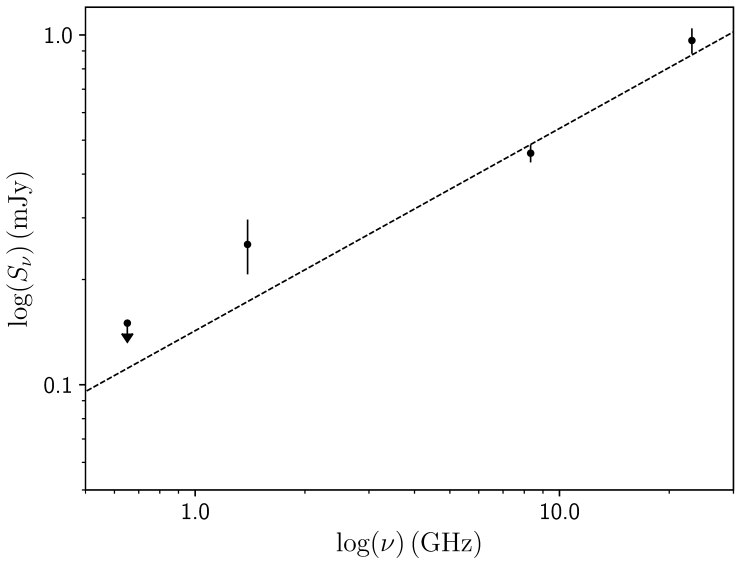

Figure 4.12: Radio SED for component R1 (IRAS 18264-1152b) using the data points at 1391.6 MHz, 8 GHz (3.6 cm) and 23 GHz (1.3 cm). At 651.4 MHz, an upper limit for the flux density is given. The straight line gives the linear fit with spectral index estimate of 0.58 ± 0.19.

The spectral index estimation of R1 obtained from the combination of uGMRT and VLA maps of Zapata et al. (2006) is in excellent agreement with value of 0.6 ± 0.1 derived by Rosero et al. (2016) using flux densities at four central frequencies (4.9 and 7.4 GHz at 6 cm and 20.9 and 25.5 GHz at 1.3 cm). In comparison, Zapata et al. (2006) obtain a lower value of 0.27 ± 0.06. The 3.6 cm flux density of IRAS 18264-1152b used by these authors would also include emission from IRAS 18264-1152a and IRAS 18264-1152c thus rendering a shallower slope. Based on the weak emission, elongated morphology, association with molecular outflows and rising spectral index values, the radio emission favours shock ionization over the HII region picture. Hence, Rosero et al. (2019) list source F (R1) as a ionized jet/wind candidate. Inference of a likely thermal jet or a partially optically thick HII region is drawn by Zapata et al. (2006) as well. The identification of R1 as a thermal jet is well supported by the detection of several shock-excited H_2 lines in the UKIRT-NIR

spectra of G19.88-0.53 presented in Section 4.2. To the best of our knowledge, this is the first detection of the ionized jet associated with G19.88-0.53 at the lower frequency regime of uGMRT. Similar result is obtained for EGO G12.42+0.50 discussed in Chapter 3. The authors propose the coexistence of a thermal jet and a UC H II region driven by the same MYSO to explain the observed radio, mm, and IR emission for G12.42+0.50.

4.6 A protocluster revealed

EGO G19.88-0.53 has been proposed as an outflow powered by a MYSO (De Buizer & Vacca, 2010) and a multiple outflow source (Varricatt et al., 2010). Several studies (e.g. Cyganowski, Brogan & Hunter, 2007; Cyganowski et al., 2011b) have shown that MYSOs are actually protoclusters harbouring protostars with different masses and in various stages of evolution. Given the predilection of high-mass stars to form in clustered environments, it is likely that EGOs, in fact harbour protoclusters rather than single high-mass stars. Based on SOFIA FORCAST imaging and archival infrared data of twelve EGOs, Towner et al. (2019) suggest the number of massive sources per EGO to be between 0.9 to 1.9. Similar inferences have been drawn from studies towards other identified EGOs (e.g. Brogan et al., 2011; Cyganowski et al., 2012).

The 870 μm clump cocoons the EGO G19.88-0.53 where the extended 4.5 μm emission lies towards the centre as is seen in Figure 4.5(a). In Fig. 4.13, we present the various radio and mm sources associated with this EGO. The 2.7 mm dust emission, with the cluster of detected cores lie deeply embedded within the 4.5 μm emission. Portion of the 3σ contour of the 4.5 μm emission is seen in the region displayed in the figure. Within the dust emission lie the two radio components R1 and R2 mapped at 1391.6 MHz with uGMRT. As discussed in the previous section, R1 (VLA source F) is most likely an ionized thermal jet. Regarding component R2 (VLA source A) and the other six compact VLA sources (B, C, D, E, G, and H) located within the EGO, Rosero et al. (2016) discuss the likelihood of them being H II regions around rapidly accreting massive stars that quench the UV photons thus giving rise to weak radio sources. They also keep alive the debate of these being ionized jets instead. Zapata et al. (2006) also suggest that the component IRAS 18264-1152c (VLA source E) is likely to be an optically thick H II region. These authors detect an additional component IRAS 18264-1152a of similar nature taking the number of distinct radio sources to be nine. Furthermore, from the analysis of ALMA 2.7 mm high-resolution continuum map, we discover six compact cores located within the EGO. Table 4.6 lists the radio and mm sources and their cross-identification.

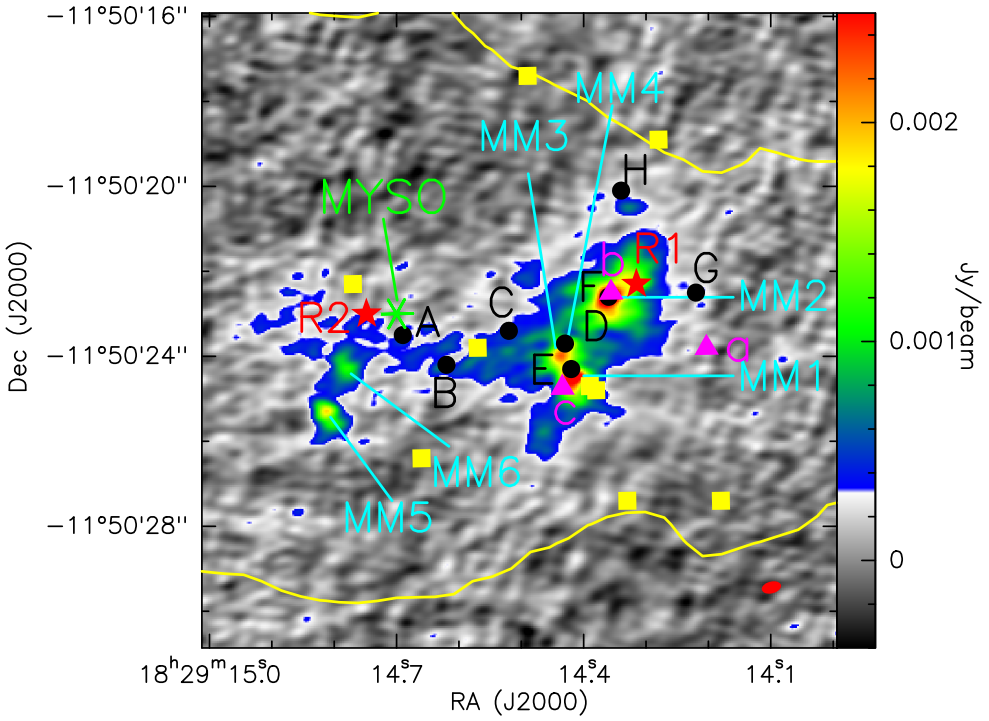

Figure 4.13: Multifrequency picture of the various components of the protocluster. The ALMA 2.7 mm map is depicted in the colour scale. The yellow contour traces the 3σ level of the 4.5μm emission. The red stars mark the positions of the radio components R1 and R2 from the uGMRT map. The black filled circles indicate the positions of the radio sources identified by Rosero et al. (2016). The magenta triangles represent the radio components from Zapata et al. (2006). The position of the MYSO associated with G19.88-0.53 is indicated with '$*$'. The filled yellow squares are the 44 GHz methanol masers spots in the vicinity of G19.88-0.53 identified by Rodríguez-Garza et al. (2017).

Table 4.6: Identified radio and mm components of the protocluster associated with G19.88-0.53.

Compact radio sources VLA[1]	Radio components VLA[2]	Radio components uGMRT 1391.6 MHz[3]	Millimeter cores ALMA 2.7 mm [3]	Remark
A	-	R2	-	MYSO[4]/Ionized jet
B	-	-	-	UC H II/Ionized jet
C	-	-	-	UC H II/Ionized jet
D	-	-	MM3 & MM4	UC H II/Ionized jet
E	IRAS 18264-1152c	-	MM1	UC H II/Ionized jet
F	IRAS 18264-1152b	R1	MM2	Ionized jet
G	-	-	-	UC H II/Ionized jet
H	-	-	-	UC H II/Ionized jet
-	IRAS 18264-1152a	-	-	UC H II/Ionized jet
-	-	-	MM5	Dense core
-	-	-	MM6	Dense core

[1]Rosero et al. (2016); [2] Zapata et al. (2006); [3]This work; [4]De Buizer & Vacca (2010)

Given the detection of several radio components and mm cores, the picture of a protocluster with multiple (eleven) members is clearly perceivable. The observational signatures of the members show clear evidence of different evolutionary phases. However, high-sensitivity radio surveys of ionized jets have shown association with extended lobes and string of radio knots (e.g. Garay et al., 2003; Guzmán, Garay & Brooks, 2010; Hofner et al., 2017; Purser et al., 2016). From the alignment of the radio sources B, C and F, and the spectral index of F, one can visualize a similar scenario. It is thus plausible that we are probing a string of knots of a single ionized jet driven by R1/MM2/F. Similarly, the components A and G could be part of this jet system though the possibility of another jet driven by R2/MYSO/A cannot be ruled out. If these radio components are indeed knots/lobes of the identified jet-systems, then the number of distinct members of the detected protocluster would be less than eleven. Further studies are required to interpret the exact nature the compact radio sources.

4.6.1 CH_3OH rotational temperature

Molecular line transitions can be used to analyse the core properties. As seen in Fig. 4.8, multiple transitions of $\mathrm{CH_3OH}$ are detected towards the mm cores associated with G19.88-0.53. This motivates us to use rotational temperature diagram (RTD) (also referred to as Boltzman diagram) to estimate the rotational temperature and the beam averaged column density of the identified mm cores. To generate the RTDs, we use the low-resolution ($5.3'' \times 2.6''$) ALMA data cubes. Given the beam size, we extract the spectrum covering three regions (1) MM1, MM3, and MM4, (2) MM2, and (3) MM5 and MM6. The retrieved spectra are shown in Fig. 4.14 and the line parameters are listed in Table 4.8,4.9, and 4.10. The detected methanol lines have linewidths of several $\mathrm{km\,s^{-1}}$ and none show unusually high line intensities. Thus these are unlikely to be associated with maser excitations.
Considering the molecular emission to be optically thin, the column density of the upper level, $N_{\rm u}$ can be computed from the integrated line intensity following the expression,

$$N_{\rm u} = \frac{8\pi k\nu^2}{hc^3 A_{\rm u}} \int I_\nu(\mathrm{Jy\,beam^{-1}}) dV(\mathrm{km\,s^{-1}})/\eta_{\rm bf} \tag{4.1}$$

where $A_{\rm u}$ is Einstein coefficient and $\eta_{\rm bf}$ is the beam-filling factor, taken to be 1 since the emission region is larger than the beam size (Ren et al., 2012). Further, under conditions of local thermodynamic equilibrium, the measured line intensities are proportional to the level populations that are characterized by a single rotational temperature. The rotational temperature, $T_{\rm rot}$ and the beam averaged column density, $N_{\rm T}$ can be determined using the

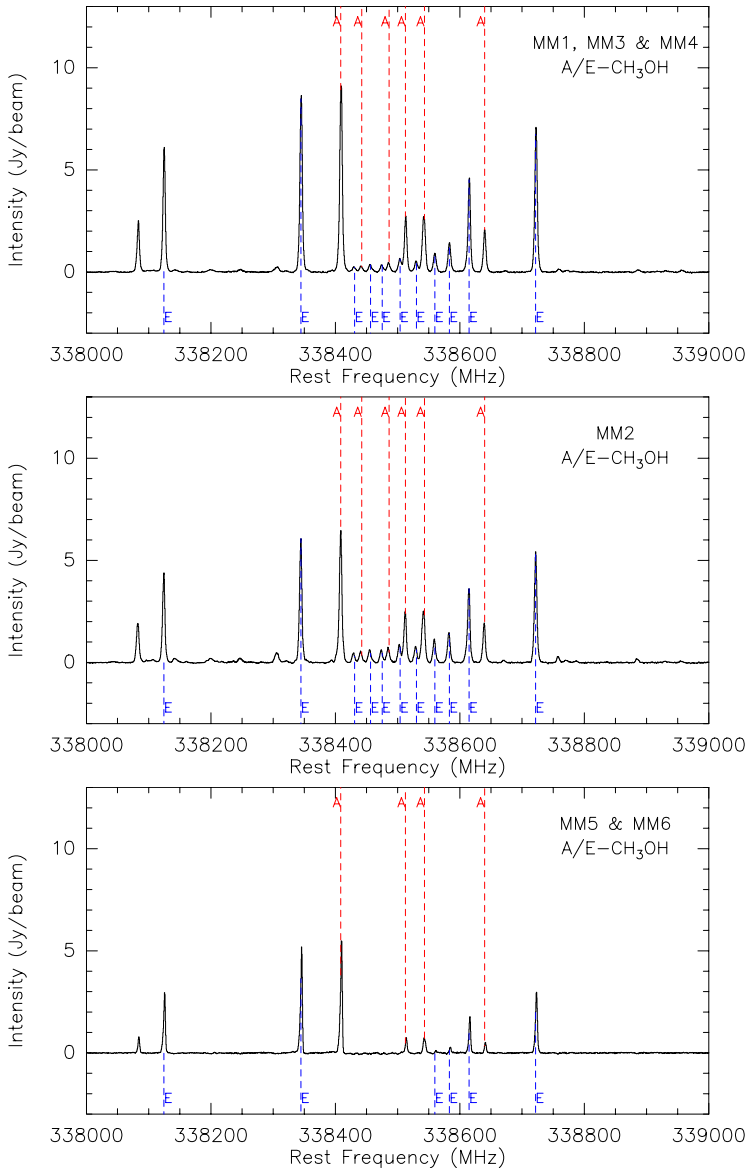

Figure 4.14: Spectra of the $A/E-\mathrm{CH_3OH}$ lines detected towards G19.88-0.53 extracted over three regions from the low-resolution Band 7 spectral cube. The top panel is the spectrum extracted over the region covering MM1, MM3 and MM4, middle panel corresponds to MM2 and the bottom panel is over the region covering MM5 and MM6. The dashed red and blue lines indicate the peak positions of the $A-\mathrm{CH_3OH}$ and $E-\mathrm{CH_3OH}$ lines, respectively.

expression (Blake et al., 1987; Liu et al., 2002; Remijan et al., 2004),

$$\ln\left(\frac{N_{\rm u}}{g_{\rm u}}\right) = \ln\left(\frac{N_{\rm T}}{Q_{\rm rot}}\right) - \frac{E_{\rm u}}{T_{\rm rot}}$$
$$= \ln\left[2.04\times10^{20}\frac{\int I_\nu(\mathrm{Jy\,beam^{-1}})dV(\mathrm{km\,s^{-1}})}{\theta_a\theta_b\,(\mathrm{arcsec^2})\nu^3(\mathrm{GHz})\mathrm{S}\mu^2(\mathrm{debye^2})}\right] \quad (4.2)$$

where, $N_{\rm u}$, $g_{\rm u}$ and $E_{\rm u}$ are the upper-level column density, rotational degeneracy factor, and energy, respectively, $Q_{\rm rot}(= 1.23T_{\rm rot}^{1.5})$ is the rotational partition function (Remijan et al., 2004; Ren et al., 2012), θ_a and θ_b are the beam sizes, ν is the rest frequency, S is the line strength, μ is the dipole moment, and the integration of I_ν over velocity, V, is the integrated line intensity. Values for $E_{\rm u}$ and $S\mu^2$ for detected transitions are retrieved from *splatalogue - database for astronomical spectroscopy*[7] and compiled in Table 4.7. The generated RTDs towards the mm cores are plotted in Fig. 4.15. Linear least-square fits to the data points gives the estimate of the rotational temperature, $T_{\rm rot}$ and the beam averaged column density, $N_{\rm T}$ of the cores and are listed in Table 4.11. For cores MM1, MM3, and MM4, the estimates would be an average value of the three clumps as is the case with the estimates for MM5 and MM6. Estimated values of $T_{\rm rot}$ and $N_{\rm T}$ lie in the range $\sim 47 - 116\,{\rm K}$ and $\sim 0.7 - 4 \times 10^{15}\,{\rm cm}^{-2}$, respectively with core MM2 being the hottest with a rotational temperature of 115.9 K. The rotational temperatures for the cores are greater than the average cold dust temperature of 18.6 K deduced for the dust clump (Section 4.3.1). The difference in these temperatures could be that the CH_3OH emission arises from the hot cores. The gas and dust could also be thermally decoupled and the higher rotational temperatures could be the result of enhanced collisional excitations of the molecular gas by shocks in the outflow region. A large scatter is seen in the combined RTD of MM5 and MM6 possibly indicating more than one temperature components. However, higher resolution and better signal-to-noise ratio data are required to address this.

To examine the assumption of optically thin transitions, we derived the optical depth of the CH_3OH lines adopting the following expression from Ren et al. (2012)

$$\tau = \frac{c^3\sqrt{4\ln 2}}{8\pi\nu^3\sqrt{\pi}\Delta V} N_{\rm u} A_{\rm u} \left[\exp\left(\frac{h\nu}{kT_{\rm rot}}\right) - 1 \right] \tag{4.3}$$

The estimated values are listed in Table 4.8,4.9, and 4.10. Only two transitions for the combined cores of MM1, MM3, and MM4 show values ~ 0.1. Rest of the lines are far more optically thin. Considering T_d (18.6 K) instead of $T_{\rm rot}$, to account for temperature uncertainties, if any, also gives optically thin estimates for the transitions. In case of optically thick lines, effects of optical depth can be taken into account by multiplying the term $N_{\rm u}/g_{\rm u}$ with a correction factor $C_\tau = \tau/(1 - {\rm e}^{-\tau})$ and subsequently fitting for the rotational temperature iteratively (Ren et al., 2012). We also estimate the relative abundance of CH_3OH with respect to the H_2 molecule and tabulate the values in Table 4.11 along with the H_2 number density.

[7] http://www.cv.nrao.edu/php/splat/

Table 4.7: Spectroscopic parameters of the $A - CH_3OH$ and $E - CH_3OH$ lines detected towards G19.88-0.53 taken from the spectroscopic databases, CDMS and JPL from *splatalogue*.

Transition J_k	Frequency (MHz)	E_u (K)	$S\mu^2$ (debye^2)
$A - CH_3OH$			
$7_0 - 6_0$	338408.698	64.98	5.66
$7_6 - 6_6$	338442.367	258.7	3.01
$7_5 - 6_5$	338486.322	202.88	5.57
$7_4 - 6_4$	338512.632	145.33	3.82
$7_3 - 6_3$	338543.152	114.79	4.61
$7_2 - 6_2$	338639.802	102.72	5.23
$2_2 - 3_1$	340141.143	44.67	0.31
$E - CH_3OH$			
$3_3 - 4_2$	337135.853	61.64	0.99
$7_0 - 6_0$	338124.488	78.08	5.65
$7_{-1} - 6_{-1}$	338344.588	70.55	5.55
$7_6 - 6_6$	338430.981	253.95	1.50
$7_{-5} - 6_{-5}$	338456.521	189.00	2.76
$7_5 - 6_5$	338475.217	201.06	2.76
$7_{-4} - 6_{-4}$	338504.065	152.89	3.81
$7_4 - 6_4$	338530.256	160.99	3.82
$7_{-3} - 6_{-3}$	338559.963	127.71	4.64
$7_3 - 6_3$	338583.216	112.71	4.63
$7_1 - 6_1$	338614.936	86.05	5.68
$7_2 - 6_2$	338721.693	87.26	5.14

Menten et al. (1986), in their study of E-type methanol lines towards a few Galactic molecular line sources concluded that these lines originate from hot clumps embedded in the molecular gas and have densities $\sim 10^6 - 10^7\,\mathrm{cm}^{-3}$, temperatures $\sim 100\,\mathrm{K}$, and sizes $\sim 1\,\mathrm{pc}$. The abundance relative to the H_2 molecule was found to be in the range of $10^{-7} - 10^{-6}$. In another study of molecular clouds, Leurini et al. (2007) study the early phases of high-mass stars, particularly the protostellar objects and IRDCs, using methanol as a diagnostic tool. In their study, they discuss on the origin of CH_3OH lines which could arise from the different components of the protostellar object, which includes the overall emission from the clump and the dense, hot core. In some cases contribution of outflow emission is also included. Temperatures, densities, and abundances fall in the range of

Table 4.8: $A-\mathrm{CH_3OH}$ and $E-\mathrm{CH_3OH}$ lines towards MM1, MM3 and MM4 of G19.88-0.53. Columns 1 and 2 are the transitions and the corresponding frequencies, respectively. Columns 3-5 are the parameters and the uncertainties from the Gaussian fits to each line; they are line flux ($\int I_\nu dV$), LSR velocity ($V_{\rm LSR}$), and the line width (ΔV). Column 6 is the optical depth for each transition with two values, the first for $T_{\rm rot}$ and the second for $T_d = 18.6\,\mathrm{K}$, respectively.

Transition J_k	Frequency (MHz)	$V_{\rm LSR}$ ($\mathrm{km\,s^{-1}}$)	$\int I_\nu dV$ ($\mathrm{Jy\,beam^{-1}\,km\,s^{-1}}$)	ΔV ($\mathrm{km\,s^{-1}}$)	$\tau_{T_{\rm rot}}/\tau_{T_d}$
$A-\mathrm{CH_3OH}$					
7_0-6_0	338408.698	43.6±0.4	40.3±0.9	4.1±0.4	0.112/0.496
7_6-6_6	338442.367	44.9±0.1	1.6±0.1	5.6±0.3	0.003/0.015
7_5-6_5	338486.322	44.7±0.1	2.5±0.1	5.4±0.2	0.005/0.023
7_4-6_4	338512.632	43.7±0.1	11.9±0.5	4.2±0.2	0.032/0.142
7_3-6_3	338543.152	44.8±0.4	15.7±0.4	5.4±0.4	0.033/0.147
7_2-6_2	338639.802	43.9±0.4	9.0±0.6	4.3±0.4	0.024/0.106
2_2-3_1	340141.143	44.3±0.03	2.4±0.1	4.7±0.1	0.006/0.025
$E-\mathrm{CH_3OH}$					
3_3-4_2	337135.853	44.6±0.1	1.8±0.05	5.0±0.1	0.004/0.016
7_0-6_0	338124.488	43.6±0.01	23.9±0.2	3.7±0.03	0.073/0.324
$7_{-1}-6_{-1}$	338344.588	43.6±0.01	36.4±0.2	3.9±0.02	0.105/0.466
7_6-6_6	338430.981	44.9±0.1	1.5±0.1	6.0±0.3	0.003/0.013
$7_{-5}-6_{-5}$	338456.521	44.8±0.2	1.9±0.2	5.0±0.6	0.004/0.019
7_5-6_5	338475.217	44.8±1.1	1.7±0.8	4.7±2.1	0.004/0.018
$7_{-4}-6_{-4}$	338504.065	44.0±0.1	4.0±0.2	6.1±0.4	0.007/0.033
7_4-6_4	338530.256	44.3±0.2	3.2±0.3	6.2±0.7	0.006/0.026
$7_{-3}-6_{-3}$	338559.963	44.1±0.1	4.7±0.3	4.9±0.3	0.011/0.048
7_3-6_3	338583.216	43.9±0.1	6.9±0.3	4.7±0.2	0.017/0.075
7_1-6_1	338614.936	43.7±0.4	18.9±0.5	3.9±0.4	0.055/0.246
7_2-6_2	338721.693	44.4±0.4	30.3±0.7	4.0±0.4	0.085/0.380

$17-36\,\mathrm{K}$, $2\times10^5-3\times10^6\,\mathrm{cm^{-3}}$, and $7\times10^{-10}-2\times10^{-8}$, respectively, if the molecular transition occurs from the bulk emission of the clump. The range changes to $60-300\,\mathrm{K}$, $\gtrsim 10^6\mathrm{cm^{-3}}$, and $\gtrsim 10^{-7}$, respectively for hot cores. The estimated values for cores associated with G19.88-0.53 indicates the origin of the $\mathrm{CH_3OH}$ emission from hot cores, especially for MM1 to MM4.

Table 4.9: Same as Table 4.8 for MM2 towards G19.88-0.53.

Transition (MHz)	Frequency ($\mathrm{km\,s^{-1}}$)	$V_{\rm LSR}$ ($\mathrm{Jy\,beam^{-1}\,km\,s^{-1}}$)	$\int I_\nu dV$ ($\mathrm{km\,s^{-1}}$)	ΔV	$\tau_{T_{\rm rot}}/\tau_{T_d}$
$A-\mathrm{CH_3OH}$					
7_0-6_0	338408.698	44.1±0.02	27.5±0.2	4.1±0.04	0.054/0.335
7_6-6_6	338442.367	45.6±0.4	2.8±0.5	5.0±1.1	0.004/0.028
7_5-6_5	338486.322	45.4±0.2	3.8±0.3	5.2±0.4	0.006/0.037
7_4-6_4	338512.632	44.4±0.1	11.3±0.6	4.3±0.3	0.021/0.131
7_3-6_3	338543.152	45.5±0.2	14.3±0.9	5.4±0.4	0.022/0.135
7_2-6_2	338639.802	44.5±0.02	8.2±0.1	4.0±0.1	0.016/0.102
2_2-3_1	340141.143	45.3±0.4	3.6±0.1	5.0±0.4	0.006/0.036
$E-\mathrm{CH_3OH}$					
3_3-4_2	337135.853	45.5±0.1	2.3±0.1	4.4±0.1	0.004/0.026
7_0-6_0	338124.488	44.3±0.4	18.7±0.4	4.2±0.4	0.036/0.227
$7_{-1}-6_{-1}$	338344.588	44.2±0.01	25.7±0.1	4.1±0.02	0.051/0.316
7_6-6_6	338430.981	45.7±0.4	2.3±0.4	4.7±0.9	0.004/0.025
$7_{-5}-6_{-5}$	338456.521	45.3±0.4	3.2±0.1	5.0±0.4	0.005/0.032
7_5-6_5	338475.217	45.3±0.2	3.0±0.2	4.7±0.4	0.005/0.032
$7_{-4}-6_{-4}$	338504.065	45.0±0.2	4.7±0.4	5.3±0.5	0.007/0.045
7_4-6_4	338530.256	45.2±0.1	4.1±0.1	5.2±0.2	0.006/0.040
$7_{-3}-6_{-3}$	338559.963	44.9±0.2	5.3±0.5	4.5±0.5	0.009/0.059
7_3-6_3	338583.216	44.8±0.1	6.9±0.2	4.6±0.2	0.012/0.076
7_1-6_1	338614.936	44.4±0.4	15.4±0.4	4.0±0.4	0.031/0.193
7_2-6_2	338721.693	44.9±0.01	23.9±0.1	4.3±0.01	0.045/0.280

4.6.2 Nature of mm cores

To decipher the nature of the mm cores, we estimate the masses. This is done following the formalism described in Cheng et al. (2018). Assuming optically thin emission, the core masses can be expressed as

$$\begin{aligned} \mathrm{M} &= 0.0417\,M_\odot \left(\mathrm{e}^{0.533(\lambda/1.3\,\mathrm{mm})^{-1}(T/20\,\mathrm{K})^{-1}}-1\right)\left(\frac{F_\nu}{\mathrm{mJy}}\right) \\ &\times \left(\frac{\kappa_\nu}{0.00638\,\mathrm{cm^2\,g^{-1}}}\right)^{-1}\left(\frac{d}{2.4\,\mathrm{kpc}}\right)^2\left(\frac{\lambda}{1.3\,\mathrm{mm}}\right)^3 \end{aligned} \tag{4.4}$$

where the opacity

$$\kappa_\nu = 0.1(\nu/1000\,\mathrm{GHz})^\beta\,\mathrm{cm^2\,g^{-1}} \tag{4.5}$$

Table 4.10: Same as Table 4.8 for MM5 and MM6 towards G19.88-0.53.

Transition (MHz)	Frequency ($\mathrm{km\,s^{-1}}$)	$V_{\rm LSR}$ ($\mathrm{Jy\,beam^{-1}\,km\,s^{-1}}$)	$\int I_\nu dV$ ($\mathrm{km\,s^{-1}}$)	ΔV	$\tau_{T_{\rm rot}}/\tau_{T_d}$
$A-\mathrm{CH_3OH}$					
7_0-6_0	338408.698	42.7±0.01	9.6±0.6	2.1±0.04	0.091/0.230
7_4-6_4	338512.632	42.8±0.04	2.3±0.1	3.1±0.1	0.015/0.038
7_3-6_3	338543.152	44.0±0.05	3.2±0.1	4.2±0.1	0.015/0.039
7_2-6_2	338639.802	42.9±0.02	1.6±0.03	2.9±0.1	0.011/0.027
2_2-3_1	340141.143	43.0±0.1	0.2±0.02	2.5±0.3	0.002/0.005
$E-\mathrm{CH_3OH}$					
7_0-6_0	338124.488	42.8±0.01	4.5±0.2	2.1±0.04	0.043/0.109
$7_{-1}-6_{-1}$	338344.588	42.9±0.01	13.3±0.1	2.5±0.02	0.107/0.271
$7_{-3}-6_{-3}$	338559.963	42.5±0.1	0.3±0.04	2.3±0.4	0.003/0.007
7_3-6_3	338583.216	42.7±0.4	0.8±0.3	2.7±1.0	0.006/0.015
7_1-6_1	338614.936	43.1±0.1	5.5±0.2	3.0±0.1	0.036/0.092
7_2-6_2	338721.693	43.7±0.02	9.4±0.1	3.0±0.03	0.062/0.158

with β, the dust emissivity spectral index, fixed at 2.0 is the same as used for modelling the FIR SED. F_ν is the integrated flux density of each component, d is the distance to the source and λ is the wavelength taken as 2.7 mm. Since we do not have the information of dust temperatures at the dense core scales, we use the estimated $T_{\rm rot}$ values in the above expression to derive masses. Compared to the average dust temperature of the clump, these temperatures would be a better choice to represent the hot cores. The mass estimates range between $10-30\,M_\odot$ and are listed in Table 4.11. Angular sizes given in Table 4.4 are converted to linear sizes and listed in the table. From the estimated masses and sizes, the detected cores satisfy the criterion, $m(r) > 870\,M_\odot(r/\mathrm{pc})^{1.33}$ (Kauffmann et al., 2010b) and qualify as high-mass star forming cores. In comparison to the numbers discussed by Towner et al. (2019), we detect as many as eleven possible distinct massive components in the G19.88-0.53 protocluster that include MYSOs driving ionized jets/outflows and UC H II regions.

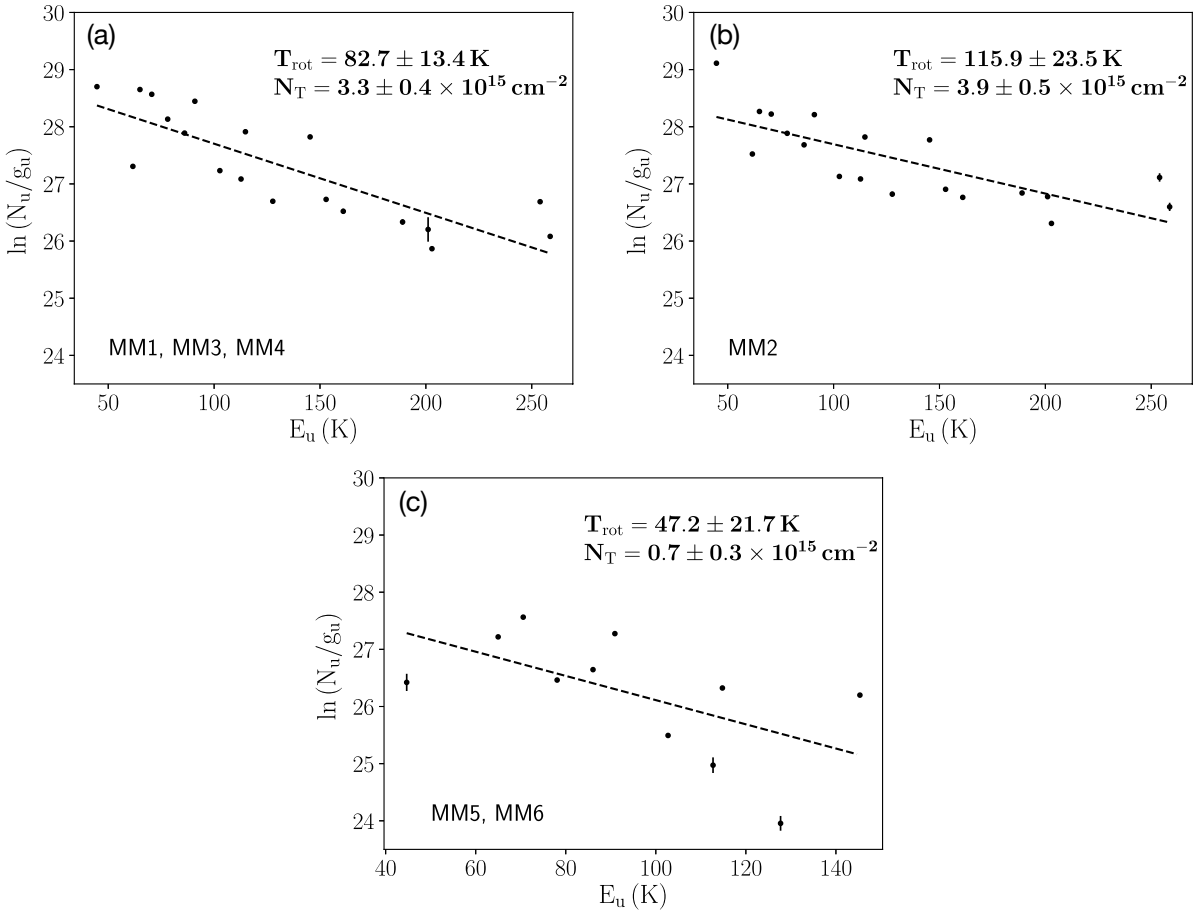

Figure 4.15: The rotational temperature diagram of the CH_3OH lines at the mm cores, MM1 through MM6 towards G19.88-0.53. The circles indicate the data points with 3σ error bars. The linear least-squares fit is indicated by the dashed line.

Table 4.11: Derived parameters of the mm cores associated with G19.88-0.53.

Core	Radius (10^{-3} pc)	$T_{\rm rot}$ (K)	$N_{\rm T}$ (10^{15} cm^{-2})	$N_{\rm T}/N({\rm H_2})$ (10^{-7})	Mass$_{T_{\rm rot}}$ ($M_\odot$)	$n({\rm H_2})$ (10^8 cm^{-3})
MM1	5.4	82.7±13.4	3.3±0.4	0.6	14.5	3.2
MM2	10.1	115.9±23.5	3.9±0.5	0.7	29.6	1.0
MM3 & MM4	6.6	82.7±13.4	3.3±0.4	0.6	16.1	1.9
MM5	5.2	47.2±21.7	0.7±0.3	0.1	13.1	3.2
MM6	5.3	47.2±21.7	0.7±0.3	0.1	9.5	2.2

4.7 Kinematics of the protocluster G19.88-0.53

4.7.1 Infall signature in MM6

As discussed in Section 4.4, CO transitions from higher energy levels are likely tracers of the inner parts of molecular clouds. The $C^{17}O\,(3-2)$ molecular transition shows an inverse P-Cygni profile for core MM6. Inverse P-Cygni profiles are generally considered as evidence of gas infall (Liu, Wu & Zhang, 2013; Wu et al., 2009). In such profiles, the redshifted absorption feature originates from the dense gas along the line-of-sight and located towards the near side of the observer and moving away. The emission component is due to the gas on the far side of the central source with its motion towards the observer. Although several studies have attributed the presence of an inverse P-Cygni or redshifted absorption profile to possible gas inflow to the central core (e.g. Keto, Ho & Reid, 1987; Liu et al., 2013; Liu, Wu & Zhang, 2013; Qin et al., 2008; Zapata et al., 2008), detailed investigations of inverse P-Cygni profiles of CO lines in high-mass star forming regions are fairly limited (e.g. Beltrán et al., 2011; Klaassen et al., 2011; Wu et al., 2009).

Table 4.12: The infall velocity, $V_{\rm inf}$ and mass infall rate, $\dot{M}_{\rm inf}$ of core MM6 associated with G19.88-0.53, estimated using the $C^{17}O\,(3-2)$ line.

Core	$V_{\rm LSR}$ ($\rm km\,s^{-1}$)	$V_{\rm R}$ ($\rm km\,s^{-1}$)	$V_{\rm inf}$ ($\rm km\,s^{-1}$)	$\dot{M}_{\rm inf}$ ($10^{-3}\,M_{\odot}\,\rm yr^{-1}$)
MM6	42.3	45.2	2.9	16.1

We make use of the $C^{17}O\,(3-2)$ line profile to estimate the infall velocity and the mass infall rate of the compact core, MM6 associated with G19.88-0.53. The infall velocity is estimated as $V_{\rm inf} = |V_{\rm LSR} - V_{\rm R}|$ (Beltrán et al., 2011), where $V_{\rm R}$ is the peak of the redshited absorption. From the infall velocity, the mass infall rate is determined following the expression $\dot{M}_{\rm inf} = 4\pi R^2 V_{\rm inf}\rho$ (López-Sepulcre, Cesaroni & Walmsley, 2010), where ρ is the average volume density of the cores, given by $\rho = M/\frac{4}{3}\pi R^3$. From the estimated core mass and radius, the infall velocity and mass infall rate are calculated to be $2.9\,\rm km\,s^{-1}$ and $16.1\times10^{-3}\,M_{\odot}\,\rm yr^{-1}$, respectively and listed in Table 4.12. The infall velocity and mass infall rate are consistent with the typical values of several $\rm km\,s^{-1}$ and $\sim 10^{-3}$–$10^{-2}\,M_{\odot}\,\rm yr^{-1}$, respectively, found towards hot molecular cores (Liu, Wu & Zhang, 2013).

4.7.2 Outflow activity

Co-existing with ionized jets, molecular outflows are ubiquitous in active star forming cores (e.g. Beuther et al., 2002c; Purser et al., 2016). These outflows are understood to be driven by the jets that entrain the gas and dust from the surrounding clump. Based on a large number of studies, broad wings of CO lines are accepted as signatures of molecular outflow (Beuther et al., 2002c; Qiu et al., 2009). The detection of the isotopologues of CO towards G19.88-0.53 enables us to investigate the associated outflow(s). Towards this, we construct the zeroth moment map of the $C^{18}O\,(1-0)$ emission from the low-resolution cube using the CASA task, `IMMOMENTS`. The velocity range to integrate is estimated from the extracted spectra discussed earlier and shown in Fig. 4.9(b). Following Sanna et al. (2014) and Issac et al. (2019), we define the inner limits of the velocity at $\sim V_{\rm LSR} \pm {\rm FWHM}/2$, where FWHM is the $C^{18}O$ linewidth. Thus, for the blue wing, the emission is integrated over the velocity range of 36.1 to 42.1 $\rm km\,s^{-1}$. Similarly, for the red wing the integration is done from 45.1 to 51.1 $\rm km\,s^{-1}$. The spatial extent and morphology of the outflow is revealed in Fig. 4.16(a). To facilitate morphological correlation of the outflow with the EGO, the contours of the blue and red lobes are overlaid on the *Spitzer* IRAC colour composite image. Magenta ellipses denote the location of the H_2 knots identified by Lee et al. (2012) and Varricatt et al. (2010) from the continuum subtracted H_2 image. Two distinct and spatially separated outflow lobes in the north-east and south-west direction are identified with the central part of G19.88-0.53 located towards the centroid of the outflow. The direction and location of the blue lobe is towards MHOs 2203 and 2205. In their survey of massive molecular outflows in high-mass star forming regions using the $^{12}CO\,(2-1)$ transition, Beuther et al. (2002c) discuss the detection of a bipolar CO outflow towards the infrared source, IRAS 18264-1152, associated with G19.88-0.53. The orientation is consistent with that seen in Fig. 4.16(a).

The figure also shows the 2.7 mm emission outlined by the black contour. A zoomed-in picture of the 2.7 mm map covering the central part of the extended green emission is displayed in Fig. 4.16(b) and (c). We investigate outflow signatures in the high-resolution $C^{17}O\,(3-2)$ and $C^{18}O\,(1-0)$ emission in Band 7 and Band 3 cubes, respectively. From a visual inspection of the outflow wings seen in the spectra presented in Fig. 4.10, the moment zero maps of the $C^{17}O\,(3-2)$ over the velocity ranges 36.1 to 42.1 $\rm km\,s^{-1}$ and 45.1 to 51.1 $\rm km\,s^{-1}$ are constructed. The contours of the moment zero maps are overlaid in Fig. 4.16(b). Similarly, for the $C^{18}O\,(1-0)$ emission, the moment zero maps are built over the velocity ranges 41.6 to 43.6 $\rm km\,s^{-1}$ and 43.6 to 45.6 $\rm km\,s^{-1}$, the contours of

which are overlaid on Fig. 4.16(c). Since the high-resolution $C^{18}O\,(1-0)$ data have poor signal-to-noise ratio in comparison to the high-resolution $C^{17}O\,(3-2)$, no emission was detected above the noise beyond the outer limits, 41.6 and 45.6 $\mathrm{km\,s^{-1}}$ of the blue and red lobes, respectively. Interestingly, from the contours of the moment zero maps overlaid in Fig. 4.16(b) and (c), the high-resolution data traces another relatively collimated outflow in the south-east and north-west direction with core MM2 located in the close vicinity of its centroid.

To delve further, we generate channel maps of the high-resolution $C^{17}O\,(3-2)$ transition shown in Fig. 4.17. The emission in the velocity range $39.1-42.1\,\mathrm{km\,s^{-1}}$ is elongated towards south-east of core MM2, whereas the emission with velocities $45.1-48.1\,\mathrm{km\,s^{-1}}$, the elongation is towards north-west of MM2 thus giving clear indication of the presence of an outflow. The channel map of the high-resolution $C^{18}O\,(1-0)$ transition, shown in Fig. 4.18 corroborates this picture where the emission with velocities $41.6-43.6\,\mathrm{km\,s^{-1}}$ is elongated towards south-east of core MM2 and the emission with velocities $44.6-45.6\,\mathrm{km\,s^{-1}}$ is elongated north-west of MM2. Close to the LSR velocity of the MM2 ($44.6\,\mathrm{km\,s^{-1}}$), as expected, there is overlap of emission from the blue and the red components. The small projected velocities seen is possibly due to the effect of small inclination angle.

Using the high-resolution $SiO(2-1)$ emission, Qiu et al. (2007) detected the presence of two quasi-perpendicular collimated outflows, one in the south-east and north-west direction and one in the north-east direction. Our high-resolution ALMA map probes the central portion of the outflow presented in Qiu et al. (2007). A close visual scrutiny of the figures presented by these authors indicate that the south-east and north-west SiO outflow is aligned with the $C^{17}O\,(3-2)$ and $C^{18}O\,(1-0)$ outflows displayed in Fig. 4.16(b) and (c). Comparison with the H_2 outflows and the MHOs show a possible alignment with MHO 2204. Further, the direction of north-east $SiO(2-1)$ outflow is consistent with MHO 2245. SiO is believed to be an excellent tracer of collimated molecular jets and shocks in the interstellar molecular clouds, since it is formed due to the sputtering of Si atoms from the grains due to fast shocks (Hatchell, Fuller & Millar, 2001; López-Sepulcre et al., 2011; Miettinen et al., 2006). In studies of several massive star forming regions, protostellar jets were revealed by SiO emission (e.g. Cesaroni et al., 1999; Codella et al., 2013; Leurini et al., 2013). From their study of the massive star formation region IRAS 19410+2336, Widmann et al. (2016) conclude that the SiO emission is possible from the high-velocity C-type or CJ-type shocks associated with protostellar jets. uGMRT results have identified an ionized jet with the core MM2 which is in excellent agreement with the collimated outflow from high-resolution $C^{18}O\,(1-0)$ transition and the co-spatial SiO outflow of Qiu et al. (2007). Several studies

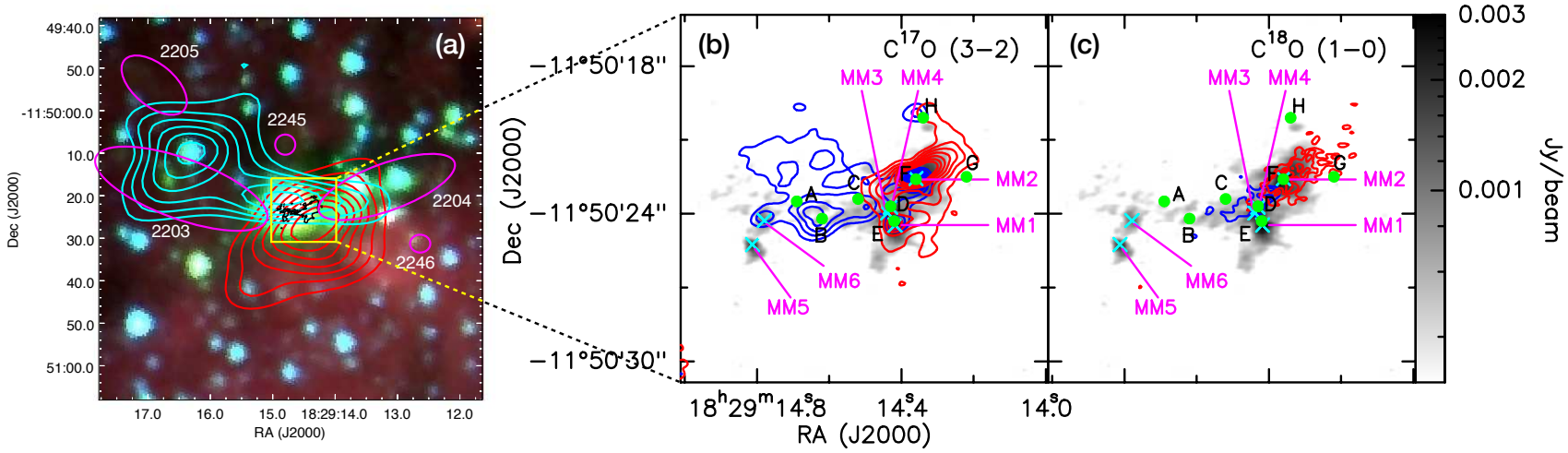

Figure 4.16: (a) The *Spitzer* IRAC colour composite image of G19.88-0.53 with the 3σ ($\sigma = 0.12\,\mathrm{mJy\,beam^{-1}}$) ALMA 2.7 mm emission contours in black. The moment zero map from the the low-resolution data of the $C^{18}O\,(1-0)$ line integrated from 36.1 to 42.1 $\mathrm{km\,s^{-1}}$ and from 45.1 to 51.1 $\mathrm{km\,s^{-1}}$ are represented using blue and red contours, respectively. The contours start from the 3σ level for both the blue and red lobes and increase in steps of 2σ ($\sigma = 0.1$ (blue); $0.2\,\mathrm{Jy\,beam^{-1}\,km\,s^{-1}}$ (red)). Magenta ellipses denote the location of the H_2 knots identified by Lee et al. (2012); Varricatt et al. (2010). (b) The 2.7 mm emission is depicted in the grey scale. The positions of the mm cores are marked using 'x's. The moment zero map from the high-resolution data of $C^{17}O\,(3-2)$ line over the velocity ranges 36.1 to 42.1 $\mathrm{km\,s^{-1}}$ and 45.1 to 51.1 $\mathrm{km\,s^{-1}}$, covering the blue and red lobes are illustrated in blue and red contours, respectively. The contours star from 5σ level for both lobes and increase in steps of 4σ ($\sigma = 16.2\,\mathrm{mJy\,beam^{-1}\,km\,s^{-1}}$). The filled circles correspond to the radio sources detected by Rosero et al. (2016). (c) Same as (b) for the high-resolution $C^{18}O\,(1-0)$ line integrated over the velocity ranges 41.6 to 43.6 $\mathrm{km\,s^{-1}}$ and 43.6 to 45.6 $\mathrm{km\,s^{-1}}$ covering the blue and red lobes, respectively. The contours star from 3σ level for both lobes and increase in steps of 1σ ($\sigma = 7.7\,\mathrm{mJy\,beam^{-1}\,km\,s^{-1}}$).

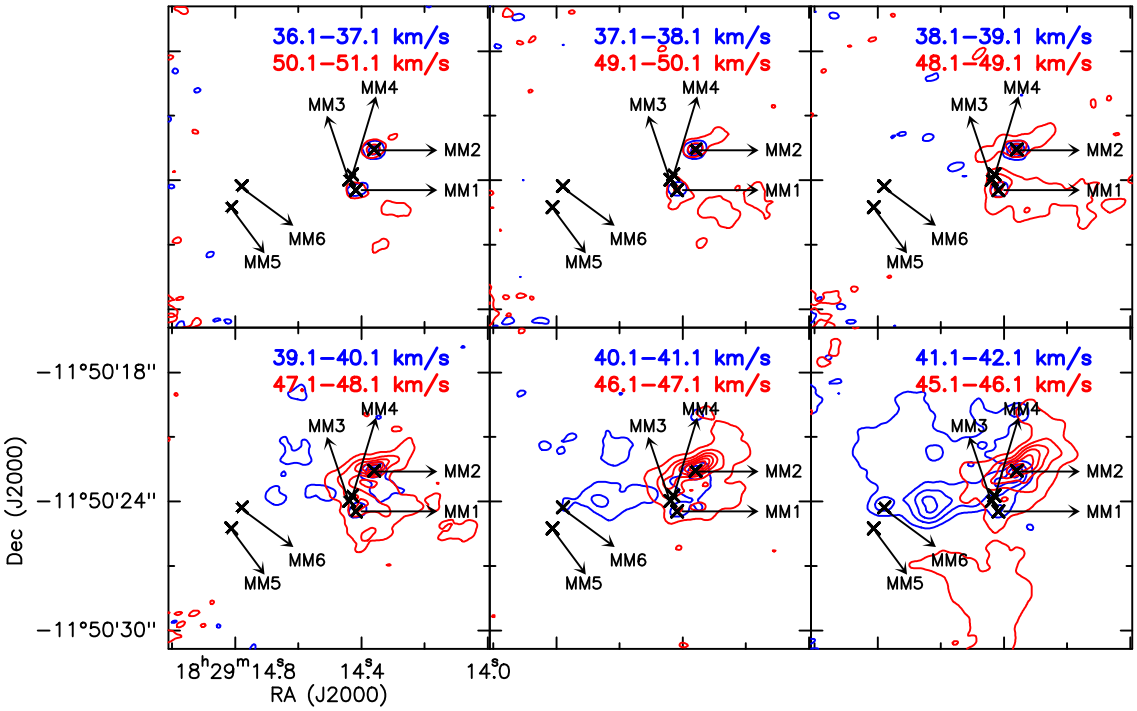

Figure 4.17: Channel maps of $C^{17}O\,(3-2)$ line associated with G19.88-0.53 with a velocity resolution of $1\,\mathrm{km\,s^{-1}}$ from the high-resolution data. Each box contains a pair of maps corresponding to the red and blueshifted emissions at the same offset from the LSR velocity. Channel widths are indicated at the top left of each map. The contours start from the 4σ level of each map and increases in steps of 8σ. The positions of MM1, MM2, MM3, MM4, MM5, and MM6 are marked.

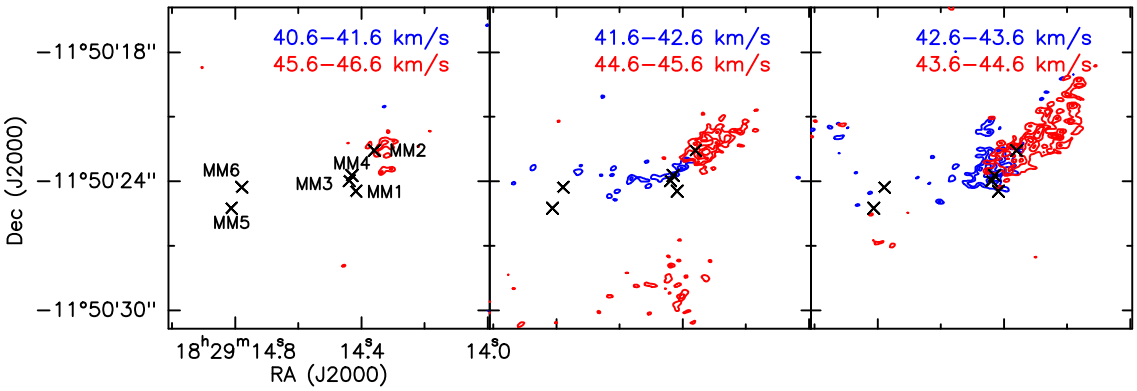

Figure 4.18: Same as Fig. 4.17, but for the high-resolution $C^{18}O\,(1-0)$ data associated with G19.88-0.53. The contours start from the 3σ level of each map and increases in steps of 1σ.

point to the possibility that the massive outflows are powered by mm sources (e.g. Beuther et al., 2002c; Marseille et al., 2008). From the spatial extent and the maximum velocity of

the flow, the dynamical timescale ($T_{\rm dyn} = L_{\rm flow}/v_{\rm max}$) is estimated to be of the order of $10^4\,{\rm yr}$ which is typical of outflows originating from mm cores rather than UC H II regions (Qiu et al., 2009; Shepherd, Testi & Stark, 2003; Shepherd et al., 1998). This lends crucial support to our conclusion of R1 (MM2) being an ionized jet.
Based on multiwavelength data, the results and discussion presented in this chapter enables us to draw a comprehensive picture of the star forming region associated with G19.88-0.53. The EGO, which is embedded in a massive cold clump within an IRDC, is unveiled to be a young and active protocluster harbouring several massive components in early evolutionary phases. In conjunction with ionized and H_2 jets, the kinematic picture reveals multiple molecular outflows driven by one or more members of the protocluster.

4.8 Summary

From the multi-frequency and multi-phase study of the EGO, G19.88-0.53 an interesting picture of it being a protocluster is revealed with multiple components spanning a wide evolutionary spectrum from hot cores in accretion phase to cores driving multiple outflows to possible UC H II regions. The main results are summarized below:

1. G19.88-0.53 is located within a massive dust clump of mass $1911\,M_{\odot}$, identified from the 870 μm map with the 4.5 μm emission towards its centre. Deeply embedded within this are nine distinct radio components and six dense mm cores unraveling a protocluster.

2. Deep uGMRT observations detect weak radio emission associated with G19.88-0.53. The radio continuum emission at 1391.6 MHz exhibits a linear structure consisting of two radio components, R1 and R2, in the east-west direction. The spectral index estimate of the radio component, R1, 0.58 ± 0.19, confirms it as a thermal jet.

3. The shock-excited H_2 emission is established from the NIR spectroscopy in concordance with the jet/outflow scenario.

4. Six dense and compact dust cores (MM1-MM6) are identified from the high resolution *ALMA* map at 2.7 mm map. The brightest of these cores, MM2, is coincident with the radio component R1. Based on the mass and size estimates, the cores qualify as high-mass star forming cores.

5. RTDs from detected CH_3OH transitions yield rotational temperature and beam averaged column densities that are consistent with hot cores.

6. The $J = 3 - 2$ transition of $C^{17}O$ towards MM6 show a clear inverse P-Cygni profile which is a signature of protostellar infall.

7. From the $J = 1 - 0$ transition of the $C^{18}O$, we detect the presence of a large scale molecular outflow in the direction of one of the lobes of the bipolar H_2 outflow. At higher resolution an additional collimated, bipolar outflow in the south-east and north-west direction is detected likely powered by MM2. This suggests that G19.88-0.53 harbours multiple outflows.

Chapter 5

G133.50+9.01: A likely cloud-cloud collision complex triggering the formation of filaments, cores and a stellar cluster

In this chapter, we investigate the Planck Galactic Cold Clump (PGCC), G133.50+9.01, using molecular line observation. Located in the field of the classical Cepheid SU Cas, a young cluster associated with G133.50+9.01 is identified by Majaess, Turner & Gieren (2012) using 2MASS and WISE photometry. The cluster that contains countless young stellar objects (YSOs) deviates from spherical symmetry and exhibits an apparent diameter of $3' \times 6'$. Zhang et al. (2018) detected 18 dust cores from the 850 μm map. We present new results on this complex based on a comprehensive analysis of the CO line kinematics and morphology in conjunction with infrared and sub-mm data to understand the related stellar population and dust component.

5.1 Distance to G133.50+9.01

Citing the nature of CO and HI emission, Majaess, Turner & Gieren (2012) speculate that the cluster may coincide with the complex in the foreground of SU Cas (which is at a distance of $418 \pm 12\,\mathrm{pc}$) or, beyond it at a distance, $d \leq 950\,\mathrm{pc}$. In their study, Zhang et al. (2018) use the Bayesian distance estimation method proposed by Reid et al. (2016). Here, trigonometric parallaxes from the Bar and Spiral Structure Legacy Survey and Japanese VLBI Exploration of Radio Astrometry are combined with the probability density function (PDF) for kinematic distance, displacement from the plane, and proximity to individual parallax sources to generate a combined PDF. Taking the observed centroid velocity of the $^{13}\mathrm{CO}\,(1-0)$ line, Zhang et al. (2018) estimate the distance to G133.50+9.01 to be

$0.61 \pm 0.14\,\mathrm{kpc}$. In this work, we implement an alternate approach to estimate the distance following the method outlined in Gong et al. (2017). This procedure makes use of the 3D dust reddening map[1] from Green et al. (2019). The dust reddening maps presented by these authors are based on 2MASS and Pan-STARRS 1 photometric data in combination with GAIA parallaxes. The distance to estimated by measuring the cumulative reddening, $E(B-V)$, along the line-of-sight. Four sightlines, marked by crosses in Fig. 5.2(b), are selected. The median cumulative reddening towards these four sightlines are plotted as a function of the distance in Fig. 5.1. The reddening plot towards the sightlines 1 and 3 overlap. The plot shows a steep rise in $E(B-V)$ at a distance of $\sim 840\,\mathrm{pc}$. Such a steep rise can be attributed to the dust reddening in G133.50+9.01. $E(B-V)$ towards the sightline 4 shows an additional steep rise at a distance of $\sim 4.2\,\mathrm{kpc}$. This possibly indicates the presence of a background, unrelated cloud. In the analysis presented in this chapter, we have taken $840\,\mathrm{pc}$ as the distance to G133.50+9.01.

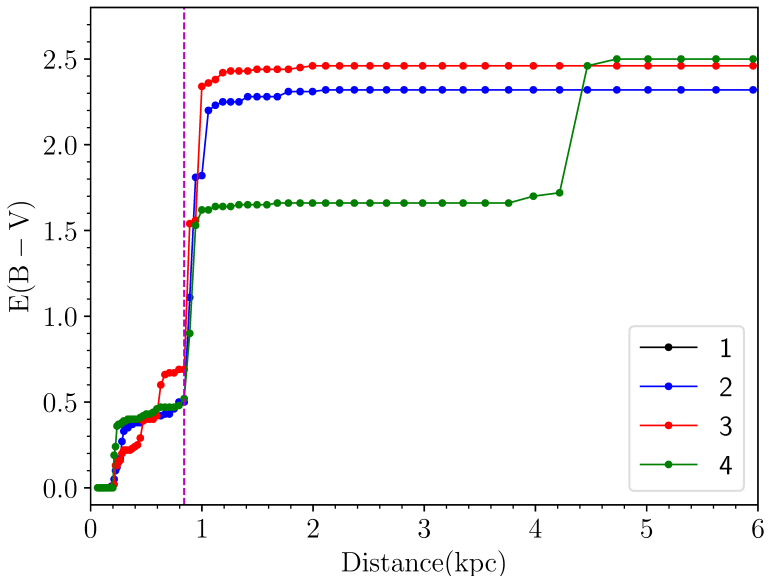

Figure 5.1: The cumulative reddening along four sightlines marked by crosses in Fig. 5.2(b). The reddening plot towards sightline 1 overlaps with that towards sightline 3. The dashed vertical line indicates the estimated distance to G133.50+9.01.

[1] http://argonaut.skymaps.info

5.2 CO morphology of G133.50+9.01 complex

Morphology of the G133.50+9.01 complex is deciphered using molecular line observations of CO. The ^{12}CO $(1-0)$ emission is usually considered to be optically thick throughout the molecular cloud, and hence an excellent tracer of its spatial extent, rather than the density distribution. The ^{13}CO $(1-0)$ emission, on the other hand, is less optically thick and probes the denser regions of the molecular cloud. The integrated intensity maps of ^{12}CO $(1-0)$ and ^{13}CO $(1-0)$ line emission towards G133.50+9.01 in three velocity ranges are shown in Fig. 5.2(a)-(c). Similar morphology is displayed in both emission lines. The molecular cloud has an elongated morphology in the north-east direction in the velocity range -19.4 to $-16.9\,\mathrm{km\,s^{-1}}$ as is evident from Fig. 5.2(a), an arc like morphology in the velocity range -16.9 to $-14.1\,\mathrm{km\,s^{-1}}$, shown in Fig. 5.2(b). In the range -14.1 to $-11.6\,\mathrm{km\,s^{-1}}$, a hemispherical, 'boomerang-like' morphology with a cavity opening towards the north-east and extended emission towards the north-west is noticeable in Fig. 5.2(c). The emission morphology seen in the above velocity ranges suggests the likely presence of two coalescing molecular clouds (hereafter G133a and G133b) associated with G133.50+9.01. The ^{12}CO $(1-0)$ and ^{13}CO $(1-0)$ spectra extracted, sampling these clouds and the intersection region is plotted in Fig. 5.2(d)-(f). The spectra corresponding to G133a and G133b have single peaked line profiles. From the peak of the ^{13}CO $(1-0)$ line, the systemic velocities of G133a and G133b are estimated to be $-16.9\,\mathrm{km\,s^{-1}}$ and $-14.1\,\mathrm{km\,s^{-1}}$, respectively. The intersection region clearly shows two velocity components. From the spectra of the interaction region presented, it is seen that for cloud G133b, the peak velocity of the ^{13}CO $(1-0)$ line is offset from the estimated systemic velocity of $-14.1\,\mathrm{km\,s^{-1}}$. This can be attributed to the interaction of the colliding clouds resulting in an intermediate velocity in the intersection region.

Fig. 5.2(d)-(f) show an additional velocity component at $\sim -10\,\mathrm{km\,s^{-1}}$ in all three spectra presented. To understand this, we construct channel maps of ^{12}CO $(1-0)$ and ^{13}CO $(1-0)$ emission in the velocity range -19.0 to $-7.0\,\mathrm{km\,s^{-1}}$. These are plotted in Fig. 5.3. As can be seen from the maps, emission from G133a and G133b peaks in the velocity range -18.0 to $-16.0\,\mathrm{km\,s^{-1}}$ and -15.0 to $-13.0\,\mathrm{km\,s^{-1}}$, respectively. An arc like morphology, as seen in Fig. 5.2(b) is evident at intermediate velocities. In the channel maps for the velocity range, -12.0 to $-9.0\,\mathrm{km\,s^{-1}}$, another component is visible which is consistent with the spectra in Fig. 5.2(d)-(f). As discussed in Section 5.1, the reddening plot along the sightline covering this component (# 4) shows two steep rises at distances 0.84 kpc and 4.2 kpc. Given that the velocity is $\sim -10\,\mathrm{km\,s^{-1}}$, this cloud is likely to be at a similar

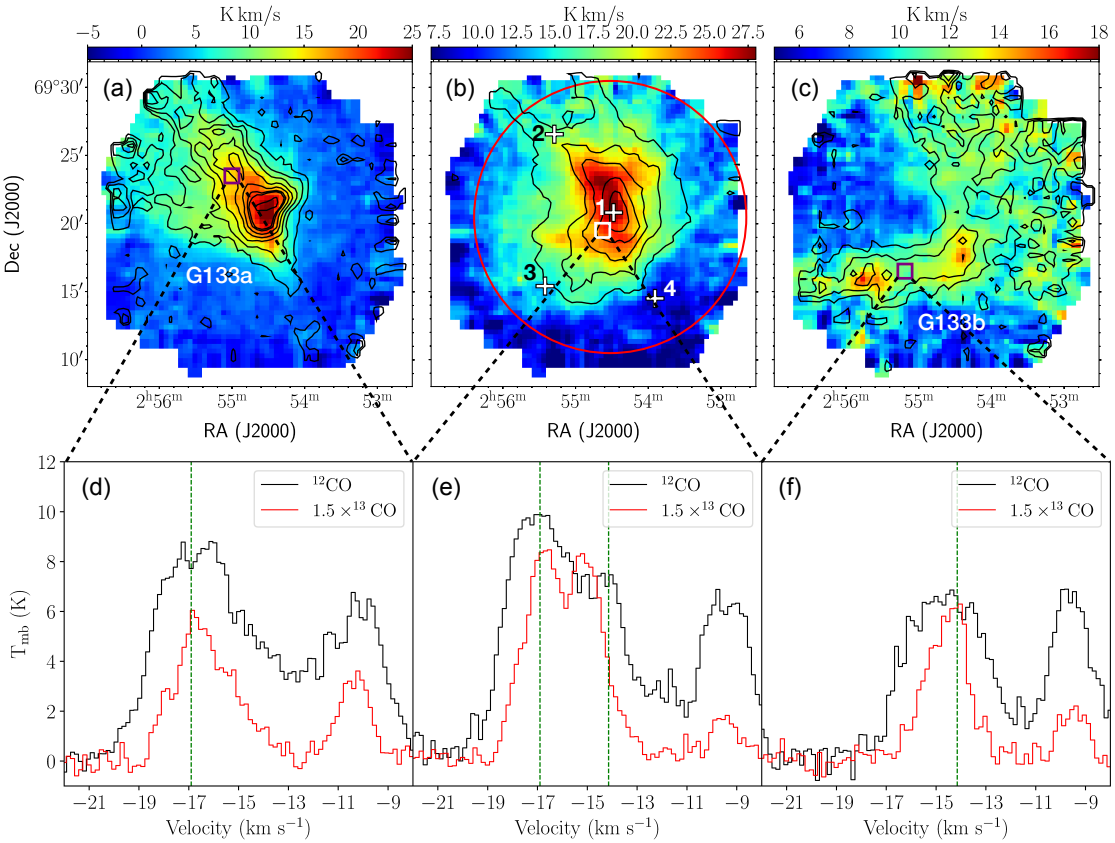

Figure 5.2: (a) The colour scale depicts the ^{12}CO $(1-0)$ integrated intensity within the velocity -19.4 to $-16.9\,\mathrm{km\,s^{-1}}$. The contours of the ^{13}CO $(1-0)$ emission over the same velocity range is overlaid in black with levels starting from 3σ and increasing in steps of 3σ ($\sigma = 0.5\,\mathrm{K\,km\,s^{-1}}$). (b) Same as (a) with the integration velocity range -16.9 to $-14.1\,\mathrm{km\,s^{-1}}$. The ^{13}CO $(1-0)$ contours start from 3σ and increases in steps of 2σ ($\sigma = 1.0\,\mathrm{K\,km\,s^{-1}}$). The white crosses mark the regions towards which the median cumulative reddening is estimated to find the distance. The red circle describes a region of radius $10'$ over which the young stellar population is identified (Section 5.6). (c) Same as (a) with the integration velocity range -14.1 to $-11.6\,\mathrm{km\,s^{-1}}$. The ^{13}CO $(1-0)$ contours start from 3σ and increases in steps of 2σ ($\sigma = 0.6\,\mathrm{K\,km\,s^{-1}}$). (d)-(f) The ^{12}CO $(1-0)$ (black) and ^{13}CO $(1-0)$ (red) spectra extracted at three different positions of the cloud complex G133.50+9.01, indicated by squares in (a)-(c). The vertical green lines indicate the systemic velocities of G133a and G133b as estimated from the ^{13}CO $(1-0)$ line.

distance as that of G133a and G133b with a background, unassociated cloud farther away. Under the assumption of local thermodynamic equilibrium, the total mass of the molecular clouds can be estimated from the optically thin ^{13}CO emission. Following Szűcs, Glover & Klessen (2016), the column density of ^{13}CO is calculated and from the abundance ratio of ^{13}CO to H_2, the H_2 column density is estimated. To determine the ^{13}CO column density,

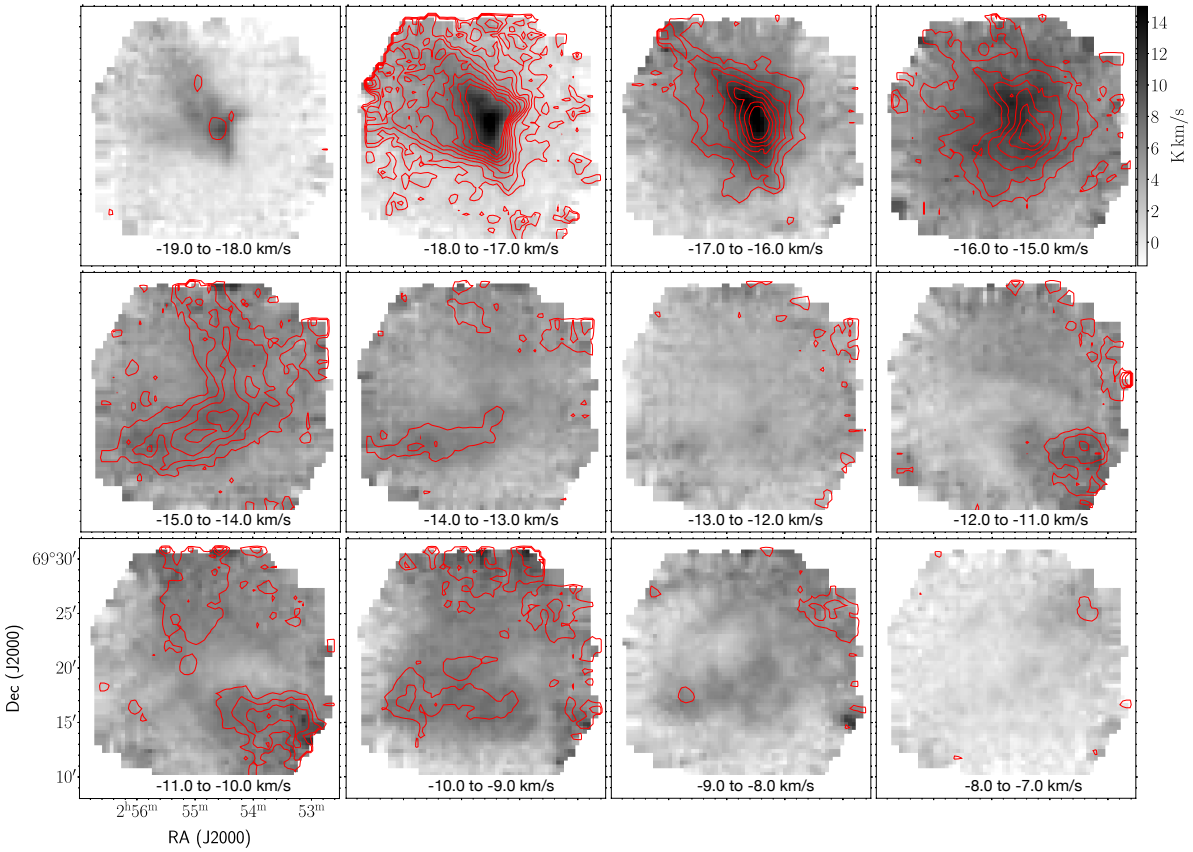

Figure 5.3: Chanel maps for region associated with G133.50+9.01. The grey scale shows the ^{12}CO $(1-0)$ channel map. Each map has a channel width of $1\,\mathrm{km\,s^{-1}}$. The contours of the ^{13}CO $(1-0)$ emission at each velocity channel is overlaid in red. The contours start at 3σ ($\sigma = 0.5\,\mathrm{K\,km\,s^{-1}}$) and increases in steps of 2σ.

the effective line-of-sight excitation temperature is determined. Combining the radiative transfer equation and the Rayleigh-Jeans law, the brightness temperature can be expressed as,

$$T_{\mathrm{mb}} = T_0 \left(\frac{1}{\mathrm{e}^{T_0/T_{\mathrm{ex}}} - 1} - \frac{1}{\mathrm{e}^{T_0/T_{\mathrm{bg}}} - 1} \right) (1 - \mathrm{e}^{-\tau}) \tag{5.1}$$

Here $T_0 = h\nu/k_{\mathrm{B}}$, h is the Planck's constant, k_{B} is the Boltzmann's constant, $T_{\mathrm{bg}} = 2.7\,\mathrm{K}$ is the background temperature, and τ is the optical depth. Assuming that the ^{12}CO $(1-0)$ emission is optically thick ($\tau \gg 1$), the excitation temperature per pixel of ^{12}CO $(1-0)$

spectral cube is given by

$$T_{\rm ex} = 5.5 \ln \left(1 + \frac{5.5}{T^{12}_{\rm mb,peak} + c_1} \right)^{-1} \tag{5.2}$$

where, $T^{12}_{\rm mb,peak}$ is the peak intensity of ^{12}CO $(1-0)$ at each pixel, $5.5\,{\rm K} = h\nu(^{12}{\rm CO})/k_{\rm B}$, and constant $c_1 = 0.82$ for $T_{\rm bg} = 2.7\,{\rm K}$. From the ^{12}CO $(1-0)$ spectral cube, the $T^{12}_{\rm mb,peak}$ map is built, from which, using Equation 5.2, the excitation temperature map of ^{12}CO $(1-0)$ is constructed which is shown in Fig. 5.4(a). We assume that the excitation temperatures of ^{12}CO $(1-0)$ and ^{13}CO $(1-0)$ are equal along the line-of-sight. Substituting for $T_{\rm ex}$ and the ^{13}CO $(1-0)$ peak brightness temperature in Equation 5.1, the pixel-wise optical depth can be derived following the equation,

$$\tau_{13} = -\ln \left[1 - \frac{T^{13}_{\rm mb,peak}}{5.3} \left\{ \left({\rm e}^{5.3/T_{\rm ex}} - 1 \right)^{-1} - c_2 \right\}^{-1} \right] \tag{5.3}$$

where, $T^{13}_{\rm mb,peak}$ is the peak brightness temperature of ^{13}CO $(1-0)$, $5.3\,{\rm K} = h\nu(^{13}{\rm CO})/k_{\rm B}$, and $c_2 = 0.16$. Assuming that the excitation temperature equals the kinetic temperature for all the energy states and the levels are populated according to Boltzmann distribution, the ^{13}CO column density is calculated from the optical depth using the following expression

$$N(^{13}{\rm CO}) = 3.0 \times 10^{14} \times \frac{\tau_{13}}{1 - e^{-\tau_{13}}} \times \frac{\int T^{13}_{\rm mb}(v) dv}{1 - e^{-5.3/T_{\rm ex}}} \tag{5.4}$$

$\int T^{13}_{\rm mb}(v) dv$ is the integrated intensity over velocity in units of ${\rm km\,s^{-1}}$. Fig. 5.4(b) shows the H_2 column density map constructed with a constant $[^{12}{\rm CO}/^{13}{\rm CO}]$ isotopic ratio of 77 (Wilson & Rood, 1994) and a $[{\rm H_2}/^{12}{\rm CO}]$ abundance ratio of 1.1×10^4 (Frerking, Langer & Wilson, 1982).

Considering the region within the 3σ level of the ^{13}CO $(1-0)$ emission integrated over the velocity range -19.4 to $-11.6\,{\rm km\,s^{-1}}$, the mean line-of-sight H_2 column density, $N({\rm H_2})$, is calculated to be $8.7 \times 10^{21}\,{\rm cm^{-2}}$. Subsequently, the total mass of the molecular cloud complex ($= N({\rm H_2})\mu_{\rm H_2} m_{\rm H} A$; A is the physical area of the cloud complex, $m_{\rm H}$ is the mass of hydrogen atom) is estimated to be $2.6 \times 10^3\,M_\odot$. Here, the mean molecular weight, $\mu_{\rm H_2}$ is taken to be 2.8. The individual masses of G133a and G133b are computed to be $1.1 \times 10^3\,M_\odot$ and $1.4 \times 10^3\,M_\odot$, respectively, with the assumption that both clouds have equal contribution to the mass at the intersection.

Fig. 5.4(a) shows the ^{12}CO $(1-0)$ excitation temperature map overlaid with the contours of ^{13}CO $(1-0)$ emission integrated over the velocity range -16.9 to $-14.1\,{\rm km\,s^{-1}}$. The

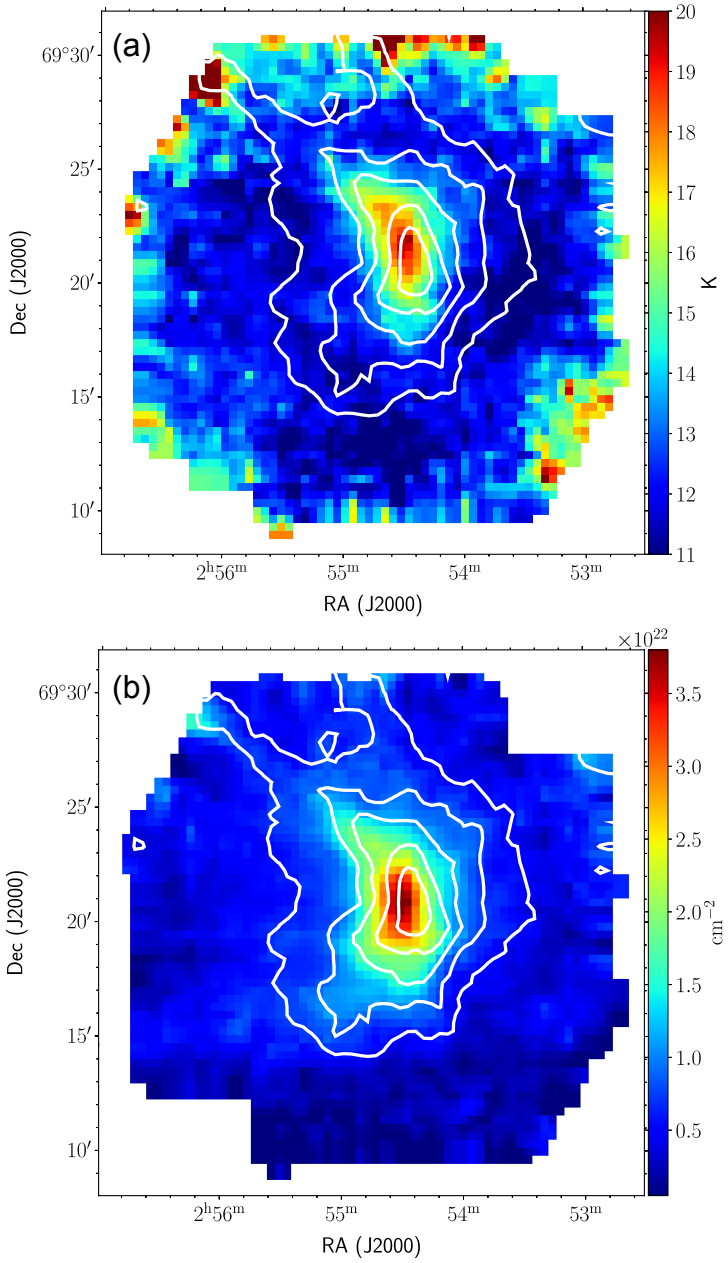

Figure 5.4: (a) The excitation temperature map of G133.50+9.01 derived from the peak intensity of the ^{12}CO $(1-0)$ emission. (b) The H_2 column density map of the region associated with G133.50+9.01 constructed following the steps described in Section 5.2. The white contours correspond to the ^{13}CO $(1-0)$ emission within the velocity range -16.9 to $-14.1\,\mathrm{km\,s^{-1}}$. The contour levels are same as in Fig. 5.2(b).

intersection of the clouds, G133a and G133b reveals an open arc structure. The ^{13}CO emission also follows a similar arc like morphology. The radius of curvature of the arc is $\sim 1.6\,\mathrm{pc}$. The excitation temperatures within this arc varies from $13-20\,\mathrm{K}$ and is higher

than that of the ambient cloud ($\sim 11\,\mathrm{K}$). The H_2 column density map given in Fig. 5.4(b) also reveals a density enhancement along this arc.

5.3 Cloud kinematics

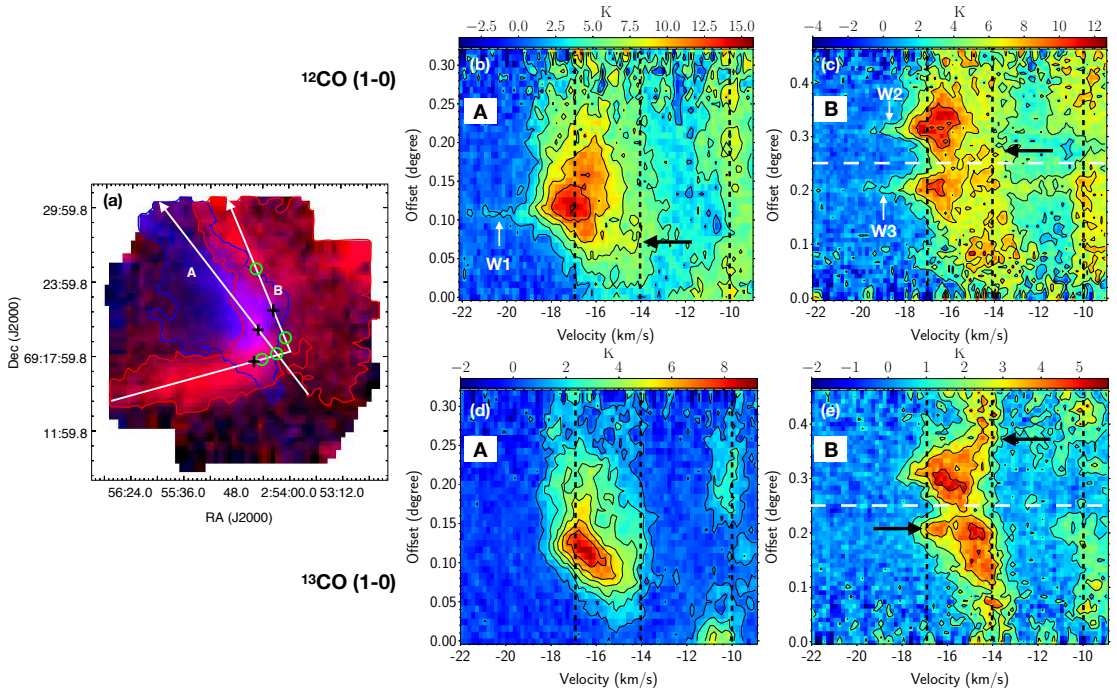

Figure 5.5: (a) Two-colour composite integrate intensity map of ^{12}CO $(1-0)$ integrated between -19.4 to $-16.9\,\mathrm{km\,s^{-1}}$ (blue) and -14.1 to $-11.6\,\mathrm{km\,s^{-1}}$ (red) of the G133.50+9.01 complex. The 3σ contour of the ^{13}CO $(1-0)$ emission (same as in Fig. 5.2a and c) at both velocity ranges is overlaid in blue and red. A and B are the cuts along which the PV slices are extracted, sampling G133a and G133b, respectively. (b) and (d) PV diagram of ^{12}CO and ^{13}CO, respectively along the cut A. (c) and (e) Same as (b) and (d) along the cut B. The horizontal dashed line delineates the PV slices on either side of the bend in B. The contours start at 3σ and increases in steps of 4σ ($\sigma = 0.6\,\mathrm{K}$ for ^{12}CO and 0.3 K for ^{13}CO). The vertical dashed lines represent the systemic velocities of G133a, G133b and the cloud at $\sim -10\,\mathrm{km\,s^{-1}}$. The bridging features with intermediate velocity are marked by black arrows. The positions of the bridging features on the PV cut is marked by green circles in (a). The ^{12}CO wings are indicated by white arrows and their positions on the PV cut are indicated by black crosses in (a).

The ^{12}CO $(1-0)$ and ^{13}CO $(1-0)$ position-velocity (PV) diagram of the G133.50+9.01 complex is constructed to understand its velocity structure. Fig. 5.5(a) depicts the two-colour composite integrated intensity map of ^{12}CO $(1-0)$ integrated between -19.4 to $-16.9\,\mathrm{km\,s^{-1}}$ (blue) and -14.1 to $-11.6\,\mathrm{km\,s^{-1}}$(red). The 3σ contours of the integrated

$^{13}\mathrm{CO}\,(1-0)$ within the same velocity ranges is overlaid. PV slices are extracted along two directions, A and B, highlighted in Fig. 5.5(a). These slices probe G133a and G133b, respectively. Both, $^{12}\mathrm{CO}\,(1-0)$ and $^{13}\mathrm{CO}\,(1-0)$ emission show intermediate "bridging features" between the peak velocities, -16.9 and $-14.1\,\mathrm{km\,s^{-1}}$ highlighted by black arrows in Fig. 5.5(b), (c) and (e). Apart from these, in Fig. 5.5(b) and (c), high-velocity $^{12}\mathrm{CO}$ wings are also evident.

5.4 Dust filaments and cores

Fig. 5.6 shows the $850\,\mu\mathrm{m}$ dust emission towards G133.50+9.01. A visual inspection of the $850\,\mu\mathrm{m}$ map reveals that the emission from the dust component has a filamentary structure in the north-south direction that bifurcates at the ends. The skeletons of the filaments are overlaid on the image. Localized dust peaks are seen along the filaments. We use the FellWalker clump identification algorithm (Berry, 2015), which is part of the Starlink CUPID package, to identify the dust cores in this region. A detection threshold of 2.5σ ($\sigma = 18.1\,\mathrm{mJy\,beam^{-1}}$) is used and pixels outside the 2.5σ level are considered noise. Using this method we detect 14 dust cores along the filaments that are named according to their positions in the field. Relative to the central core, C1, four cores, N1-N4, extend towards the north and five cores, S1-S5, extend towards the south along one of the filaments. The remaining four cores, NE1 and SE1-SE3 lie along the other filaments in the north-east and south-east directions, respectively. The retrieved apertures of these cores are superimposed on the $850\,\mu\mathrm{m}$ map shown in Fig. 5.6. Correlation with Fig. 5.4(b) shows that the detected cores are located within the arc structure displaying enhanced column density. The mass of each core is estimated from the total $850\,\mu\mathrm{m}$ flux density integrated within the core aperture. Assuming thermal emission from optically thin dust, the following expression is used,

$$M_C = \frac{S_\nu d^2}{\kappa_\nu B_\nu(T_d)} \tag{5.5}$$

Here, S_ν is the flux density at $850\,\mu\mathrm{m}$, d is the distance, T_d is the dust temperature of the cores taken to be the mean excitation temperature, 15.3 K, within the open arc structure, and $\kappa_\nu = 0.1(\nu/1200\,\mathrm{GHz})^\beta$ is the dust opacity. β, the dust emissivity index, is assumed to be 2. The effective radii, $r = (A/\pi)^{0.5}$, of the dust cores are determined from the area, A, enclosed within the retrieved apertures. Peak positions, radii and masses of the dust cores are tabulated in Table 5.1.

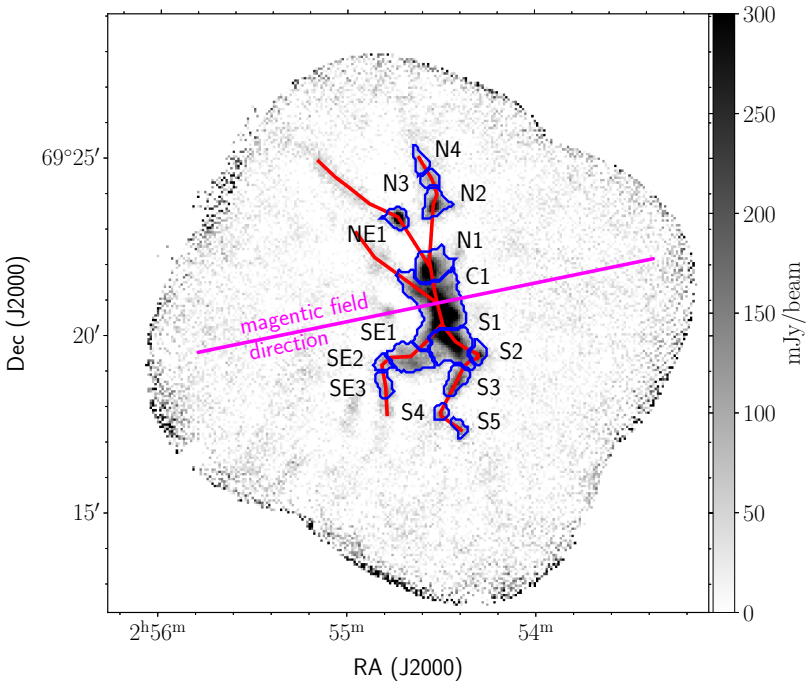

Figure 5.6: The dust emission at 850 μm in the region surrounding G133.50+9.01 is presented here. The FellWalker retrieved apertures of the dust cores are outlined in blue and are labelled according to their positions in the field. The skeletons of the visually identified filaments are sketched in red. The magenta line represents the orientation of the magnetic field with respect to the filaments.

5.5 Magnetic field orientation

Planck polarization data is used to determine the magnetic field orientation in the vicinity of G133.50+9.01. Following the IAU convention, the linear polarization angle (PA) is given by, $\psi_{\rm IAU} = 0.5 \times arctan(-U/Q)$ in the Galactic coordinate system (Planck Collaboration et al., 2015). The plane of sky orientation of the magnetic field is obtained by adding 90° to the PA ($\chi' = \psi_{\rm IAU} + 90^{\circ}$). The position angle of the magnetic field in the equatorial coordinate system, FK5, is then estimated following the discussion in Corradi, Aznar & Mampaso (1998), where

$$\psi = arctan \left[\frac{cos\left(l - 32.9^{\circ}\right)}{cos\, b\, cot\, 62.9^{\circ} \; - \; sin\, b\, sin\left(l - 32.9^{\circ}\right)} \right] \tag{5.6}$$

Here, ψ is the angle subtended by the directions of the equatorial north and the Galactic north at each pixel of the *Planck* polarization maps. The orientation of the magnetic field at each pixel with Galactic coordinates, l and b is then transformed from the Galactic

Table 5.1: Physical parameters of the identified dust cores associated with G133.50+9.01.

Dust Core	Peak position		Radius	Mass
	α(J2000) ($^{\rm h\,m\,s}$)	δ(J2000) ($^\circ\,'\,''$)	(pc)	($M_\odot$)
C1	2 54 30.33	69 20 39.80	0.20	86.0
N1	2 54 34.11	69 21 51.80	0.12	27.9
N2	2 54 31.84	69 23 39.80	0.09	10.8
N3	2 54 31.84	69 24 15.80	0.06	2.8
N4	2 54 35.63	69 24 43.80	0.07	2.5
NE1	2 54 43.21	69 23 19.78	0.08	9.5
S1	2 54 25.80	69 19 47.79	0.14	34.6
S2	2 54 17.49	69 19 27.76	0.06	5.2
S3	2 54 25.05	69 18 43.79	0.09	8.6
S4	2 54 30.34	69 17 47.80	0.05	2.5
S5	2 54 24.31	69 17 23.79	0.05	2.6
SE1	2 54 37.89	69 19 15.80	0.12	13.3
SE2	2 54 47.70	69 19 15.76	0.05	2.0
SE3	2 54 46.94	69 18 27.76	0.07	3.7

coordinate system (χ') to the equatorial system (χ) using the relation,

$$\chi = \chi' - \psi \tag{5.7}$$

The mean magnetic field orientation is determined by taking the average of the χ values that lie within the 3σ level of the ^{13}CO $(1-0)$ emission over the velocity range -19.4 to $-11.6\,{\rm km\,s^{-1}}$. The orientation is estimated to be $99.1 \pm 5.6^\circ$ east of north and is traced in Fig. 5.6 with respect to the filaments identified from the 850 μm map.

5.6 Associated young stellar population

Using 2MASS-$K_{\rm s}$ and WISE photometry data, Majaess, Turner & Gieren (2012) have discovered a crowded cluster of 53 YSOs associated with G133.50+9.01. We revisit the cluster detection and YSO identification by considering a larger (radius of $10'$) region, centred at 02:54:31.4 +69:20:32.5, which effectively samples the entire G133.50+9.01 cloud complex. The circular region over which the YSOs are identified is sketched in Fig. 5.2b and Fig. 5.9. For YSO identification, we implement the colour classification scheme of Koenig & Leisawitz (2014) using the improved ALLWISE catalogue (Cutri & et al., 2013). After removal of fake or spurious sources and extragalactic contaminants, a WISE colour-colour

diagram is constructed and shown in Fig. 5.7. Using the colour criteria set by Koenig & Leisawitz (2014), we identify 11 (39%) Class I and 14 (50%) Class II sources in our field. Sources not satisfying the prescribed criteria could be either Class III/weak disk YSOs, blue transition disk objects, or AGB stars. Comparing our results with that of Majaess, Turner & Gieren (2012), we find that 41 ($\sim 77\%$) of the sources classified as YSOs by Majaess, Turner & Gieren (2012), are filtered out as spurious sources on using the stringent and improved source reliability approach proposed by Koenig & Leisawitz (2014).

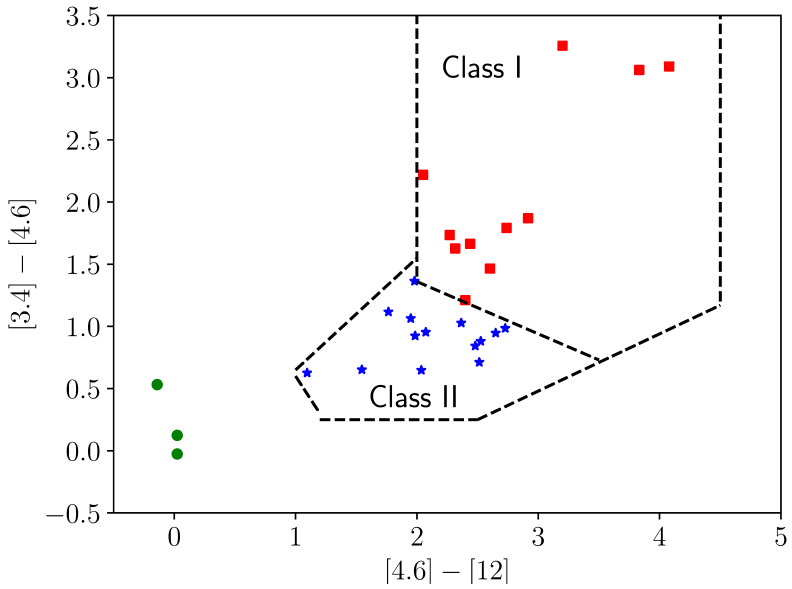

Figure 5.7: WISE color-color diagram for the bands, 3.4, 4.6 and 12 μm used to identify and classify YSOs associated with G133.50+9.01. The dashed lines denotes the criteria used by Koenig & Leisawitz (2014) to delineate the YSO classes. Green circles denote the sources that do not satisfy the YSO criteria.

5.7 Signatures of cloud-cloud collision

The observed CO morphology and kinematics suggest a cloud-cloud collision scenario for G133.50+9.01 with two distinct cloud components, G133a and G133b. We analyse this complex along the lines discussed in Gong et al. (2017) for the dark cloud L1188. Before we discuss the distinct observational features seen, it is crucial to examine the possibility of the two cloud components being gravitationally bound. The virial mass of the cloud

complex can be estimated using the expression (Pillai et al., 2011),

$$M_{\rm vir} = \frac{5\,\sigma^2\,R}{G} \tag{5.8}$$

where, R is the effective radius of the cloud and $\sigma(=\Delta{\rm V}/\sqrt{8\ln2})$ is the velocity dispersion. Both these parameters are obtained using the ^{13}CO $(1-0)$ line. R is taken to be equal to $(A/\pi)^{0.5}$, where A is the area considered to derive the total cloud mass and is estimated to be ~ 2.1 pc. Fitting a Gaussian profile to the ^{13}CO $(1-0)$ spectrum of the entire cloud, we get the line width, ΔV to be $3.5\,{\rm km\,s^{-1}}$. Similar line width is obtained for the spectrum of the intersection region. Taking this, the velocity dispersion is calculated to be $1.5\,{\rm km\,s^{-1}}$. Using these values, we compute the virial mass to be $5.8\times10^3\,M_\odot$, which is more than twice the total mass of the cloud complex, $2.6\times10^3\,M_\odot$. Within the uncertainties involved in the mass estimations, it is seen that the total mass of the G133.50+9.01 cloud complex is not large enough to be able to gravitationally bind the two clouds. This suggests that the physical association of G133a and G133b with each other must be an accidental event.

In recent years, numerical hydrodynamical simulations and observational studies (e.g. Fukui et al., 2018; Takahira, Tasker & Habe, 2014; Torii et al., 2017) have shed light on the various characteristic signatures of cloud-cloud collision. As is evident in Fig. 5.2, the two clouds, G133a and G133b, are separated by a velocity difference of $\sim 2.8\,{\rm km\,s^{-1}}$. This separation provides a lower limit to the relative collision velocity. The actual collision velocity might be higher than this because of the projection effect (Fukui et al., 2015). As propounded by Inoue & Fukui (2013) and Fukui et al. (2015), the isotropic turbulence is enhanced at the collision-shocked layer, irrespective of the direction of collision. Hence, the velocity spread at the shocked layer can be taken to be similar as the relative collision velocity. Following this, we assume the relative velocity to be the FWHM of the ^{12}CO $(1-0)$ line extracted over the intermediate velocity range (-16.9 to $-14.1\,{\rm km\,s^{-1}}$) that corresponds to the shock-compressed layer. The FWHM of this line is found to be $5.0\,{\rm km\,s^{-1}}$. Comparing with the velocity difference between the two clouds, the relative collision velocity translates to a relative motion of the two clouds of $\sim 56^\circ$ with respect to the line-of-sight.

Another pronounced observational signature of cloud-cloud collision is the “bridging features" detected in the PV diagram. Haworth et al. (2015a,b) made synthetic ^{12}CO PV diagrams using the cloud-cloud collision model data simulated by Takahira, Tasker & Habe (2014). From these observations it was found that the shocked layer is characterised by broad intermediate velocity features, that bridge the colliding clouds in the velocity space. The bridging features often appear at the spots of collision. Several recent studies have provided observational confirmation of such features in the colliding cloud complexes (e.g.

Fukui et al., 2016; Gong et al., 2017; Torii et al., 2017). On examining the PV diagram of G133.50+9.01 along the two identified directions A and B as depicted in Fig. 5.5, we find at least four bridging features clearly visible in the $^{12}\mathrm{CO}\,(1-0)$ and $^{13}\mathrm{CO}\,(1-0)$ emission in the intermediate velocity range of -16.9 to $-14.1\,\mathrm{km\,s^{-1}}$. The green circles in Fig. 5.5(a) indicate the positions where the bridges appear along the PV cuts. These positions correspond to the spots of collision of the two clouds consistent with the discussions in Fukui et al. (2018). The presence of these bridging features suggests the existence of turbulent gas in the shocked layer that is excited by the collision of the clouds. In addition, the velocity structure in G133.50+9.01 further reveals three high-velocity $^{12}\mathrm{CO}\,(1-0)$ wings, W1, W2 and W3. The locations of these identified wings along the PV cuts are shown in Fig. 5.5(a). As discussed by Gong et al. (2017, 2019), these high-velocity wings could stem from the outflow(s) driven by one or more YSOs or protostellar cores that have been identified in the intersection region (see Section 5.8).

We examine the cloud at $-10\,\mathrm{km\,s^{-1}}$ in the plotted PV diagrams. This cloud displays a rather diffuse morphology in the PV diagrams and is well separated from G133a and G133b. Along the cut B shown in Fig. 5.5c, an apparent connecting feature is seen but does not resemble a typical 'bridging' structure expected in collision events. Thus, in all likelihood this cloud could well be in the foreground and not physically associated with the G133.50+9.01 complex.

The morphology of the G133.50+9.01 cloud complex as seen in Figs. 5.2(a)-(c) and 5.5(a), unveils the picture of an elongated and smaller cloud, G133a, likely in collision with the larger cloud, G133b which displays a 'boomerang-like' structure with a cavity opening in the north-east direction. This is in concordance with simulations done by Anathpindika (2010), Habe & Ohta (1992), Takahira, Tasker & Habe (2014) and Torii et al. (2017). These authors show that when two clouds of different sizes collide, the smaller cloud creates a cavity on the surface of the larger cloud. Evidence supporting this picture was first perceived in the Galactic H II region, RCW 120 (Torii et al., 2015). Here, the observed infrared bubble (or ring) morphology is well explained by cavity creation due to cloud-cloud collision rather than attributing the same to the conventional expansion of HII region scenario for the bubble origin.

5.8 Induced filament, core and cluster formation

As discussed in Section 5.4, distinct filaments are identified which are located in the intersection region of clouds G133a and G133b. As seen in Figs. 5.6 and 5.9(b), the filaments

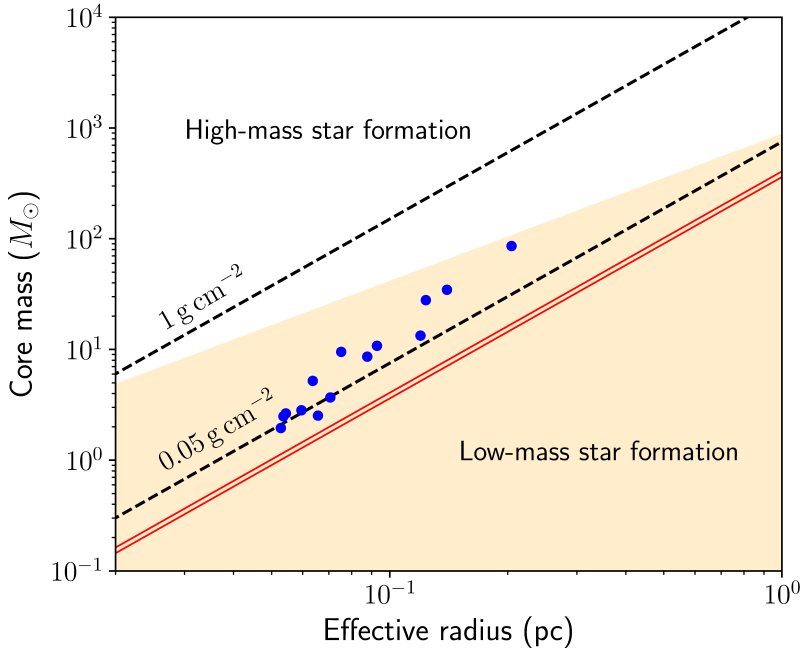

Figure 5.8: The mass of the dense cores, M_C, identified from the 850 μm map of G133.50+9.01 is plotted as a function of effective radii, r and depicted by blue circles. The red lines indicate the surface density thresholds of 116 $M_\odot\,\mathrm{pc}^{-2}(\sim 0.024\,\mathrm{g\,cm}^{-2})$ and 129 $M_\odot\,\mathrm{pc}^{-2}(\sim\ 0.027\,\mathrm{g\,cm}^{-2})$ for active star formation from Lada, Lombardi & Alves (2010) and Heiderman et al. (2010), respectively. The shaded region delineates the low-mass star forming region that do not satisfy the criterion $m(r) > 870\,M_\odot(r/\mathrm{pc})^{1.33}$ (Kauffmann et al., 2010b). The black dashed lines represent the surface density threshold of 0.05 and 1 $\mathrm{g\,cm}^{-2}$ defined by Urquhart et al. (2014) and Krumholz & McKee (2008), respectively.

detected in G133.50+9.01 present a hub-filament structure. Filament formation is generally understood from the hierarchical collapse of molecular clouds (Motte, Bontemps & Louvet, 2018, and references therein). Following the Hydrodynamic simulations by Habe & Ohta (1992) and Anathpindika (2010), it is seen that the sites of cloud-cloud collision are characterised by a shock compressed layer due to a bow-shock driven by the smaller cloud into the larger cloud. This augurs well with alternate hypothesis for filament formation that has been presented by Inoue & Fukui (2013) and Inoue et al. (2018). Based on their numerical studies using isothermal MHD simulations, these authors conclude that the collision of inhomogeneous clouds lead to the formation of dense filaments in the shock compressed layer, where the magnetic field is amplified in the direction perpendicular to the filament. The clouds are compressed multi-dimensionally except in the direction perpendicular to

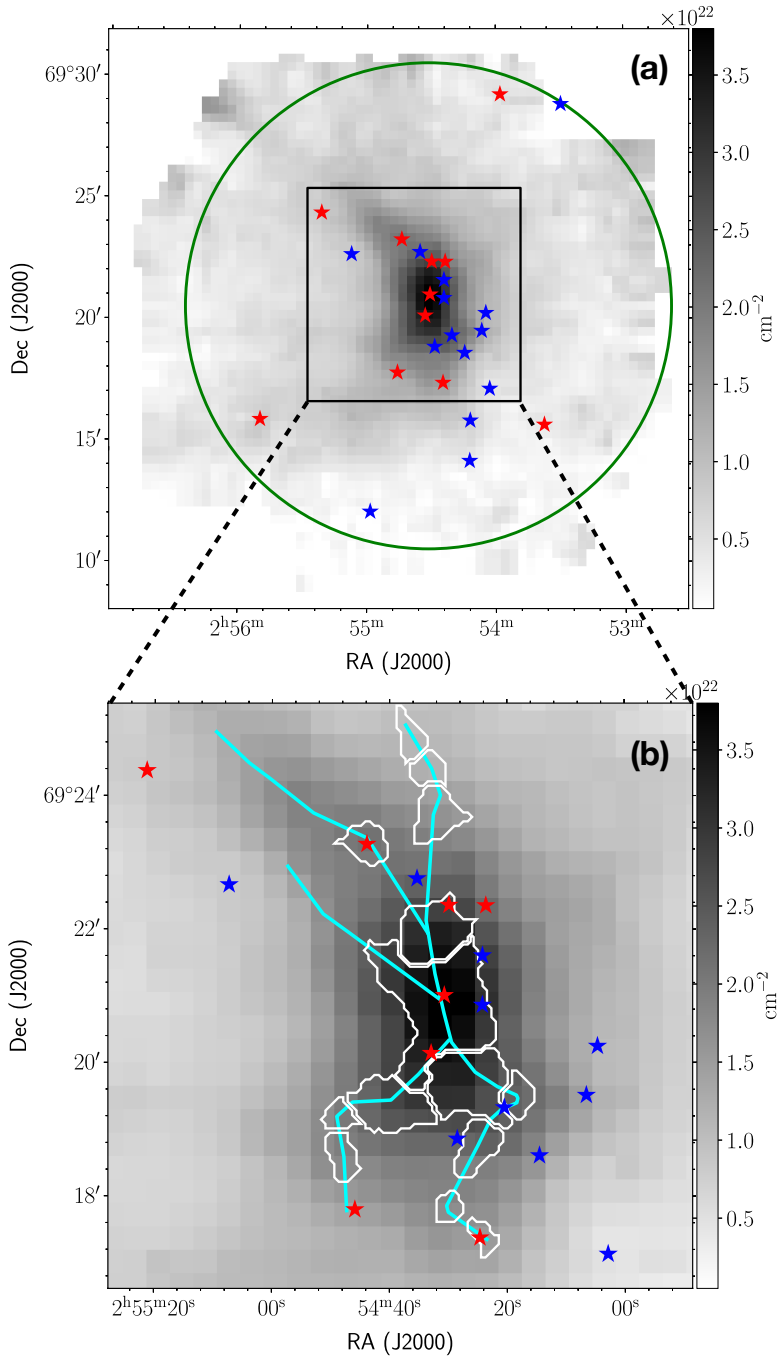

Figure 5.9: (a) The H_2 column density map same as in Fig. 5.4(b). The green circle indicates the region over which the YSOs are identified. (b) A zoom-in on the arc which has an enhanced column density. The Class I and Class II YSOs identified, as discussed in Section 5.6, are marked by red and blue stars, respectively. The apertures of the 850 μm dense cores and the skeletons of the filaments are overlaid on (b).

the background magnetic field, which results in filamentary structures.

In the case of G133.50+9.01, the shock compressed layer created at the interacting front manifests as an open arc structure in the $^{12}\mathrm{CO}\,(1-0)$ and $^{13}\mathrm{CO}\,(1-0)$ maps in the intermediate velocity range, -16.9 to $-14.1\,\mathrm{km\,s^{-1}}$ as is seen in Fig. 5.2(b). This arc has a high excitation temperature ($13-20\,\mathrm{K}$), compared to the ambient medium and an enhanced H_2 column density, evident from Fig. 5.4. The increase in the H_2 column density within the arc can be due to the multi-dimensional compression of the shocked layer. The filaments detected in the $850\,\mu\mathrm{m}$ map of G133.50+9.01 follows the same orientation of the arc structure. The direction of the magnetic field in the region associated with G133.50+9.01 is determined in Section 5.5, and is sketched in Fig. 5.6. Concurrent with the results from the MHD simulation by Inoue & Fukui (2013), the background magnetic field, probed using *Planck* data, is seen to be oriented perpendicular to the filamentary structure. It should be noted that the arc could also be the result of stellar feedback (radiation pressure, expanding HII region, outflows from YSOs). From our literature survey, we find no HII region associated with G133.50+9.01, however given the YSOs detected, one cannot conclusively rule out stellar feedback.

Collision induced enhanced density in the intersection region triggers formation of dense cores that accrete matter from the natal filaments. We have detected 14 dust cores in G133.50+9.01, the masses of which are estimated and found to lie within $\sim 2-86\,M_{\odot}$ with sizes ranging between $\sim 0.05-0.2\,\mathrm{pc}$. In comparison, Zhang et al. (2018) detect 18 dust cores from the $850\,\mu\mathrm{m}$ continuum map. They use the GaussClumps algorithm for core identification, where only the cores with peak intensities above 5σ are considered. Correlating the dust cores identified by these authors with the ones we extracted using the FellWalker algorithm, we find that majority of the core peaks match. Further, the central core, C1, detected by us encompasses five core peaks identified by Zhang et al. (2018).

In Fig. 5.8, which is adapted from Yuan et al. (2017) and Liu et al. (2020), we correlate the mass and effective radius of the clumps and interpret their nature. As is discernible from the figure, the dust cores associated with G133.50+9.01 lie comfortably above the mass surface density threshold for active star formation proposed by Lada, Lombardi & Alves (2010) and Heiderman et al. (2010). Probing the mass regime possible, we examine the empirical relation, $m(r) > 870\,M_{\odot}(r/\mathrm{pc})^{1.33}$, given by Kauffmann et al. (2010b) for high-mass star forming cores. From the estimated mass and radius, the cores associated with G133.50+9.01 do not qualify this threshold and hence should be devoid of high-mass stars. This is somewhat contrary with regards to the limit of $0.05\,\mathrm{g\,cm^{-2}}$ on surface density set by Urquhart et al. (2014) for massive star formation. Barring one, all the active star-forming

cores are above this threshold. Hence, it is likely that the more massive cores in our sample are potential high-mass star-forming regions.

We also probe the star formation activity associated with G133.50+9.01 by inspecting the distribution of the identified YSOs in the region. In Fig. 5.9(a), we show the YSOs overlaid on the column density map. Of the 25 YSOs detected, a distinct cluster of 18 YSOs is seen to be located in the intersection region. Fig. 5.9(b) shows an enlarged view with the detected filaments and cores overlaid. From the relative collision velocity of the clouds which is estimated to be $5.0\,\mathrm{km\,s^{-1}}$, we compute the timescale of collision between G133a and G133b. The ratio of the cloud size, 4.2 pc, to the relative collision velocity gives a collision timescale of $\sim 0.8\,\mathrm{Myr}$. It should however be noted that this gives an order-of-magnitude estimate, at best. The value might vary by a factor of ~ 2 owing to projection effects in space and velocity and to the unknown configuration of the clouds before collision (Fukui et al., 2014). Nonetheless, the timescale derived is longer than the typical lifetimes of Class I YSOs and is comparable to the lifetime of Class II YSOs. As discussed in Dunham et al. (2015) and Evans et al. (2009), the age estimates of Class I and Class II YSOs are 0.4-0.7 Myr and $2 \pm 1\,\mathrm{Myr}$, respectively. The scenario that has unfolded in G133.50+9.01 gives compelling evidence of this being a bona fide case of collision induced cluster formation. Similar results are obtained in several other studies focused towards cloud collision and induced cluster formation (e.g. Gong et al., 2017; Torii et al., 2011).

5.9 Conclusions

Gas kinematics studied using the CO lines show a picture of colliding clouds G133a and G133b triggering the formation of a complex network of filaments, dense cores and YSOs in G133.50+9.01 complex. Fig. 5.10 depicts a schematic of the chain of events occurring. Clouds G133a and G133b with a velocity difference of $\sim 2.8\,\mathrm{km\,s^{-1}}$ are likely to have collided forming a shock-compressed layer in the intersection region. Conforming to MHD simulations, the formation of a complex network of filaments is deduced from the $850\,\mu\mathrm{m}$ map. 14 dust cores that accrete matter from the natal filaments are also identified. The over-density of Class I and II YSOs along the intersection arc advocates for collision induced cluster formation in G133.50+9.01. Keeping in mind that the PMO observations presented in this chapter might not have sampled the entire complex, an accurate interpretation of the morphology of the colliding clouds is difficult. Further, the resolution of the data used is not adequate to correlate the observed scenario with either the spherical cloud collision models (e.g. Habe & Ohta, 1992; Takahira, Tasker & Habe, 2014) or filamentary cloud

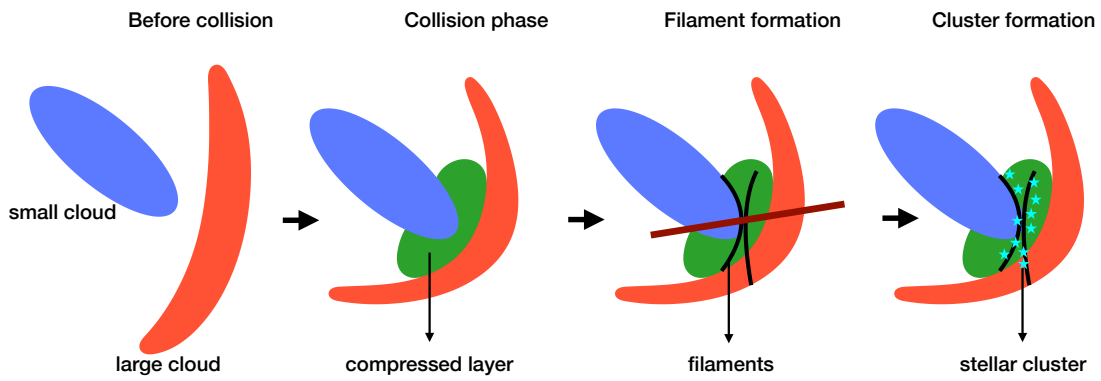

Figure 5.10: A schematic of the cloud-cloud collision in G133.50+9.01 depicting the scheme of events from the time of collision of G133a (small cloud) with G133b (large cloud). The orientation of the background magnetic field is indicated by the maroon line.

collision simulations (Li, Klein & McKee, 2018). Nonetheless, observational features seen makes G133.50+9.01 an interesting candidate to probe cloud-cloud collision. With follow-up high-resolution molecular line and dust continuum observations, viable models can be explored to explain the observed signatures.

Chapter 6

Conclusion and Future Work

High-mass stars play a major role in deciding the fate of the Universe. Despite being a major contributor to the energetics and chemistry of galaxies, our understanding of high-mass star formation is sparse, more so for the initial phases of their formation. A universal theory elucidating the formation mechanism across the mass range, though is much sought after, is still elusive. The potential of high-sensitivity and high-resolution observation in addressing and validating the proposed theories is well chronicled. With the aim of exploring the poorly understood processes involved in the early stages of high-mass star formation, in-depth observational investigation of a few high-mass star-forming regions is carried out in this thesis work. The GLIMPSE survey, with its detection of a large population of EGOs, that are now believed to trace the earliest phases of high-mass star formation, opened an excellent window of opportunity for research in this direction. The work in this thesis is primarily focussed towards these objects. Following a multiwavelength approach has enabled in constructing a detailed account of the star formation activity and also helped in studying the surrounding medium of the regions under scrutiny. Key results from this research work, that utilized several dedicated observations as well as data from archives, are summarised in this chapter. In addition, potential future research that is planned to be undertaken is briefly discussed.

6.1 Summary of investigations

A multiwavelength study of the EGO, G12.42+0.50 and its associated environment is the first case study and presented in Chapter 3. Low-frequency radio continuum map of G12.42+0.50 at 1390 MHz reveals a linear structure extended in the north-east and south-west direction, comprising of two compact radio components, R1 and R2. The low-resolution 610 MHz map shows a single component coincident with R1, and a discernible

elongation is evident towards R2. Two scenarios unfold in understanding the nature of the radio emission. Given the spherical and compact morphology of R1, the radio emission is investigated under the UC H II region framework. Assuming the emission at 1390 MHz to be optically thin and arising from a homogeneous and spherical medium, the Lyman continuum flux from R1 translates to an ionizing source of spectral type of $\mathrm{B1} - \mathrm{B0.5}$ that is suggestive of a star of mass $\sim 9 - 12\,M_{\odot}$. Motivated by the very nature of G12.42+0.50, which is identified as an EGO and hence likely associated with jets/outflows, we explore an alternate scenario along the lines of a possible ionized jet. The spectral index values of $0.3 - 0.9$ along R1 and R2, and various observed characteristics are consistent with radio emission originating due to thermal *free-free* emission from an ionized jet. Presence of shock-excited H_2 and [FeII] line emission, as confirmed from NIR narrow-band imaging and spectroscopy, lend support to the jets/outflows picture. With compelling evidence advocating for both the UC H II region and ionized jet scenario, we are prompted to consider the co-existence of the UC H II region with an ionized jet being powered by the same YSO. A massive clump, C1, of mass 1375 $M_{\odot}$ and total luminosity $2.8\times10^4\,L_{\odot}$, is identified from the APEX+Planck 870 μm map, which envelopes the detected radio and the enhanced, extended 4.5 μm emission. The high-resolution 1.1 mm SMA map probes the inner regions of the clump where it harbours two, dense and bright compact cores, SMA1 and SMA2. Two-component modelling of C1 reveals the presence of an inner warm component enveloped by an extended outer, cold component.

Of the seven molecular species, from the MALT90 survey, detected towards G12.42+0.50, the optically thick lines, $\mathrm{HCO^+}$ and HCN show signatures of protostellar infall. The infall velocity and the mass infall rate are estimated to be $1.8\,\mathrm{km\,s^{-1}}$ and $9.9 \times 10^{-3}\,M_{\odot}\,\mathrm{yr^{-1}}$, respectively, from the $\mathrm{HCO^+}$ line. The molecular line observations of $^{12}\mathrm{CO}\,(3-2)$, $^{13}\mathrm{CO}\,(3-2)$ and $\mathrm{C^{18}O}\,(3-2)$ towards G12.42+0.50 are obtained from the archives of JCMT. From these observations we detect the presence of a wide-angle bipolar outflow. The dynamical timescale, 1.3×10^5 yr, of the bipolar outflow suggests that it is likely driven by the same source powering the UC H II region, though the possibility of the SMA cores (SMA1 and SMA2) being the driving source(s) cannot be ruled out. The 8.0 μm and FIR images unfold the presence of large-scale filaments, all converging at the location of the clump, C1, resembling a hub-filament system. A detailed study of the gas kinematics agrees with bulk motion in the filaments, suggesting a gas inflow along the filaments to C1. Overall, G12.42+0.50 renders the picture of an active star-forming region with very early evolutionary cores, and an accreting MYSO in the initial phase of an UC H II region and driving an ionized jet.

The next investigation is focussed towards G19.88-0.53, where an interesting picture of it being a protocluster is deciphered and the detailed study of the complex associated with G19.88-0.53 is presented in Chapter 4. With multiple detected radio and mm components, G19.88-0.53 unravels as harbouring a protocluster, rather than a single MYSO. G19.88-0.53 is cocooned within a massive cold dust clump of mass $1911\ M_{\odot}$, identified from the APEX+Planck 870 μm map. The extended 4.5 μm emission lies towards the centre of the clump. ALMA 2.7 mm dust emission, with a cluster of six dense cores (MM1-MM6) lie deeply embedded within the 4.5 μm emission. Within the dust emission lies two radio components detected from deep uGMRT observations. At 1391.6 MHz, the weak radio emission exhibits a linear structure comprising of radio components, R1 and R2, in the east-west direction. The spectral index estimate of 0.58 ± 0.19, confirms the component R1 as a thermal jet. Concurrent with the thermal jet scenario is the strong detection of shock-excited H_2 emission lines in the NIR spectra extracted towards G19.88-0.53. The H_2 emission exhibits a bipolar outflow morphology in the direction of the ionized jet.

We construct RTDs of the six dense cores from the detected CH_3OH transitions. The rotational temperatures and beam averaged column densities determined from the RTDs are found to be consistent with HMCs. Based on the mass and sizes, these qualify as potential high-mass star-forming cores. The ionized jet is found to be associated with the brightest of the dense cores, MM2. From the $J = 1 - 0$ transition of $C^{18}O$, a large-scale molecular outflow is detected in the direction of one of the lobes of the bipolar H_2 outflow. High resolution observations reveal an additional collimated, bipolar outflow in the south-east and north-west direction, likely powered by MM2 indicating that G19.88-0.53 harbours multiple outflows. The $C^{17}O\ (3-2)$ transition towards core, MM6, shows clear inverse P-Cygni profile, a signature of protostellar infall. From this molecular transition, the infall velocity and the mass infall rate towards MM6 are estimated to be $2.9\,\mathrm{km\,s^{-1}}$ and $16.1 \times 10^{-3}\,M_{\odot}\,\mathrm{yr^{-1}}$, respectively, and are consistent with the typical values found towards HMCs. A detailed investigation confirms G19.88-0.53 as an active protocluster with high-mass star-forming components spanning a wide evolutionary spectrum from hot cores in accretion phase to cores driving multiple outflows to possible UC H II regions.

In another interesting study detailed in Chapter 5, we present compelling evidence of the complex, G133.50+9.01 being a bona fide cloud-cloud collision candidate with signatures of induced filament, core, and cluster formation. The CO line observations from PMO reveal that the G133.50+9.01 complex is comprised of two colliding clouds, G133a and G133b, with systemic velocities $-16.9\,\mathrm{km\,s^{-1}}$ and $-14.1\,\mathrm{km\,s^{-1}}$, respectively. The morphology of the cloud complex unveils the picture of the elongated smaller cloud, G133a, in

collision with the larger cloud, G133b, which displays a 'boomerang-like' structure with a cavity opening in the north-east direction. The PV diagram of G133.50+9.01 along the directions of both clouds reveals at least four bridging features in the intersection region of the clouds, a characteristic signature of cloud-cloud collision. Collision of the clouds leads to the formation of a shock-compressed layer in the intersection region which manifests as an open arc structure with enhanced density and temperature. Conforming to MHD simulations, a complex network of filaments is detected in the SCUBA 850 μm image, spatially well correlated with the shock compressed layer. The direction of the magnetic field probed using *Planck* data, is seen to be oriented perpendicular to the filamentary structure, as expected in a cloud-cloud collision event. Fourteen dust cores, that are possibly accreting matter from the natal filaments, are also identified from the 850 μm image. The masses of the cores lie within $\sim 2 - 86\, M_{\odot}$ with sizes ranging between $\sim 0.05 - 0.2$ pc. It is likely that the more massive cores in the sample are potential high-mass star-forming cores. We probe the star formation activity associated with G133.50+9.01 by inspecting the YSO population in the region. Of the 25 YSOs detected, 18 are seen to be located in the intersection region along the direction of the filaments. The over-density of Class I and II YSOs along the intersection arc advocates for collision induced cluster formation in G133.50+9.01.

Though statistical studies on massive star formation are plenty in literature, dedicated multiband studies, aimed at providing deeper insight into individual star-forming regions are few. Notwithstanding the abundance of information that can be availed from large-scale surveys and statistical studies of the star-forming complexes, the importance of detailed multiwavelength studies is well established. With a multiwavelength approach, this thesis work has extensively scrutinized a selected sample of high-mass star-forming regions, exploring the properties of various components associated with the regions studied. A broader perspective of massive star formation is gained by employing various observational techniques at different wavelengths. While the results from NIR spectroscopic and imaging observations of the studied EGOs conform with the hypothesis that EGOs are driven by jets/outflows from a protostar(s) in the early stages of evolution, low frequency radio observations of these sources confirm the presence of ionized jets associated with them. Investigation at mm and sub-mm wavelengths reveal kinematic signatures such as mass infall and molecular outflows towards the HMCs as well as the cold dust components associated with these EGOs. In addition, the study of the molecular cloud complex G133.50+9.01 provides crucial evidence supporting cluster formation triggered by cloud-cloud collision. Each source and its associated environment, critically examined in this thesis work, has a different story to tell, unravelling the intricacies involved, and thus confirming the impor-

tance of exhaustive exploration of individual high-mass star-forming regions.

6.2 Ongoing work

Probing the ionized emission from EGOs at low radio frequencies

As an extension to this thesis work, we have initiated a search for ionized jets towards EGOs using uGMRT. EGO G34.26+0.15 is one of the four "outflow-only" sources catalogued by Cyganowski et al. (2008), associated with a well known star-forming region that harbours H_2O and CH_3OH masers (e.g. Imai et al., 2011; Kim, Kim & Kim, 2019). Fig. 6.1 shows the *Spitzer*-IRAC three colour composite image of G34.26+0.15. Extended green emission towards the north-west direction is clearly seen in this figure. Located at a distance of 3.8 kpc, G34.26+0.15 is associated with an UC H II region and two HC H II regions, where the UC H II region has a cometary morphology and the HC components have sizes $1000 - 1300$ AU (Avalos et al., 2006). Gas infall motion have also been detected towards the cometary UC H II region associated with this source (Liu, Wu & Zhang, 2013).

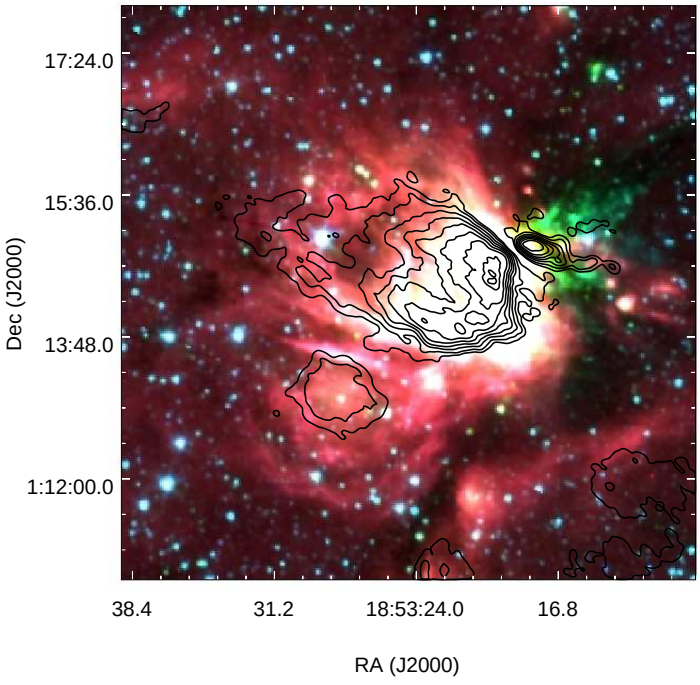

Figure 6.1: *Spitzer*-IRAC colour composite image of EGO G34.26+0.15. Black contours correspond to radio emission at 610 MHz (GMRT) with contour levels at 3, 10, 30, 60, 100, 150, 210, 280, and 315σ ($\sigma = 2.5 \times 10^{-4}$ Jy beam^{-1}).

Low-frequency radio continuum observations are carried out towards this EGO at Band 4 (550−850 MHz) and Band 5 (1050−1450 MHz) of uGMRT. The radio continuum emission associated with G34.26+0.15 at 610 MHz is depicted by black contour lines in Fig. 6.1. The radio emission shows two distinct components. The component towards the east has an extended morphology similar to the emission at 8.0 μm in the colour-composite image. The radio component towards the west extends in the direction of the extended 4.5 μm emission. Imaging of this source at other frequencies is underway. With the low-frequency radio maps, we intend to compute the spectra index values to get a better picture of the nature of radio emission associated with G34.26+0.15. Archival molecular line data will be used to get a comprehensive picture of this complex.

6.3 Future work

The work done in this thesis provides a prologue to future endeavours in the investigation of the early stages of other star-forming regions. Some of the works that are planned for the future towards gaining a better understanding of the field of high-mass star formation is discussed in this section.

- **Early stages high-mass star formation: tracing hot molecular cores**

  Large-scale surveys like ATLASGAL and *Structure, excitation, and dynamics of the inner Galactic interstellar medium* (SEDIGISM) give a broad view of the distribution of the molecular component within the Galactic interstellar medium. However, deep and high-angular resolution studies of these regions is not as extensive. The HMC phase marks the beginning of the formation of a protostar. They have little to no emission at centimeter wavelengths and are also too young and embedded to be detected at optical and IR wavelengths. This makes the emission from HMCs exclusive to millimeter and submillimeter wavelengths.

  High angular resolution probing of the hot cores at mm and sub-mm wavelengths will give a plethora of information regarding the evolutionary phase of the protoclusters and sub-structures at the scales of the core ($\sim 10,000$ AU). Interferometric study of a large sample of HMCs in active star-forming regions can reveal if the cores in the cloud are likely to evolve to a massive star or a cluster of low- and/or high-mass stars. Since the HMC phase is a stage where accretion is active and has a temperature that is higher than the ambient molecular cloud, the chemical nature of these objects would differ from that of the cold molecular clouds. Also, kinematically, the hot core phase

is characterised by highly collimated jets/outflows. Molecular line mapping of the hot cores will give insights into their chemical makeup and also help in understanding the intricacies involved in the kinematics of these objects.

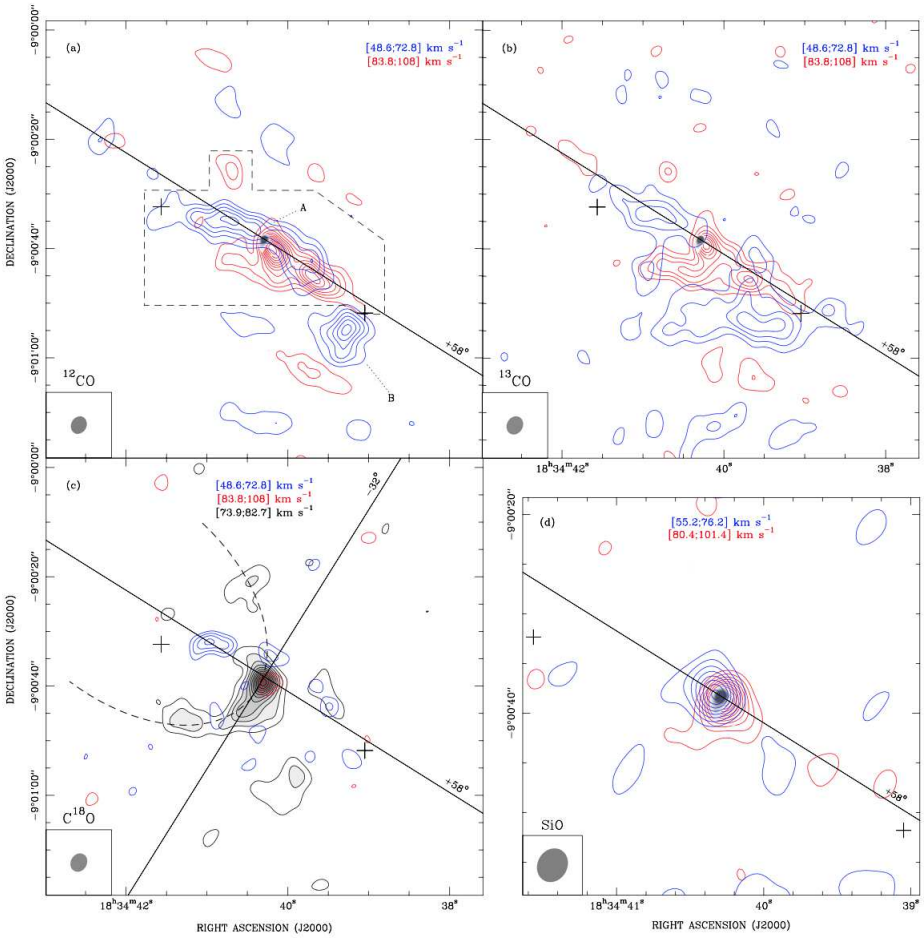

Figure 6.2: SMA maps of the outflow emission from G023.01-00.41. (a) Grey scale represents the 1.3 mm continuum map of the HMC associated with G023.01-00.41. The red and blue contours correspond to the integrated ^{12}CO $(2-1)$ emission within the velocity ranges indicated in the top right corner. The blue and red velocities are symmetric with respect to the systemic velocity, $V_{\rm sys}$. (b) Same as (a) for the ^{13}CO $(2-1)$ line emission. (c) Same as (a) for the C^{18}O $(2-1)$ line emission. The gray-scale corresponds to the C^{18}O bulk emission integrated over the FWHM of the CH3CN lines (more details can be found in Sanna et al. 2014). (d) Same as (a) for the SiO $(5-4)$ line emission with a zoom of two times the field of view. This figure is taken from Sanna et al. (2014).

Recent years have seen several studies focussed towards deciphering the properties of HMCs. For instance, Sanna et al. (2014) have carried out subarcsecond resolution observations using SMA to unveil the gas structure and kinematics of a HMC in the

high-mass star-forming region, G023.01-00.41. The study is focussed on the comparison of the gas dynamics in the inner HMC, having scales $\lesssim 0.01$ pc, with that is inferred for scales $\gtrsim 0.1$ pc. It is found that the HMC drives a well-collimated CO and SiO outflow. Fig. 6.2 shows the SMA outflow maps from both these molecules from the HMC associated with G023.01-00.41. The HMC is located at the centroid of the outflow, illustrated by the red and blue contours in all the maps. Such studies, though extremely crucial in detecting and probing the nature of HMCs, are very limited. With the proposed plan we intend to build an extensive database of HMCs and their properties through subarcsecond continuum mapping at millimeter wavelengths, and also probe their kinematic signatures with high-resolution molecular line observations.

- **Tracing disk-jet systems in high-mass star-forming regions**

  Circumstellar accretion disks are intimately coupled with jets/outflows that allow the conservation of angular momentum, while protostars actively accrete matter through the disk. The role of disks in the formation of high-mass stars is being widely investigated (e.g. Cesaroni et al., 2006; Krumholz et al., 2009). Circumstellar disks are believed to alleviate or solve the radiation pressure problem, because they channel the accretion through the disks and allow a large portion of the stellar photons to escape through cavities carved by bipolar jets along the disk axis, thus allowing the star to grow beyond the the "classical" maximum of $8\,M_{\odot}$ (Kuiper et al., 2010). There are models predicting massive star formation in a disk-jet system, where the circumstellar disks could reach radii between 1000-2000 AU (Harries, Douglas & Ali, 2017; Kuiper et al., 2011). But the observational evidence to support the interplay between disks and jets at these scales is very limited, as opposed to low- and intermediate-mass stars. Also, the scenario of the accretion through disks in early-O type stars is still rather elusive.

  In their recent work, Sanna et al. (2019) compare the relative orientation of the disk profile with that of the radio thermal jet emission detected at 22 GHz and 45 GHz towards G023.01-00.41 (Sanna et al., 2016) and found they are clearly perpendicular to each other as is evident in Fig. 6.3. From ALMA observations, targeted at the HMC associated with G023.01-00.41, at wavelengths near 1 mm, Sanna et al. (2019) have resolved a molecular disk-jet system around a young star that has currently attained a mass of $20\,M_{\odot}$. From the kinematic analysis of this system, the authors infer that the disk is close to free-fall and slowly rotating with sub-Keplarian velocities. This study

provides substantial evidence for accretion through disks in high-mass protostars and driving high collimated jets. To get a wider picture, a large sample of known outflow sources will provide promising targets for the search for circumstellar disks around MYSOs. EGOs are excellent outflow candidates, driven by highly collimated H_2 jets/outflows, suggesting a disk origin. They would, hence, represent an impressive statistical sample to look for disk-jet systems in high-mass star-forming regions.

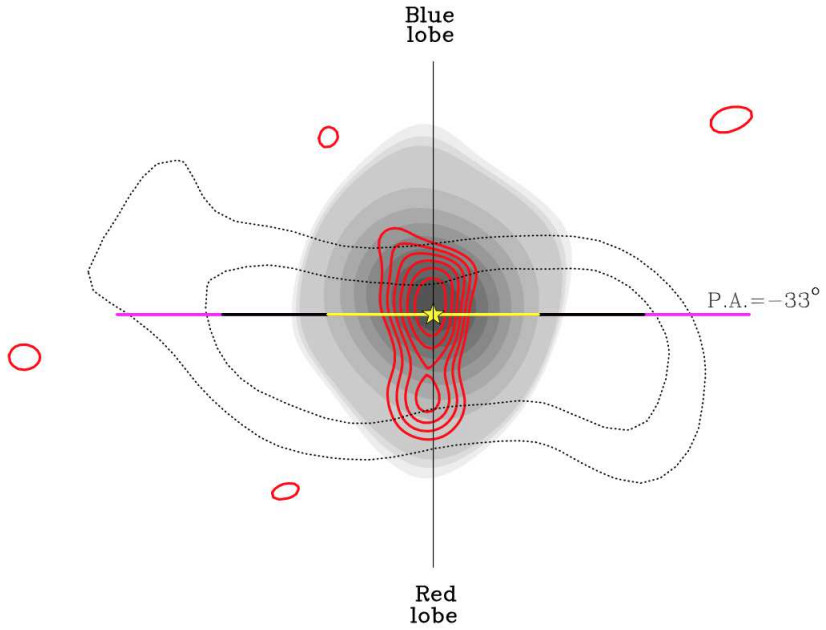

Figure 6.3: Comparison between the disk emission and the emission from ionized thermal jet. Dotted contours represent the CH_3OH $(4_{2,2} - 3_{1,2})$ E line emission indicating the emission from the disk. The radio emission at 22 GHz (gray scale) and 45 GHz (red contours) detected towards G023.01-00.41 traces an ionized thermal jet (Sanna et al., 2016). The black line indicates the direction of the outflow perpendicular to the disk plane. The star marks the position of the HMC driving the jet. This figure is taken from Sanna et al. (2019).

We propose to carry out (sub)mm continuum observations at subarcsecond resolutions to detect circumstellar disks around MYSOs driving jets. The high angular resolution observations, employing interferometric technique, can isolate the driving sources of the jets. With high-resolution NIR and MIR spectroscopic observations of these systems, we intend to probe the spectral signatures of circumstellar disks as well as the jets. In addition, with radio continuum observations, one can get valuable insight into the nature of these jets by examining the signatures of thermal and non-thermal emission. Through a multiwavelength approach, this work will yield a

comprehensive database of disk-jet systems in high-mass star-forming regions.

- **Search for cloud-cloud collision candidates**

  Given that high-mass stars often form in clustered environments, there is growing evidence supporting cloud-cloud collision induced massive star and cluster formation. According to a recent review by Fukui et al. (2020), only a handful of observational studies (~ 50) have been able to provide evidence for cloud-cloud collision triggered high-mass star formation. The theoretical models for two-cloud collisions (Habe & Ohta, 1992) describes three observational signatures of cloud-cloud collision: (1) the complementary distribution of the colliding clouds with each other, (2) a connecting feature between the two clouds called the "bridging-feature", and (3) a 'U' shape or a 'boomerang-like' morphology in the final phase. The gas dynamics in cloud-cloud collision events is highly directional due to the collision velocity. This is in contrast with the isotropic gas dynamics of a turbulent cloud without collision. These morphological signatures can be used to identify cloud-cloud collision candidates from large-scale ^{12}CO and ^{13}CO maps over a large range of cloud sizes, from 1 pc to 1 kpc.

  With large-scale molecular line data, we aim at identifying cloud-cloud collision candidates from the various morphological signatures they exhibit. The study can further be extended to probe these candidates at (sub)mm wavelengths to investigate the nature of the shock-compressed layer developed at the interface of the collision and the dense filaments and cores formed there.

The field of high-mass star formation is vast wherein every aspect has plenty in store to be explored and investigated. The research work carried out in this thesis has enabled the building of a strong foundation in utilizing observations across the spectrum to understand key aspects of high-mass star formation. The various techniques explored as part of the investigations have strengthened the skills to take on the future challenges in this very exciting and promising field of stellar astrophysics.

Bibliography

Adams F. C., Lada C. J., Shu F. H., 1987, ApJ, 312, 788

Anathpindika S. V., 2010, MNRAS, 405, 1431

Anderson L., Armentrout W. P., Bania T. M., Balser D. S., Luisi M., Wenger T. V., Roshi D. A., 2019, Bulletin of the American Astronomical Society, 51

Anderson L. D. et al., 2010, A&A, 518, L99

André P., Di Francesco J., Ward-Thompson D., Inutsuka S. I., Pudritz R. E., Pineda J. E., 2014, in Protostars and Planets VI, Beuther H., Klessen R. S., Dullemond C. P., Henning T., eds., p. 27

André P. et al., 2010, A&A, 518, L102

Anglada G., 1996, in Astronomical Society of the Pacific Conference Series, Vol. 93, Radio Emission from the Stars and the Sun, Taylor A. R., Paredes J. M., eds., pp. 3–14

Anglada G., Rodríguez L. F., Carrasco-González C., 2018, A&ARv, 26, 3

Anglada G., Rodriguez L. F., Girart J. M., Estalella R., Torrelles J. M., 1994, ApJL, 420, L91

Anglada G., Villuendas E., Estalella R., Beltrán M. T., Rodríguez L. F., Torrelles J. M., Curiel S., 1998, AJ, 116, 2953

Aniano G., Draine B. T., Gordon K. D., Sandstrom K., 2011, PASP, 123, 1218

Arce H. G., Shepherd D., Gueth F., Lee C. F., Bachiller R., Rosen A., Beuther H., 2007, in Protostars and Planets V, Reipurth B., Jewitt D., Keil K., eds., p. 245

Arthur S. J., Kurtz S. E., Franco J., Albarrán M. Y., 2004, ApJ, 608, 282

Avalos M., Lizano S., Rodríguez L. F., Franco-Hernández R., Moran J. M., 2006, ApJ, 641, 406

Battersby C. et al., 2011, A&A, 535, A128

Battersby C., Bally J., Jackson J. M., Ginsburg A., Shirley Y. L., Schlingman W., Glenn J., 2010, ApJ, 721, 222

Beckwith S. V. W., Sargent A. I., Chini R. S., Guesten R., 1990, AJ, 99, 924

Beltrán M. T., Cesaroni R., Moscadelli L., Sá nchez-Monge Á., Hirota T., Kumar M. S. N., 2016, A&A, 593, A49

Beltrán M. T., Cesaroni R., Neri R., Codella C., 2011, A&A, 525, A151

Benjamin R. A. et al., 2003, PASP, 115, 953

Berry D., 2015, Astronomy and Computing, 10, 22

Bertoldi F., McKee C. F., 1992, ApJ, 395, 140

Beuther H., Churchwell E. B., McKee C. F., Tan J. C., 2007, in Protostars and Planets V, Reipurth B., Jewitt D., Keil K., eds., p. 165

Beuther H., Kainulainen J., Henning T., Plume R., Heitsch F., 2011, A&A, 533, A17

Beuther H., Schilke P., Gueth F., McCaughrean M., Andersen M., Sridharan T. K., Menten K. M., 2002a, A&A, 387, 931

Beuther H., Schilke P., Menten K. M., Motte F., Sridharan T. K., Wyrowski F., 2002b, ApJ, 566, 945

Beuther H., Schilke P., Menten K. M., Motte F., Sridharan T. K., Wyrowski F., 2005, ApJ, 633, 535

Beuther H., Schilke P., Sridharan T. K., Menten K. M., Walmsley C. M., Wyrowski F., 2002c, A&A, 383, 892

Beuther H., Schilke P., Stanke T., 2003, A&A, 408, 601

Beuther H., Shepherd D., 2005, Precursors of UchII Regions and the Evolution of Massive Outflows, Kumar M. S. N., Tafalla M., Caselli P., eds., Vol. 324, p. 105

Beuther H., Walsh A., Schilke P., Sridharan T. K., Menten K. M., Wyrowski F., 2002d, A&A, 390, 289

Binney J., Tremaine S., 1987, Galactic dynamics

Blake G. A., Sutton E. C., Masson C. R., Phillips T. G., 1987, ApJ, 315, 621

Bonnell I. A., Bate M. R., 2006, MNRAS, 370, 488

Bonnell I. A., Bate M. R., Clarke C. J., Pringle J. E., 1997, MNRAS, 285, 201

Bonnell I. A., Bate M. R., Clarke C. J., Pringle J. E., 2001, MNRAS, 323, 785

Bonnell I. A., Bate M. R., Zinnecker H., 1998, Monthly Notices of the Royal Astronomical Society, 298, 93âĂŞ102

Brogan C. L., Hunter T. R., Cyganowski C. J., Friesen R. K., Chandler C. J., Indebetouw R., 2011, ApJL, 739, L16

Bronfman L., Alvarez H., Cohen R. S., Thaddeus P., 1989, ApJS, 71, 481

Buckle J. V. et al., 2009, MNRAS, 399, 1026

Caratti o Garatti A., Stecklum B., Linz H., Garcia Lopez R., Sanna A., 2015, A&A, 573, A82

Casali M. et al., 2007, A&A, 467, 777

Cesaroni R., Felli M., Jenness T., Neri R., Olmi L., Robberto M., Testi L., Walmsley C. M., 1999, A&A, 345, 949

Cesaroni R., Galli D., Lodato G., Walmsley C. M., Zhang Q., 2007, in Protostars and Planets V, Reipurth B., Jewitt D., Keil K., eds., p. 197

Cesaroni R., Galli D., Lodato G., Walmsley M., Zhang Q., 2006, Natur, 444, 703

Chambers E. T., Jackson J. M., Rathborne J. M., Simon R., 2009, ApJS, 181, 360

Chen X., Ellingsen S. P., Shen Z. Q., 2009, MNRAS, 396, 1603

Chen X., Ellingsen S. P., Shen Z.-Q., Titmarsh A., Gan C.-G., 2011, ApJS, 196, 9

Chen X., Gan C.-G., Ellingsen S. P., He J.-H., Shen Z.-Q., Titmarsh A., 2013a, ApJS, 206, 9

Chen X., Gan C.-G., Ellingsen S. P., He J.-H., Shen Z.-Q., Titmarsh A., 2013b, ApJS, 206, 22

Chen X., Shen Z.-Q., Li J.-J., Xu Y., He J.-H., 2010, ApJ, 710, 150

Cheng Y., Tan J. C., Liu M., Kong S., Lim W., Andersen M., Da Rio N., 2018, ApJ, 853, 160

Churchwell E., 2002, ARA&A, 40, 27

Codella C., Beltrán M. T., Cesaroni R., Moscadelli L., Neri R., Vasta M., Zhang Q., 2013, A&A, 550, A81

Contreras Y., Garay G., Rathborne J. M., Sanhueza P., 2016, MNRAS, 456, 2041

Corradi R. L. M., Aznar R., Mampaso A., 1998, MNRAS, 297, 617

Cragg D. M., Sobolev A. M., Godfrey P. D., 2005, MNRAS, 360, 533

Crowther P. A., Schnurr O., Hirschi R., Yusof N., Parker R. J., Goodwin S. P., Kassim H. A., 2010, MNRAS, 408, 731

Csengeri T. et al., 2016, A&A, 585, A104

Curiel S., Rodriguez L. F., Moran J. M., Canto J., 1993, ApJ, 415, 191

Currie M. J., Draper P. W., Berry D. S., Jenness T., Cavanagh B., Economou F., 2008, in Astronomical Society of the Pacific Conference Series, Vol. 394, Astronomical Data Analysis Software and Systems XVII, Argyle R. W., Bunclark P. S., Lewis J. R., eds., p. 650

Cutri R. M., et al., 2013, VizieR Online Data Catalog, II/328

Cyganowski C. J., Brogan C. L., Hunter T. R., 2007, AJ, 134, 346

Cyganowski C. J., Brogan C. L., Hunter T. R., Churchwell E., 2009, ApJ, 702, 1615

Cyganowski C. J., Brogan C. L., Hunter T. R., Churchwell E., 2011a, ApJ, 743, 56

Cyganowski C. J., Brogan C. L., Hunter T. R., Churchwell E., Zhang Q., 2011b, ApJ, 729, 124

Cyganowski C. J., Brogan C. L., Hunter T. R., Zhang Q., Friesen R. K., Indebetouw R., Chand ler C. J., 2012, ApJL, 760, L20

Cyganowski C. J., Koda J., Rosolowsky E., Towers S., Donovan Meyer J., Egusa F., Momose R., Robitaille T. P., 2013, ApJ, 764, 61

Cyganowski C. J. et al., 2008, AJ, 136, 2391

Das S. R., Tej A., Vig S., Liu H.-L., Liu T., Ishwara Chandra C. H., Ghosh S. K., 2017, MNRAS, 472, 4750

Das S. R., Tej A., Vig S., Liu T., Ghosh S. K., Chandra C. H. I., 2018, A&A, 612, A36

Davies B., Hoare M. G., Lumsden S. L., Hosokawa T., Oudmaijer R. D., Urquhart J. S., Mottram J. C., Stead J., 2011, MNRAS, 416, 972

Davis C. J., Gell R., Khanzadyan T., Smith M. D., Jenness T., 2010, A&A, 511, A24

Davis C. J., Kumar M. S. N., Sandell G., Froebrich D., Smith M. D., Currie M. J., 2007, MNRAS, 374, 29

Davis C. J., Smith M. D., Stern L., Kerr T. H., Chiar J. E., 2003, MNRAS, 344, 262

De Buizer J. M., Vacca W. D., 2010, AJ, 140, 196

de Graauw T. et al., 2010, A&A, 518, L6

De Vries C. H., Myers P. C., 2005, ApJ, 620, 800

Deharveng L. et al., 2015, A&A, 582, A1

Dempsey J. T. et al., 2013, MNRAS, 430, 2534

Di Francesco J., Myers P. C., Wilner D. J., Ohashi N., Mardones D., 2001, ApJ, 562, 770

Dunham M. M. et al., 2015, ApJS, 220, 11

Ellingsen S. P., 2006, ApJ, 638, 241

Elmegreen B. G., Lada C. J., 1977, ApJ, 214, 725

Evans, Neal J. I., 1999, ARA&A, 37, 311

Evans, Neal J. I. et al., 2009, ApJS, 181, 321

Fazio G. G. et al., 2004, ApJS, 154, 10

Ferrière K. M., 2001, Reviews of Modern Physics, 73, 1031

Foster J. B. et al., 2011, ApJS, 197, 25

Frerking M. A., Langer W. D., Wilson R. W., 1982, ApJ, 262, 590

Froebrich D. et al., 2011, MNRAS, 413, 480

Fukui Y., Habe A., Inoue T., Enokiya R., Tachihara K., 2020, arXiv e-prints, arXiv:2009.05077

Fukui Y. et al., 2015, ApJL, 807, L4

Fukui Y. et al., 2014, ApJ, 780, 36

Fukui Y. et al., 2018, ApJ, 859, 166

Fukui Y. et al., 2016, ApJ, 820, 26

Garay G., Brooks K. J., Mardones D., Norris R. P., 2003, ApJ, 587, 739

Ge J. X., He J. H., Chen X., Takahashi S., 2014, MNRAS, 445, 1170

Gomez Y., Rodriguez L. F., Marti J., 1995, ApJ, 453, 268

Gong Y. et al., 2017, ApJL, 835, L14

Gong Y. et al., 2019, A&A, 632, A115

Green G. M., Schlafly E., Zucker C., Speagle J. S., Finkbeiner D., 2019, ApJ, 887, 93

Griffin M. J. et al., 2010, A&A, 518, L3

Gupta Y. et al., 2017, Current Science, 113, 707

Guzmán A. E., Garay G., Brooks K. J., 2010, ApJ, 725, 734

Guzmán A. E., Garay G., Rodríguez L. F., Contreras Y., Dougados C., Cabrit S., 2016, ApJ, 826, 208

Habe A., Ohta K., 1992, PASJ, 44, 203

Harries T. J., Douglas T. A., Ali A., 2017, MNRAS, 471, 4111

Haslam C. G. T., Salter C. J., Stoffel H., Wilson W. E., 1982, A&AS, 47, 1

Hatchell J., Fuller G. A., Millar T. J., 2001, A&A, 372, 281

Haworth T. J., Shima K., Tasker E. J., Fukui Y., Torii K., Dale J. E., Takahira K., Habe A., 2015a, MNRAS, 454, 1634

Haworth T. J. et al., 2015b, MNRAS, 450, 10

Hayashi K. et al., 2020, PASJ

He J. H., Takahashi S., Chen X., 2012, ApJS, 202, 1

He Y.-X. et al., 2015, MNRAS, 450, 1926

Heap S. R. et al., 1991, ApJL, 377, L29

Heiderman A., Evans, Neal J. I., Allen L. E., Huard T., Heyer M., 2010, ApJ, 723, 1019

Herbig G. H., 1962, Advances in Astronomy and Astrophysics, 1, 47

Herbst E., van Dishoeck E. F., 2009, ARA&A, 47, 427

Hildebrand R. H., 1983, QJRAS, 24, 267

Hoare M. G., Kurtz S. E., Lizano S., Keto E., Hofner P., 2007, in Protostars and Planets V, Reipurth B., Jewitt D., Keil K., eds., p. 181

Hoare M. G., Roche P. F., Glencross W. M., 1991, MNRAS, 251, 584

Hofner P., Cesaroni R., Kurtz S., Rosero V., Anderson C., Furuya R. S., Araya E. D., Molinari S., 2017, ApJ, 843, 99

Högbom J. A., 1974, A&AS, 15, 417

Holland W. S. et al., 2013, MNRAS, 430, 2513

Houck J. R. et al., 2004, ApJS, 154, 18

Iben, Icko J., 1965, ApJ, 141, 993

Imai H., Omi R., Kurayama T., Nagayama T., Hirota T., Miyaji T., Omodaka T., 2011, PASJ, 63, 1293

Inoue A. K., Hirashita H., Kamaya H., 2001, ApJ, 555, 613

Inoue T., Fukui Y., 2013, ApJL, 774, L31

Inoue T., Hennebelle P., Fukui Y., Matsumoto T., Iwasaki K., Inutsuka S.-i., 2018, PASJ, 70, S53

Ioannidis G., Froebrich D., 2012, MNRAS, 421, 3257

Issac N., Tej A., Liu T., Varricatt W., Vig S., Ishwara Chandra C. H., Schultheis M., 2019, MNRAS, 485, 1775

Jackson J. M., Finn S. C., Chambers E. T., Rathborne J. M., Simon R., 2010, ApJL, 719, L185

Jackson J. M. et al., 2013, PASA, 30, e057

Jaffe D. T., Guesten R., Downes D., 1981, ApJ, 250, 621

Jaffe D. T., Hildebrand R. H., Keene J., Harper D. A., Loewenstein R. F., Moran J. M., 1984, ApJ, 281, 225

Johnston K. J., Gaume R., Stolovy S., Wilson T. L., Walmsley C. M., Menten K. M., 1992, ApJ, 385, 232

Kahn F. D., 1974, A&A, 37, 149

Kalenskii S. V., Johansson L. E. B., Bergman P., Kurtz S., Hofner P., Walmsley C. M., Slysh V. I., 2010, MNRAS, 405, 613

Kalenskii S. V., Kurtz S., Bergman P., 2013, Astronomy Reports, 57, 120

Kauffmann J., Bertoldi F., Bourke T. L., Evans, II N. J., Lee C. W., 2008, A&A, 487, 993

Kauffmann J., Pillai T., Shetty R., Myers P. C., Goodman A. A., 2010a, ApJ, 712, 1137

Kauffmann J., Pillai T., Shetty R., Myers P. C., Goodman A. A., 2010b, ApJ, 716, 433

Kaufman M. J., Wolfire M. G., Hollenbach D. J., Luhman M. L., 1999, ApJ, 527, 795

Kendall T. R., de Wit W. J., Yun J. L., 2003, A&A, 408, 313

Kennicutt R. C., Evans N. J., 2012, ARA&A, 50, 531

Keto E. R., Ho P. T. P., Reid M. J., 1987, ApJL, 323, L117

Kim W.-J., Kim K.-T., Kim K.-T., 2019, ApJS, 244, 2

Klaassen P. D., Wilson C. D., 2007, ApJ, 663, 1092

Klaassen P. D., Wilson C. D., Keto E. R., Zhang Q., Galván-Madrid R., Liu H. Y. B., 2011, A&A, 530, A53

Klessen R. S., Ballesteros-Paredes J., Vázquez-Semadeni E., Durán-Rojas C., 2005, ApJ, 620, 786

Kobulnicky H. A., Johnson K. E., 1999, ApJ, 527, 154

Koenig X. P., Leisawitz D. T., 2014, ApJ, 791, 131

Kong S., Tan J. C., Caselli P., Fontani F., Liu M., Butler M. J., 2017, ApJ, 834, 193

Kroupa P., 2001, MNRAS, 322, 231

Krumholz M. R., Bonnell I. A., 2009, Models for the formation of massive stars, Chabrier G., ed., Cambridge Contemporary Astrophysics, Cambridge University Press, pp. 288–320

Krumholz M. R., Klein R. I., McKee C. F., 2007, ApJ, 656, 959

Krumholz M. R., Klein R. I., McKee C. F., Offner S. S. R., Cunningham A. J., 2009, Science, 323, 754

Krumholz M. R., McKee C. F., 2008, Natur, 451, 1082

Kuiper R., Klahr H., Beuther H., Henning T., 2010, ApJ, 722, 1556

Kuiper R., Klahr H., Beuther H., Henning T., 2011, ApJ, 732, 20

Kumar M. S. N., Palmeirim P., Arzoumanian D., Inutsuka S. I., 2020, A&A, 642, A87

Kurtz S., 2002, in Astronomical Society of the Pacific Conference Series, Vol. 267, Hot Star Workshop III: The Earliest Phases of Massive Star Birth, Crowther P., ed., p. 81

Kurtz S., Cesaroni R., Churchwell E., Hofner P., Walmsley C. M., 2000, Protostars and Planets IV, 299

Kurtz S., Churchwell E., Wood D. O. S., 1994, ApJS, 91, 659

Kurtz S., Hofner P., Álvarez C. V., 2004, ApJS, 155, 149

Kutner M. L., Tucker K. D., 1975, ApJ, 199, 79

Kwan J., 1997, ApJ, 489, 284

Lada C. J., Lada E. A., 2003, ARA&A, 41, 57

Lada C. J., Lombardi M., Alves J. F., 2010, ApJ, 724, 687

Lada C. J., Shu F. H., 1990, Science, 248, 564

Ladd N., Purcell C., Wong T., Robertson S., 2005, PASA, 22, 62

Lamarre J. M. et al., 2010, A&A, 520, A9

Launhardt R. et al., 2013, A&A, 551, A98

Lee H.-T. et al., 2013, ApJS, 208, 23

Lee H.-T., Takami M., Duan H.-Y., Karr J., Su Y.-N., Liu S.-Y., Froebrich D., Yeh C. C., 2012, ApJS, 200, 2

Leurini S., Codella C., Gusdorf A., Zapata L., Gómez-Ruiz A., Testi L., Pillai T., 2013, A&A, 554, A35

Leurini S., Schilke P., Wyrowski F., Menten K. M., 2007, A&A, 466, 215

Leurini S. et al., 2019, A&A, 621, A130

Li P. S., Klein R. I., McKee C. F., 2018, MNRAS, 473, 4220

Lis D. C., Menten K. M., 1998, ApJ, 507, 794

Liu H. B., Quintana-Lacaci G., Wang K., Ho P. T. P., Li Z.-Y., Zhang Q., Zhang Z.-Y., 2012, ApJ, 745, 61

Liu H. B., Zhang Q., Ho P. T. P., 2011, ApJ, 729, 100

Liu H.-L. et al., 2016a, ApJ, 818, 95

Liu S.-Y., Girart J. M., Remijan A., Snyder L. E., 2002, ApJ, 576, 255

Liu T. et al., 2020, MNRAS, 496, 2790

Liu T. et al., 2018a, ApJS, 234, 28

Liu T. et al., 2018b, ApJS, 234, 28

Liu T. et al., 2017, ApJ, 849, 25

Liu T. et al., 2018c, ApJ, 859, 151

Liu T., Wu Y., Wu J., Qin S.-L., Zhang H., 2013, MNRAS, 436, 1335

Liu T., Wu Y., Zhang H., 2012, ApJS, 202, 4

Liu T., Wu Y., Zhang H., 2013, ApJ, 776, 29

Liu T. et al., 2016b, ApJ, 824, 31

Lo N., Wiles B., Redman M. P., Cunningham M. R., Bains I., Jones P. A., Burton M. G., Bronfman L., 2015, MNRAS, 453, 3245

López-Sepulcre A., Cesaroni R., Walmsley C. M., 2010, A&A, 517, A66

López-Sepulcre A. et al., 2011, A&A, 526, L2

Lovas F. J., 2004, Journal of Physical and Chemical Reference Data, 33, 177

Lucas P. W. et al., 2008, MNRAS, 391, 136

Lumsden S. L., Hoare M. G., Urquhart J. S., Oudmaijer R. D., Davies B., Mottram J. C., Cooper H. D. B., Moore T. J. T., 2013, ApJS, 208, 11

Mainzer A. et al., 2011, ApJ, 731, 53

Majaess D., Turner D. G., Gieren W., 2012, MNRAS, 421, 1040

Mallick K. K., Ojha D. K., Tamura M., Linz H., Samal M. R., Ghosh S. K., 2015, MNRAS, 447, 2307

Marcote B., Ribó M., Paredes J. M., Ishwara-Chand ra C. H., 2015, MNRAS, 451, 59

Mardones D., Myers P. C., Tafalla M., Wilner D. J., Bachiller R., Garay G., 1997, ApJ, 489, 719

Marseille M., Bontemps S., Herpin F., van der Tak F. F. S., Purcell C. R., 2008, A&A, 488, 579

Marston A. P. et al., 2004, ApJS, 154, 333

Masqué J. M., Jeyakumar S., Trinidad M. A., Rodríguez-Esnard T., Ishwara-Chandra C. H., 2019, MNRAS, 483, 1184

McKee C. F., Ostriker E. C., 2007, ARA&A, 45, 565

McKee C. F., Tan J. C., 2003, ApJ, 585, 850

McMullin J. P., Waters B., Schiebel D., Young W., Golap K., 2007, in Astronomical Society of the Pacific Conference Series, Vol. 376, Astronomical Data Analysis Software and Systems XVI, Shaw R. A., Hill F., Bell D. J., eds., p. 127

Menten K. M., Walmsley C. M., Henkel C., Wilson T. L., 1986, A&A, 157, 318

Mezger P. G., Smith L. F., 1977, in Star Formation, de Jong T., Maeder A., Pikel'Ner S. B., eds., Vol. 75, p. 133

Miettinen O., 2014, A&A, 562, A3

Miettinen O., Harju J., Haikala L. K., Pomrén C., 2006, A&A, 460, 721

Molinari S. et al., 2010, PASP, 122, 314

Motte F., Bontemps S., Louvet F., 2018, ARA&A, 56, 41

Mottram J. C. et al., 2011, A&A, 525, A149

Müller H. S. P., Schlöder F., Stutzki J., Winnewisser G., 2005, Journal of Molecular Structure, 742, 215

Myers P. C., 2009, ApJ, 700, 1609

Myers P. C., Benson P. J., 1983, ApJ, 266, 309

Noriega-Crespo A. et al., 2004, ApJS, 154, 352

Obonyo W. O., Lumsden S. L., Hoare M. G., Purser S. J. D., Kurtz S. E., Johnston K. G., 2019, MNRAS, 486, 3664

Onaka T., Mori T., Sakon I., Ardaseva A., 2016, ApJ, 829, 106

Osterloh M., Henning T., Launhardt R., 1997, ApJS, 110, 71

Panagia N., 1973, AJ, 78, 929

Panagia N., Felli M., 1975, A&A, 39, 1

Paron S., Petriella A., Ortega M. E., 2011, A&A, 525, A132

Peretto N., André P., Belloche A., 2006, A&A, 445, 979

Peretto N. et al., 2012, A&A, 541, A63

Peretto N., Fuller G. A., 2009, A&A, 505, 405

Peretto N. et al., 2014, A&A, 561, A83

Peretto N. et al., 2013, A&A, 555, A112

Peretto N. et al., 2010, A&A, 518, L98

Perez M. S., Blundell K. M., 2009, MNRAS, 397, 849

Pickett H. M., Poynter R. L., Cohen E. A., Delitsky M. L., Pearson J. C., Müller H. S. P., 1998, JQSRT, 60, 883

Pilbratt G. L. et al., 2010, A&A, 518, L1

Pillai T., Kauffmann J., Wyrowski F., Hatchell J., Gibb A. G., Thompson M. A., 2011, A&A, 530, A118

Plambeck R. L., Menten K. M., 1990, ApJ, 364, 555

Planck Collaboration et al., 2016a, A&A, 594, A1

Planck Collaboration et al., 2015, A&A, 576, A104

Planck Collaboration et al., 2016b, A&A, 594, A26

Planck Collaboration et al., 2011, A&A, 536, A1

Poglitsch A. et al., 2010, A&A, 518, L2

Pokhrel R. et al., 2018, ApJ, 853, 5

Price S. D., Egan M. P., Carey S. J., Mizuno D. R., Kuchar T. A., 2001, AJ, 121, 2819

Purcell C. R. et al., 2006, MNRAS, 367, 553

Purser S. J. D. et al., 2016, MNRAS, 460, 1039

Qin S.-L., Zhao J.-H., Moran J. M., Marrone D. P., Patel N. A., Wang J.-J., Liu S.-Y., Kuan Y.-J., 2008, ApJ, 677, 353

Qiu K., Zhang Q., Beuther H., Yang J., 2007, ApJ, 654, 361

Qiu K., Zhang Q., Wu J., Chen H.-R., 2009, ApJ, 696, 66

Quireza C., Rood R. T., Bania T. M., Balser D. S., Maciel W. J., 2006, ApJ, 653, 1226

Ragan S. et al., 2012, A&A, 547, A49

Ragan S. E., Henning T., Tackenberg J., Beuther H., Johnston K. G., Kainulainen J., Linz H., 2014, A&A, 568, A73

Ramachandran V., Das S. R., Tej A., Vig S., Ghosh S. K., Ojha D. K., 2017, MNRAS, 465, 4753

Ramírez E. A., Tadhunter C. N., Axon D., Batcheldor D., Young S., Packham C., Sparks W. B., 2009, MNRAS, 399, 2165

Ramsay Howat S. K. et al., 2004, in SPIE, Vol. 5492, Ground-based Instrumentation for Astronomy, Moorwood A. F. M., Iye M., eds., pp. 1160–1171

Rathborne J. M., Jackson J. M., Chambers E. T., Simon R., Shipman R., Frieswijk W., 2005, ApJL, 630, L181

Rathborne J. M., Jackson J. M., Simon R., 2006, ApJ, 641, 389

Rathborne J. M. et al., 2014, ApJ, 786, 140

Rathborne J. M., Simon R., Jackson J. M., 2007, ApJ, 662, 1082

Reach W. T. et al., 2006, AJ, 131, 1479

Reid M. J., Dame T. M., Menten K. M., Brunthaler A., 2016, ApJ, 823, 77

Remijan A., Shiao Y.-S., Friedel D. N., Meier D. S., Snyder L. E., 2004, ApJ, 617, 384

Ren Z., Wu Y., Zhu M., Liu T., Peng R., Qin S., Li L., 2012, MNRAS, 422, 1098

Reynolds S. P., 1986, ApJ, 304, 713

Rieke G. H. et al., 2004, ApJS, 154, 25

Robitaille T. P., Whitney B. A., Indebetouw R., Wood K., Denzmore P., 2006, ApJS, 167, 256

Rodriguez L. F., 1997, in IAU Symposium, Vol. 182, Herbig-Haro Flows and the Birth of Stars, Reipurth B., Bertout C., eds., pp. 83–92

Rodriguez L. F., Marti J., Canto J., Moran J. M., Curiel S., 1993, RMxAA, 25, 23

Rodríguez-Garza C. B., Kurtz S. E., Gómez-Ruiz A. I., Hofner P., Araya E. D., Kalenskii S. V., 2017, ApJS, 233, 4

Roger R. S., Costain C. H., Landecker T. L., Swerdlyk C. M., 1999, A&AS, 137, 7

Roman-Duval J., Jackson J. M., Heyer M., Johnson A., Rathborne J., Shah R., Simon R., 2009, ApJ, 699, 1153

Rosero V. et al., 2016, ApJS, 227, 25

Rosero V. et al., 2019, ApJ, 880, 99

Rygl K. L. J., Wyrowski F., Schuller F., Menten K. M., 2013, A&A, 549, A5

Salpeter E. E., 1955, ApJ, 121, 161

Sanhueza P., Garay G., Bronfman L., Mardones D., May J., Saito M., 2010, ApJ, 715, 18

Sanhueza P., Jackson J. M., Foster J. B., Garay G., Silva A., Finn S. C., 2012, ApJ, 756, 60

Sanna A., Cesaroni R., Moscadelli L., Zhang Q., Menten K. M., Molinari S., Caratti o Garatti A., De Buizer J. M., 2014, A&A, 565, A34

Sanna A. et al., 2019, A&A, 623, A77

Sanna A., Moscadelli L., Cesaroni R., Caratti o Garatti A., Goddi C., Carrasco-González C., 2016, A&A, 596, L2

Sano H. et al., 2018, PASJ, 70, S43

Schilke P., 2015, in EAS Publications Series, Vol. 75-76, EAS Publications Series, pp. 227–235

Schmiedeke A. et al., 2016, A&A, 588, A143

Schneider N., Csengeri T., Bontemps S., Motte F., Simon R., Hennebelle P., Federrath C., Klessen R., 2010, A&A, 520, A49

Schuller F. et al., 2009, A&A, 504, 415

Seifried D., Banerjee R., Klessen R. S., Duffin D., Pudritz R. E., 2011, MNRAS, 417, 1054

Shan W. et al., 2012, IEEE Transactions on Terahertz Science and Technology, 2, 593

Shepherd D. S., Testi L., Stark D. P., 2003, ApJ, 584, 882

Shepherd D. S., Watson A. M., Sargent A. I., Churchwell E., 1998, ApJ, 507, 861

Shinn J.-H. et al., 2014, ApJS, 214, 11

Shirley Y. L., Evans, II N. J., Young K. E., Knez C., Jaffe D. T., 2003, ApJS, 149, 375

Shu F. H., Adams F. C., Lizano S., 1987, ARA&A, 25, 23

Simon R., Rathborne J. M., Shah R. Y., Jackson J. M., Chambers E. T., 2006, ApJ, 653, 1325

Simpson J. P., Cotera A. S., Burton M. G., Cunningham M. R., Lo N., Bains I., 2012, MNRAS, 419, 211

Smith M. D., Rosen A., 2005, MNRAS, 357, 1370

Smith R. J., Shetty R., Beuther H., Klessen R. S., Bonnell I. A., 2013, ApJ, 771, 24

Spitzer L., 1978, Physical processes in the interstellar medium

Sridharan T. K., Beuther H., Schilke P., Menten K. M., Wyrowski F., 2002, ApJ, 566, 931

Stahler S. W., Palla F., 2004, The Formation of Stars

Svoboda B. E. et al., 2016, ApJ, 822, 59

Swarup G., 1991, Astronomical Society of the Pacific Conference Series, Vol. 19, Giant metrewave radio telescope (GMRT), Cornwell T. J., Perley R. A., eds., pp. 376–380

Szűcs L., Glover S. C. O., Klessen R. S., 2016, MNRAS, 460, 82

Szymczak M., Pillai T., Menten K. M., 2005, A&A, 434, 613

Tackenberg J. et al., 2014, A&A, 565, A101

Takahira K., Shima K., Habe A., Tasker E. J., 2018, PASJ, 70, S58

Takahira K., Tasker E. J., Habe A., 2014, ApJ, 792, 63

Takami M., Chen H.-H., Karr J. L., Lee H.-T., Lai S.-P., Minh Y.-C., 2012, ApJ, 748, 8

Tan J. C., Beltrán M. T., Caselli P., Fontani F., Fuente A., Krumholz M. R., McKee C. F., Stolte A., 2014, Protostars and Planets VI, 149

Tan J. C., Kong S., Butler M. J., Caselli P., Fontani F., 2013, ApJ, 779, 96

Tasker E. J., Tan J. C., 2009, ApJ, 700, 358

Torii K. et al., 2011, ApJ, 738, 46

Torii K. et al., 2015, ApJ, 806, 7

Torii K. et al., 2017, ApJ, 835, 142

Towner A. P. M., Brogan C. L., Hunter T. R., Cyganowski C. J., Friesen R. K., 2019, ApJ, 875, 135

Urquhart J. S. et al., 2009, A&A, 501, 539

Urquhart J. S. et al., 2014, MNRAS, 443, 1555

van der Tak F. F. S., Black J. H., Schöier F. L., Jansen D. J., van Dishoeck E. F., 2007, A&A, 468, 627

Varricatt W. P., Davis C. J., Adamson A. J., 2005, MNRAS, 359, 2

Varricatt W. P., Davis C. J., Ramsay S., Todd S. P., 2010, MNRAS, 404, 661

Vasyunina T., Linz H., Henning T., Zinchenko I., Beuther H., Voronkov M., 2011, A&A, 527, A88

Veena V. S., Vig S., Tej A., Varricatt W. P., Ghosh S. K., Chandrasekhar T., Ashok N. M., 2016, MNRAS, 456, 2425

Vig S., Veena V. S., Mandal S., Tej A., Ghosh S. K., 2018, MNRAS, 474, 3808

Vutisalchavakul N., Evans, II N. J., 2013, ApJ, 765, 129

Ward-Thompson D., Robson E. I., 1990, MNRAS, 244, 458

Watson C. et al., 2008, ApJ, 681, 1341

Widmann F., Beuther H., Schilke P., Stanke T., 2016, A&A, 589, A29

Williams J. P., Blitz L., McKee C. F., 2000, in Protostars and Planets IV, Mannings V., Boss A. P., Russell S. S., eds., p. 97

Williams J. P., de Geus E. J., Blitz L., 1994, ApJ, 428, 693

Wilson T. L., Rood R., 1994, ARA&A, 32, 191

Wirström E. S. et al., 2011, A&A, 533, A24

Wolfire M. G., Cassinelli J. P., 1987, ApJ, 319, 850

Wood D. O. S., Churchwell E., 1989, ApJS, 69, 831

Wright E. L. et al., 2010, AJ, 140, 1868

Wu J., Evans, II N. J., 2003, ApJL, 592, L79

Wu Y., Henkel C., Xue R., Guan X., Miller M., 2007, ApJL, 669, L37

Wu Y., Liu T., Meng F., Li D., Qin S.-L., Ju B.-G., 2012, ApJ, 756, 76

Wu Y., Qin S.-L., Guan X., Xue R., Ren Z., Liu T., Huang M., Chen S., 2009, ApJL, 697, L116

Wyrowski F. et al., 2016, A&A, 585, A149

Xue X. X. et al., 2008, ApJ, 684, 1143

Yu N., Wang J.-J., 2015, MNRAS, 451, 2507

Yu N., Xu J., 2016, ApJ, 833, 248

Yu N.-P., Wang J.-J., 2013, Research in Astronomy and Astrophysics, 13, 28

Yuan J. et al., 2018, ApJ, 852, 12

Yuan J. et al., 2017, ApJS, 231, 11

Zapata L. A., Palau A., Ho P. T. P., Schilke P., Garrod R. T., Rodríguez L. F., Menten K., 2008, A&A, 479, L25

Zapata L. A., Rodríguez L. F., Ho P. T. P., Beuther H., Zhang Q., 2006, AJ, 131, 939

Zhang C.-P. et al., 2018, ApJS, 236, 49

Zhang C.-P., Yuan J.-H., Li G.-X., Zhou J.-J., Wang J.-J., 2017, A&A, 598, A76

Zhang Q., Hunter T. R., Brand J., Sridharan T. K., Molinari S., Kramer M. A., Cesaroni R., 2001, ApJL, 552, L167

Zhang Q., Wang Y., Pillai T., Rathborne J., 2009, ApJ, 696, 268

Zinnecker H., Yorke H. W., 2007, ARA&A, 45, 481

List of Publications

Publications based on the Thesis

1. **G133.50+9.01: A likely cloud-cloud collision complex triggering the formation of filaments, cores and a stellar cluster**, N. Issac, A. Tej, T. Liu, Y. Wu, 2020, MNRAS, 499, 3620

2. **Multiwavelength investigation of extended green object G19.88-0.53: Revealing a protocluster**, N. Issac, A. Tej, T. Liu, W. Varricatt, S. Vig, C. H. Ishwara-Chandra, M. Schultheis, G. Nandakumar, 2020, MNRAS, 497, 5454

3. **Initial phases of high-mass star formation: a multiwavelength study towards the extended green object G12.42+0.50**, N. Issac, A. Tej, T. Liu, W. Varricatt, S. Vig, C. H. Ishwara-Chandra, M. Schultheis, 2019, MNRAS, 485, 1775

Other publications

1. **ATOMS: ALMA three-millimeter observations of massive star-forming regions - II. Compact objects in ACA observations and star formation scaling relations**, T. Liu et al., and 43 co-authors including N. Issac, 2020, MNRAS, 496, 2821

2. **ATOMS: ALMA Three-millimeter Observations of Massive Star-forming regions - I. Survey description and a first look at G9.62+0.19**, T. Liu et al., and 44 co-authors including N. Issac, 2020, MNRAS, 496, 2790